Final project

SMOS Flight external calibration and monitoring

Author:

Israel Durán Martínez

Department of Signal Theory and Communications

Universitat Politècnica de Catalunya (UPC)

C/Jordi Girona 1-3, D3-116 Campus Nord, 08034 Barcelona (Spain)

Project Advisors:

Prof. Francesc Torres Torres

Prof. Núria Duffo Úbeda

[xtorres,duffo]@tsc.upc.edu

Department of Signal Theory and Communications

Universitat Politècnica de Catalunya (UPC)

Barcelona, July 2010

Acknowledgments

I would like to express my gratitude to Prof. Francesc Torres and Prof. Núria Duffo , my project directors, for their support and suggestions during the development of this project.

I would like to express my gratitude in special manner to Prof. Ignasi Corbella, Prof. Mercè Vall-llossera, Verónica González and Miriam Pablos who have provided me assistance in numerous ways.

Thanks to my workmates Wu Lin and Ruben Davila.

I would like to show my gratitude to Davinia. She has helped me in difficult times during the project.

Finally, I would also like to thank my parents. They have always supported and encouraged me to do my best in these studies.

Contents

List of Figures

List of Tables

List of Acronyms

CAS	CAlibration Subsystem
CDTI	Centro para el Desarrollo Tecnológico Industrial
CMN	Control and Monitoring Node
CNES	Centre National d'Etudes Spatiales
ESA	European Space Agency
LICEF	Light-Weight Cost Effective Front-End
MIRAS	Microwave Imaging Radiometer with Aperture Synthesis
MIRAS-TS	MIRAS Testing Software
NIR	Noise Injection Radiometer
PMS	Power Measurement System
SMOS	Soil Moisture Ocean Salinity
TSC	Theory of Signal and Communications
UPC	Universitat Politècnica de Catalunya
MDB	MIRAS Data Base

Chapter 1

1 Introduction

1.1 Scope of the final project

One of the main objectives of any mission is to obtain and provide stable and accurate data. So, a well-calibrated instrument provides the basis for stable measurements. The calibration of any Earth Observation sensor is a key stage which encompasses those tasks which are necessary to convert the raw measurement data into science data.

The scope of this final project is to analyze the flight external calibration of the instrument, mainly by developing a new tool that performs calibration and obtains a better output image.

This project has been developed in the frame of projects devoted to asses and characterize the Microwave Imaging Radiometer by Aperture Synthesis (MIRAS), the single payload of the European Space Agency (ESA) Soil Moisture and Ocean Salinity (SMOS) mission.

The first steps of this project were in September 2009 in the Remote Sensing Laboratory Group of TSC (Theory of Signal and Communications Department) at UPC. Shortly after, the satellite was launched on November 2009 after years of hard research work. So, once the instrument was in orbit it started to send flight data that was the key to carrying out the activities presented in this work.

1.2 Objectives of the final project

This project has been devoted to develop several tools to assess in-flight performance of the MIRAS SMOS amplitude calibration. It has been mainly focused to analyze the performance of current internal calibration by means of the so-called one-point calibration. This allowed to develop External CAS and Antenna efficiency correction parameters to improve overall MIRAS amplitude calibration accuracy.

Once the final calibration procedure has been frozen, this work has aimed to analyze MIRAS long term stability by estimating the drift of the main calibration parameters: PMS gain and offset, receiver temperature, fringe wash coefficient, etc.

Finally a tool called CQC (Calibration Quality Check) has been developed to easily monitor the quality of SMOS calibration events along the operational cycle of the instrument.

All activities have used flight data from December 2009 to June 2010 to cover the so-called SMOS commissioning phase. Once successfully characterized, SMOS has started its 3-5 years operational life on May 2010.

1.3 Organization of the final project

This section is devoted to describe the project organization, which is divided into nine chapters. The first chapters are devoted to introduce the reader in the context of the SMOS mission, as well as to give a general description of the instrument and the basic concepts of calibration. The following chapters present all related with External CAS and Antenna efficiency correction and further analysis with calibration parameters, and results from programs developed for checking calibration quality.

In this sense, Chapter 2 describes the basic concepts of radiometry.

Chapter 3 gives an overview of the SMOS mission and the instrument, in order to describe the context in which this project has been carried out.

Chapter 4 describes the amplitude calibration approach.

Chapter 5 shows the equations of CAS coefficients and some preliminary results.

Chapter 6 illustrates the method of computing External CAS factors and External Antenna efficiency and it presents results.

Chapter 7 shows the analysis of the long term stability of calibration parameters because is an important task to know if different parameters of the instrument are stable in time.

Chapter 8 describes the CQC (Calibration Quality Check) Tool presenting results with real data.

Finally, Chapter 9 summarizes the main conclusions of this work. This is completed by the list of publications as presented in the annex.

Chapter 2

2 Basic concepts of radiometry

SMOS is a radiometer. That is, it is a passive instrument that collects the natural thermal emission of a body. In this sense, this chapter describes the basic concepts of radiometry to give a grasp on the fundamentals of its application to remote sensing.

2.1 Brightness and power measured by the antenna

The power emitted by a body at a solid angle per unit area is called brightness [$W\ sr^{-1}\ m^{-2}$]. If the area radiates with a pattern $F_t(\theta,\phi)$, the brightness $B(\theta,\phi)$ can be defined as:

$$B(\theta,\phi) = \frac{F_t(\theta,\phi)}{A_t} \quad \textbf{(2.1)}$$

where A_t is the total area that is radiating.

If it is considered the case of two lossless antennas separated a distance R, oriented in the direction of maximum directivity with an effective area A_t for the transmitting antenna and A_r for the receiving antenna, being R large enough to be considered constant power over a solid angle Ω_r,then the measured power by the receiver antenna is described by the next equation:

$$P_r = S_t \cdot A_r \quad \textbf{(2.2)}$$

In the previous expression S_t is the radiation power and can be defined as:

$$S_t = \frac{F_t}{R^2} \quad \textbf{(2.3)}$$

Replacing the expressions *(2.1) and (2.3) in the equation (2.2)* ,the power measured by the antenna depending on the brightness is:

$$P_r = B \cdot A_r \cdot \frac{A_t}{R^2} \quad \textbf{(2.4)}$$

where the solid angle observed by the receiver antenna is:

$$\Omega_t = \frac{A_t}{R^2} \quad \textbf{(2.5)}$$

So, the power measured by the antenna can be expressed as:

$$P_r = B \cdot A_r \cdot \Omega_t \quad \textbf{(2.6)}$$

If the emitting surface is not observed by the receiver antenna in the maximum direction of the radiation pattern, the diagram must be added:

$$dP = A_r \cdot B(\theta,\phi) \cdot \left|F_n(\theta,\phi)\right|^2 \quad \textbf{(2.7)}$$

If the brightness is not constant with frequency, it is defined the spectral brightness density $B_f(\theta,\phi)$ [$W \;\; sr^{-1} \;\; m^{-2} \;\; Hz^{-1}$]. The total power measured by the antenna can be obtained by integrating the expression in bandwidth and space system:

$$P = \frac{1}{2} A_r \int_f^{f+B} \iint_{4\pi} B_f(\theta,\phi) \left|F_n(\theta,\phi)\right|^2 d\Omega df \quad \textbf{(2.8)}$$

The term $\frac{1}{2}$ in the previous expression takes into account that the antenna that presents a polarization determined, only measures half the thermal power emitted if the source emission is randomly polarized.

2.2 Thermal radiation

All bodies that are at a higher temperature above 0 K emit electromagnetic radiation.

According to quantum theory, each spectral line corresponds to the transition of an electron from an atomic energy level ε_1 to a lower energy level ε_2. Radiation occurs at a frequency given by the Bohr equation:

$$f = \frac{\varepsilon_1 - \varepsilon_2}{h} \quad \textbf{(2.9)}$$

where the parameter h corresponds to Planck's constant.

Atomic emission is caused by a collision with another atom or particle. The probability of emission is higher for atomic and kinetic higher energy densities. According to Kirchoff's law in thermodynamic equilibrium, all the energy absorbed is re-emitted.

In the case of a black body (opaque perfectly ideal body that absorbs all incident radiation of all frequencies, without reflecting anything) the radiated energy follows Planck's law, so radiates uniformly in all directions with a spectral brightness [$W\ m^{-2}\ sr^{-1}\ Hz^{-1}$] which corresponds to the following expression:

$$B_f = \frac{2hf^3}{c^2} \cdot \frac{1}{e^{\frac{h \cdot f}{k_B \cdot T_{ph}}} - 1} \quad \textbf{(2.10)}$$

In the previous expression f corresponds to the frequency (Hz), k_B is the Boltzmann's constant, T_{ph} is the absolute temperature in Kelvin and c is the speed of light.

It's possible to obtain an expression for the total brightness by integrating the equation *(2.10)* on the whole spectrum, so that the brightness of a black body responds to the expression:

$$B_{bb} = \int_0^\infty B_f df = \frac{\sigma \cdot T_{ph}^4}{\pi} \quad \textbf{(2.11)}$$

Where the parameter $\sigma = 5.673 \cdot 10^{-8}$ [$W\ m^{-2}\ sr^{-1}\ k^{-4}$] is the Stefan-Boltzmann's constant.

The *Fig. 2.1* shows the brightness spectral density versus frequency for different physical temperatures. The curves illustrate two variations of brightness with distinct wavelengths. For high frequencies, equation *(2.10)* is reduced to the following expression (Wien's law):

$$B_f = \frac{2h}{c^2} \cdot f^3 \cdot e^{\frac{h \cdot f}{k_B \cdot T_{ph}}} \quad \textbf{(2.12)}$$

In the case of low frequencies the function approaches the Rayleigh-Jeans law. As shown in equation *(2.13)*, there is a linear relationship between spectral brightness density and physical temperature.

$$B_f = \frac{2 f^2 k_B T_{ph}}{c^2} = \frac{2 k_B T_{ph}}{\lambda^2} \quad \textbf{(2.13)}$$

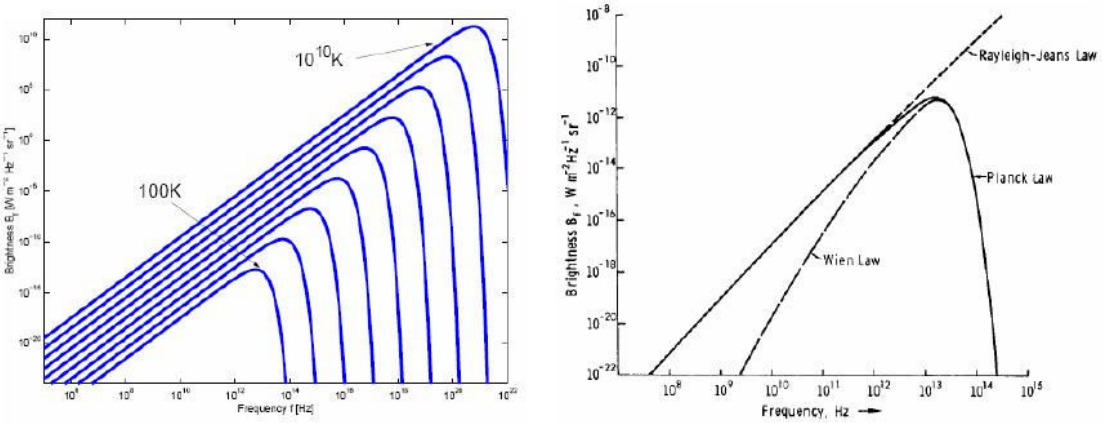

Fig. 2.1 Top left:brightness spectral density vs frequency for different physical temperatures, above right, approaches the Planck's radiation law: the law of Rayleigh-Jeans(low frequency) and Wien's law(high Frequency)

2.3 Gray body radiation. Brightness temperature and emissivity

A black body, in thermal equilibrium, radiates all the energy it has absorbed and therefore emits as much energy to a specific physical temperature.

On the other hand, real materials (also called gray bodies) emit less power than a black body because they do not absorb all the energy incident on them.

In the case of a gray body, the brightness emitted depends on the direction $B(\theta,\phi)$ and can be expressed as follows:

$$B(\theta,\phi) = 2 \cdot \frac{k_B}{\lambda^2} \cdot T_B(\theta,\phi) \cdot B \quad \textbf{(2.14)}$$

where T_B is the brightness temperature and B is the bandwidth .

The relationship between brightness $B(\theta,\phi)$ of a material and the brightness of a black body that is on the same physical temperature is called emissivity:

$$e(\theta,\phi) = \frac{B(\theta,\phi)}{B_{bb}} = \frac{T_B(\theta,\phi)}{T_{ph}} \quad \textbf{(2.15)}$$

Where $0 \le e(\theta,\phi) \le 1$. The brightness temperature of a gray body expresses its emission properties (angular dependent) compared with that of a black body.

Since the brightness temperature of a gray body is less than of a black body, the brightness temperature of a material is always less or equal than its physical temperature. Therefore, the emissivity has value 0 for a fully reflective material and has value 1 for a perfect absorber (black body).

2.4 Apparent temperature

The incident radiation over an antenna consists of several items from various sources: the radiation emitted by the ground, T_B, the radiation emitted by the atmosphere and the radiation emitted by the atmosphere that falls on the ground and that is reflected.

Apparent radiometric temperature, $T_{AP}(\theta,\phi)$, is the distribution of the temperature of an equivalent black body, and its brightness distribution, $B_i(\theta,\phi)$, is the incident energy over the antenna:

$$B_i(\theta,\phi) = \frac{2k_B}{\lambda^2} \cdot T_{AP}(\theta,\phi) \cdot \Delta f \quad \textbf{(2.16)}$$

The brightness temperature, $T_B(\theta,\phi)$, is related to the radiation received on a surface or volume, while the apparent temperature, $T_{AP}(\theta,\phi)$, is related to the incident energy received by the antenna. In the case of atmosphere losses were negligible, the apparent temperature would be equal to the brightness temperature.

As seen, the brightness's distribution of a gray body can be expressed in terms of the apparent temperature. Thus, taking into account the previous theory and the expression *(2.8)* the power received by the antenna can be expressed as follows:

$$P = \frac{1}{2} \cdot A_r \cdot \iint_{4\pi} \frac{2k}{\lambda^2} \cdot T_{AP}(\theta,\phi) \cdot \Delta f \cdot F_n(\theta,\phi) \cdot d\Omega \quad \textbf{(2.17)}$$

When computing the transfer function of the receiver, measuring the output voltage as a function of physical temperature of a load placed at the receiver input, it's possible to obtain the noise power, P_N, which is proportional to physic temperature. If the correspondence is done with the power supplied by the antenna to the receiver, it is called radiometric antenna temperature, T_A, such as an equivalent resistance to deliver the same power:

$$P_n = P = k \cdot T_A \cdot \Delta f \quad \textbf{(2.18)}$$

Therefore, the antenna temperature can be expressed in terms of the normalized radiation diagram of the antenna, $F_n(\theta,\phi)$, and its effective area, A_r as follows:

$$T_A = \frac{A_r}{\lambda^2} \cdot \iint_{4\pi} T_{AP}(\theta,\phi) \cdot F_n(\theta,\phi) \cdot d\Omega \quad \textbf{(2.19)}$$

A passive radiometer is an instrument that measures the spontaneous electromagnetic emission. This radiation is normally associated with thermal effect: the brightness temperature.

Unlike other receivers, such as radar receivers that consider the antenna radiometric temperature T_A is a noise contribution, the radiometers obtain from the signal information on the emission characteristics of the scene being viewed.

2.5 Total power radiometer

So far, all microwave radiometers used for observation of the earth have been real aperture radiometers. The more simplified version of this type of radiometers is the Total Power Radiometers (TPR).

A total power radiometer consists of an antenna connected to a superheterodyne receiver with bandwidth B and total gain G, followed by a power detector and a lowpass filter (*Fig. 2.2*). The power delivery by the antenna is usually noise with higher noise than the range of the receiver. The antenna receives the RF power emitted by the material observed and an RF amplifier (low noise) increases the noise power of the signal acquired. The bandpass filter selects the desired frequency band which is converted in the mixer. The signal is amplified before passing through the power detector. Finally, it is necessary to use a low pass filter to average the obtained voltage. In a total power radiometer, the output voltage is proportional to the noise temperature of the system and can be written as:

$$V_{out} = k \cdot T_{sys} \cdot B \quad \textbf{(2.20)}$$

where $T_{sys} = T_A + T_R$ is the system noise temperature, T_A is the equivalent noise temperature measured by the antenna, T_R is the equivalent noise temperature of the receiver and B is the bandwidth.

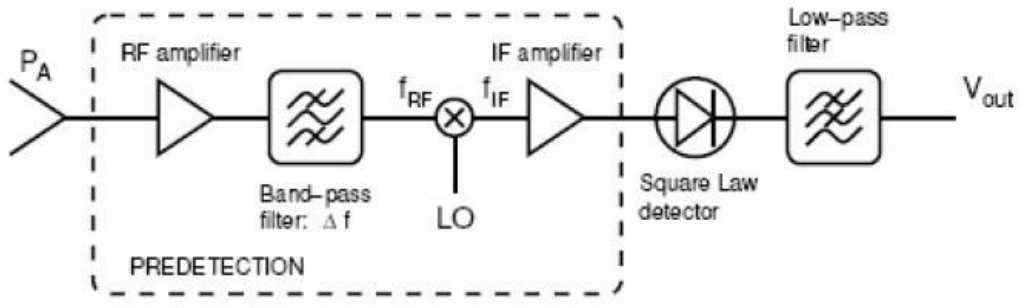

Fig. 2.2 TPR Block Diagram

In order to calibrate a total power radiometer is enough to measure the output voltage corresponding for two noise temperatures in the input (cold and hot load). So, a TPR requires only external calibration (*Fig. 2.3*).

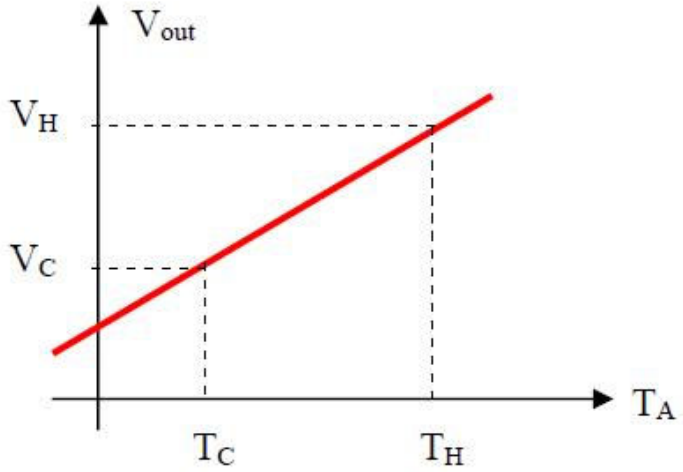

Fig. 2.3 TPR calibration using a hot and cold load

2.6 Interferometric Radiometer with aperture synthesis

The spatial resolution that can reach a radiometer is limited by the size of the antenna. The measurements of geophysical parameters such as soil moisture and ocean salinity at L-band require high spatial resolution, and therefore the size of the antenna of a real aperture radiometer to allow such resolution is not technologically viable. For this reason, it is necessary to use an interferometric radiometer by aperture synthesis of 2D for the realization of these measurements.

An interferometric radiometer consists of an array of antennas. The output voltages of different pairs of antennas are correlated and return the visibility function. From the samples of this function, using image inversion algorithms, the image is reconstructed obtaining brightness temperature maps of the scene. Chapter 3 gives a summarized description of radiometric interferometry principles

Chapter 3

3 The SMOS mission

The SMOS mission (Soil Moisture and Ocean Salinity) has been designed to observe soil moisture over the Earth's landmasses and salinity over the oceans.

SMOS is the second Earth Explorer Opportunity mission to be developed as part of ESA's Living Planet Programme [1], in cooperation with Centre National d'Etudes Spatiales (CNES) in France and Centro para el Desarrollo Tecnológico Industrial (CDTI) in Spain, and some European institutions, including UPC have taken part in the instrument development and in the measurement campaigns.
The main contribution in the design and analysis of instrument operation was performed by the radiometric team of TSC (Theory of Signal and Communications Department) at UPC [3]. European Universities and other institutions, among them the SMOS Barcelona Expert Centre on Radiometric Calibration and Ocean Salinity (SMOS-BEC) [4] are also involved in the data processing.

Basically, the data acquired from this mission will contribute to understand the Earth's water cycle. Additionally, SMOS data will lead to better weather and extreme-event forecasting, and contribute to seasonal-climate forecasting. As a secondary objective, SMOS will also provide observations over regions of snow and ice, contributing to studies of the cryosphere.

Fig. 3.1 SMOS in orbit

3.1 SMOS objectives

SMOS has been designed to observe soil moisture over the Earth's landmasses and salinity over the oceans. Soil moisture data are urgently required for hydrological studies and data on ocean salinity are necessary to improve our knowledge of ocean circulation patterns.

The method of measuring Soil Moisture is related to the amount of water within a given volume of material (usually in percentage). While Salinity describes the concentration of dissolved salts in water, it measures the practical salinity units (psu).

On the one hand, soil only holds a small percentage of the total global water budget, soil moisture plays an important role in the global water cycle. However, measurements of soil moisture are sparse so more data is urgently required to improve our understanding of the water cycle.

Fig. 3.2 Dry soil and Ocean salinity

On the other hand, there are few historical measurements of ocean salinity, and only a small fraction of the ocean is currently sampled on any regular basis. Salinity and temperature determine the density of seawater, and in turn density is an important factor driving the currents in our oceans. Ocean circulation plays a crucial role in moderating the climate by, for example, transporting heat from the Equator to the poles. Ocean salinity is therefore one of the key variables for monitoring and modeling ocean circulation.

3.2 MIRAS instrument

MIRAS comprises a single payload instrument known as the Microwave Imaging Radiometer with Aperture Synthesis coupled to a PROTEUS platform [5].

MIRAS synthesizes a large aperture from a reasonably sized 2-D array of passive microwave radiometers. By using interferometric techniques, the required coverage and spatial resolution can be achieved without the need for a large antenna.

It is the first ever satellite in the world designed both to map sea surface salinity and to monitor soil moisture on a global scale. It features a unique interferometric radiometer that will enable passive surveying of the water cycle between oceans, the atmosphere and land.

In readiness for launch on 2 November, ESA's SMOS satellite – encapsulated in the launcher fairing – was transported from the cleanroom and installed in the launch tower at the Plesetsk Cosmodrome in northern Russia.

Fig. 3.3 Transfer to launch pad by train

The satellite was launched atop a Rockot launch vehicle provided by Eurockot GmbH [2]. Liftoff from the Plesetsk Cosmodrome in northern Russia took place at 01:50 UTC (02:50 CET) on Monday 2 November.

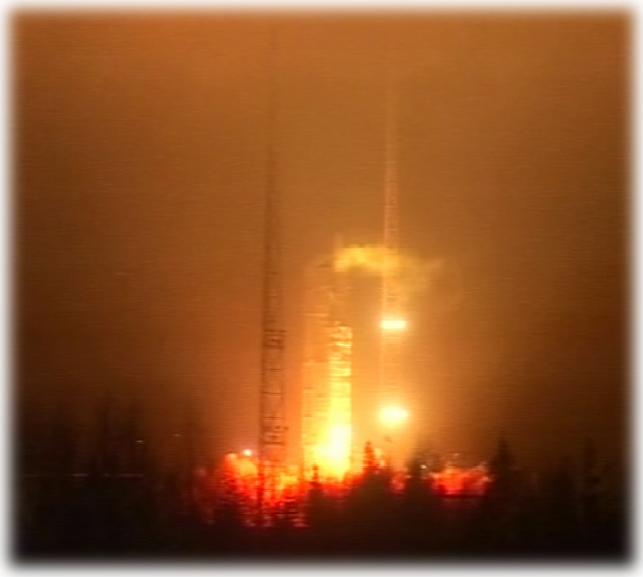

Fig. 3.4 SMOS liftoff

Some 70 minutes after launch, SMOS successfully separated from the Rockot's Breeze-KM upper stage. Shortly after, the satellite's initial telemetry was acquired by the Hartebeesthoek ground station in South Africa. The upper stage then performed additional manoeuvres to arrive at a slightly lower orbit.

The satellite is currently circling the Earth on their respective sun-synchronous orbits, at an altitude of about 760 km.

Fig. 3.5 SMOS separation from Breeze

3.2.1 Instrument architecture

MIRAS instrument consists of a Y-shape synthetic aperture radiometer operating at L-band (1,4 GHz) formed by 72 receivers called LICEFs (Light-Weight Cost Effective Front-End), equally distributed along the three deployable arms, which are connected to a central structure called HUB.

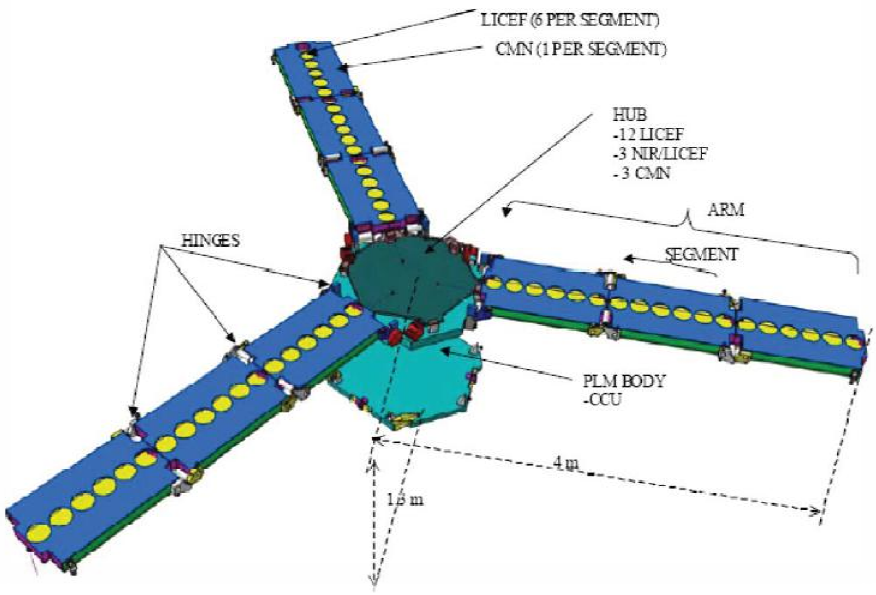

Fig. 3.6 Instrument architecture

The central HUB is 1.3 m. in diameter with three arms extending up to 8 m. in diameter. The arms are equally spaced with an angular separation of 120 degrees. Each arm comprises three segments, each containing six L-band receivers. The line of 18 receivers in each arm is complemented by a further four receivers in the central HUB, making a total of 66 receivers, 12 in the HUB and 54 in the arms. Due to their design, these receivers are known as lightweight cost-effective front-ends (LICEFs).

In addition, there are three noise injection radiometers (NIRs) placed in the central HUB. These NIRs are included to complete the calibration concept. Each NIR also performs as two different LICEFs placed in the same position. In practice, each NIR consists of two LICEF receivers coupled to a single antenna. Thus, in total, the MIRAS comprises 69 antennas (for the 66 LICEFs and 3 NIRs) but 72 receivers (66 LICEFs plus 6 for the NIRs).

The function of the LICEFs and NIRs is to measure the antenna radiometric temperature which represents the radiation noise power delivered by the antenna (corresponding to the brightness temperature of the scene) to the receiver.

Each segment of the instrument also contains a Control and Monitoring Node (CMN) that provides power and a phased local oscillator to each LICEF.

3.2.2 Operating principle

Each LICEF is an antenna-received integrated unit that measures the radiation emitted from the Earth or Space at L-band (1,4 GHz). This acquired signal is then transmitted to a central correlator unit that performs interferometry cross-correlations of the signals between all possible combinations of receiver pairs (called baselines), providing the samples of the so-called visibility function:

$$V_{kj}(u,v) = \frac{1}{k_B\sqrt{B_k B_j}\sqrt{G_K G_j}} \cdot \frac{1}{2} < b_k \cdot b_j^* > \quad \textbf{(3.1)}$$

where (u,v) correspond to the set of spatial frequencies where the visibility function is sampled (antenna separation in wavelengths), G_k, G_j are the power gains of each receiver chain and B_k, B_j correspond to the equivalent noise bandwidths.

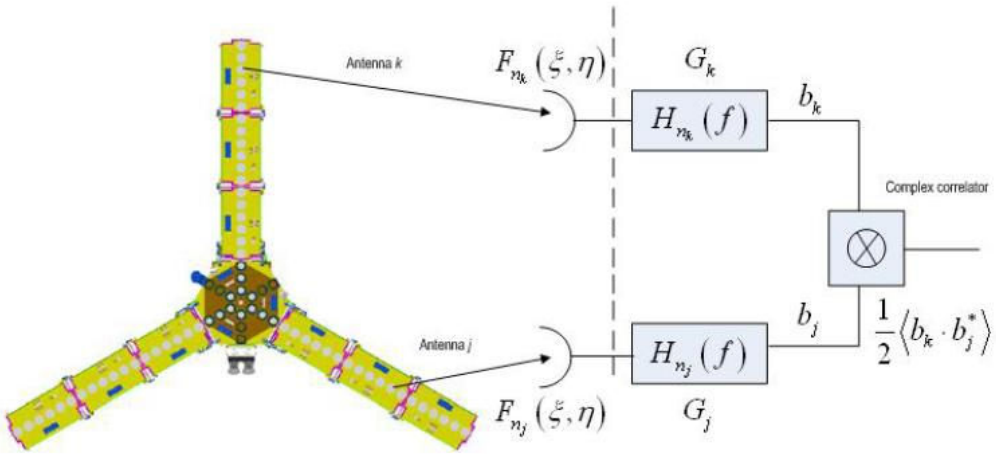

Fig. 3.7 Block diagram of a single baseline relating the measurement of a sample of the visibility function

One of the main differences between real aperture and interferometric radiometers is that the last one gives a multipixel image after a Fourier Transform of the visibility function. So, the interferometric radiometer does not perform a direct measurement of the brightness temperature because computes a set of samples of its Fourier Transform.

The following expression shows the visibility function of any pair of receivers k and j in terms of the brightness temperature:

$$V_{kj}(u,v) = \iint_{\xi^2+\eta^2\le 1} \frac{T_B(\xi,\eta) - T_r}{\sqrt{1-\xi^2-\eta^2}} \cdot \frac{F_{n_k}(\xi,\eta)\cdot F_{n_j}^*(\xi,\eta)}{\sqrt{\Omega_k \Omega_j}} \cdot \tilde{r}_{kj}\left(\frac{-u\xi+v\eta}{f_0}\right) \cdot e^{-j2\pi(u\xi+v\eta)} d\xi d\eta \quad \textbf{(3.2)}$$

where $\bar{r}_{kj}()$ corresponds to the Fringe Washing function normalized to unity at origin and it is related to the spatial decorrelation errors, $T_B(\xi,\eta)$ is the brightness temperature, $F_{n_k}(\xi,\eta)$, $F_{n_j}(\xi,\eta)$ are the normalized voltage antenna patterns, Ω_k, Ω_j correspond to the equivalent solid angle of the antennas and (ξ,η) are the director cosines with respect to X and Y axes, respectively.

The calibrated visibility samples are inverted by the image reconstruction algorithm to get the brightness temperature maps as a function of the director cosines at the antenna reference plane. In a first approach, (identical antenna patterns, negligible spatial decorrelation and no antenna positioning errors), this image reconstruction algorithm is performed by an inverse Fourier transform:

$$V_{kj}(u,v) = F[T_B(\xi,\eta)] \quad \textbf{(3.3)}$$

3.2.3 Observation modes

There are two main MIRAS instrument modes:

1. Measurement mode
2. Calibration mode

The measurement mode supports two further observation modes:

1. Dual-polarization mode
2. Full-polarization mode

On the one hand, in the dual-polarization measurement mode, the brightness temperatures are alternately measured in each polarization using an integration period, or epoch duration, of 1.2 s. In any epoch, all the LICEFs measure the same polarization. This produces 2346 baselines from the receivers in the same polarization (HH or VV), with an additional three measurements from the NIR receivers in the opposite polarization.

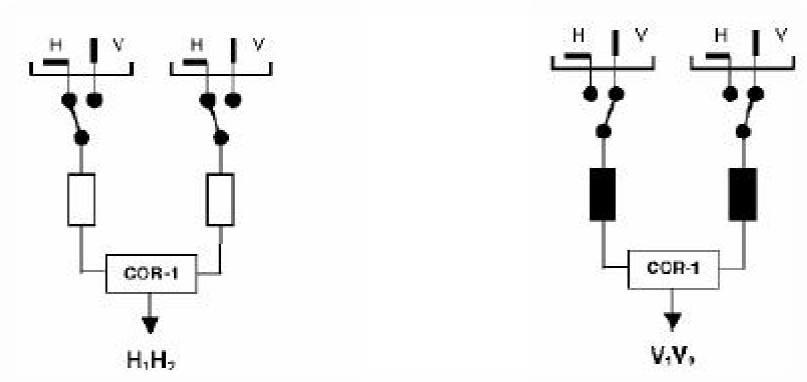

Fig. 3.8 Scheme Dual-polarization mode

On the other hand, in the full-polarization measurement mode, both the third and fourth Stokes parameters are also acquired. The timing cycle is based on a four-epoch sequence. For once epoch, all receivers measure one polarization, and for another epoch, all receivers measure the other polarization. In the other two epochs, the polarization of one arm (and corresponding HUB segment) is the opposite of the other two arms. The arm (and HUB segment), which is in the alternative polarization (to the other two arms), rotates in a clockwise direction.

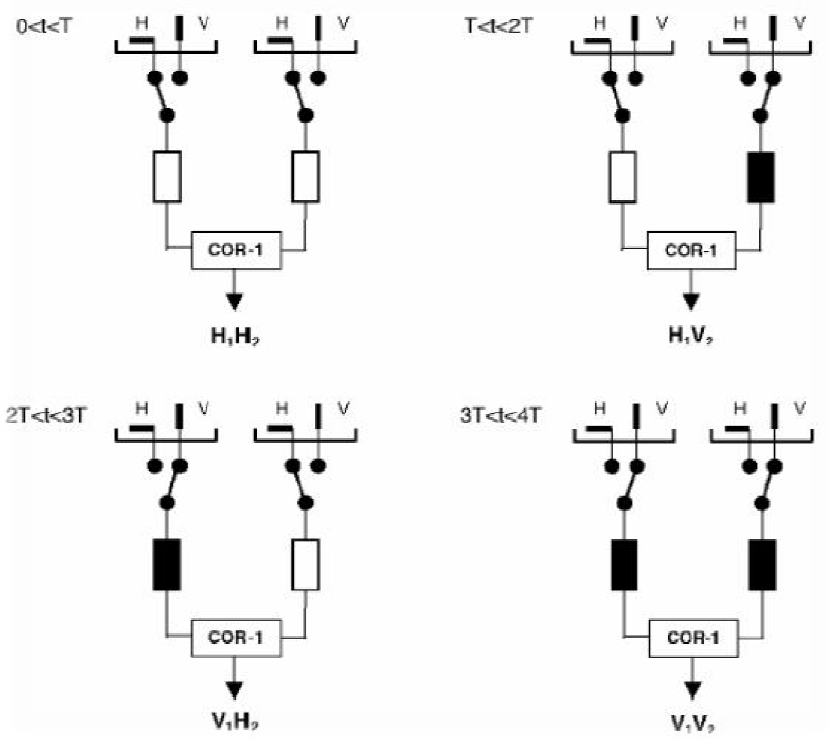

Fig. 3.9 Scheme Full-polarization mode

Finally, *Fig. 3.10* shows the measurement mode observation geometry:

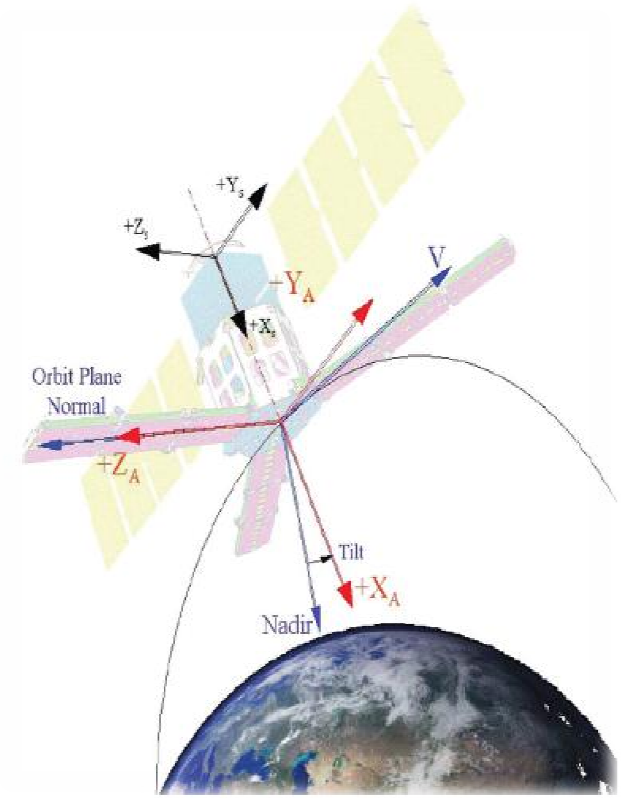

Fig. 3.10 Measurement mode observation geometry

3.2.4 MIRAS description

3.2.4.1 LICEF and NIR description

A LICEF is basically a radiometric receiver integrated with an antenna. Each LICEF has four inputs:

- 2 inputs from the antenna (H and V ports)
- 1 C-calibration input
- 1 U-load input

The outputs of each LICEF are the digitized downconverted I and Q components of the radio-frequency (RF) input plus the power level of the I-branch signal as sensed by the PMS circuitry. The cross correlations between the I/Q outputs of all LICEF receiver pairs are used to produce the MIRAS instrument system response function, which, after calibration and Fourier transformation in the Level 1 ground processor, become the brightness temperature map.

A block diagram and photographs of the LICEF are shown in *Fig. 3.11*:

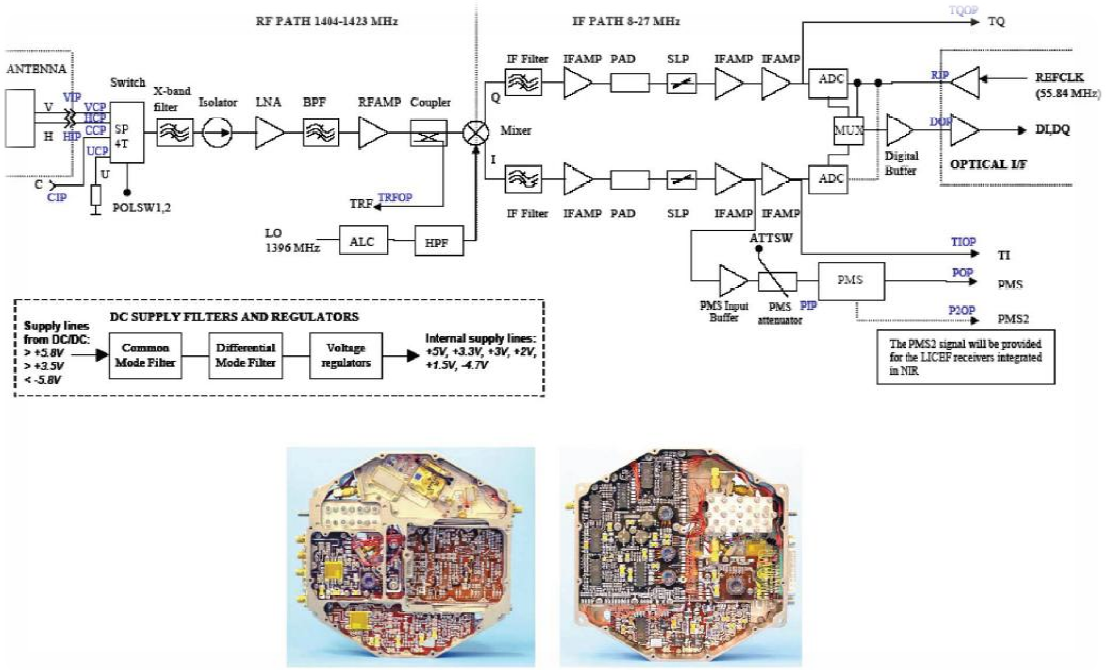

Fig. 3.11 (Upper) LICEF block diagram with photograph of LICEF (lower left) antenna side and (lower right) bottom side

The instrument carries three NIRs to measure:

- The full polarimetric antenna noise temperature
- The amplitude of the noise injected by the onboard CAS (Calibration Subsystem) with high precision.

The antenna temperature information is required for the retrieval of SMOS brightness temperature map, whereas the calibration of the output level of the centralized noise source is essential to calibrate the power level of the LICEF receivers. Additionally, each NIR will form interferometer baselines (called mixed baselines) with all LICEF units or other NIR units in a total power measurement mode.

Each NIR consists of one NIR controller unit (NIC) and two LICEF receivers, as shown in *Fig. 3.12* (lower), which indicates the flight hardware configuration of the NIR instrument as mounted on the HUB of MIRAS. An antenna identical to that of a LICEF is mounted on the NIC unit, and each polarization (H and V) is routed to one standard LICEF receiver through an "antenna branch". In each antenna branch, a noise pulse of variable length is added via a coupler to measure the antenna temperature. The length of the pulse is adjusted to keep the average input power to the LICEF receivers equal to the physical temperature of the internal LICEF U-matched load.

During onboard calibration, the NIR-LICEF receivers are switched to measure the CAS output, and the noise pulse is injected through a different "reference branch". The reference branch incorporates a reference-matched load in this case. A NIR uses two absolute calibration loads: the internal U-matched load of the LICEF and cold sky. To view the cold sky, the full SMOS satellite pointing is changed from earthfixed to inertial pointing periodically during one orbit. A software correction over temperature using in-orbit characterization coefficients has been computed for that purpose, which has been the main work of this final project.

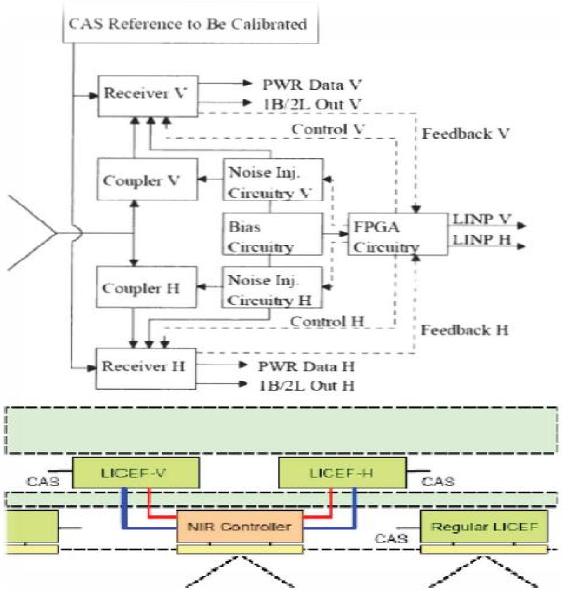

Fig. 3.12 (Upper) NIR block and (lower) flight configuration, showing NIR controller plus antenna (NIC) and LICEF H and V receivers

3.2.4.2 CAS (Calibration system and noise sources)

The onboard CAS provides a correlated noise reference to calibrate the noise temperature and relative phase characteristics between the LICEF receivers. CAS is based on a distributed noise injection. Three Arm Noise Sources (ANS) per arm and one HUB Noise Sourced (HNS), generate two different levels of reference noise (*Fig. 3.13*). This noise is split using two-by-six port Power Dividers (PD) for a set of 12 LICEFs with an overlap of six LICEFs so that every receiver can receive calibration noise from two adjacent noise sources, one at a time. The overlapping scheme is needed to keep track of the phase and amplitude of the signal over the whole calibration network.

CAS is basically a multiport structure with strict requirements on amplitude and phase difference between output ports, port isolation, and port matching. Careful prelaunch characterization and modeling of CAS has been necessary to meet these performance requirements. Moreover, since the physical temperature in-orbit varies between individual components of CAS, it is mandatory to determine CAS characteristics for all possible temperature distribution.

This is accomplished by:

1. Measuring, over temperature, the generated noise level and S-parameters of all individual NS units and the S-parameters of the PD units and adjacent cables
2. Combining the results in a mathematical model to simulate the behavior of the integrated CAS

The amplitude of the noise generated by CAS is periodically calibrated in-flight using the NIR receivers. The nominal levels of noise at the CAS outputs (and therefore LICEF inputs) are 75 K for the “warm” level and 1200 K for the “hot” level.

Fig. 3.13 Photographs of noise source (left) and power divider (right)

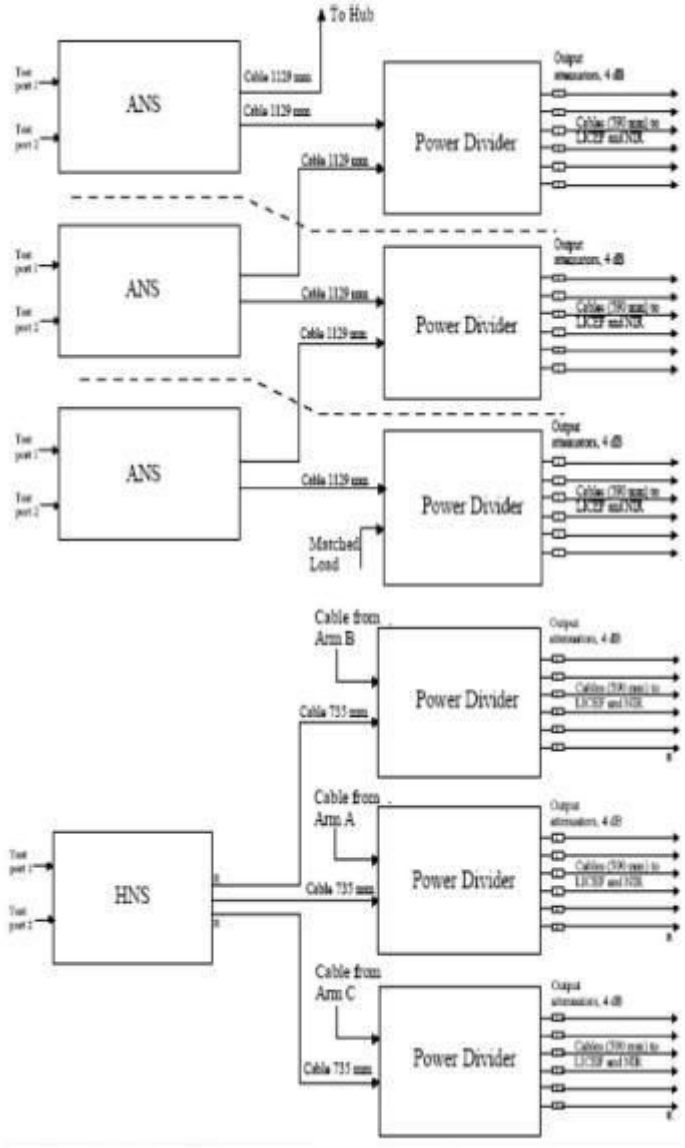

Fig. 3.14 Distributed CAS system for (upper) arm, (top) HUB

3.2.4.3 DICOS (Digital Correlator System)

Each Digital correlator of the instrument is called DICOS (Digital Correlator System). The digital signals produced by each LICEF are transmitted by optical fiber to the central matrix of correlators.

Each correlator is an exclusive NOR gate, so the output is only '1' if the two input signals are equal. The correlation is measured accumulating its output during the integration time using the clock frequency $f_S = 55.84MHz$.

At the end of the integration time the correlation accounts are read and reset the accumulator for the next period of integration.

Therefore, the correlation accounts of DICOS output for each pair of receivers correspond to the number of bits that matches between the input signals of the correlator during integration time.

MIRAS consists of 72 receivers, and then there are 2556 different baselines (72 I signals, 72 Q signals, and constant channels '1' and '0').

3.2.4.4 CMN (Control and Monitoring Node) and Local Oscillators

The CMN (Control and Monitoring Node) acts as a remote terminal of the CCU (Instrument Central Computer Unit). Each of the three arms of MIRAS contains three identical segments of six LICEFs each. In each segment, there is one CMN responsible for the control and monitoring of that segment. The HUB is divided in three sectors-each equipped with one CMN serving four LICEFs and two NIR-LICEFs. In addition, the CMN is used to control the onboard CAS.

Each CMN, in turn, provides power and a phased local oscillator (LO) signal controlled by a 55.84 MHz reference clock supplied by the optical link MOHA (MIRAS Optical Harness) to each LICEF.

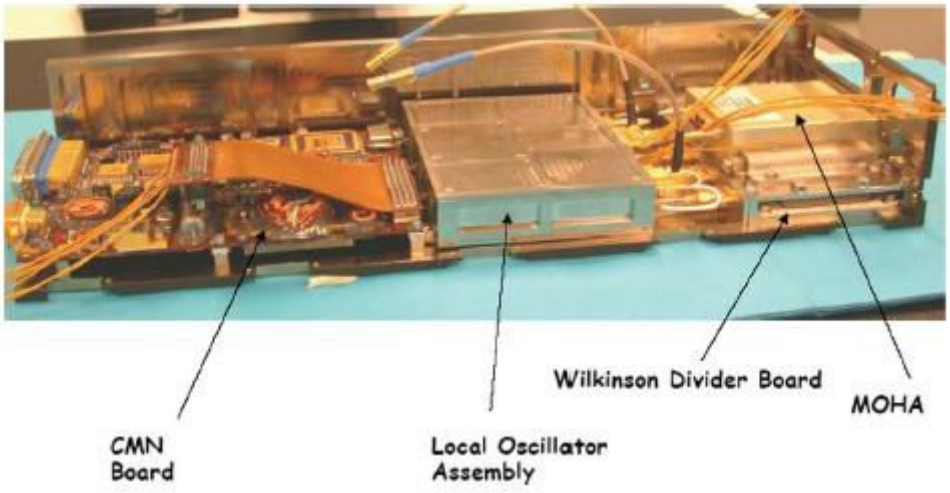

Fig. 3.15 Photographs of CMN main component elements

3.2.4.5 PMS (Power Measurement System)

Each LICEF receiver contains a Power Measurement System (PMS). The PMS of each LICEF performs the conversion to power of the received signal voltage.

Each power measurement system consists of a diode detector and integrator and its behavior is equivalent to a total power radiometer. The PMS block diagram is shown in *Fig. 3.16*:

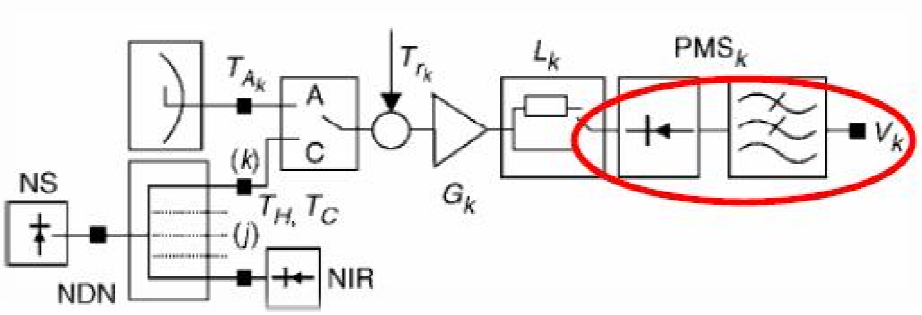

Fig. 3.16 PMS scheme

The output voltage of PMS can be approximated for the next equation:

$$v_k = G_k \cdot (T_{A_k} + T_{r_k}) + v_{off} \quad \textbf{(3.4)}$$

Where G_k and v_{off} are gain and offset of PMS, respectively.

The system temperature is defined by:

$$T_{sys_k} = T_{A_k} + T_{r_k} \quad \textbf{(3.5)}$$

Both the gain and offset are parameters that are computed in the PMS calibration.

The visibility samples are normalized to the system temperature, then, is necessary to know the value of this parameter. Using the voltage measurement of PMS in each moment, if gain and offset are known, is possible to compute the system temperature:

$$T_{A_k} + T_{r_k} = \frac{v_k - v_{off}}{G_k} \quad \textbf{(3.6)}$$

3.2.4.6 Thermal Control System (HEATERS)

The thermal control subsystem is designed to minimize the temperature differences between all the LICEF and the NIR units. This is achieved by placing all these units on thermal doublers (aluminum plates used to equalize the temperature of arm-segment and HUB LICEF units) which are controlled in temperature by heaters.

The temperature sensors that are built into the LICEFs and NIRs are read by the CMN units, and the data are relayed to the CCU. The thermal control software in the CCU commands solid state switches in the CMNs that operate the heaters as required. In the early orbit phases and in any situation where the payload is switched off, these heaters are controlled by thermostats to prevent the instrument from becoming too cold [6].

Chapter 4

4 SMOS Calibration

One of the main objectives of any mission is to obtain and provide stable and accurate data (in SMOS case this refers to the radiometric performance). So, a well-calibrated instrument provides the basis for stable measurements.

The calibration of any Earth Observation sensor is a key stage which encompasses those tasks which are necessary to convert the raw measurement data into science data. Calibration is basically the process of quantitatively defining the system responses to known controlled signal input*s*.

One of the important prerequisites to the performance verification and the validation of geophysical parameters is calibration which demonstrates that the instrument meets its requirements.

On the one hand, characterization is the measurement of the typical behavior of instrument properties, including subsystems, which may affect the accuracy or quality of its response or derived data products. The characterization activities are mainly performed on-ground before launch but are also performed in-flight thus being a prerequisite for the calibration activities.

On the other hand, verification encompasses the testing and analysis necessary to provide confirmation that all instrument requirements have been met.

Finally, validation is the process of assessing the quality of the data products derived from the system outputs.

4.1 The amplitude calibration

End-to-end calibration of MIRAS radiometer refers to processing the measured raw data up to brightness temperature maps over the Earth's surface [8]. The procedure starts with a self-correction of comparators offset and quadrature errors and it is followed by the calibration procedure itself.

The calibration procedure involves the injection of correlated and uncorrelated noise in the receivers and post-processing on ground the correlation results.

A noise distribution network called the calibration subsystem (CAS) is applied to calibrate the receiver noise temperature and the relative phase characteristics of the receivers. Some ancillary data of different subsystems (such as relative S-parameters of the CAS and of the input switch), measured on ground, are required for the calibration procedure.

Fig. 4.1 shows a detailed block diagram of a baseline, which consists in two LICEF receivers and the complex 1-bit correlator. Moreover it includes the reference radiometer (NIR) and the different planes where the calibration equations are defined.

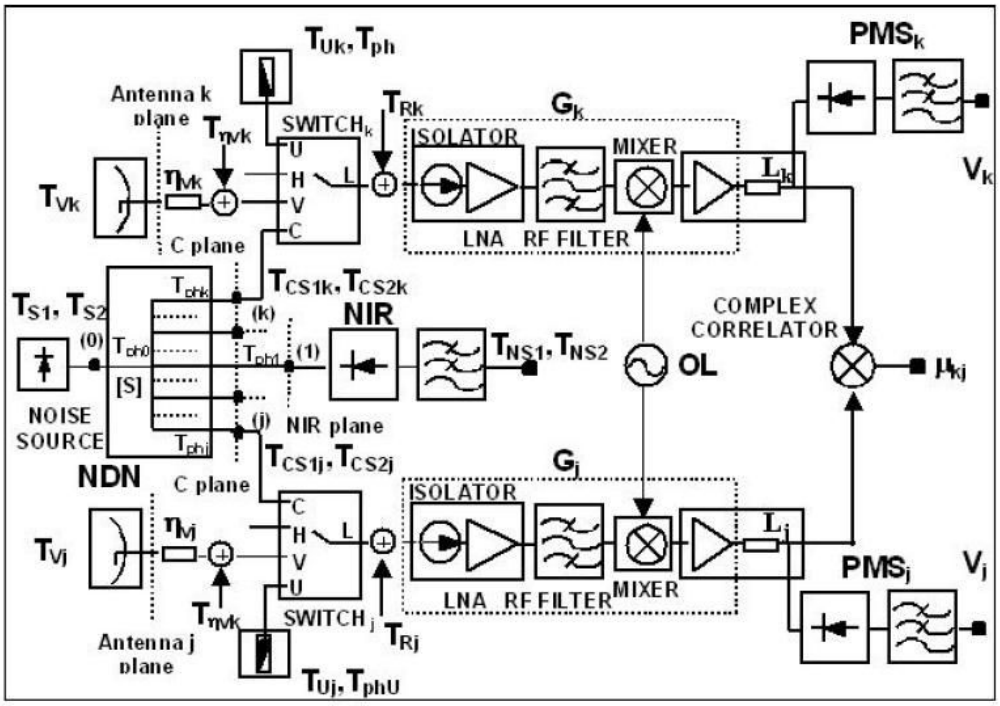

Fig. 4.1 Block diagram of a single baseline, which consists in two LICEF units and a complex 1-bit correlator

In summary the visibility samples can be denormalized and corrected from instrumental errors according to the following expression:

$$V_{kj}^{A} = \frac{\sqrt{T_{sysk}^{A} \cdot T_{sysj}^{A}}}{G_{kj}^{A}} \cdot M_{kj} = H_{kj} \cdot M_{kj} \cdot e^{j\phi_{kj}} \quad \textbf{(4.1)}$$

$$H_{kj} = \frac{\sqrt{T_{sysk}^{A} T_{sysj}^{A}}}{\left|G_{kj}^{A}\right|} \quad \textbf{(4.2)}$$

where M_{kj} is the normalized complex correlations computed from the correlation counts after the self-calibration procedure. T_{sysk}^{A} and T_{sysj}^{A} are the system temperature referred to the antenna plane of LICEF k and LICEF j, respectively. G_{kj}^{A} is the Fringe Wash function term referred to the antenna plane:

$$G_{kj}^{H,V} = G_{kj}^{C} \frac{\overline{S}_{LHk,LVk} \overline{S}_{LHj,LVj}^{*}}{\overline{S}_{LCk} \overline{S}_{LCj}^{*}} e^{j(\phi_{Hk,Vk} - \phi_{Hj,Vj})} \quad \textbf{(4.3)}$$

where G_{kj}^{C} is:

$$G_{kj}^{C} = \frac{M_{kj}^{C2} \sqrt{v_{2k}^{'} v_{2j}^{'}} - M_{kj}^{C1} \sqrt{v_{1k}^{'} v_{1j}^{'}}}{\sqrt{(v_{2k} - v_{1k})(v_{2j} - v_{1j})}} \frac{\left|S_{k0}\right|\left|S_{j0}\right|}{S_{k0} S_{j0}^{*}} \quad \textbf{(4.4)}$$

The amplitude calibration is basically the estimation of the unknown parameter H_{kj} in the previous expression which includes the system temperatures and the non-separable amplitude term.

Both are determined by different procedures:

- T_{sysk}^{A} and T_{sysj}^{A} are the global system temperature measured at system input of receivers k,j. They are measured by means of the PMS (Power Measurement System) placed at each LICEF receiver.

- $\left|G_{kj}^{A}\right|$ is the modulus of the fringe-washing term evaluated at the origin, where it has been assumed that the modulus of the fringe-wash term is the same for the (ii) and (qi) paths. It is measured by means of the correlated noise injection.

4.1.1 Internal calibration

4.1.1.1 The four-point measurement technique

This technique is based on a linear model of the PMS. Hence, the measured output voltage of the PMS, v_{PMS}, when an equivalent system temperature T_{sys} is present at system input, is given by:

$$v_{PMS} = v_{off} + GT_{sys} \quad \textbf{(4.5)}$$

where T_{sys} can be split into two terms relating the equivalent system noise temperature T_r, and the external temperature to be characterized T_{ext}:

$$T_{sys} = T_{ext} + T_r \quad \textbf{(4.6)}$$

The PMS is calibrated once the unknown parameters v_{off}, G and T_r are estimated. If the desired magnitude to be estimated is T_{sys}, then only v_{off} and G are required:

$$T_{sys} = \frac{v_{PMS} - v_{off}}{G} \quad \textbf{(4.7)}$$

Note that in such cases where only differential knowledge of T_{ext} is required, the T_r term is irrelevant:

$$T_{sys2} - T_{sys1} = T_{ext2} - T_{ext1} \quad \textbf{(4.8)}$$

It's necessary to know the external temperatures T_{C1} and T_{C2} where $T_{C1} < T_{C2}$. Hence T_{C1} is the so-called WARM temperature and T_{C2} the so-called HOT temperature. So, the overall system gain can be switched between two values G and $\frac{G}{L}$ by means of a suitable attenuator placed in the signal path at a point that it can be considered noiseless. Then, the four voltage measurements out of the PMS are given by the following set of equations:

$$\begin{aligned}
v_1 &= v_{off} + G(T_{C1} + T_r) && \text{PMS output WARM noise source=ON and L=OFF} \\
v_2 &= v_{off} + G(T_{C2} + T_r) && \text{PMS output HOT noise source=ON and L=OFF} \\
v_3 &= v_{off} + \frac{G}{L}(T_{C1} + T_r) && \text{PMS output WARM noise source=ON and L=ON} \\
v_4 &= v_{off} + \frac{G}{L}(T_{C2} + T_r) && \text{PMS output HOT noise source=ON and L=ON}
\end{aligned} \quad \textbf{(4.9)}$$

The desired parameters can be readily obtained as:

$$v_{off} = \frac{v_2 v_3 - v_1 v_4}{(v_2 - v_4) - (v_1 - v_3)} \text{ and } G = \frac{v_2 - v_1}{(T_{C2} - T_{C1})} \quad \textbf{(4.10)}$$

And the estimated system temperature is obtained through:

$$T_{sys} = \frac{v - v_{off}}{(v_2 - v_1)} (T_{C2} - T_{C1}) \quad \textbf{(4.11)}$$

4.1.1.2 Distributed calibration

A noise distributed network is implemented in the instrument to calibrate the HUB and the 3 ARMS [7].

The distributed calibration begins in the HUB calibrating the LICEFs using NIRs as reference (the calibrated LICEFs are coloured in yellow). This first step is so-called centralized calibration.

The centralized calibration has been used for receivers in the HUB except for those acting as NIR. The offset for the *k*-LICEF into the HUB has been computed using this formula:

$$v^h_{off_k} = \frac{v^h_{2k} v^h_{3k} - v^h_{1k} v^h_{4k}}{v^h_{2k} - v^h_{4k} - v^h_{1k} + v^h_{3k}} \quad \textbf{(4.12)}$$

where v^h_{1k} is the voltage for WARM NS and no attenuator, v^h_{2k} is the voltage for HOT NS and no attenuator, v^h_{3k} is the voltage for WARM NS with attenuator and v^h_{4k} is the voltage for HOT NS with attenuator.

The gain at C-plane for the *k*-LICEF in the HUB has been computed as:

$$G^{hC}_k = \frac{v^h_{2k} - v^h_{1k}}{\frac{|S_{k0}|^2}{6} \sum_{N=1}^{6} \frac{(T^{hC_2C}_{sys_N} - T^{hC_1C}_{sys_N})}{|S_{N0}|^2}} \quad \textbf{(4.13)}$$

where v^h_{2k} is the voltage for HOT NS and no attenuator, v^h_{1k} is the voltage for WARM NS and no attenuator, S_{k0} are the S-parameters between port "*0*" and port "*k*", S_{N0} are the S-parameters between port "*0*" and NIR port "*N*", $T^{hC_2C}_{sys_N}$ are the noise injection temperature measured by NIR when the switch are in the position HOT and even source, and finally, $T^{hC_1C}_{sys_N}$

are the noise injection temperature measured by NIR when the switch are in the position WARM and even source. The number "6" appears in the denominator of the expression because is an average of the 6 NIR channels located in the hub.

HUB	ARM A			ARM B			ARM C		
0	1	2	3	4	5	6	7	8	9
1	1	7	13	25	31	37	49	55	61
2*	2*	8	14	26*	32	38	50*	56	62
3**	3**	9	15	27**	33	39	51**	57	63
4	4	10	16	28	34	40	52	58	64
5	5	11	17	29	35	41	53	59	65
6	6	12	18	30	36	42	54	60	66
25	7	13	19	31	37	43	55	61	67
26*	8	14	20	32	38	44	56	62	68
27**	9	15	21	33	39	45	57	63	69
28	10	16	22	34	40	46	58	64	70
29	11	17	23	35	41	47	59	65	71
30	12	18	24	36	42	48	60	66	72
49									
50*									
51**									
52									
53									
54									

Table 4.1 Distributed calibration in the HUB

Next, the calibration continues with the three arms (using as reference the previous calibrated receivers for each section).

For the others receivers, the distributed calibration has been used as shown in *Table 4.2*. The offset voltage can be computed independently for each case. Its final value for those receivers driven twice noise source (even and odd) is the average of both:

$$v^{e}_{off_k} = \frac{v^{e}_{2k} v^{e}_{3k} - v^{e}_{1k} v^{e}_{4k}}{v^{e}_{2k} - v^{e}_{4k} - v^{e}_{1k} + v^{e}_{3k}}$$

$$v^{o}_{off_k} = \frac{v^{o}_{2k} v^{o}_{3k} - v^{o}_{1k} v^{o}_{4k}}{v^{o}_{2k} - v^{o}_{4k} - v^{o}_{1k} + v^{o}_{3k}} \qquad \textbf{(4.14)}$$

$$v_{off_k} = \frac{1}{2}\left[v^{e}_{off_k} + v^{o}_{off_k} \right]$$

The gain from measurements with odd noise sources for receivers in first section *l*-LICEF and NIR-LICEF receivers can be computed as:

$$T_{sys_h}^{C} = \frac{v_h - v_{off_h}}{G_h^C}$$

$$G_l^C = \frac{v_{2l} - v_{1l}}{\frac{|S_{l0}|^2}{4}\sum_{h=1}^{4}\frac{(T_{sys_h}^{C_2C} - T_{sys_h}^{C_1C})}{|S_{h0}|^2}} \qquad \textbf{(4.15)}$$

where $T_{sys_h}^{C}$ is the system temperature at C-plane, v_h is the voltage, v_{off_h} corresponds to the offset voltage and G_h^C is the gain of *h*-LICEFs with calibrated PMS. The number "4" appears in the denominator of the expression because is an average of the 4 LICEF already calibrated in the HUB (all the receivers in the section which are not NIR).

Source number / Receiver number	HUB	ARM A			ARM B			ARM C		
	0	1	2	3	4	5	6	7	8	9
1	1	1	7	13	25	31	37	49	55	61
2*	2*	2*	8	14	26*	32	38	50*	56	62
3**	3**	3**	9	15	27**	33	39	51**	57	63
4	4	4	10	16	28	34	40	52	58	64
5	5	5	11	17	29	35	41	53	59	65
6	6	6	12	18	30	36	42	54	60	66
25	7	7	13	19	31	37	43	55	61	67
26*	8	8	14	20	32	38	44	56	62	68
27**	9	9	15	21	33	39	45	57	63	69
28	10	10	16	22	34	40	46	58	64	70
29	11	11	17	23	35	41	47	59	65	71
30	12	12	18	24	36	42	48	60	66	72
49	*h*	*l*	*m*	*n*	*l*	*m*	*n*	*l*	*m*	*n*
50*										
51**										
52										
53										
54										

* NIR-LICEF H input
** NIR-LICEF V input

Table 4.2 Distributed noise injection

The gain from measurements with even NS for receivers in second section *m*-LICEF is computed as follows:

$$T_{sys_l}^{C} = \frac{v_l - v_{off_l}}{G_l^C}$$

$$G_m^C = \frac{v_{2m} - v_{1m}}{\frac{|S_{m0}|^2}{6}\sum_{l=1}^{6}\frac{(T_{sys_l}^{C_2C} - T_{sys_l}^{C_1C})}{|S_{l0}|^2}} \qquad \textbf{(4.16)}$$

with $T_{sys_l}^{C}$ being the system temperature at C-plane of *l*-LICEF in the second section of each arm, v_l is the PMS voltage and v_{off_l} is the offset voltage of *l*-LICEF with calibrated PMS. The number "6" appears in the denominator of the expression because is an average of the 6 LICEF already calibrated.

The gain from measurements with odd NS for receivers in third section *n*-LICEF can be computed as:

$$T_{sys_m}^{C} = \frac{v_m - v_{off_m}}{G_m^C}$$

$$G_n^C = \frac{v_{2n} - v_{1n}}{\frac{|S_{n0}|^2}{6}\sum_{m=1}^{6}\frac{(T_{sys_m}^{C_2C} - T_{sys_m}^{C_1C})}{|S_{m0}|^2}} \qquad \textbf{(4.17)}$$

where $T_{sys_m}^{C}$ is the system temperature at C-plane of *m*-LICEF in the third section of each arm, v_m is the PMS voltage and v_{off_m} is the offset voltage of *m*-LICEF with calibrated PMS.

It must be pointed out that all receivers in the hub and in the first and second sections of each arm are driven twice (for even and odd NS), while the receivers in the third section are only driven once.

HUB	ARM A			ARM B			ARM C		
0	1	2	3	4	5	6	7	8	9
1	1	7	13	25	31	37	49	55	61
2*	2*	8	14	26*	32	38	50*	56	62
3**	3**	9	15	27**	33	39	51**	57	63
4	4	10	16	28	34	40	52	58	64
5	5	11	17	29	35	41	53	59	65
6	6	12	18	30	36	42	54	60	66
25	7	13	19	31	37	43	55	61	67
26*	8	14	20	32	38	44	56	62	68
27**	9	15	21	33	39	45	57	63	69
28	10	16	22	34	40	46	58	64	70
29	11	17	23	35	41	47	59	65	71
30	12	18	24	36	42	48	60	66	72
49									
50*									
51**									
52									
53									
54									

Table 4.3 Distributed calibration in ARMS (section 1)

HUB	ARM A			ARM B			ARM C		
0	1	2	3	4	5	6	7	8	9
1	1	7	13	25	31	37	49	55	61
2*	2*	8	14	26*	32	38	50*	56	62
3**	3**	9	15	27**	33	39	51**	57	63
4	4	10	16	28	34	40	52	58	64
5	5	11	17	29	35	41	53	59	65
6	6	12	18	30	36	42	54	60	66
25	7	13	19	31	37	43	55	61	67
26*	8	14	20	32	38	44	56	62	68
27**	9	15	21	33	39	45	57	63	69
28	10	16	22	34	40	46	58	64	70
29	11	17	23	35	41	47	59	65	71
30	12	18	24	36	42	48	60	66	72
49									
50*									
51**									
52									
53									
54									

Table 4.4 Distributed calibration in ARMS (section 2)

HUB	ARM A			ARM B			ARM C		
0	1	2	3	4	5	6	7	8	9
1	1	7	13	25	31	37	49	55	61
2*	2*	8	14	26*	32	38	50*	56	62
3**	3**	9	15	27**	33	39	51**	57	63
4	4	10	16	28	34	40	52	58	64
5	5	11	17	29	35	41	53	59	65
6	6	12	18	30	36	42	54	60	66
25	7	13	19	31	37	43	55	61	67
26*	8	14	20	32	38	44	56	62	68
27**	9	15	21	33	39	45	57	63	69
28	10	16	22	34	40	46	58	64	70
29	11	17	23	35	41	47	59	65	71
30	12	18	24	36	42	48	60	66	72
49									
50*									
51**									
52									
53									
54									

Table 4.5 Distributed calibration in ARMS (section 3)

4.1.1.3 Impact of PMS non linearity

The performance of the PMS used to denormalize the digital correlations in interferometric radiometers is degraded due to its non-linear behavior [10]. So, the PMS behavior is very well modeled by means of a second order response:

$$v_k = v_{off_k} + G_k T_{sys_k} + a_k T_{sys_k}^2 \qquad \textbf{(4.18)}$$

where a_k is the non-linear term that introduce an error in the estimation of system temperature.

4.1.2 External calibration

External calibration is a new method to calibrate the instrument based on a combination of internal and external signals [11]. This so-called one point calibration makes use of deep sky views as single external calibration target.

Fig. 4.2 illustrates the one-point calibration. The switch has four positions: antenna (A=H/V), matched load (U) and a port devoted to calibration (C). If the front end is in thermal equilibrium and perfectly matched, injecting noise at the U port by means of a matched load is equivalent to place a perfect absorber in front of the antenna at the same temperature:

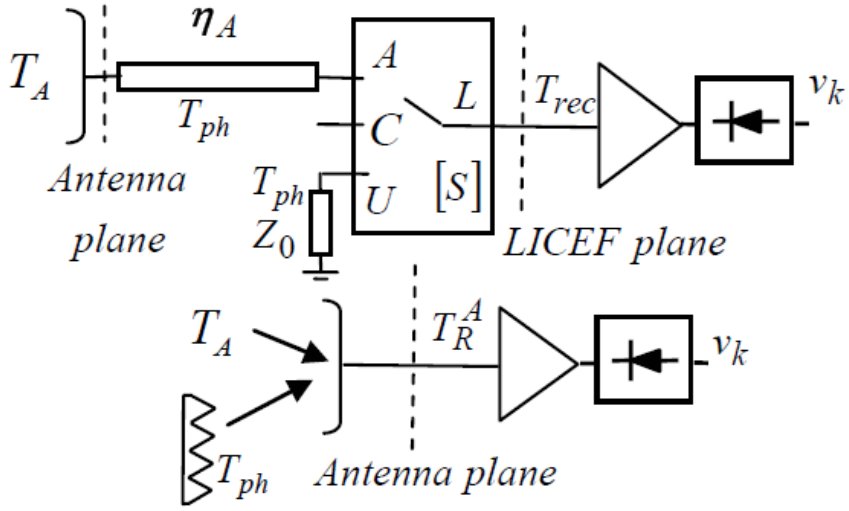

Fig. 4.2 LICEF/PMS front-end scheme of one-point calibration

The linear relation between PMS voltage and input temperature can be written either as a function of antenna temperature or system temperature as:

$$v_A = G^A T_{sys_A} + v_{off} = G^A T_A + v'_{off} \qquad \textbf{(4.19)}$$
$$v'_{off} = v_{off} + G^A T_R^A$$

where T_R^A is the equivalent receiver noise temperature referred to the antenna plane.

Once the offset term is calibrated, the PMS can be modeled as a zero offset detector:

$$v_A = G^A T_{sys_A} = G^A (T_A + T_R^A) \qquad \textbf{(4.20)}$$

Since there are two unknowns (gain and noise temperature) the PMS requires two known input signals to be calibrated. The payload performs periodic pointing to the deep sky in order to calibrate the reference radiometer. During these cold sky views the PMS units are also switched between the U-load (WARM noise) and the antenna ($T_A = T_{sky}$, COLD noise). Taking into account the block diagram in *Fig. 4.2*, the equivalent system temperature at antenna plane in both positions of the switch is given by:

$$T_{sysW}^{A} = \frac{1}{\eta_A \left|S_{LA}\right|^2}(T_{ph} + T_{rec})$$
$$T_{sysC}^{A} = T_{sky} + \frac{T_{ph}(1-\eta_A \left|S_{LA}\right|^2) + T_{rec}}{\eta_A \left|S_{LA}\right|^2} \quad \textbf{(4.21)}$$

If the WARM and COLD PMS regarding are written as:

$$v_W = G^A T_{sysW}^A \quad v_C = G^A T_{sysC}^A \quad \textbf{(4.22)}$$

The PMS gain, so-called External Gain, can be expressed:

$$G^A = \frac{v_W - v_C}{T_{sysW}^A - T_{sysC}^A} \quad \textbf{(4.23)}$$

And the expression in *(4.23)* simplifies to the following:

$$G^A = \frac{v_W - v_C}{T_{ph} - T_{sky}} \quad \textbf{(4.24)}$$

From this equation it is derived that, in the case that the radiometer front end is at the same physical temperature T_{ph}, switching to the internal matched load is equivalent to place a perfect absorber in front of the antenna at the same physical temperature. This result has very important implications in the design of the calibration pattern, both in front end configuration and reference signals to be measured. It is far much simpler to place an internal matched load than to design target with good return loss and constant temperature distribution.

Moreover, receiver temperature can also be computed as:

$$T_R^A = \frac{v'_C T_{ph} - v'_W T_{sky}}{v_W - v_C} \quad \textbf{(4.25)}$$

where v'_C and v'_W are the voltages with the offset subtracted.

4.1.3 One-point calibration

PMS calibration parameters, as retrieved during the cold sky views, cannot be used directly in observation mode due to temperature changes. The receivers (LICEFs) suffer a temperature drift of about $2^{o}C$ peak to peak along each orbit. So, PMS gain and offset are corrected for temperature drift.

In the case that PMS gain needs recalibration along each orbit the most simple and accurate way that has been foreseen to do it is by U-noise injection (switch to matched load). In such case, the PMS gain, so-called Gain one-point, is retrieved as:

$$G^{A}_{PMS1} = \frac{v_U - v_{off_1}}{T^{A}_{R_1} + T_{ph}} \quad \textbf{(4.26)}$$

where v_U is PMS voltage when the switch is the U position (matched load) and $T^{A}_{R_1}$ is the receiver noise temperature at the antenna plane at its physical temperature T_{ph}.

Chapter 5

5 In-orbit CAS validation SW

Next figure illustrates the block diagram of the PMS front end, showing the main 1P calibration magnitudes. During periodic deep sky views, the PMS is simultaneously calibrated by means of the internal 4P CAS system at the calibration CIP plane and by means of the external 1P calibration at the antenna planes (HAP/VAP).

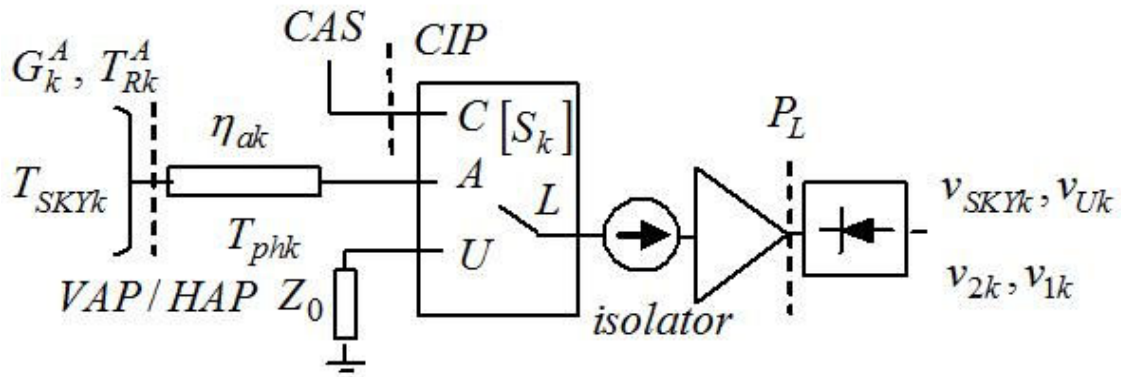

Fig. 5.1 LICEF/PMS front-end scheme to illustrate the one-point calibration scheme

For a perfectly matched passive front end at a constant temperature T_{phk}, chapter 4 shows that switching the instrument to the internal matched load (U port) is equivalent to place an absorber at the same physical temperature in front of the antenna. In this way, 1P PMS_k gain at the antenna plane is given by:

$$G_{1Pk}^A = \frac{v_{Uk} - v_{SKYk}}{T_{phk} - T_{SKYk}} \qquad \textbf{(5.1)}$$

On the other hand, when translated to the antenna plane, the internal PMS 4P gain is given by:

$$G_{4Pk}^A = \frac{v_{2k} - v_{1k}}{T_{CASN}^2 - T_{CASN}^1} \frac{\left|S_{LA_k}\right|^2}{\left|S_{LC_k}\right|^2} \frac{\left|S_{N0}\right|^2}{\left|S_{k0}\right|^2} \eta_{A_k} \qquad \textbf{(5.2)}$$

where $T_{CASN}^{1,2}$ are the CAS HOT and WARM temperatures as measured by the reference radiometer (NIR) at CAS port N, S_{N0}, S_{k0} are the CAS S-parameters from the noise source to the reference radiometer and PMS_k calibration ports, respectively, η_{A_k} is the antenna efficiency (A=V/H) and, finally, S_{LA_k}, S_{LC_k} are the switch S-parameters.

As the 1P and 4P gains are computed at the same plane and at the same temperature, an error free instrument would yield:

$$G_{1Pk}^{A} = G_{4Pk}^{A} \quad \textbf{(5.3)}$$

In order to evaluate the error and compute a correction coefficient, the magnitudes are rearranged in the so-called C_{Nk} coefficients. One of them is computed from the on-ground parameters:

$$C_{Nk}^{gnd} = \frac{\left|S_{LA_k}\right|^2}{\left|S_{LC_k}\right|^2} \frac{\left|S_{N0}\right|^2}{\left|S_{K0}\right|^2} \eta_{A_k} \quad \textbf{(5.4)}$$

The other one uses the flight measurements and is computed during each external calibration:

$$C_{Nk}^{A} = \frac{T_{CASN}^{2} - T_{CASN}^{1}}{v_{2k} - v_{1k}} \frac{v_{Uk} - v_{SKYk}}{T_{Uk} - T_{SKYk}^{A}} \quad \textbf{(5.5)}$$

The error in the C_{Nk} coefficients can be assigned to a CAS correction factor to be applied to the CAS ground coefficients. In order to check the consistency of this correction, some analysis has been undertaken and presented hereafter [12].

5.1 CAS validation during deep-sky views

This section provides the SMOS in-orbit calibration equations as described at the end of phase C/D activities [13]. The CAS validation during deep-sky views equations in the first version have been updated according to the distributed approach.

Besides, a new tool computed in Matlab has made possible to compute CAS coefficients from ground/deep-sky views and CAS coefficient errors with flight data. All results are represented and validated.

OUTPUT DATA		
CAS unbalance coefficient $C_{k.}$ Measured from deep-sky views to be compared against ground measured coefficients.		C_k^{sky}
CAS unbalance coefficient $C_{k.}$ Measured from ground LICEF and CAS parameters		C_k^{gnd}
INPUT DATA		Origin
Description	Variables	
PMS voltages **UNITS [mV]**	$v_{1k,}$ $v_{2k,}$	WARM PMS voltages HOT PMS voltages Internal 4-point short calibration (for Hub, even and odd noise injection sources).
PMS voltages **UNITS [mV]**	$v_{Uk,}$	PMSk voltage in U-mode (WARM PMS reading during deep-sky one-point calibration).
PMS voltages **UNITS [mV]**	v_{SKYk}	PMSk voltage in A-mode (A=H,V) sky (COLD PMS reading during deep-sky one point calibration)
CAS temperature measured by NIR in NIR-R mode.	$T^1_{CAS_N}$ $T^2_{CAS_N}$	WARM temperature measured by NIR-R HOT temperature measured by NIR-R
Temperature [K]	T_{Uk}	LICEF U-load temperature. (WARM temperature during deep-sky one-point calibration.
Temperature [K]	T^A_{SKYk}	LICEFk antenna temperature. (A=H,V). (COLD temperature during deep-sky one point calibration)

STP	EQUATIONS	COMMENT
1	$C_{Nk}^{h} = \frac{T_{CAS\,N}^{2} - T_{CAS_N}^{1}}{v_{2k}^{h} - v_{1k}^{h}} \frac{v_{Uk} - v_{SKYk}}{T_{Uk} - T_{SKYk}^{A}}$	For each of the N reference paths in the hub there is a set of 12 "k" coefficients C_{Nk}^{h} . N=6
2	$C_{Nk}^{gnd} = \frac{\left\|S_{LA_k}\right\|^2}{\left\|S_{LC_k}\right\|^2} \frac{\left\|S_{N0}\right\|^2}{\left\|S_{k0}\right\|^2} \eta_{A_k}$	CAS coefficient computed from ground data
3	$eC_{Nk}^{h} = 10\log_{10}\left[\frac{C_{Nk}^{h}}{C_{Nk}^{gnd}}\right] \; dB$	CAS coefficients error in dB. Compute mean and std for each set
4	$C_{rk}^{o} = \frac{1}{G_r^C} \frac{v_{2r}^{o} - v_{1r}^{o}}{v_{2k}^{o} - v_{1k}^{o}} \frac{v_{Uk} - v_{SKYk}}{T_{Uk} - T_{SKYk}^{A}}$	ODD measurements (8 coefficients for the first step and 6 coefficients for the third step C_{rk}^{o} each) **select as reference receiver the calibrated LICEF from the previous step.** r=4 (first step) and r=6 (third step). The reference gain is computed as the mean value of PMS gain obtained in the previous steps. (A=H/V)
5	$C_{rk}^{e} = \frac{1}{G_r^C} \frac{v_{2r}^{e} - v_{1r}^{e}}{v_{2k}^{e} - v_{1k}^{e}} \frac{v_{Uk} - v_{SKYk}}{T_{Uk} - T_{SKYk}^{A}}$	EVEN measurements (6 coefficients C_{rk}^{o} each) **select as reference receiver the calibrated LICEF from the previous step.** r=6 (second step). The reference gain is computed as the mean value of PMS gain obtained in the previous steps (A=H/V)
6	$eC_{rk}^{e} = 10\log_{10}\left[\frac{C_{rk}^{e}}{C_{rk}^{gnd}}\right] \; dB$	CAS coefficients error in dB. Compute mean and std for each set
7	$eC_{rk}^{o} = 10\log_{10}\left[\frac{C_{rk}^{o}}{C_{rk}^{gnd}}\right] \; dB$	CAS coefficients error in dB. Compute mean and std for each set

Table 5.1 CAS validation during deep-sky views

5.2 Analysis with flight data

In order to analyze the first external calibration with real data a new tool was coded in Matlab to compute the CAS coefficient errors. This tool is necessary to compare CAS coefficients measured from deep-sky views with CAS coefficients measured from ground tests.

First, the CAS coefficients measured from ground were computed at horizontal and vertical polarization in dB units. Next, the CAS coefficients were measured from deep-sky views with the same structure than CAS coefficients from ground.

Finally, CAS coefficient errors were computed and represented in dB units with two kinds of graphics (one with LICEFs references on the x-axis and other with LICEFs to calibrate on the x-axis). This allows computing the mean error, which is assigned a CAS S-parameter error.

From the final output of the Consistency tool [14] an amplitude correction factor can be retrieved for the two possible configurations (nominal and redundant). These factors were obtained from the differences $T_{syskr}^{HOT} - T_{syskr}^{WARM}$ at the common reference port and after equalizing the different noise injection levels.

Using flight data obtained from December (2009-12-08T16-40-00) tests, it was possible to generate a preliminary table of CAS correction factors to substitute the old ones (the on-ground factors that were computed before launch).

HUB	ARM A			ARM B			ARM C		
NS-HUB	NS-A1	NS-A2	NS-A3	NS-B1	NS-B2	NS-B3	NS-C1	NS-C2	NS-C3
0,998529863	1,00620802	1,00015126	1,01080256	0,99372343	1,00504653	1,01334584	1,00487205	0,99424706	1,00642469
1,007051105	1,0064079	1,00194968	1,00617882	1,0060782	1,01138042	0,99072485	1,01961287	1,00195719	1,01100925
1,006625734	1,02222112	1,0081898	1,00155403	1,0067595	1,0058404	1,01047061	1,02164242	1,01068352	0,99923276
0,981354429	0,98984158	1,0086953	1,00581721	1,00759658	1,00321505	1,00497217	1,01572575	1,01333921	0,9950384
1,004542456	1,01312683	1,00330302	1,0009078	1,00555721	1,00759658	1,0083674	1,00147305	1,00008824	0,99815548
0,986708903	0,99499977	1,0075092	1,01503339	1,01703257	1,01424158	1,00767731	0,99412147	1,01150561	1,00375763
0,977744801	0,98935065	0,99985762	1,00279468	0,98944865	1,00166028	0,98886637	0,97601902	1,00020496	1,00026759
0,993475714	0,99200322	0,9950153	0,99791321	0,99194195	0,97716751	0,99395011	0,98604948	1,00375325	0,99103797
0,988590804	0,99727144	0,9896042	0,98570509	0,98839568	0,99614034	0,99302492	0,99369479	0,99090391	0,99862185
0,989603452	0,99691079	0,99452774	0,99318048	0,98464838	0,98893411	0,99461198	0,99625788	0,98830518	1,00438491
0,988267243	0,9912871	0,98873198	0,99018666	0,98992101	0,99446336	1,00370803	0,98306531	0,98926901	0,99305665
0,997727471	0,99713087	1,00281738	0,990487	0,99569158	0,99524714	0,99053167	0,99401516	0,99609293	0,99916833
1,004380114									
1,022428345									
1,015958544									
1,013163419									
1,000292241									
0,990911178									

Table 5.2 External CAS S-parameter correction

This CAS correction table (*Table 5.2*) was preliminary, since further analysis was required in that moment. However, the results were good enough to give some preliminary conclusions.

The table was computed by equalling the PMS gain at HAP/VAP between the 1P external calibration and the 4P gain at HAP/VAP using CAS, which is the basis of the computation of the C_{nk} factors (CAS in-orbit validation).

In addition:

- The correction factors were computed as the mean for the correction factors in H and V polarization. It must be pointed out that the differences between H and V polarizations were very low (±0.1 dB), according to *Fig. 5.4*.

- The 2nd order PMS correction was not included (bug in the program by the time of the simulations).

This chapter devoted to highlight the differences by means of the PMS CAS in-orbit validation tool, between the three following cases:

a) CAS in-orbit validation results without CAS correction factor

b) CAS in-orbit validation tool results with ON-GROUND CAS correction factor (consistency tool)

c) CAS in-orbit validation results with External CAS correction factor

In order to compute the maximum and minimum error to validate the results, the success criteria was computed from the SMOS amplitude error budged [15]

COD.	SNAP-SHOT	Param. value (1 σ)	Units	Param. sens. to Tph	Units	Sens. to error (K/unit)	Rad. Sens. (random error)	Rad. bias. Scene bias	Rad. Accur. Pixel Bias	Data Source
	T-T0 (T0=25ºC) 2ºC peak orbit temperature drift	0	ºC							
	TA	150	K							
	TR (NF=1.91 dB)	161	K							
	Polarization (X = 1, Y = 0, XY=2)	1								
	FUNDAMENTAL LIMITATIONS						1,88	0,00	0,06	
FL1	Discretization								0,05	E
FL2	Thermal noise (Dual-Pol. τ=1.2 s, Full-Pol. τ=0.85)	1,2	s				1,98			M
	ANTENNA ERRORS						0,00	0,00	0,97	
ANT1	Antenna voltage pattern phase ripple	0,330	deg	0		1,11			0,36	R
ANT2	Antenna voltage pattern amplitude ripple	0,770	%	0		0,8			0,61	M
ANT3	Antenna XP $\pm\varepsilon_{xp}\Delta T_{max}$	0,000		0		90			0,00	M
ANT4	Switch isolation $\pm\varepsilon_{sw}\Delta T_{max}$	0,000		0		90			0,00	M
ANT5	Antenna mismatch	0,000	lin	0		0			0,00	M
ANT6	Geometric position uncertainty (x-y)	0,220	mm	0		1,99			0,43	M
ANT7	Geometric position uncertainty (z)	0,220	mm	0		0,4			0,09	M
ANT8	Array arm thermo-elastic deformation:In-plane	0,150	deg	0,015	deg/ºC	0,2			0,03	E
ANT9	Array arm thermo-elastic deformations:Off-plane	0,150	deg	0,015	deg/ºC	2			0,30	E
ANT10	Hub arm thermo-elastic deformation:In-plane	0,060	deg	0,005	deg/ºC	3,37			0,20	E
ANT11	Hub arm thermo-elastic deformation:Off-plane	0,060	deg	0,005	deg/ºC	3,45			0,20	E
ANT12	Antenna rotation(3)	0,000		0		90			0,00	E
ANT13	Pointing accuracy	0,000		0		0			0,00	E
ANT14	Antenna voltage pattern dependency on frequency	0,000		0		0			0,00	E
ANT15	Antenna-LICEF XP measured via TRFOP	0,003		0		90			0,28	E
	AMPLITUDE ERRORS									
	NOISE INJECTION RADIOMETER: V(0,0)						0,15	0,77	0,00	
AMP1	NIR: Sensitivity $\pi_{nir}/\sqrt{Br}$	0,186	K	0		1	0,15			M
AMP2	NIR: Bias error	0,31	K	0	K/ºC	1		0,31		M
AMP3	NIR: Gain error	0,0031	-	0	/ºC	148		0,46		M
	RECEIVER & BASELINE AMPLITUDE ERRORS	1,8	%				0,00	0,00	0,80	
AMP10	Amplitude calibration residual error due to noise	0,100	%	0		0,15			0,02	E
AMP11	NDN Sij relative amplitude	0,044	dB	0		8,1			0,36	M
AMP12	PMS sensitivity due to thermal noise	0,059	%	0		1,1			0,06	E
AMP13	Low-frequency PMS random gain fluctuation	0,075	%	0		1,1			0,08	E
AMP14	PMS linearity error:	0,250	%	0		1,1			0,28	M
AMP15	Reciever input path Sij relative amplitude	0,014	dB	0		8,1			0,11	R
AMP16	Antenna losses relative amplitude	0,020	dB	0		8,1			0,16	M
AMP17	Error in the relative noise injected by CAS	0,315	%	0		0,5			0,16	M
AMP18	Amplitude error due to mismatch at calibration planes	1,200	%	0		0,5			0,60	M
AMP19	FWF(0) modulus error on distributed calibration	0,100	%	0		0,21			0,02	E
	PHASE ERRORS	1,62	deg				0,00	0,00	0,41	
PHA10	In-phase cal. residual error due AM/PM conversion	0,2	deg	0		0,27			0,05	E
PHA11	NDN Sij relative phase uncertainty	1,41	deg	0		0,27			0,38	M
PHA12	Receiver input path Sij relative phase uncertainty	0,065	deg	0		0,27			0,02	R
PHA13	Path antenna plane to antenna geometric center	0,5	deg	0		0,27			0,14	E
PHA14	Residual quadrature error	0,014	deg	0		0,36			0,01	E
PHA15	Phase error due to mismatch at calibration planes	0,13	deg	0		0,27			0,04	E
PHA16	In-band freq dependent quadrature error	0	deg	0		0,025			0,00	E
PHA17	FWF(0) phase error on distributed calibration	0,02	deg	0		0,38			0,01	E
	OTHER SOURCES OF ERROR						0,00	0,00	1,02	
OS1	Sampling skew error	0,52	ns	0		0,76			0,40	M
OS2	Sampling jitter error	0,03	ns	0		5			0,15	M
OS3	Comparators threshold and U-noise injection correction	0,50	cu	0		0,83			0,42	R
OS4	Residual SELF-RFI	1,00	cu	0		0,83			0,83	R
	TOTAL RMS Sum (K)						1,99	0,77	1,87	
	TOTAL radiometric sensitivity						1,99			
	TOTAL radiometric accuracy [RMS sum of pixel bias&scene bias]								1,84	

Table 5.3 SMOS radiometric error budget at boresight for OS (TA=150 K), dual-polarization mode, antenna ref. frame (X polarization.). Reference physical temperature Tph0=25 ºC.

First, it is necessary to compute the quadratic addition of standard deviations:

$$\sigma_{totk} = \sqrt{\sigma_{FWF0k}{}^2 + \sigma^2_{RHOk} + \sigma^2_{TNCASk} + \sigma^2_{linearityk} + \sigma^2_{SWITCHk} + \sigma^2_{\eta k} + \sigma^2_{CASSijk}} \quad \textbf{(5.6)}$$

Then, the maximum and minimum error is computed in percentage in expression *(5.7)* and in dB units in expression *(5.8)*:

$$\sigma_{totk}(\%) = \sigma_{totk} \cdot 100 = \pm 5{,}17\% \quad \textbf{(5.7)}$$

$$\sigma_{totk}(dB) = 10 \cdot \log_{10}(\sigma_{totk} + 1) = \pm 0{,}22\, dB \quad \textbf{(5.8)}$$

In Annex I, the results of the three comparisons are displayed for V and H polarization. As a preliminary conclusion, **the correction by the CAS in-orbit validation tool produced a more consistent performance of the PMS gain calibration by the 4P internal calibration (CAS system).** However, additional tests were necessary to validate this technique and to assess the relative and absolute accuracy of PMS calibration of both methods: 1P PMS external calibration and 4P internal CAS calibration.

The following additional analysis were undertaken

1) Comparison of PMS gain at HAP/VAP using the in-orbit CAS correction factor (*Fig. 5.2* and *Fig. 5.3*). The pk-to-pk error is 0.9% well within the requirements, and the performance of the H and V polarizations are very similar.

2) Comparison of the CAS correction factor for two different tests
   - 8th December 2009-23rd December 2009
   - 8th December 2009-7th January 2010

   In the first case the differences were below ±0.03 dB and in the second case ±0.035 dB, showing that the correction was very stable for long periods of time (in the last case one month).

3) The NIR consistency tool (necessary to analyze NIR stability) was applied to three different days, also showing a good stability of relative errors between the 6 NIR units in NIR-R mode

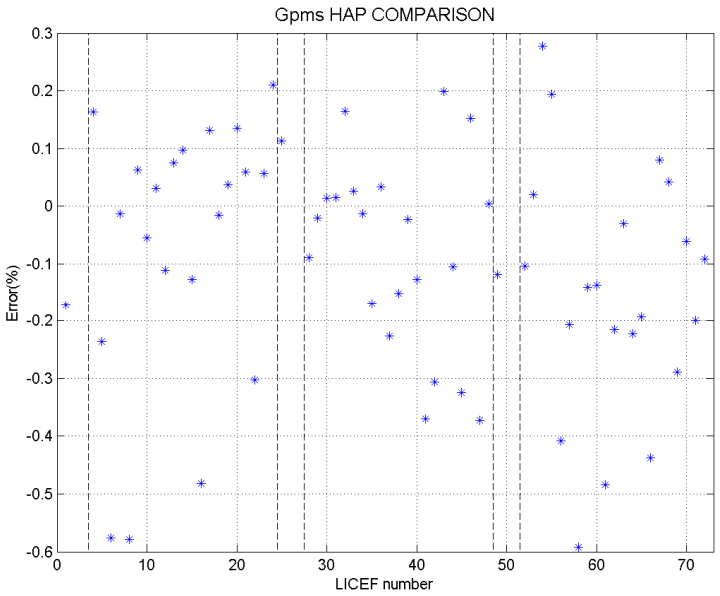

Fig. 5.2 Comparison between G1P (external) and G4P (internal) using External CAS S-parameter correction (Horizontal polarization)

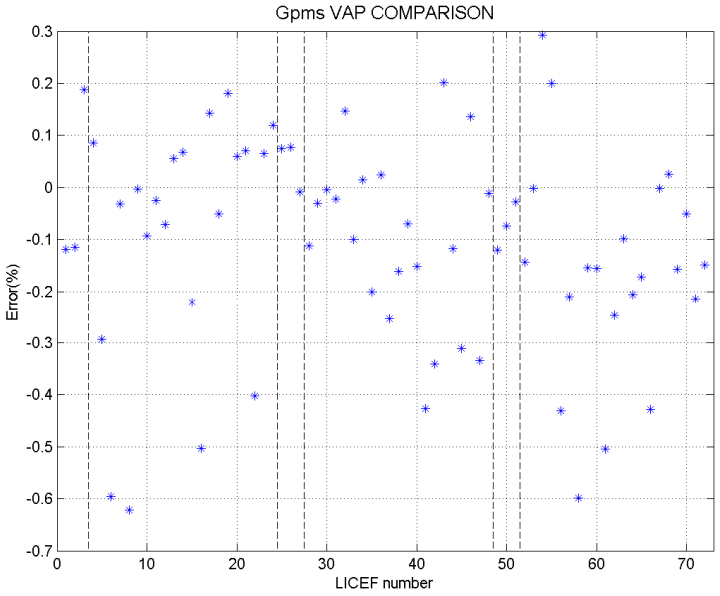

Fig. 5.3 Comparison between G1P (external) and G4P (internal) using External CAS S-parameter correction (Vertical polarization)

HUB	ARM A			ARM B			ARM C		
NS-HUB	NS-A1	NS-A2	NS-A3	NS-B1	NS-B2	NS-B3	NS-C1	NS-C2	NS-C3
0,066382421	0,0809682	0,0451731	0,0271407	-0,001955	-0,016205	0,0388978	0,0572737	-0,000235	-0,047042
-0,014765139	0,0012527	-0,10382	0,0070693	-0,011597	0,0236834	-0,010246	-0,02238	-0,014109	0,0224127
-0,014765139	-0,000779	-0,051881	0,0131606	-0,011226	0,0138346	-0,054858	-0,019637	0,019289	0,0243637
-0,017862989	-0,003277	-0,030164	0,0042004	0,0662265	-0,00151	-0,077636	0,0278499	-0,039502	0,0419916
-0,061255575	-0,04667	0,0190876	0,0333658	0,0145634	0,0043951	0,0468169	0,0207118	-0,002062	0,0049877
0,007959434	0,0225452	0,0505278	0,1046647	-0,051173	-0,011258	-0,041957	0,0281316	0,0113295	-0,032574
-0,006203637	0,0393727	0,0076307	-0,128414	-0,023542	0,0534071	0,0107578	-0,033471	-0,045322	-0,066761
-0,014765139	-0,10962	-0,012441	-0,037377	0,0163462	0,0042638	0,0413751	-0,047345	0,0241333	0,0344871
-0,014765139	-0,057682	-0,006349	0,0346124	0,0064973	-0,040349	-0,007248	-0,013947	0,0260844	0,0134541
0,061977646	-0,035965	-0,01531	-0,011216	-0,008848	-0,063127	0,0269592	-0,072738	0,0437122	0,0259851
0,010314601	0,0132871	0,0138559	-0,048344	-0,002942	0,0613262	-0,01221	-0,035298	0,0067084	0,016429
-0,055421708	0,0447274	0,0851547	-0,003236	-0,018595	-0,027448	0,0381396	-0,021906	-0,030853	-0,037547
0,067009849									
-0,014765139									
-0,014765139									
0,037586063									
0,030447975									
0,037867799									

Table 5.4 Difference in dB between External CAS S-parameter correction at horizontal and vertical polarization of flight data from 8th December 2009

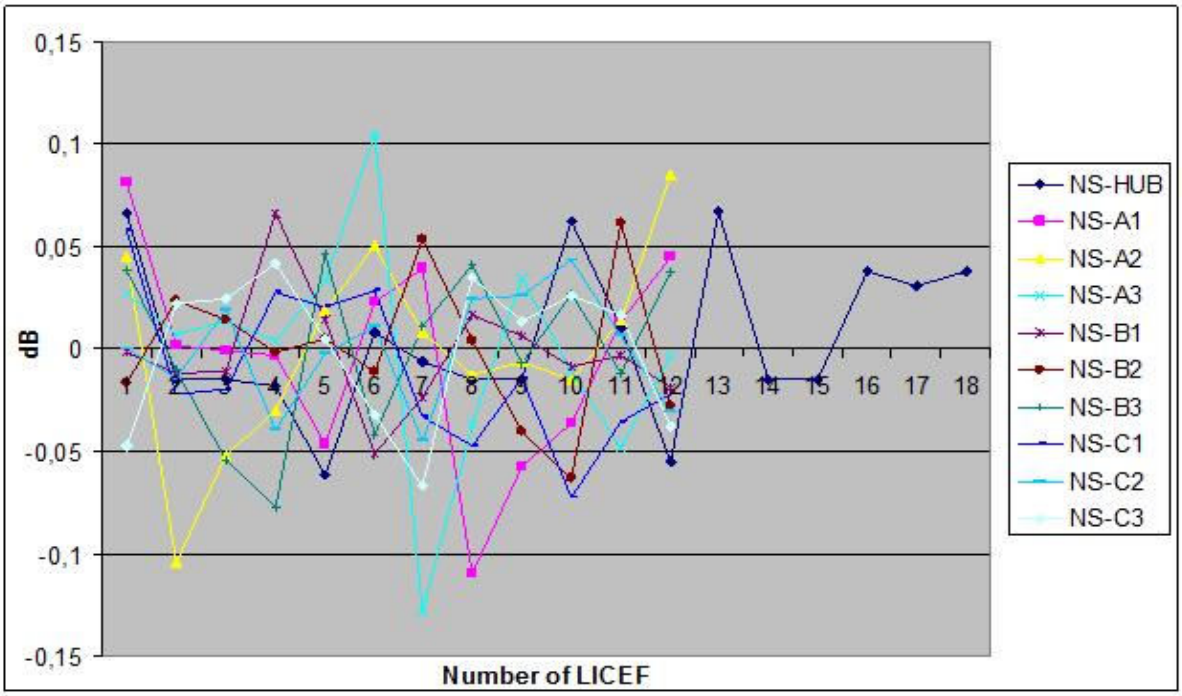

Fig. 5.4 Difference in dB between External CAS S-parameter correction at horizontal and vertical polarization of flight data from 8th December 2009

HUB	ARM A			ARM B			ARM C		
NS-HUB	NS-A1	NS-A2	NS-A3	NS-B1	NS-B2	NS-B3	NS-C1	NS-C2	NS-C3
0,007782853	-0,00329626	-0,00752057	0,01759029	0,01748416	0,01774745	0,00462425	0,00382787	0,00103349	-0,00736709
0,001398191	-0,01111546	0,00851434	-0,00471569	0,0054449	-0,00986836	0,00260111	-0,00830901	0,00833572	0,00142396
-0,001206438	-0,00848707	0,01761528	0,01256763	0,01102372	-0,01584449	-0,00030974	-0,0037881	0,00072021	-0,00600951
0,014748036	0,00658994	-0,01675382	-0,00107265	-0,01906458	-0,02002405	-0,00753135	0,01275864	0,0064044	0,00807964
-0,017273208	-0,00284544	0,00407869	0,00980587	0,01297771	0,00293253	0,01123703	-0,00946036	0,02317778	-0,01412971
0,001586991	0,00589974	0,01642071	0,0037624	-0,02960023	-0,00506806	0,01206786	-0,01956488	0,01407553	-0,00118323
0,008928039	-0,00340813	-0,00432975	-0,01320606	0,01823598	-0,00519542	0,01616314	0,01265925	-0,02055824	-0,00406929
-0,005008969	-0,00913215	-0,00987294	-0,00156694	0,00772953	0,01519964	-0,00994456	-0,00998999	-0,00978598	0,00015215
-5,54446E-06	0,01497182	0,00787664	-0,00910681	-0,01220661	0,01384226	-0,00412801	-0,00050748	0,00171438	0,02445033
-0,007836475	-0,00036078	-0,0286923	-0,00972392	-0,00890651	0,00612236	0,00335523	0,00757373	-0,00864728	-0,00400737
-0,007035213	-0,0047721	0,00218056	-0,0040887	0,00319366	-0,00163271	-0,02314581	0,01447333	0,00317463	-0,00176009
-0,016385675	0,00999057	0,01069995	-0,00028781	0,01425409	0,0011319	-0,00567122	0,00983895	-0,0198417	0,00442826
0,010069643									
0,003324611									
-0,002699386									
0,012350743									
-0,001413781									
0,002619761									

Table 5.5 Difference in dB between External CAS S-parameter correction of 8th December 2009 and 23rd December 2009 (horizontal polarization)

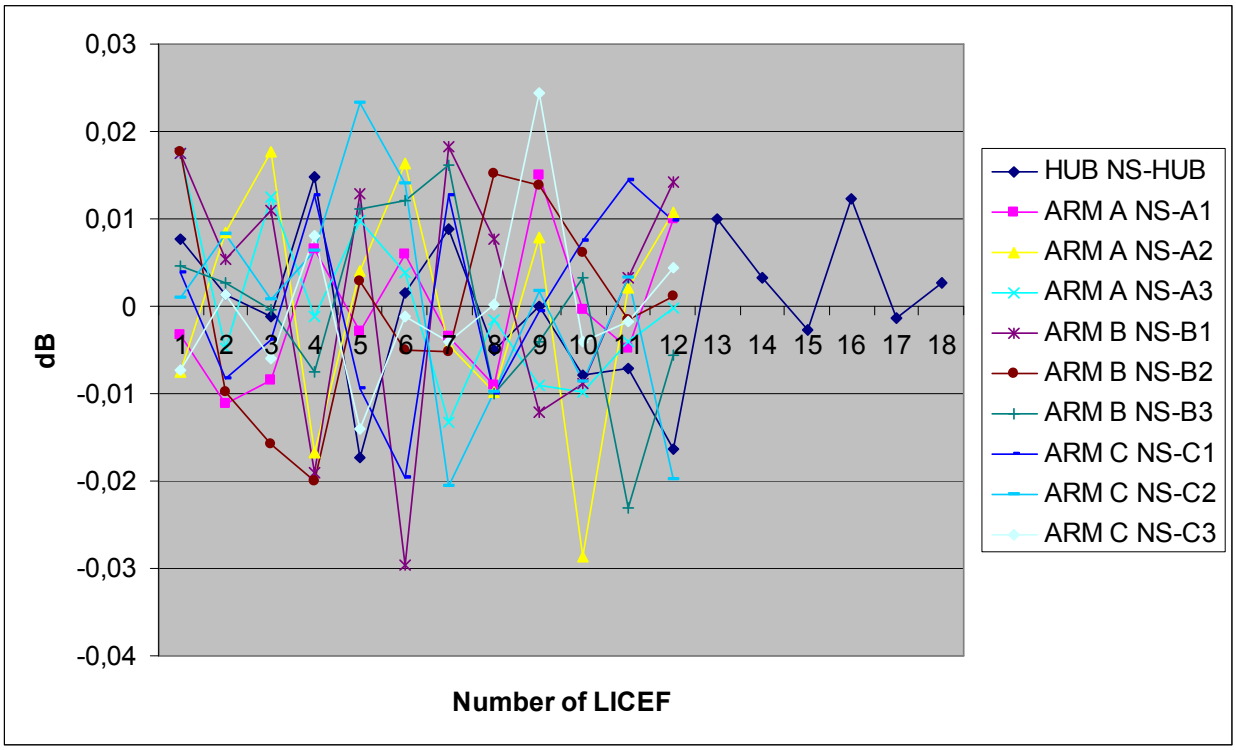

Fig. 5.5 Difference in dB between External CAS S-parameter correction of 8th December 2009 and 23rd December 2009 (horizontal polarization)

HUB	ARM A			ARM B			ARM C		
NS-HUB	NS-A1	NS-A2	NS-A3	NS-B1	NS-B2	NS-B3	NS-C1	NS-C2	NS-C3
0,005697962	-0,00579029	-0,00578215	0,0132028	0,02113221	-0,00984866	0,01875432	0,00476819	0,00220418	0,02242281
0,006005566	0,01017768	-0,01386125	0,01681137	-0,00133765	-0,00630107	0,0073207	-0,0056237	-0,00430431	0,00805253
0,002553199	0,01330427	-0,00274111	0,00638286	0,00979268	-0,00611283	0,00022671	-0,00707061	0,01173667	-0,0125497
0,006571497	-0,00716875	-0,00586213	-0,00443122	-0,00893572	-0,02210773	-0,00315642	0,0021535	0,00370495	0,00580669
-0,003223816	-0,00549435	-0,00738259	0,01630067	-0,00145405	0,01073039	0,00716487	-0,00150613	0,00017667	-0,01159283
0,013738347	0,01398755	0,00464021	0,00155144	-0,01593157	-0,00910221	0,02691369	0,0050841	0,00117072	-0,00063193
0,00449779	-0,00575455	0,001502	-0,01044934	-0,00724513	-0,00273238	0,01517255	0,00229213	0,01088504	-0,00978174
-0,002162895	-0,02116192	0,01380745	-0,02163969	0,0144648	0,01289995	-0,03053226	-0,02848556	-3,7226E-05	0,00960799
-0,004799674	0,01955792	0,00269132	0,00414468	-0,00360122	0,00123411	-0,03398805	0,00573632	-0,0066319	-0,01567529
-0,016515179	0,00156786	-0,01875009	-0,00899582	0,00397791	0,02234205	-0,01511731	-0,00135084	-0,01185465	0,0071152
-0,00966985	0,0110127	0,0222376	-0,00059716	-0,00181196	0,00561049	-0,01274734	-0,00059134	0,00871144	-0,00888687
-0,019390703	-0,01826703	0,00928363	-0,01238886	-0,00202458	0,00254565	0,01948263	0,01413336	-0,01579516	0,00583402
-0,007244184									
0,00293772									
-0,000578597									
0,01264136									
-0,004988289									
0,009343694									

Table 5.6 Difference in dB between External CAS S-parameter correction of 8th December 2009 and 7th January 2010 (horizontal polarization)

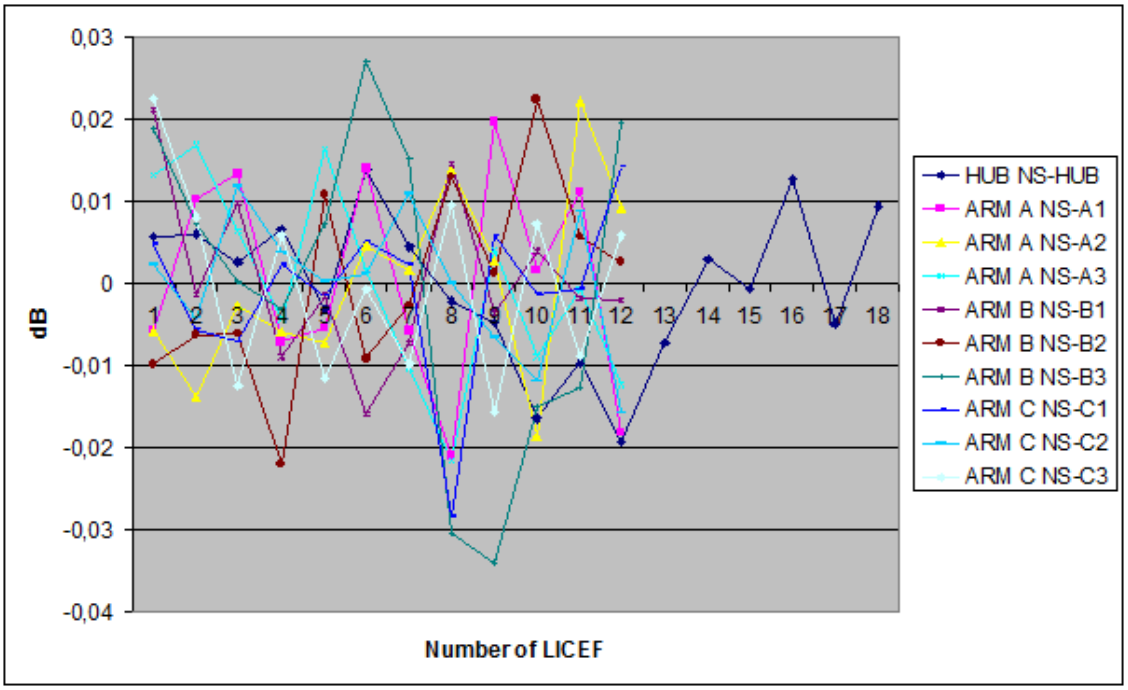

Fig. 5.6 Difference in dB between External CAS S-parameter correction of 8th December 2009 and 7th January 2010 (horizontal polarization)

5.2.1 NIR consistency Tool

During the calibration the NIR is in NIR-R mode to measure CAS HOT and WARM noise injection temperatures. The difference of these reference temperatures should be the same for all 6 NIR except for the NDN S-parameters unbalance. It is possible to check the consistency of these measurements by referring all them to a common reference port, applying the same idea that for the PMS Calibration Consistency tool [16].

The differences of CAS HOT and WARM temperatures measured by each channel of the NIR-LICEFs and the error respect the mean value of the 6 NIR-receivers was analyzed for several days of flight data. These results were compared with the previous results obtained from an IVT stability test dataset (Ground test).

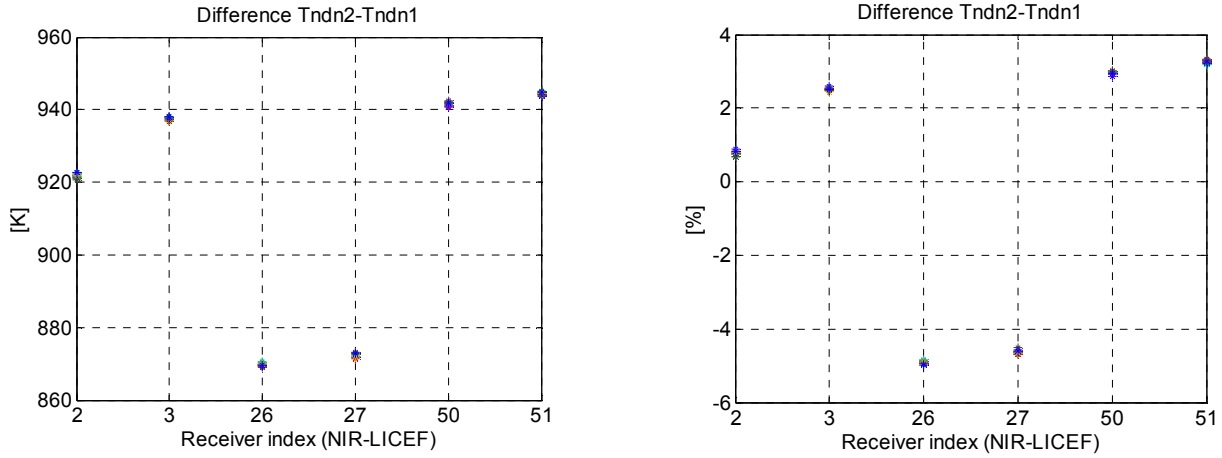

Fig. 5.7 IVT-2 STABILITY test. Left: Difference of CAS noise injection temperatures at the common reference port. Right: the same magnitude wrt the mean value of all NIR-LICEF [%]

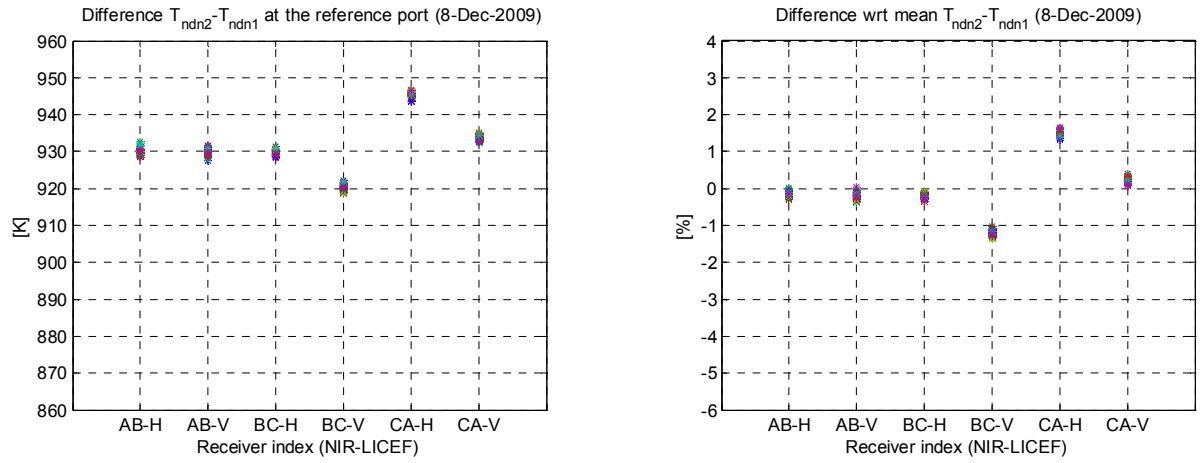

Fig. 5.8. Flight data 8th December 2009. Left: Difference of CAS noise injection temperatures at the common reference port.Right: the same magnitude wrt the mean value of all NIR-LICEF (%)

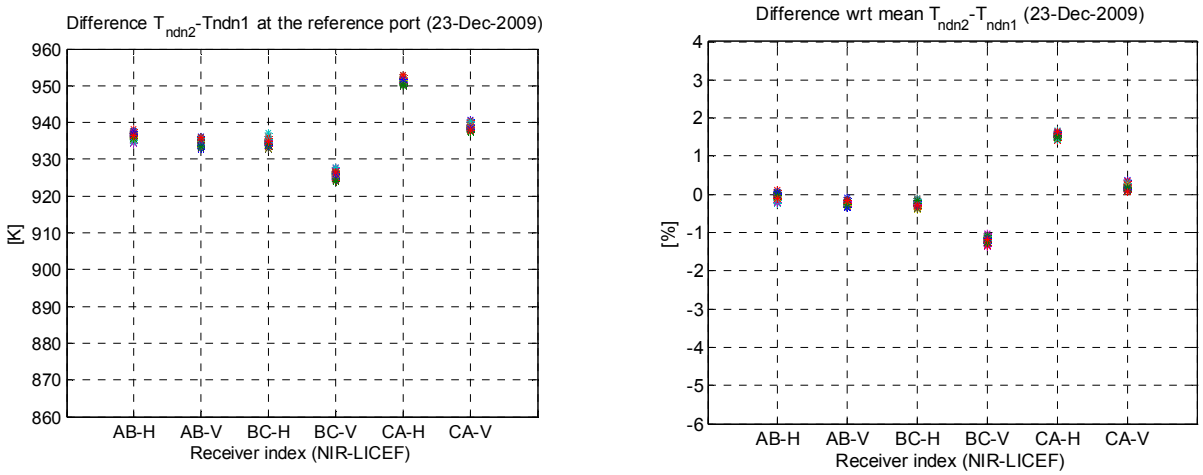

Fig. 5.9. Flight data 23rd December 2009. Left: Difference of CAS noise injection temperatures at the common reference port.Right: the same magnitude wrt the mean value of all NIR-LICEF (%)

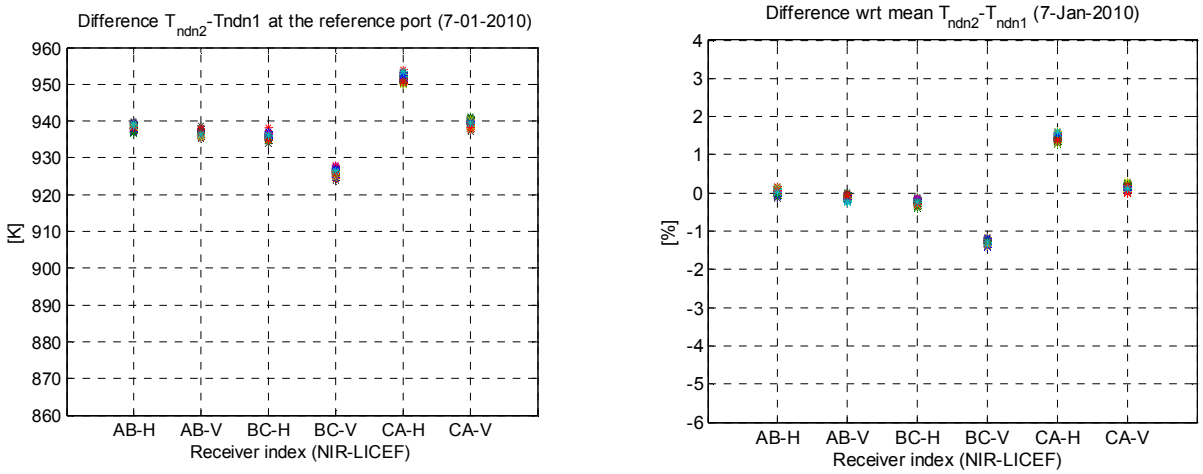

Fig. 5.10 Flight data 7th January 2009. Left: Difference of CAS noise injection temperatures at the common reference port. Right: the same magnitude wrt the mean value of all NIR-LICEF (%)

For the analysis of the IVT dataset, it must be pointed out that the NIR noise sources accuracy was based on an old ground calibration. In the case of the flight data, in each one of the three analyzed tests, the NIR-LICEFs were calibrated using the external calibration sequences showing a high degree of repeatability in a one month period.

5.3 Conclusions

These conclusions were preliminary since final conclusions required extensive comparison of data sets over longer periods of time. However, some interesting results were obtained:

- CAS S-parameters validation by means of deep sky views is a powerful tool to analyze the performance of the internal CAS calibration system. It basically works by comparison of PMS gain at VAP/HAP for two different methods: a) Internal CAS calibration and b) one-point PMS sky calibration.

- Even in the case that no CAS S-parameter correction is applied, both methods (internal CAS and external 1P) give PMS gain within 0.5 dB pk-to-pk differences with a small bias (Top plots in the appendix).
    - The on-ground CAS correction plots (middle plots in the appendix) show that the on-ground CAS correction factors in the MDB (MIRAS DataBase) 5_1, corrects CAS-parameters errors to a large extend, to be almost compliant to the error budget table (marginal non-compliances for the HUB). However, a small bias is clearly shown in some of the plots, as an indication that an additional correction can be applied.

- The CAS correction factor computed from the CAS external validation tool, is computed by equalling the 1P gain PMS sky calibration and the internal CAS 4P gain calibration (bottom plots in the appendix):
    - It is computed as the mean correction factor between H and V polarizations. The difference between both correction factors is ±0.1 dB *(Fig. 5.4).* This means that uncertainty for the switch S-parameter and the antenna efficiency (H/V) are almost negligible.
    - The external CAS correction factor is very stable in one month period ±0.035 dB (*Fig. 5.5 and Fig. 5.6*).
    - It is compatible with the current calibration scheme, since can replace the CAS correction factor in an update of the MDB v 5_1.
    - After the correction, 1P PMS external gain equals the 4P internal CAS PMS gain at VAP/HAP to 1% pk-to-pk (*Fig. 5.2 and Fig. 5.3*). Although this discrepancy is low and well within the error budget, it requires further assessment since should be lower.

- The NIR consistency tool shows that the performance of the NIR-R mode has improved with relation to the ground default behaviour, from 8% pk-to-pk differences to 2.5% pk-to-pk differences *(Fig. 5.7*). It must be pointed out that these plots have been produced with the MDB CAS correction factor and may change using the external CAS factor. The NIR-R behaviour is also very stable in a one-month period (*Fig. 5.8, Fig. 5.9 and Fig. 5.10*). This is in agreement with the stability of the external CAS correction factor.
- The external CAS correction factor given in this TN requires further assessment since:
    - It has been computed with no PMS second order correction (deflection method) because this correction was not implemented by the time of the simulations

- During the Commissioning Phase a new configuration of the instrument has been performed. It will not work for the new instrument configuration (arm A in nominal mode), since the CAS S-parameters have changed. A new CAS correction factor must be computed.
- It only proves that the internal CAS calibration can give the same results that the external 1P calibration. However, an assessment about the absolute accuracy of the two methods (1P PMS external calibration vs CAS 4P internal calibration) has not given final results so far.

Chapter 6

6 External CAS and antenna efficiency correction

This chapter is devoted to analyze the consistency of the PMS calibration products from the external calibration events at VAP/HAP planes. In case of discrepancy, comprehensive simulations are undertaken to produce correction coefficients to be tested for consistency. Such external correction factors are assigned to physical subsystems to ease traceability of the discrepancies with relation to the ground tests.

6.1 Computation of CAS and antenna efficiency coefficients

Before explaining the method to compute the CAS factors it is necessary to make a review of the theory of the previous chapter.

Both internal CAS 4P and external 1P PMS gains must be equal at VAP/HAP planes during deep sky calibration: The error can be corrected.

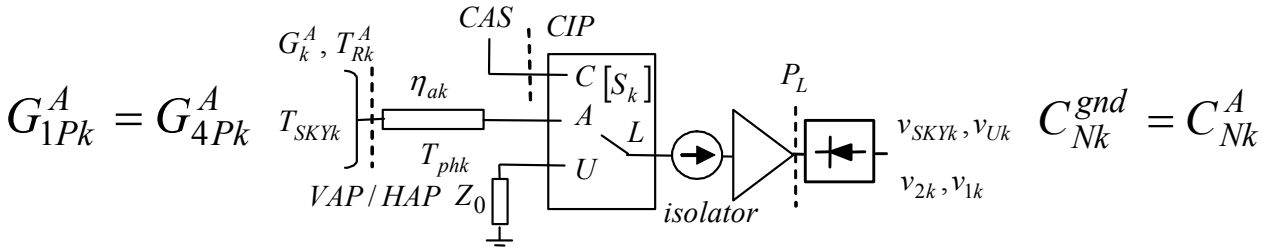

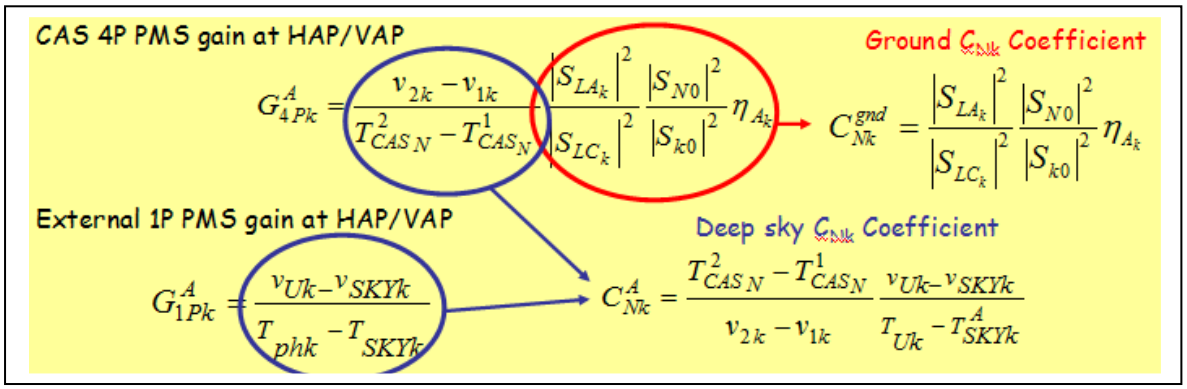

Fig. 6.1 Ground and Sky coefficients

External CAS and antenna efficiency correction

In order to equal G1P to G4P it is necessary to modify the equation of G4P using External CAS factors and External antenna efficiency:

$$G_{4Pk}^{A} = \frac{v_{2k} - v_{1k}}{T_{CAS\,N}^{2} - T_{CAS_N}^{1}} \frac{\left|S_{LA_k}\right|^2}{\left|S_{LC_k}\right|^2} \frac{\left|S_{N0}\right|^2}{\left|S_{k0}\right|^2} \frac{f_{N_{SKY}}^2}{f_{k_{SKY}}^2} \eta_{A_k} F_{Ak_{SKY}} \qquad \textbf{(6.1)}$$

First, the antenna efficiency is recomputed from external calibration to match ground receiver equivalent temperature TR measured by MIER Comunicaciones (a private company selected by the ESA in several space programs, therefore becoming the first Spanish supplier of active microwave flight equipment) before launch at CIP ($TR(MIER)$) to external 1P receiver temperature measured ad VAP/HAP using the Friis equation.

Next it's described the HAP case:

$$\begin{aligned}
&T_{R1P} = T_{RMIER} \\
&T_{R1P} = T_{ph} \cdot \left(\frac{1}{G_{ch}} - 1\right) + \frac{T_{RMIER}}{G_{ch}} \\
&G_{ch} = eta_H \cdot |\, S_{hipCip}\,|^2 \\
&T_{R1P} + T_{ph} = \frac{T_{ph} + T_{RMIER}}{G_{ch}} \qquad \textbf{(6.2)} \\
&G_{ch} = \frac{T_{ph} + T_{RMIER}}{T_{ph} + T_{R1P}} \cdot f \\
&\boxed{eta_H = \frac{G_{ch}}{|\, S_{hipCip}\,|^2}}
\end{aligned}$$

The official external antenna efficiency computed using this method is shown in the next table:

Receiver	etaH	etaV	Receiver	etaH	etaV
LCF_AB_03	0.905043015	0.921889873	LCF_A_12	0.895614827	0.894915461
NIR_AB01_H	0.972513627	0.972799339	LCF_A_13	0.899053705	0.897140962
NIR_AB01_V	0.938006148	0.938091343	LCF_A_14	0.913790352	0.915094309
LCF_A_01	0.938702967	0.93774881	LCF_A_15	0.881681888	0.897982938
LCF_A_02	0.915063708	0.904913234	LCF_A_16	0.902429549	0.875504311
LCF_A_03	0.940058355	0.944920319	LCF_A_17	0.883035498	0.869490155
LCF_A_04	0.917173236	0.924739675	LCF_A_18	0.908843562	0.910203027
LCF_A_05	0.927416168	0.902476196	LCF_A_19	0.896533186	0.889873664
LCF_A_06	0.905990105	0.89333407	LCF_A_20	0.906200831	0.889052077
LCF_A_07	0.910305046	0.89996988	LCF_A_21	0.912273993	0.905388567
LCF_A_08	0.91152064	0.91471778	LCF_BC_03	0.929025485	0.930881609
LCF_A_09	0.895377589	0.903730689	NIR_BC01_H	0.951093544	0.951143083
LCF_A_10	0.888363832	0.888137535	NIR_BC01_V	0.962543208	0.962976668
LCF_A_11	0.910644161	0.906169096	LCF_B_01	0.911161581	0.925569387

Receiver	etaH	etaV	Receiver	etaH	etaV
LCF_B_02	0.911398695	0.916068291	NIR_CA01_V	0.944902796	0.944617814
LCF_B_03	0.893123146	0.88581776	LCF_C_01	0.907836809	0.918780405
LCF_B_04	0.914695667	0.912416188	LCF_C_02	0.920384952	0.93033495
LCF_B_05	0.896018405	0.900760677	LCF_C_03	0.919879608	0.930888306
LCF_B_06	0.922138908	0.923892578	LCF_C_04	0.926609731	0.923462358
LCF_B_07	0.920852406	0.919081896	LCF_C_05	0.920093157	0.914115531
LCF_B_08	0.905272565	0.907289526	LCF_C_06	0.900761637	0.902558596
LCF_B_09	0.897240025	0.894719205	LCF_C_07	0.913016996	0.901593684
LCF_B_10	0.885676777	0.897492701	LCF_C_08	0.908294796	0.905705851
LCF_B_11	0.939007858	0.93998041	LCF_C_09	0.89562284	0.895723512
LCF_B_12	0.895242355	0.892128463	LCF_C_10	0.91369364	0.902425436
LCF_B_13	0.919586606	0.906935467	LCF_C_11	0.901498473	0.904383612
LCF_B_14	0.904458436	0.915135148	LCF_C_12	0.922141421	0.926338544
LCF_B_15	0.898833323	0.892851243	LCF_C_13	0.913292088	0.91897942
LCF_B_16	0.909548292	0.91378988	LCF_C_14	0.941266956	0.939164968
LCF_B_17	0.903713438	0.91636493	LCF_C_15	0.922607412	0.913604211
LCF_B_18	0.909115395	0.909141293	LCF_C_16	0.919447927	0.90397291
LCF_B_19	0.911096042	0.920844344	LCF_C_17	0.92332633	0.929123847
LCF_B_20	0.892199984	0.895798035	LCF_C_18	0.912441212	0.912297875
LCF_B_21	0.906011049	0.917933858	LCF_C_19	0.89731384	0.900437548
LCF_CA_03	0.907918875	0.924717246	LCF_C_20	0.924345158	0.925039608
NIR_CA01_H	0.936991143	0.936994501	LCF_C_21	0.915141254	0.905380322

Table 6.1 Official external antenna efficiency

So, the results in MATLAB confirms that computation is perfect because the difference between TR MIER and TR 1P is 0%.

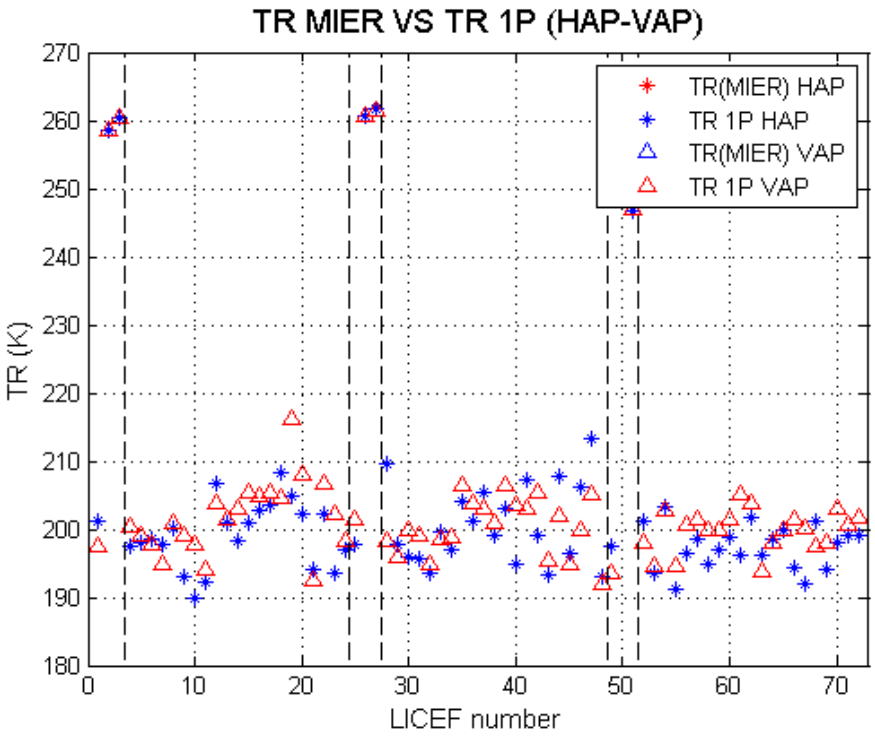

Fig. 6.2 TR MIER vs TR 1P (HAP-VAP)

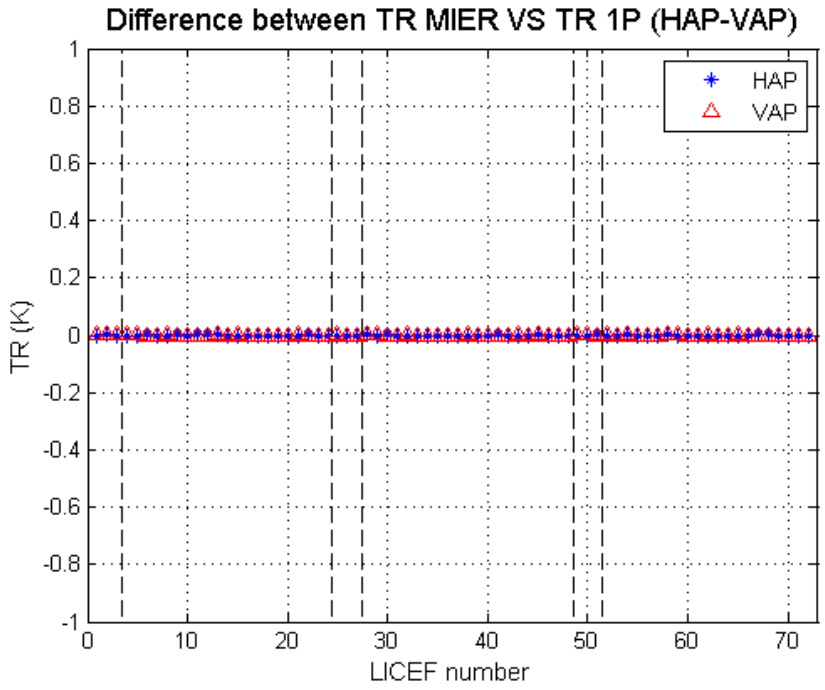

Fig. 6.3 Difference between TR MIER vs TR 1P (HAP-VAP)

In order to compute these equations it was necessary to create a MATLAB tool to obtain results with flight data:

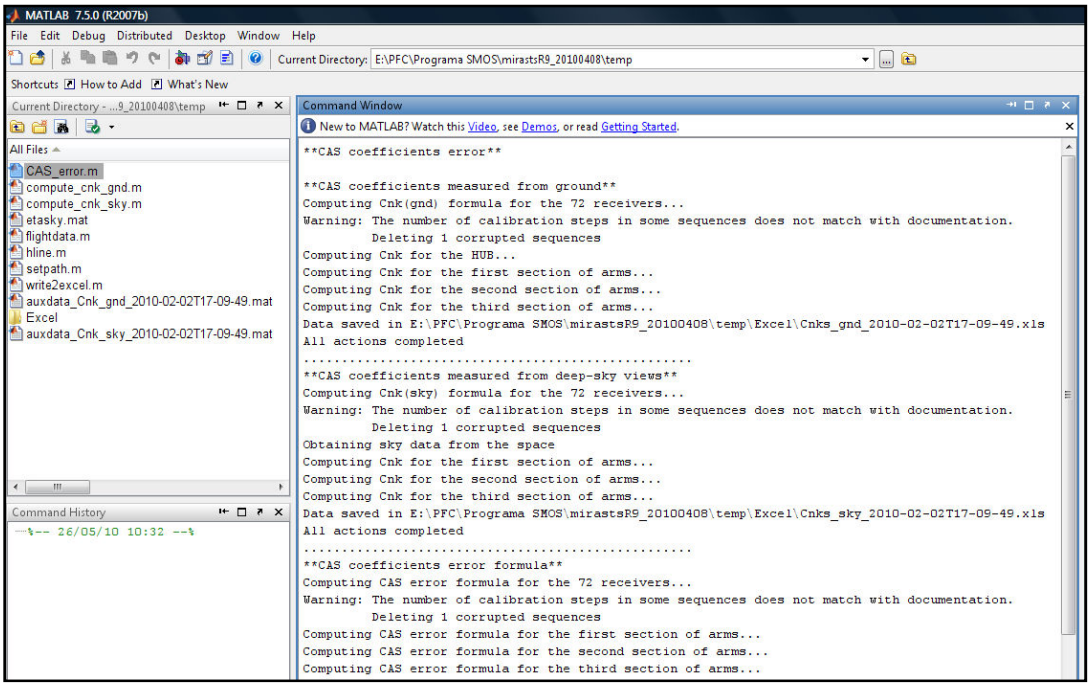

Fig. 6.4 CAS error tool

This tool creates excel files that contains all the results. The useful data to create CAS factors is the CAS error excel file (dB) that the program save in this format:

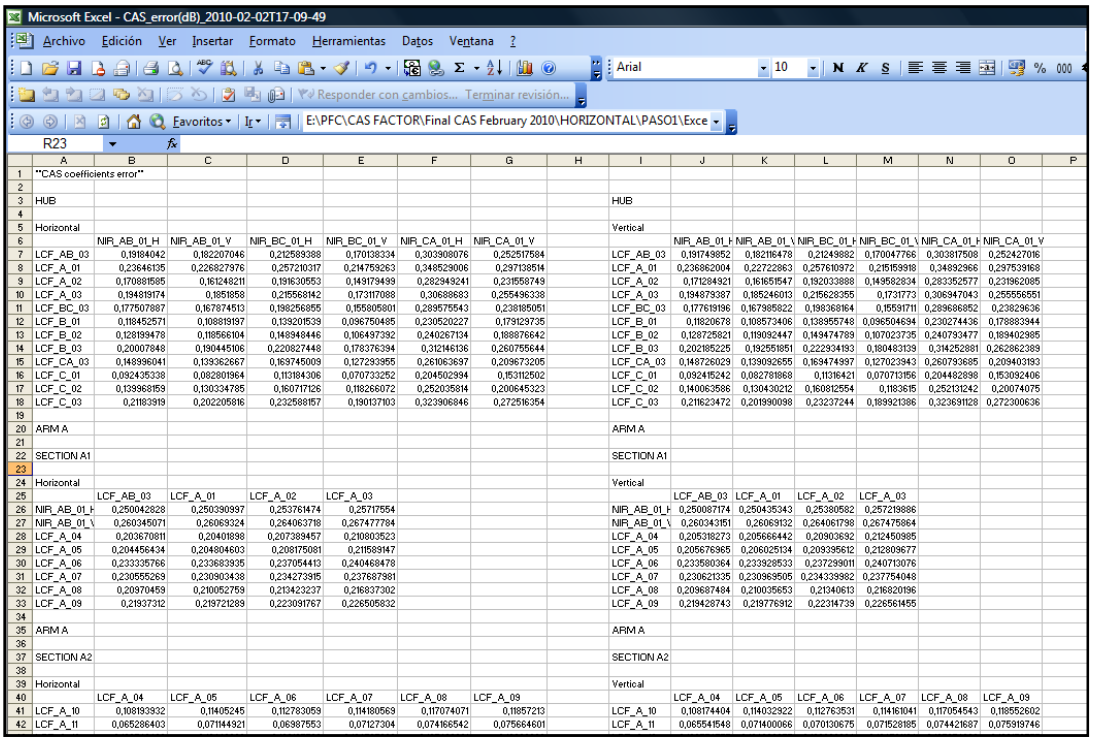

Fig. 6.5 CAS error excel file

HUB						
Horizontal						
	NIR_AB_01_H	NIR_AB_01_V	NIR_BC_01_H	NIR_BC_01_V	NIR_CA_01_H	NIR_CA_01_V
LCF_AB_03	0,19184042	0,182207046	0,212589388	0,170138334	0,303908076	0,252517584
LCF_A_01	0,23646135	0,226827976	0,257210317	0,214759263	0,348529006	0,297138514
LCF_A_02	0,170881585	0,161248211	0,191630553	0,149179499	0,282949241	0,231558749
LCF_A_03	0,194819174	0,1851858	0,215568142	0,173117088	0,30688683	0,255496338
LCF_BC_03	0,177507887	0,167874513	0,198256855	0,155805801	0,289575543	0,238185051
LCF_B_01	0,118452571	0,108819197	0,139201539	0,096750485	0,230520227	0,179129735
LCF_B_02	0,128199478	0,118566104	0,148948446	0,106497392	0,240267134	0,188876642
LCF_B_03	0,20007848	0,190445106	0,220827448	0,178376394	0,312146136	0,260755644
LCF_CA_03	0,148996041	0,139362667	0,169745009	0,127293955	0,261063697	0,209673205
LCF_C_01	0,092435338	0,082801964	0,113184306	0,070733252	0,204502994	0,153112502
LCF_C_02	0,139968159	0,130334785	0,160717126	0,118266072	0,252035814	0,200645323
LCF_C_03	0,21183919	0,202205816	0,232588157	0,190137103	0,323906846	0,272516354

Fig. 6.6 CAS error excel file

The results are structured in rows and columns depending on what LICEF is reference or not, and they are separate between HUB, ARM A, ARM B, ARM C and H/V polarization.

Once these results are obtained is possible to generate a new table of CAS factors following these steps (HUB case):

1. Convert CAS coefficients error from dB units to linear units.

HUB						
Horizontal						
	NIR_AB_01_H	NIR_AB_01_V	NIR_BC_01_H	NIR_BC_01_V	NIR_CA_01_H	NIR_CA_01_V
LCF_AB_03	1,045163037	1,042847261	1,050168382	1,03995329	1,072483965	1,059867948
LCF_A_01	1,05595676	1,053617069	1,061013798	1,050693212	1,08355984	1,070813533
LCF_A_02	1,040131283	1,037826656	1,045112532	1,034946618	1,06732068	1,0547654
LCF_A_03	1,045880143	1,043562778	1,050888923	1,040666822	1,073219816	1,060595143
LCF_BC_03	1,041719488	1,039411341	1,046708342	1,036526906	1,0689504	1,05637595
LCF_B_01	1,027650072	1,0253731	1,032571547	1,022527622	1,054513205	1,042108585
LCF_B_02	1,029959026	1,027676937	1,034891559	1,024825066	1,056882516	1,044450024
LCF_B_03	1,047147471	1,044827298	1,05216232	1,041927833	1,074520273	1,061880301
LCF_CA_03	1,0349029	1,032609858	1,03985911	1,029744297	1,061955625	1,049463456
LCF_C_01	1,021512143	1,019248771	1,026404224	1,016420288	1,048214829	1,035884298
LCF_C_02	1,032753834	1,030465553	1,037699751	1,027605943	1,059750381	1,047284154
LCF_C_03	1,049986993	1,047660528	1,055015441	1,044753201	1,077434021	1,064759774

Fig. 6.7 CAS error excel file

2. Computation of mean of each row and column using an excel tool created for implement this method:

HUB							
Horizontal							
	NIR_AB_01_H	NIR_AB_01_V	NIR_BC_01_H	NIR_BC_01_V	NIR_CA_01_H	NIR_CA_01_V	MEAN
LCF_AB_03	1,045163037	1,042847261	1,05016838	1,03995329	1,07248396	1,05986795	**1,051747314**
LCF_A_01	1,05595676	1,053617069	1,0610138	1,05069321	1,08355984	1,07081353	**1,062609035**
LCF_A_02	1,040131283	1,037826656	1,04511253	1,03494662	1,06732068	1,0547654	**1,046683862**
LCF_A_03	1,045880143	1,043562778	1,05088892	1,04066682	1,07321982	1,06059514	**1,052468937**
LCF_BC_03	1,041719488	1,039411341	1,04670834	1,03652691	1,0689504	1,05637595	**1,048282071**
LCF_B_01	1,027650072	1,0253731	1,03257155	1,02252762	1,05451321	1,04210858	**1,034124022**
LCF_B_02	1,029959026	1,027676937	1,03489156	1,02482507	1,05688252	1,04445002	**1,036447521**
LCF_B_03	1,047147471	1,044827298	1,05216232	1,04192783	1,07452027	1,0618803	**1,053744249**
LCF_CA_03	1,0349029	1,032609858	1,03985911	1,0297443	1,06195563	1,04946346	**1,041422541**
LCF_C_01	1,021512143	1,019248771	1,02640422	1,01642029	1,04821483	1,0358843	**1,027947426**
LCF_C_02	1,032753834	1,030465553	1,03769975	1,02760594	1,05975038	1,04728415	**1,039259936**
LCF_C_03	1,049986993	1,047660528	1,05501544	1,0447532	1,07743402	1,06475977	**1,056601659**
MEAN	**1,039396929**	**1,037093929**	**1,04437466**	**1,03421592**	**1,06656713**	**1,05402071**	

Fig. 6.8 CAS Generator excel file

3. Re-organize results in a table with this format (HUB and ARMs in ODD and EVEN source):

HUB	ARM A			ARM B			ARM C		
NS-HUB	NS-A1	NS-A2	NS-A3	NS-B1	NS-B2	NS-B3	NS-C1	NS-C2	NS-C3
LCF-AB-03	LCF-AB-03	LCF-A-04	LCF-A-10	LCF-BC-03	LCF-B-04	LCF-B-10	LCF-CA-03	LCF-C-04	LCF-C-10
NIR-AB-01-H	NIR-AB-01-H	LCF-A-05	LCF-A-11	NIR-BC-01-H	LCF-B-05	LCF-B-11	NIR-CA-01-H	LCF-C-05	LCF-C-11
NIR-AB-01-V	NIR-AB-01-V	LCF-A-06	LCF-A-12	NIR-BC-01-V	LCF-B-06	LCF-B-12	NIR-CA-01-V	LCF-C-06	LCF-C-12
LCF-A-01	LCF-A-01	LCF-A-07	LCF-A-13	LCF-B-01	LCF-B-07	LCF-B-13	LCF-C-01	LCF-C-07	LCF-C-13
LCF-A-02	LCF-A-02	LCF-A-08	LCF-A-14	LCF-B-02	LCF-B-08	LCF-B-14	LCF-C-02	LCF-C-08	LCF-C-14
LCF-A-03	LCF-A-03	LCF-A-09	LCF-A-15	LCF-B-03	LCF-B-09	LCF-B-15	LCF-C-03	LCF-C-09	LCF-C-15
LCF-BC-03	LCF-A-04	LCF-A-10	LCF-A-16	LCF-B-04	LCF-B-10	LCF-B-16	LCF-C-04	LCF-C-10	LCF-C-16
NIR-BC-01-H	LCF-A-05	LCF-A-11	LCF-A-17	LCF-B-05	LCF-B-11	LCF-B-17	LCF-C-05	LCF-C-11	LCF-C-17
NIR-BC-01-V	LCF-A-06	LCF-A-12	LCF-A-18	LCF-B-06	LCF-B-12	LCF-B-18	LCF-C-06	LCF-C-12	LCF-C-18
LCF-B-01	LCF-A-07	LCF-A-13	LCF-A-19	LCF-B-07	LCF-B-13	LCF-B-19	LCF-C-07	LCF-C-13	LCF-C-19
LCF-B-02	LCF-A-08	LCF-A-14	LCF-A-20	LCF-B-08	LCF-B-14	LCF-B-20	LCF-C-08	LCF-C-14	LCF-C-20
LCF-B-03	LCF-A-09	LCF-A-15	LCF-A-21	LCF-B-09	LCF-B-15	LCF-B-21	LCF-C-09	LCF-C-15	LCF-C-21
LCF-CA-03									
NIR-CA-01-H									
NIR-CA-01-V									
LCF-C-01									
LCF-C-02	Red: EVEN								
LCF-C-03	Blue: ODD								

Fig. 6.9 CAS Generator excel file

HUB	ARM A			ARM B			ARM C		
NS-HUB	NS-A1	NS-A2	NS-A3	NS-B1	NS-B2	NS-B3	NS-C1	NS-C2	NS-C3
1,011341194	1	1	1	1	1	1	1	1	1
1,030965075	1	1	1	1	1	1	1	1	1
1,030094314	1	1	1	1	1	1	1	1	1
1,05822036	1	1	1	1	1	1	1	1	1
1,016818028	1	1	1	1	1	1	1	1	1
1,049903187	1	1	1	1	1	1	1	1	1
1,070842946	1	1	1	1	1	1	1	1	1
1,003356901	1	1	1	1	1	1	1	1	1
0,993514169	1	1	1	1	1	1	1	1	1
1,031978953	1	1	1	1	1	1	1	1	1
1,035753581	1	1	1	1	1	1	1	1	1
1,030869497	1	1	1	1	1	1	1	1	1
1,000121569									
1,062690245									
1,049283652									
0,988451274									
1,014198789									
1,031309338									

Fig. 6.10 CAS Generator excel file

4. Compute CAS factors using the previous table and the next equations:

$$CAS_{factorREFERENCE} = \sqrt{f_{REFERENCE}}$$
$$CAS_{factorLICEFtocalibrate} = \frac{1}{\sqrt{f_{LICEFtocalibrate}}} \quad \textbf{(6.3)}$$

5. CAS created (only HUB):

HUB	ARM A			ARM B			ARM C		
NS-HUB	NS-A1	NS-A2	NS-A3	NS-B1	NS-B2	NS-B3	NS-C1	NS-C2	NS-C3
0,994377185	1	1	1	1	1	1	1	1	1
1,015364503	1	1	1	1	1	1	1	1	1
1,014935621	1	1	1	1	1	1	1	1	1
0,972102239	1	1	1	1	1	1	1	1	1
0,991695588	1	1	1	1	1	1	1	1	1
0,975945066	1	1	1	1	1	1	1	1	1
0,966355917	1	1	1	1	1	1	1	1	1
1,001677044	1	1	1	1	1	1	1	1	1
0,996751809	1	1	1	1	1	1	1	1	1
0,984384077	1	1	1	1	1	1	1	1	1
0,982588729	1	1	1	1	1	1	1	1	1
0,984913648	1	1	1	1	1	1	1	1	1
0,999939221									
1,030868685									
1,024345475									
1,005824864									
0,992975324									
0,984703598									

Fig. 6.11 CAS table (only HUB)

6. Next, it is possible to obtain better results making double correction using the next equations:

$$CAS_{factor(doublecorrected)} = \sqrt{f_{current}} \cdot f_{previous} \quad \textbf{(6.4)}$$

So, in each section it is necessary to compute CAS factors 2 times (factors and double correction). A new table is obtained:

HUB	ARM A			ARM B			ARM C					
NS-HUB	NS-A1	NS-A2	NS-A3	NS-B1	NS-B2	NS-B3	NS-C1	NS-C2	NS-C3	DOUBLE CORRECTION	PREVIOUS	FINAL
1,022714467	1	1	1	1	1	1	1	1	1	1,011293462	0,97508908	0,98610122
0,977790021	1	1	1	1	1	1	1	1	1	0,988832656	1,01950818	1,00812298
0,977790021	1	1	1	1	1	1	1	1	1	0,988832656	1,01837809	1,00700551
1,022714467	1	1	1	1	1	1	1	1	1	1,011293462	0,97009273	0,98104843
1,022714467	1	1	1	1	1	1	1	1	1	1,011293462	0,97744479	0,98848353
1,022714467	1	1	1	1	1	1	1	1	1	1,011293462	0,97475474	0,9857631
1,022714467	1	1	1	1	1	1	1	1	1	1,011293462	0,9766994	0,98772972
0,977790021	1	1	1	1	1	1	1	1	1	0,988832656	1,02194651	1,01053408
0,977790021	1	1	1	1	1	1	1	1	1	0,988832656	1,01696407	1,00560728
1,022714467	1	1	1	1	1	1	1	1	1	1,011293462	0,9833626	0,99446817
1,022714467	1	1	1	1	1	1	1	1	1	1,011293462	0,98225973	0,99335285
1,022714467	1	1	1	1	1	1	1	1	1	1,011293462	0,97416471	0,9851664
1,022714467										1,011293462	0,97991073	0,99097732
0,977790021										0,988832656	1,03274737	1,02121432
0,977790021										0,988832656	1,02665511	1,0151901
1,022714467										1,011293462	0,98631253	0,99745141
1,022714467										1,011293462	0,98092975	0,99200785
1,022714467										1,011293462	0,97284658	0,98383338

Fig. 6.12 CAS Generator excel file

DOUBLE CORRECTION	PREVIOUS	FINAL
1,011293462	0,97508908	0,98610122
0,988832656	1,01950818	1,00812298
0,988832656	1,01837809	1,00700551
1,011293462	0,97009273	0,98104843
1,011293462	0,97744479	0,98848353
1,011293462	0,97475474	0,9857631
1,011293462	0,9766994	0,98772972
0,988832656	1,02194651	1,01053408
0,988832656	1,01696407	1,00560728
1,011293462	0,9833626	0,99446817
1,011293462	0,98225973	0,99335285
1,011293462	0,97416471	0,9851664
1,011293462	0,97991073	0,99097732
0,988832656	1,03274737	1,02121432
0,988832656	1,02665511	1,0151901
1,011293462	0,98631253	0,99745141
1,011293462	0,98092975	0,99200785
1,011293462	0,97284658	0,98383338

Fig. 6.13 CAS Generator excel file

7. Repeat method 8 times because of the distributed calibration of the instrument. Then it is obtained the final CAS table in horizontal polarization:

HUB	ARM A			ARM B			ARM C		
NS-HUB	NS-A1	NS-A2	NS-A3	NS-B1	NS-B2	NS-B3	NS-C1	NS-C2	NS-C3
0,98610122	1,00064227	0,99511327	0,99740953	1,00478265	1,00907409	1,00721605	1,00861287	1,00117772	1,00240653
1,00812298	0,99708552	0,99569462	1,00268918	0,99469545	1,00584059	1,00606935	1,00060169	1,0054726	1,00381397
1,00700551	0,99590359	0,99224455	0,98866758	1,00260349	1,01439929	1,00316503	1,00499187	1,00481856	1,00326132
0,98104843	0,99555488	0,99272195	0,9961534	1,01217825	1,0086767	1,00621534	1,01621356	1,00965871	0,99555481
0,98848353	1,00348923	0,99543942	0,99927977	1,01077679	1,00517181	1,00958993	1,01002715	0,99714252	1,00850683
0,9857631	1,00112093	0,99450349	0,99892785	1,00265626	1,00776006	1,00310037	1,00174975	1,00253281	1,0030304
0,98772972	1,00242297	1,00643655	1,00564438	0,99151078	0,993056	0,9928822	0,98505849	0,9960869	0,9971153
1,01053408	1,00233231	1,01142056	0,99607795	0,98810809	0,9920249	0,99265595	0,98912664	0,99774468	0,99942552
1,00560728	0,99900523	0,99716879	1,00179181	0,99616039	0,98895119	0,99083745	0,98851049	0,99710914	0,99966719
0,99446817	0,99932508	1,00452686	1,00174097	0,99076626	0,99195828	1,00098658	0,99295297	0,98934163	0,99442981
0,99335285	1,00172686	1,00766754	1,00198485	0,98688922	0,99464437	0,99310826	0,98081984	1,00227785	0,99624964
0,9851664	1,00061243	1,00742527	1,00978083	0,98915472	0,98888449	0,99445958	0,98599244	0,99679509	0,99657155
0,99097732									
1,02121432									
1,0151901									
0,99745141									
0,99200785									
0,98383338									

Fig. 6.14 CAS table (only horizontal)

8. Repeat all the previous steps using data from vertical polarization and then compute mean between H and V polarization.

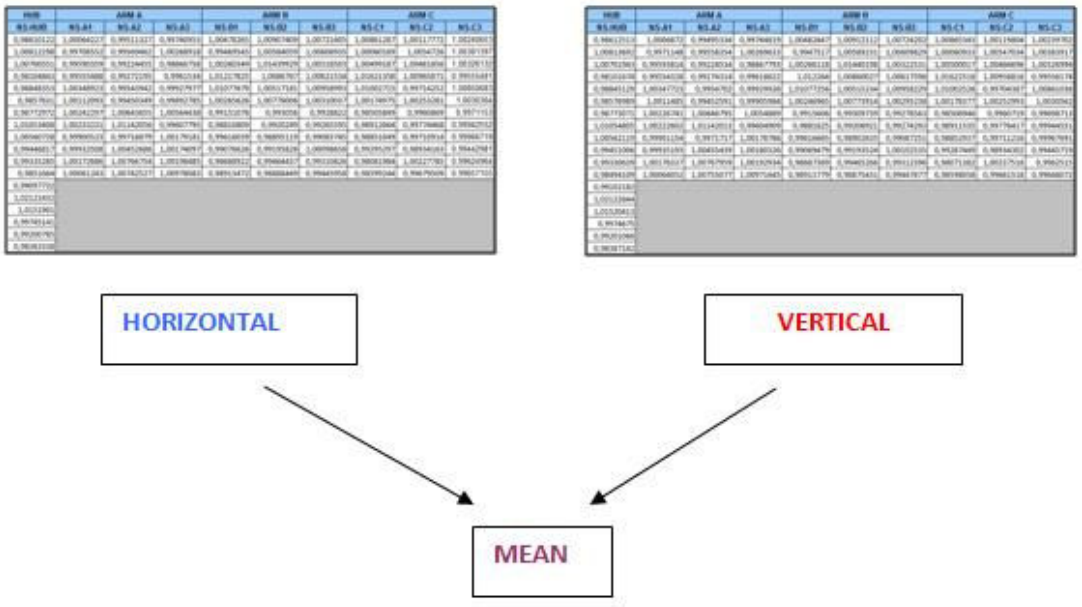

Fig. 6.15 CAS table (mean of horizontal and vertical)

9. Official CAS table is obtained from the mean of H/V polarization:

HUB	ARM A			ARM B			ARM C		
NS-HUB	NS-A1	NS-A2	NS-A3	NS-B1	NS-B2	NS-B3	NS-C1	NS-C2	NS-C3
0,98611317	1,00066473	0,9950333	0,99742886	1,00480456	1,0090976	1,00722904	1,00863315	1,00118788	1,00240177
1,00812995	0,99710016	0,99563908	1,00269275	0,99472357	1,00586645	1,00608382	1,00060551	1,00547147	1,00382657
1,00701247	0,99592086	0,99224495	0,98867275	1,00263234	1,01440064	1,00319517	1,00499602	1,00483276	1,00326563
0,98103259	0,99554908	0,99273254	0,99617081	1,01222112	1,00863849	1,00619566	1,01621937	1,00962343	0,99555828
0,98846741	1,00348323	0,99545481	0,99928953	1,01077468	1,00516208	1,00958611	1,01002621	0,99709319	1,00855859
0,98576649	1,00113472	0,9945147	0,99899384	1,00256295	1,0077496	1,00302638	1,00176676	1,00253137	1,0030433
0,98773022	1,00234519	1,00645225	1,00556664	0,99153569	0,99307669	0,99282392	0,98506398	0,9960794	0,99705121
1,01054106	1,00227916	1,01142035	0,99606352	0,9881353	0,99204706	0,99269944	0,989121	0,99775443	0,99943552
1,00561423	0,99900838	0,99717024	1,00178974	0,99616352	0,98898877	0,99085498	0,98851993	0,99711065	0,99967205
0,99448911	0,9993385	1,00454062	1,00177212	0,99073052	0,99194676	1,00100596	0,99291373	0,98934233	0,9944435
0,99332962	1,00174512	1,00767356	1,00195709	0,98688145	0,99464852	0,99311611	0,98076683	1,00232651	0,99625057
0,98505375	1,00062647	1,00748802	1,00974864	0,98914626	0,9888194	0,99446917	0,98598651	0,99680513	0,99652614
0,99099957									
1,02122138									
1,01519711									
0,99745946									
0,99200925									
0,9838524									

Fig. 6.16 Official CAS table

Finally, this table is included in MIRASTS and it is possible to confirm that the proposed approach since gives a mathematical match between External G1P and internal PMS gain G4P at VAP/HAP and between ground receiver temperatures at VAP/HAP.

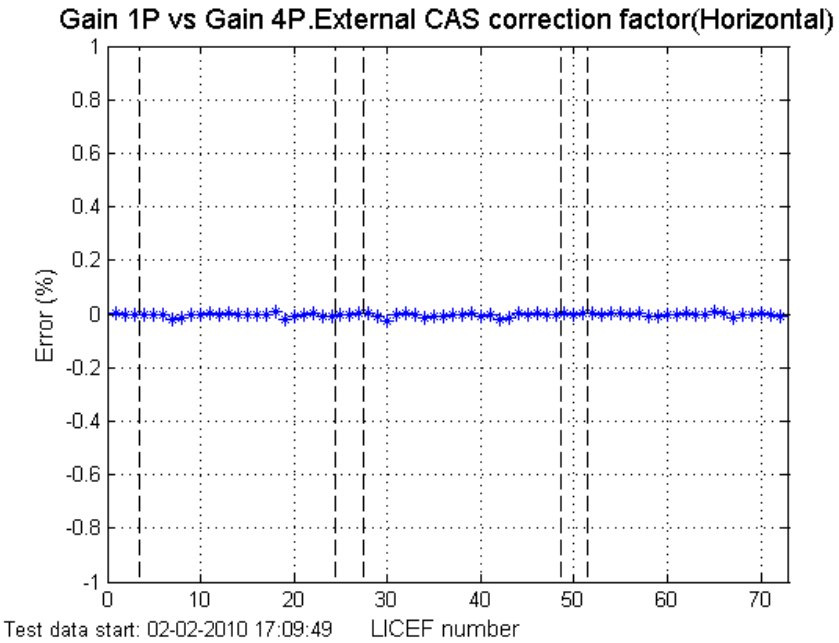

Fig. 6.17 Gain 1P vs Gain 4P. External CAS correction factor(Horizontal)

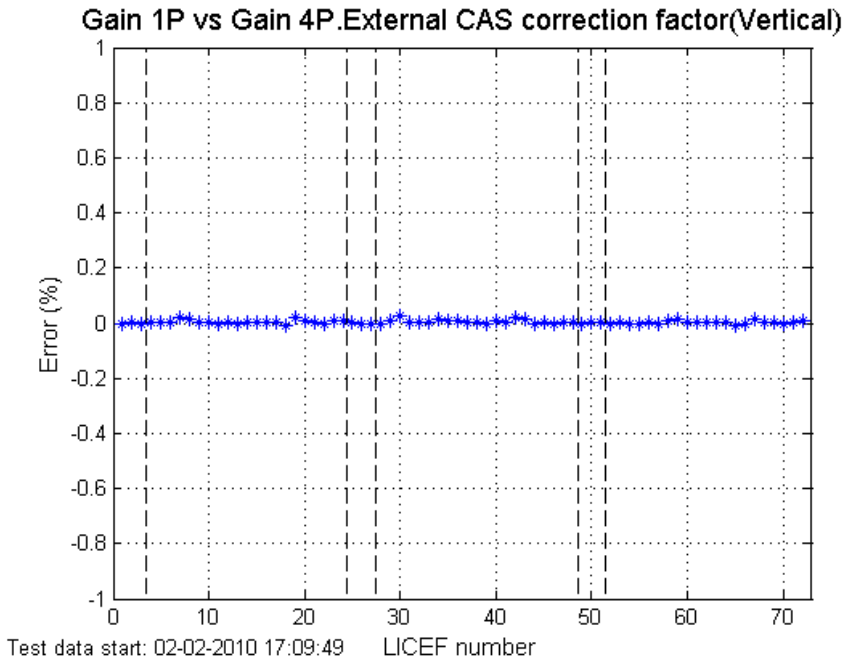

Fig. 6.18 Gain 1P vs Gain 4P. External CAS correction factor(Vertical)

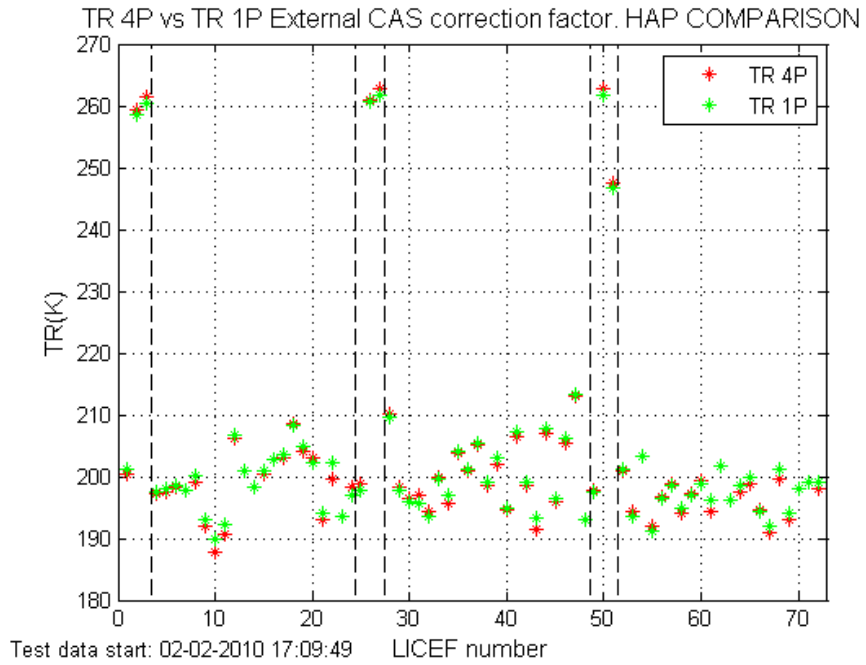

Fig. 6.19 TR 1P vs TR 4P. External antenna efficiency and External CAS correction factor (HAP)

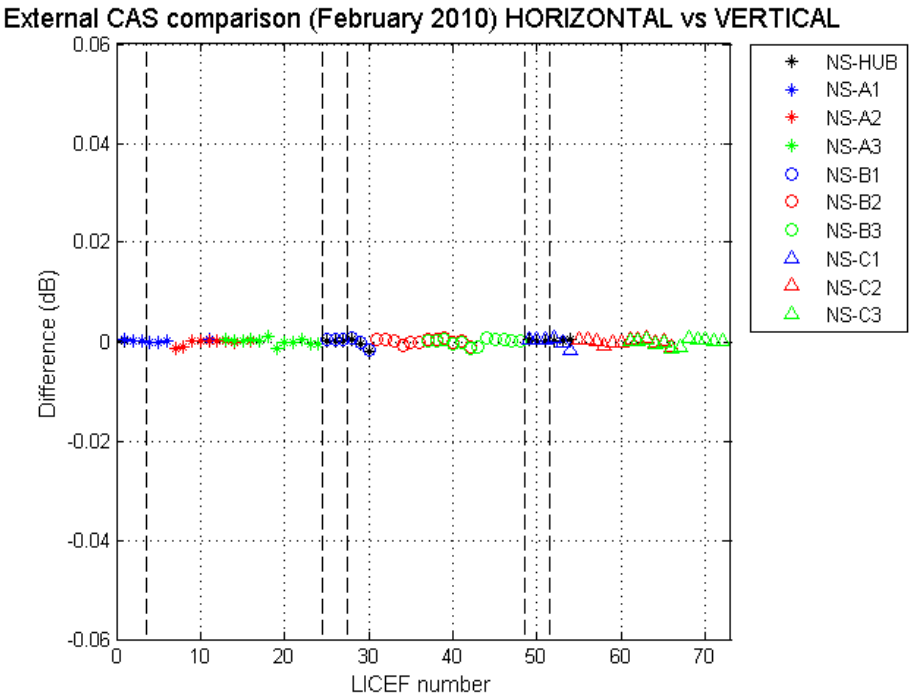

Fig. 6.20 External CAS comparison Horizontal vs Vertical

6.2 Summary of results

This section gives a summary of the results regarding the different external correction techniques that have been tested. The successive approaches are analyzed in terms of advantages and drawbacks with relation to the previous ones. **Two options (E and F) can be selected, since they are equivalent in terms of final performance. That is both give the same estimated PMS gain error.**

OPTION E: The external calibration approach proposal is as follows:

1) The antenna efficiency is recomputed from external calibration to match ground receiver equivalent temperature TR (measured at CIP) to external 1P receiver temperature measured ad VAP/HAP using the Friis equation.
    a. Output product: Antenna efficiencies: 72 values in H and 72 values in V.
2) Re-compute the External CAS coefficients using the external antenna efficiency
    a. Compute one set in H polarization
    b. Compute one set in V polarization
    c. Output product. The mean coefficient form H/V sets.

OPTION F: The external calibration approach proposal is as follows:

3) 1) The antenna efficiency is recomputed from external calibration to match internal PMS gain G4P at VAP/HAP to external G1P. The ground correction CAS factors are used with no changes.
    a. Output product: Antenna efficiencies: 72 values in H and 72 values in V.

	OPTION E	OPTION F
Advantages	G1P and G4P match to a negligible error External TR match ground TR to a negligible error As assigned (antenna efficiency and CAS), the correction factors have consistent physical values.	G1P and G4P match to negligible error Only a single set of correction factors is required (antenna efficiency in H/V) Very simple (straight forward) method to compute the correction factor from external calibration No need to recompute the CAS S-parameters, neither to refresh the CAS S-parameters, since the ground CAS factors are fixed.

Drawbacks	Need to compute two sets of correction factors in an iterative procedure: a) Computation of external antenna efficiency b) Iterative method to recompute the external CAS correction factors c) Re-computation of CAS-S-parameters to include new correction factor	It is a mathematical approach, not a physical approach. As a consequence ground TR do not match external TR at VAP/HAP. However, TR is an intermediate product with no impact in the instrument performance.

Table 6.2 Advantages and drawbacks of options E and F

Finally, a combination of both methods is selected as follows:

1) **Method E is applied once** since this method decouples the error in the CAS from the error in antenna efficiency. This gives the following results:
    a. 72 antenna efficiency External Coefficients for each polarization V/H
    b. A set of External CAS coefficients in the same format given in the MDBfactory.

2) After that, **periodic monitoring of antenna efficiency error by means of method F** (using the method E external CAS coefficients, not the ground coefficients from the MDBfactory file) can be applied. If the error is large, then the 72 antenna efficiency external coefficients can be refreshed.

AMPLITUDE CALIBRATION VALIDATION BY EXTERNAL CALIBRATION **SUMMARY OF RESULTS**	
A) No CAS Correction factor $G_{4Pk}^{A} = \frac{v_{2k} - v_{1k}}{T_{CAS\,N}^{2} - T_{CAS_N}^{1}} \frac{\left\|S_{LA_k}\right\|^2}{\left\|S_{LC_k}\right\|^2} \frac{\left\|S_{N0}\right\|^2}{\left\|S_{k0}\right\|^2} \eta_{A_k}$	-High dependency at CIP plane of G4P and TR with relation to LICEF arm position. -Consistency of G4P at a reference CIP port fail (when driven by a common noise source)
B) Correction factor assigned to CAS S-parameters Computed on-ground from consistency tool. $G_{4Pk}^{A} = \frac{v_{2k} - v_{1k}}{T_{CAS\,N}^{2} - T_{CAS_N}^{1}} \frac{\left\|S_{LA_k}\right\|^2}{\left\|S_{LC_k}\right\|^2} \frac{\left\|S_{N0}\right\|^2}{\left\|S_{k0}\right\|^2} \frac{f_{N_{GND}}^{2}}{f_{k_{GND}}^{2}} \eta_{A_k}$	-Correct CAS unbalance. However, it is a relative calibration and does not correct the absolute amplitude error. Also correction by segments of 6. -The correction is performed at CIP and does not take into account errors in the CIP to VAP/HAP. -When tested in-flight G4P fails to match G1P with a mean error of about 2%.
C) Correction factor assigned to CAS S-parameters. The factor is computed independently for H and V polarization and averaged to have a single CAS coefficient. Computed from external calibration from C_{nk} coefficients $G_{4Pk}^{A} = \frac{v_{2k} - v_{1k}}{T_{CAS\,N}^{2} - T_{CAS_N}^{1}} \frac{\left\|S_{LA_k}\right\|^2}{\left\|S_{LC_k}\right\|^2} \frac{\left\|S_{N0}\right\|^2}{\left\|S_{k0}\right\|^2} \frac{f_{N_{SKY}}^{2}}{f_{k_{SKY}}^{2}} \eta_{A_k}$	-G1P and G4P matches to 0.023dB RMS (0.53% RMS) due to the differences between H and V polarization and the need to average them. -Mier TR at VAP/HAP does not match TR external by 10K to 20 K. Some of the gain error should be assigned to the plane translation from CIP to VAP/HAP.
D) Additional correction factor assigned to antenna efficiency in addition to the ground CAS correction factor. Computed from external calibration to match ground TR at CIP to external TR at VAP/HAP. $G_{4Pk}^{A} = \frac{v_{2k} - v_{1k}}{T_{CAS\,N}^{2} - T_{CAS_N}^{1}} \frac{\left\|S_{LA_k}\right\|^2}{\left\|S_{LC_k}\right\|^2} \frac{\left\|S_{N0}\right\|^2}{\left\|S_{k0}\right\|^2} \frac{f_{N_{GND}}^{2}}{f_{k_{GND}}^{2}} \eta_{A_k} F_{Ak_{SKY}}$	- External TR at VAP/HAP matches ground TR. -G4P increases the mean error wrt external G1P from 2% to 4.5%. However, the dispersion of the error is reduced from 7.5% to 3.5% pk-to-pk. This, points to an improvement in antenna efficiency accuracy in H and V polarizations wrt to the ground single value estimation.

E) External CAS correction factor computed after applying the external antenna efficiency correction factor. $G_{4Pk}^{A} = \frac{v_{2k} - v_{1k}}{T_{CAS\,N}^{2} - T_{CAS_N}^{1}} \frac{\left\|S_{LA_k}\right\|^2}{\left\|S_{LC_k}\right\|^2} \frac{\left\|S_{N0}\right\|^2}{\left\|S_{k0}\right\|^2} \frac{f_{N_{SKY}}^{2}}{f_{k_{SKY}}^{2}} \eta_{A_k} F_{Ak_{SKY}}$	External TR at VAP/HAP matches ground TR. -G4P matches to G1P to a negligible error. External CAS coefficients in H and V polarizations are very similar, pointing to a good estimation of antenna efficiency in H and V polarization.
F) External antenna efficiency computed to match G4P to G1P when using the ground CAS correction factor. $G_{4Pk}^{A} = \frac{v_{2k} - v_{1k}}{T_{CAS\,N}^{2} - T_{CAS_N}^{1}} \frac{\left\|S_{LA_k}\right\|^2}{\left\|S_{LC_k}\right\|^2} \frac{\left\|S_{N0}\right\|^2}{\left\|S_{k0}\right\|^2} \frac{f_{N_{GND}}^{2}}{f_{k_{GND}}^{2}} \eta_{A_k} F_{Ak_{SKY}}$	Internal G4P matches G1P to a negligible error because there is no need to average H pol and V pol correction coefficients, as done in CASE C. Ground TR at VAP/HAP does not match external TR, since the fraction of the correction error related to CAS has been artificially assigned to antenna efficiency.

Table 6.3 Amplitude calibration validation by external calibration

6.3 Case A: No CAS correction factor

A) No CAS Correction factor $G_{4Pk}^{A} = \frac{v_{2k} - v_{1k}}{T_{CAS\,N}^{2} - T_{CAS_N}^{1}} \frac{\left\|S_{LA_k}\right\|^2}{\left\|S_{LC_k}\right\|^2} \frac{\left\|S_{N0}\right\|^2}{\left\|S_{k0}\right\|^2} \eta_{A_k}$	-High dependency at CIP plane of G4P and TR with relation to LICEF arm position -Consistency of G4P at a reference CIP port fails

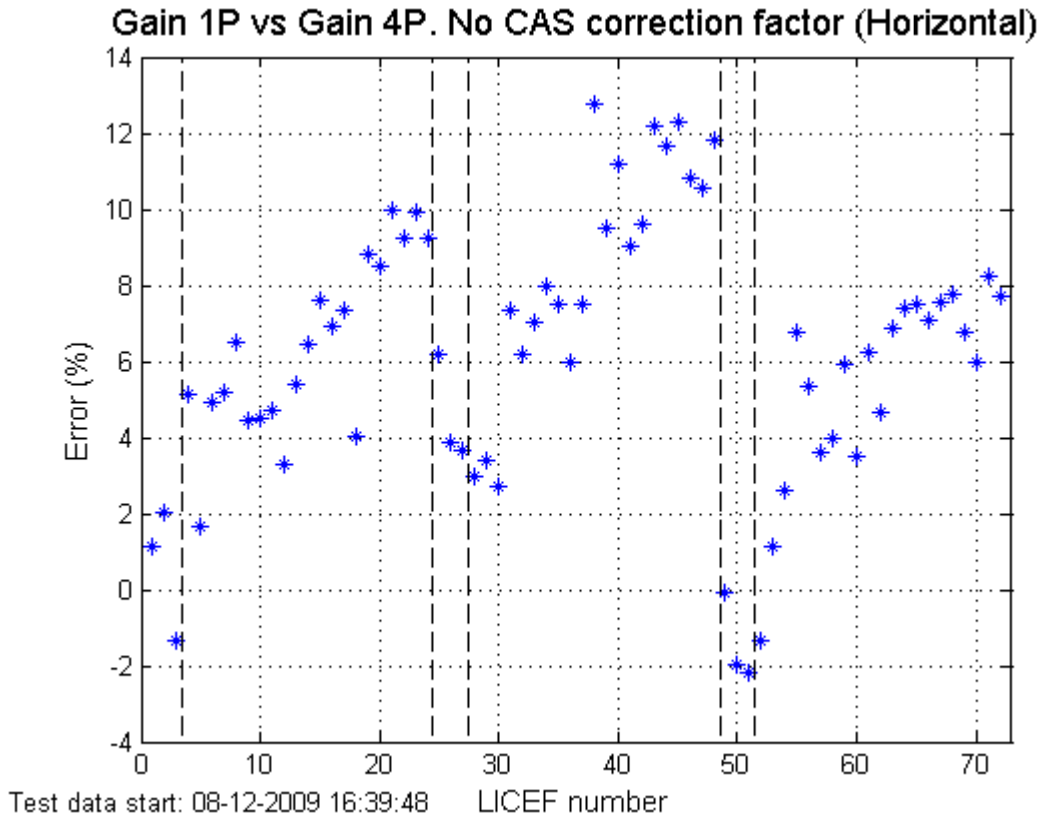

Fig. 6.21 Gain 1P vs Gain 4P. No CAS correction factor (Horizontal)

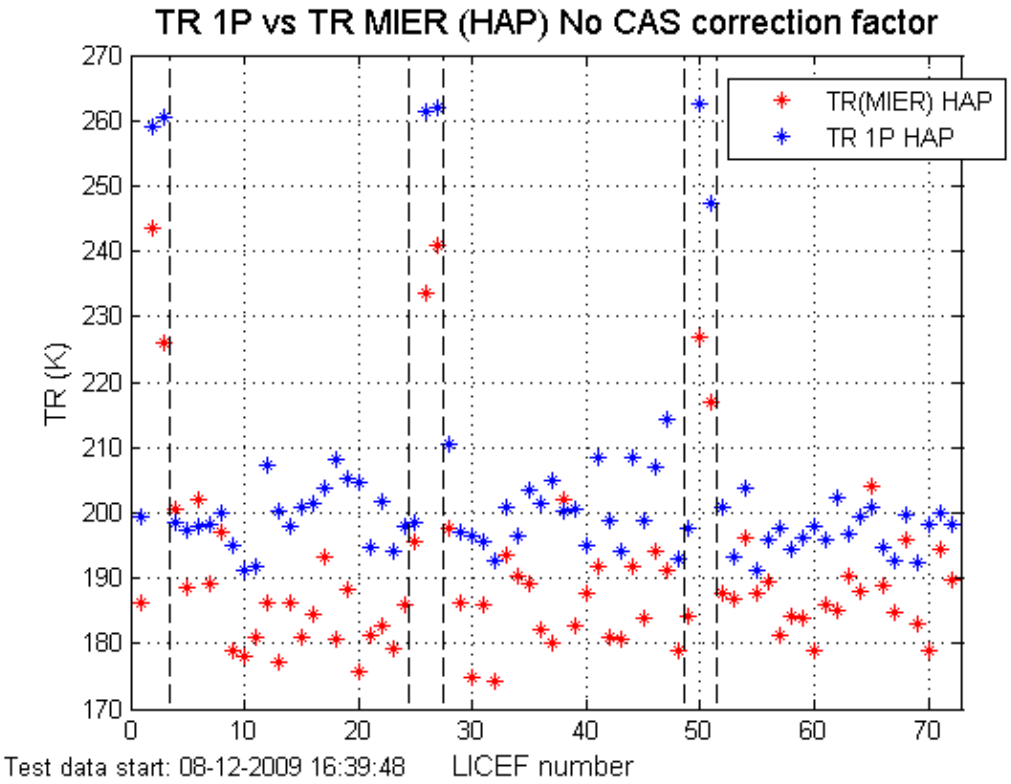

Fig. 6.22 TR 1P vs TR MIER. No CAS correction factor (Horizontal)

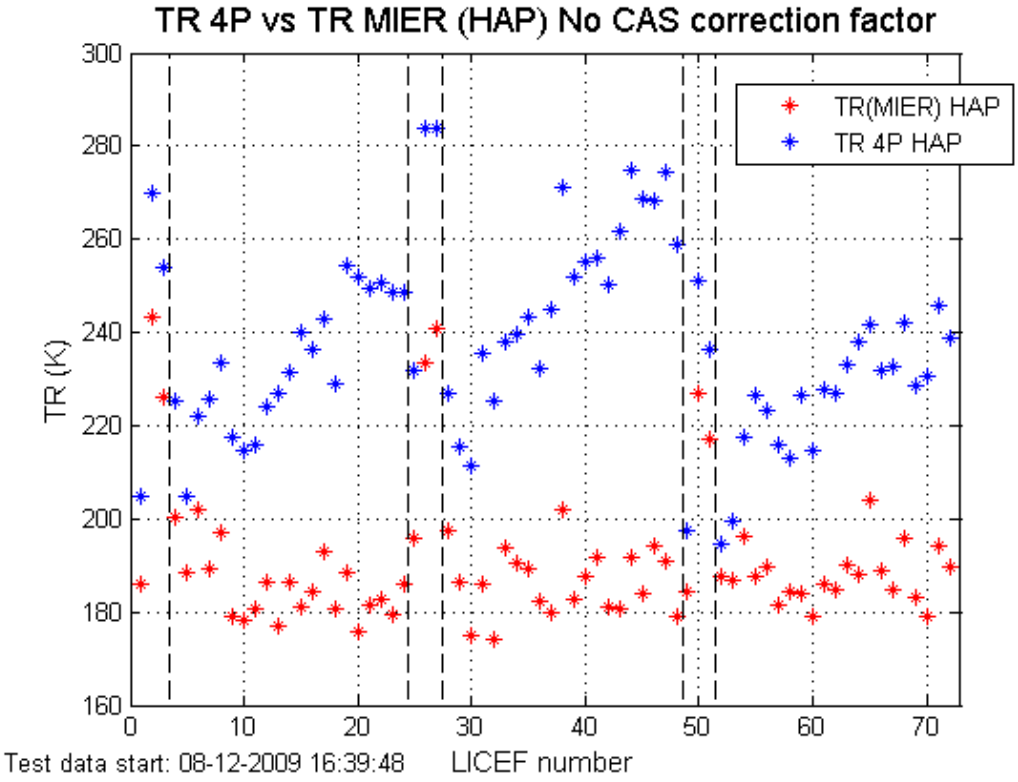

Fig. 6.23 TR 4P vs TR MIER. No CAS correction factor (Horizontal)

6.4 Case B: Ground CAS correction factor

B) Correction factor assigned to CAS S-parameters Computed on-ground from consistency tool. $G^{A}_{4Pk} = \frac{v_{2k} - v_{1k}}{T^{2}_{CAS\,N} - T^{1}_{CAS_N}} \frac{\left\|S_{LA_k}\right\|^2}{\left\|S_{LC_k}\right\|^2} \frac{\left\|S_{N0}\right\|^2}{\left\|S_{k0}\right\|^2} \frac{f^{2}_{N_{GND}}}{f^{2}_{k_{GND}}} \eta_{A_k}$	-Correct CAS unbalance. However, it is a relative calibration and does not correct the absolute amplitude error. Correction by segments of 6 and not at single LICEF level -The correction is performed at CIP and does not take into account errors in the CIP to VAP/HAP -When tested in-flight G4P fails to match G1P with a mean error of about 2%

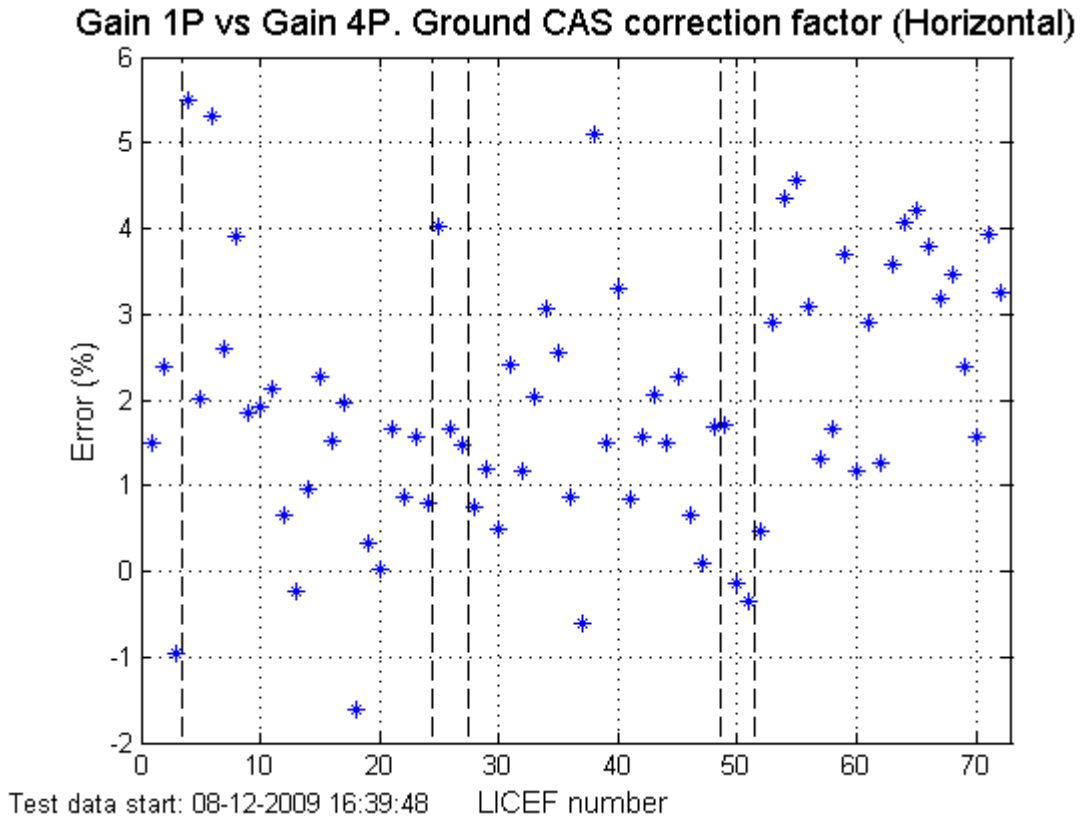

Fig. 6.24 Gain 1P vs Gain 4P. Ground CAS correction factor (Horizontal)

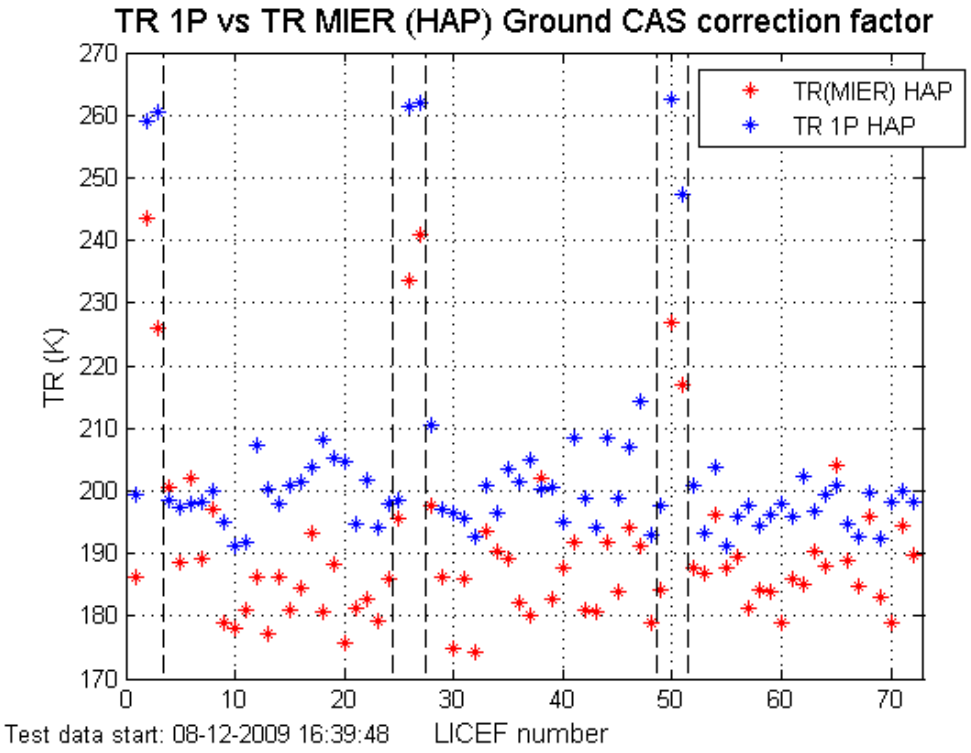

Fig. 6.25 TR 1P vs TR MIER. Ground CAS correction factor (Horizontal)

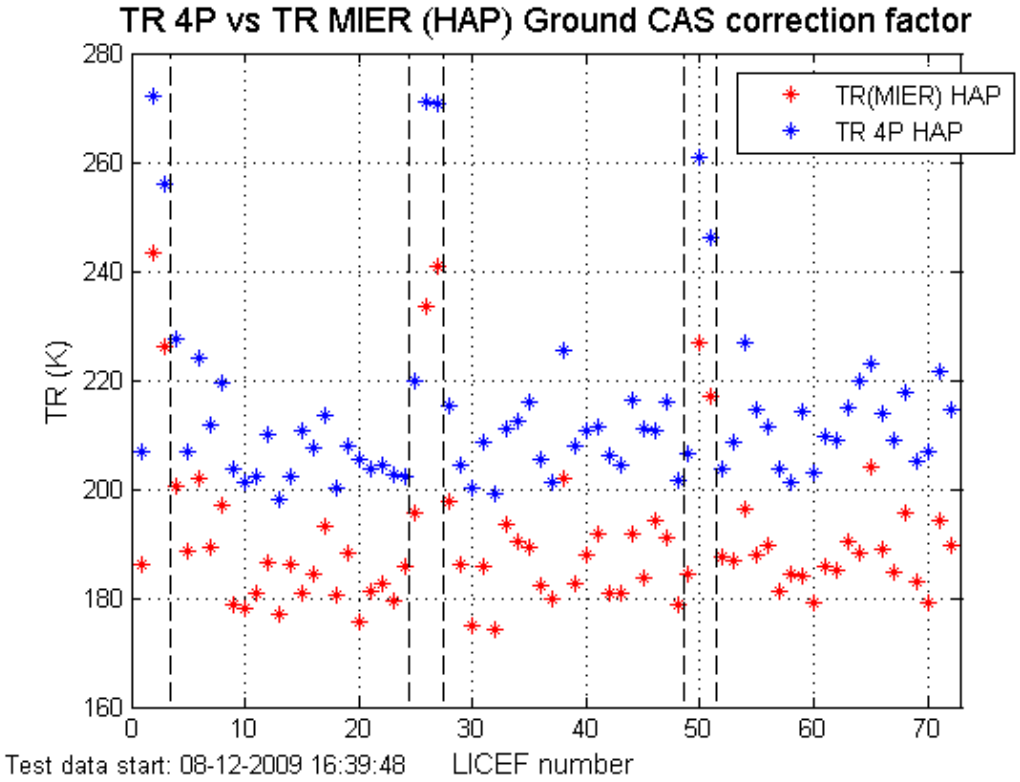

Fig. 6.26 TR 4P vs TR MIER. Ground CAS correction factor (Horizontal)

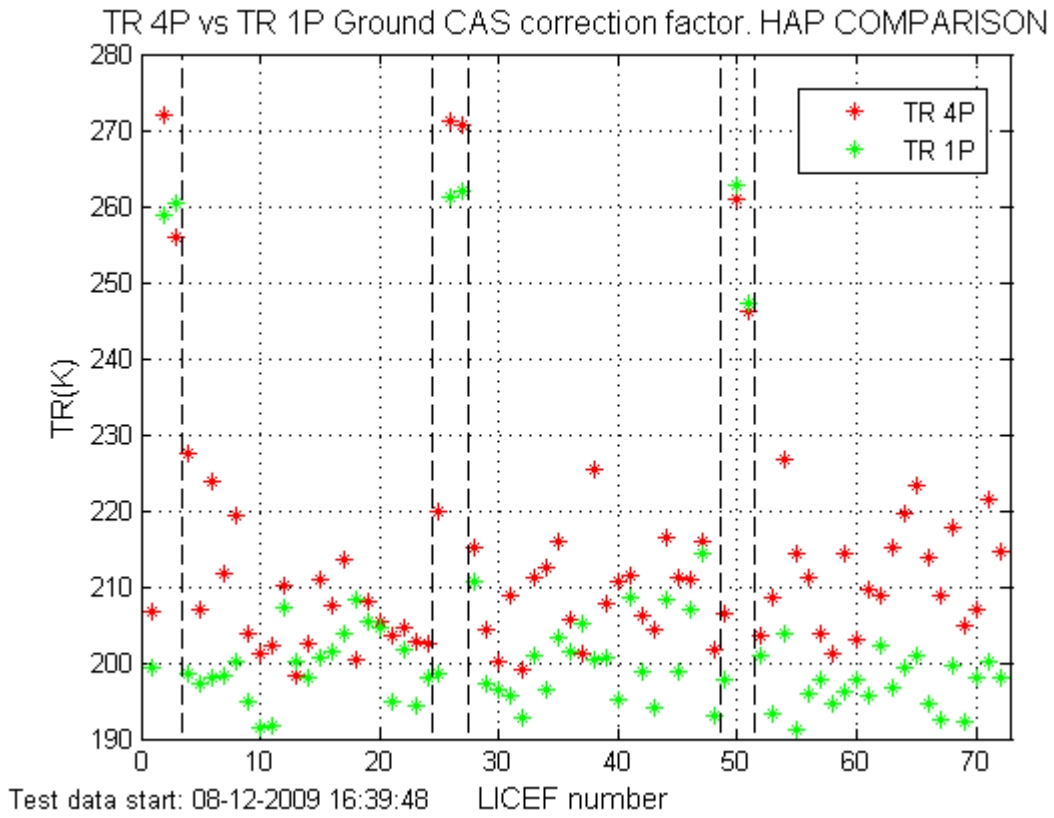

Fig. 6.27 TR 1P vs TR 4P. Ground CAS correction factor (Horizontal)

6.5 Case C: External CAS correction factor

C) Correction factor assigned to CAS S-parameters. The factor is computed independently for H and V polarization and averaged to have a single CAS coefficient. Computed from external calibration from C_{nk} coefficients $$G_{4Pk}^{A} = \frac{v_{2k} - v_{1k}}{T_{CAS\,N}^{2} - T_{CAS_N}^{1}} \frac{\left|S_{LA_k}\right|^2}{\left|S_{LC_k}\right|^2} \frac{\left|S_{N0}\right|^2}{\left|S_{k0}\right|^2} \frac{f_{N_{SKY}}^{2}}{f_{k_{SKY}}^{2}} \eta_{A_k}$$	-G1P and G4P matches to 0.023dB RMS (0.53% RMS) due to the differences between H and V polarization . -Mier TR at VAP/HAP does not match TR external by 10K to 20 K. Some of the gain error should be assigned to the plane translation from CIP to VAP/HAP

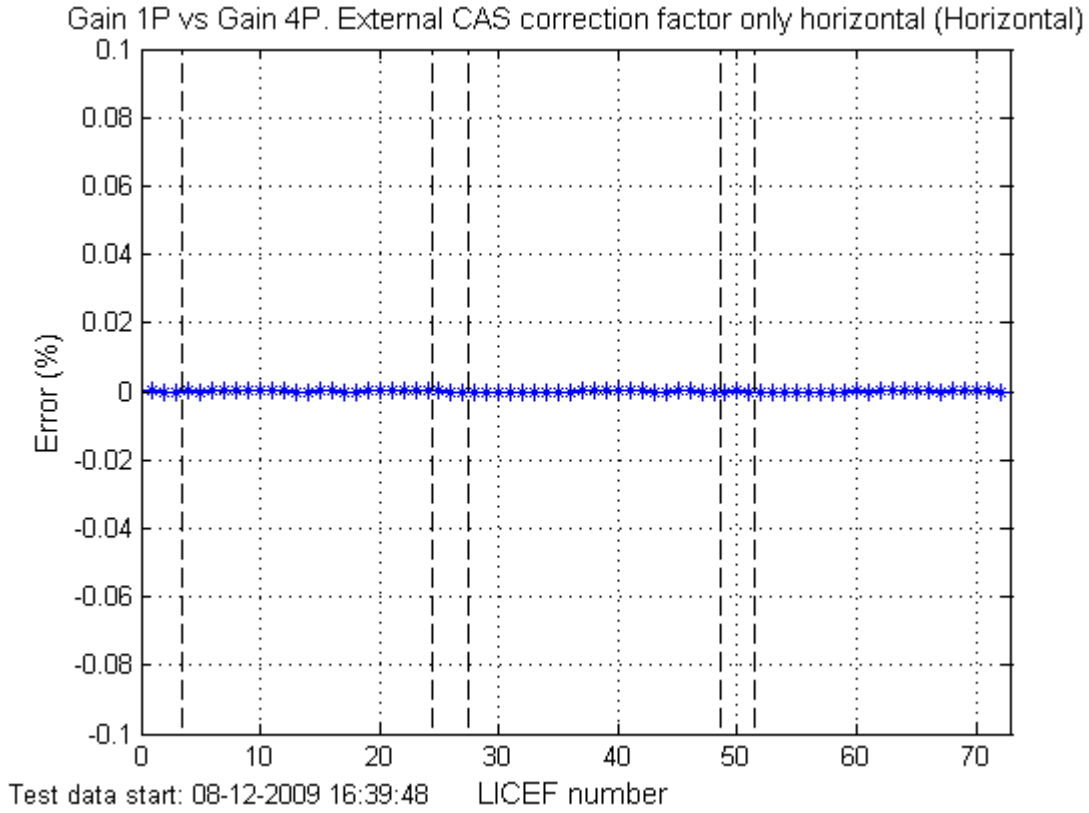

Fig. 6.28 Gain 1P vs Gain 4P. External CAS correction factor only horizontal (Horizontal)

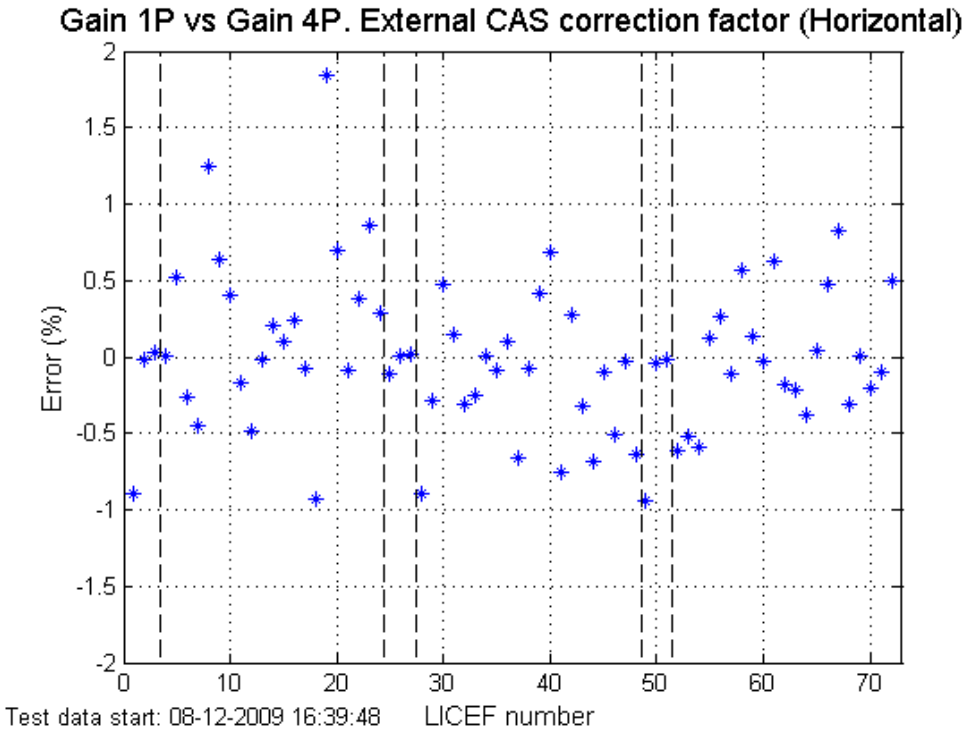

Fig. 6.29 Gain 1P vs Gain 4P. External CAS correction factor (Horizontal)

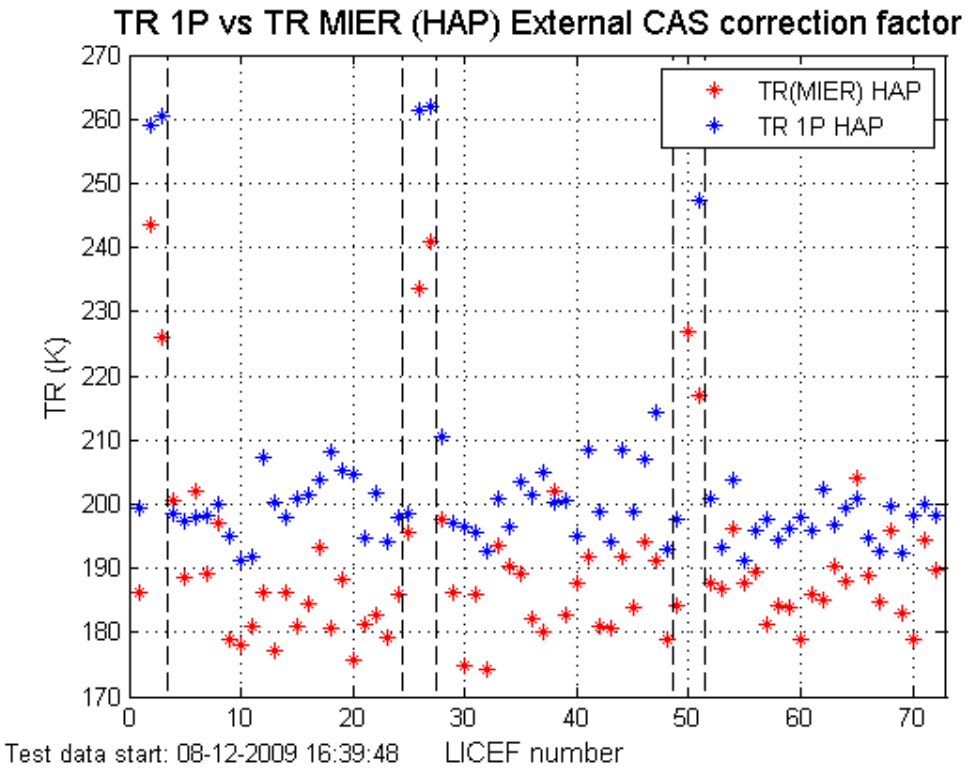

Fig. 6.30 TR 1P vs TR MIER. External CAS correction factor (Horizontal)

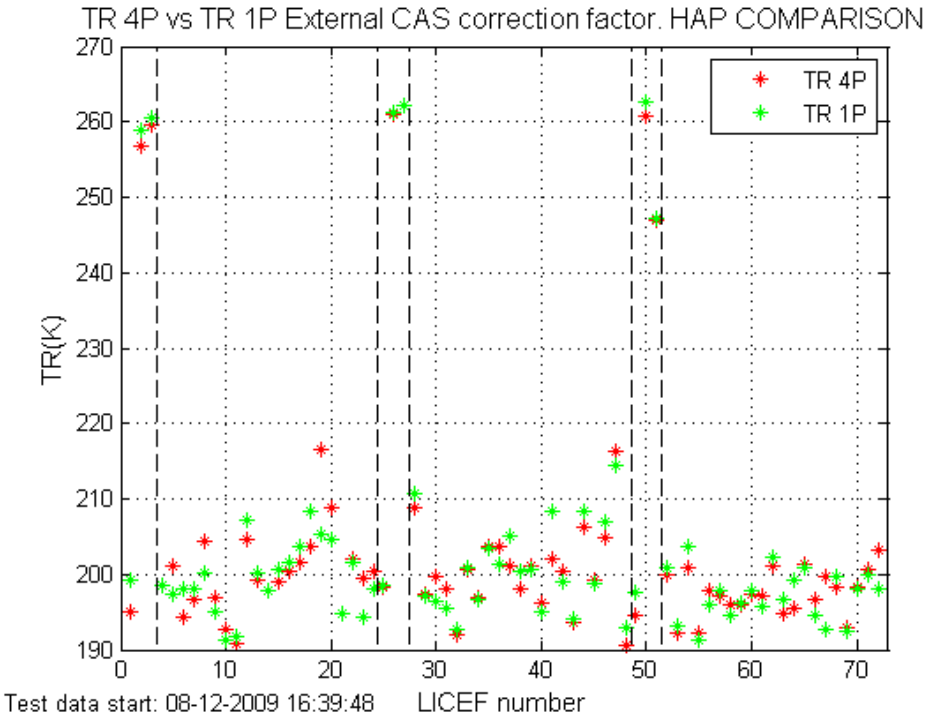

Fig. 6.31 TR 1P vs TR 4P. External CAS correction factor (Horizontal)

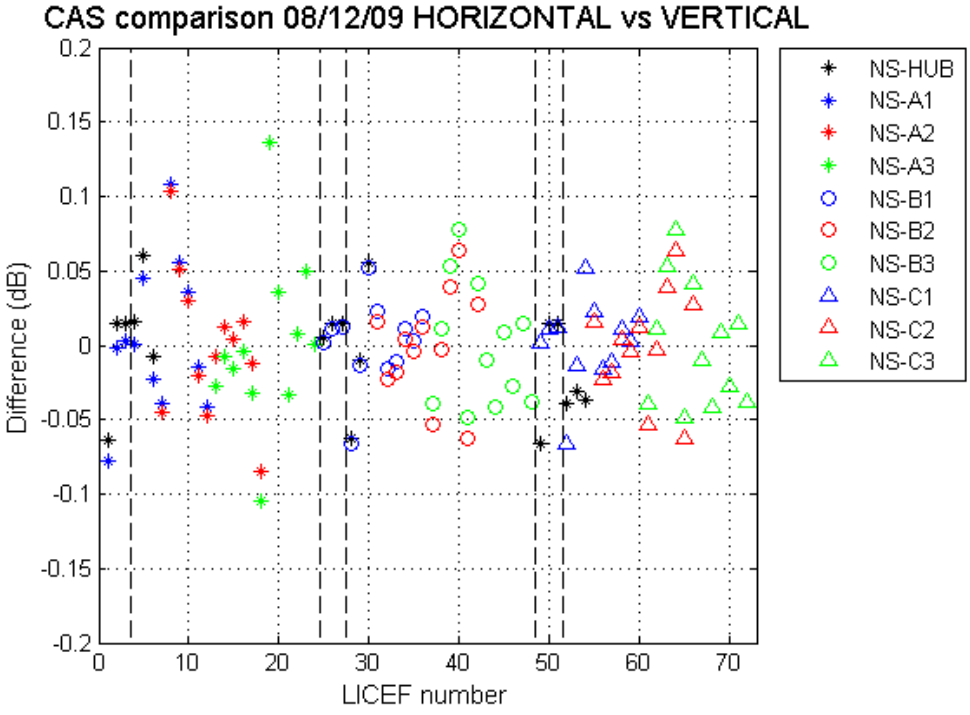

Fig. 6.32 External CAS comparison Horizontal vs Vertical

6.6 Case D: External antenna efficiency and ground CAS correction factor

D) Additional correction factor assigned to antenna efficiency in addition to the ground CAS correction factor. Computed from external calibration to match ground TR at CIP to external TR at VAP/HAP. $$G_{4Pk}^{A} = \frac{v_{2k} - v_{1k}}{T_{CAS\,N}^{2} - T_{CAS_N}^{1}} \frac{\left|S_{LA_k}\right|^2}{\left|S_{LC_k}\right|^2} \frac{\left|S_{N0}\right|^2}{\left|S_{k0}\right|^2} \frac{f_{N_{GND}}^2}{f_{k_{GND}}^2} \eta_{A_k} F_{Ak_{SKY}}$$	- External TR at VAP/HAP matches ground TR. -G4P increases the mean error wrt external G1P from 2% to 4.5%. However, the dispersion of the error is reduced from 7.5% to 3.5% pk-to-pk. This, points to an improvement in antenna efficiency accuracy in H and V polarizations wrt to the ground single value estimation.

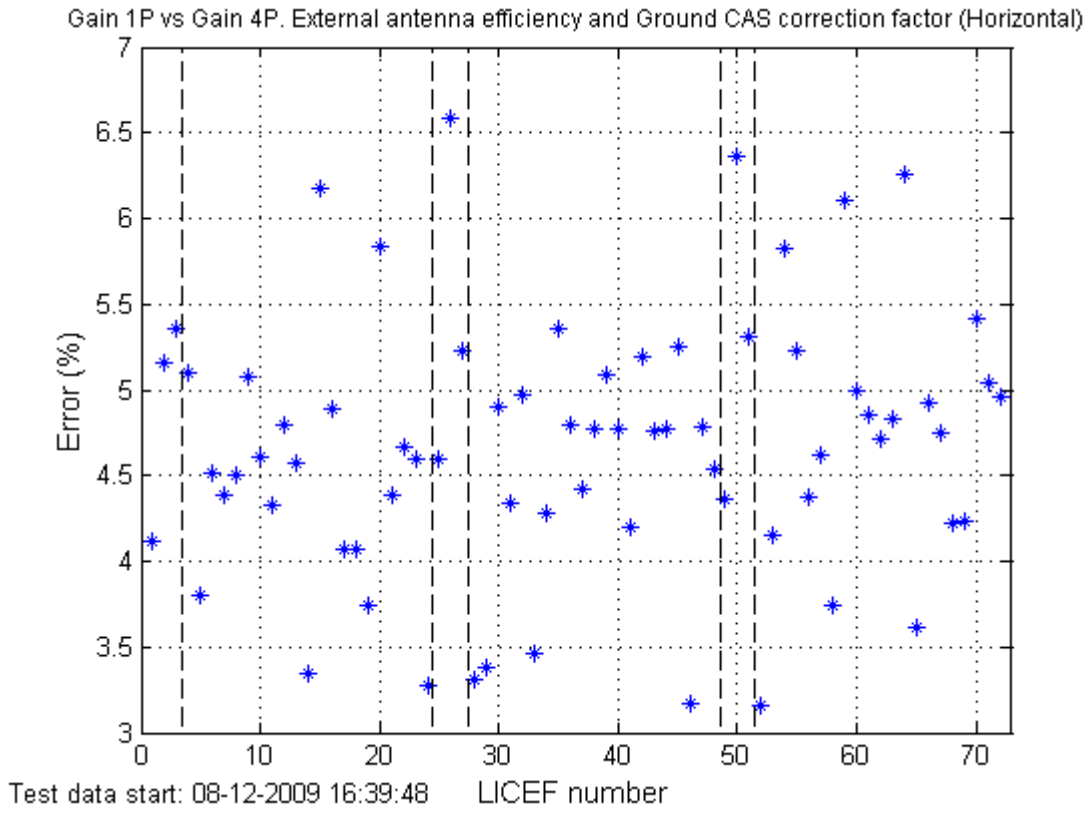

Fig. 6.33 Gain 1P vs Gain 4P. External antenna efficiency and Ground CAS correction factor (Horizontal)

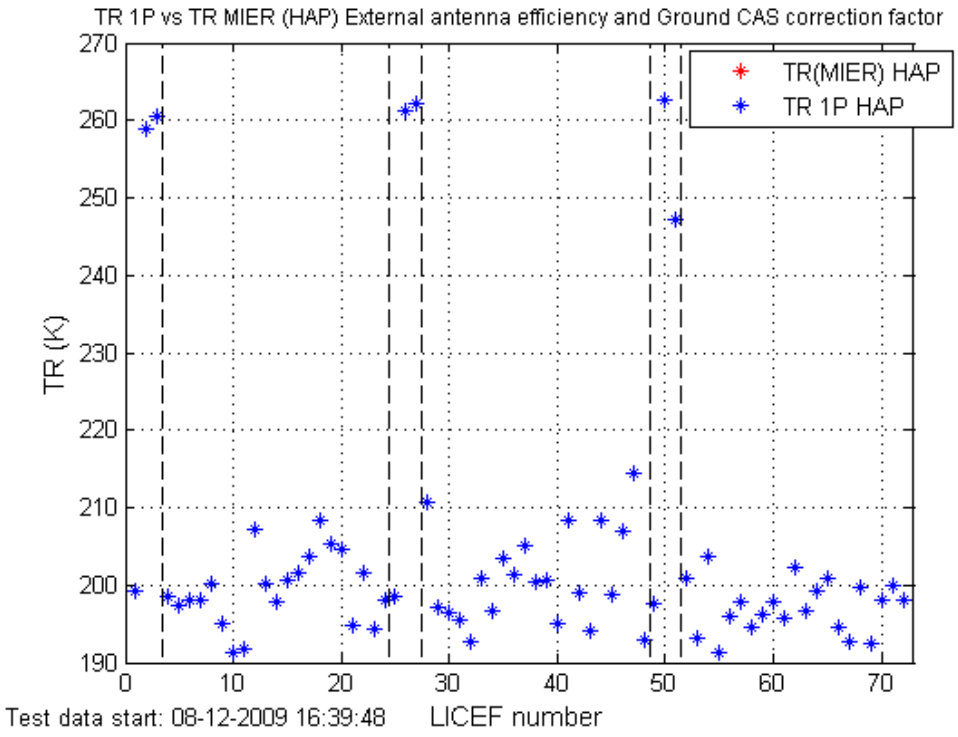

Fig. 6.34 TR 1P vs TR MIER. External antenna efficiency and Ground CAS correction factor (Horizontal)

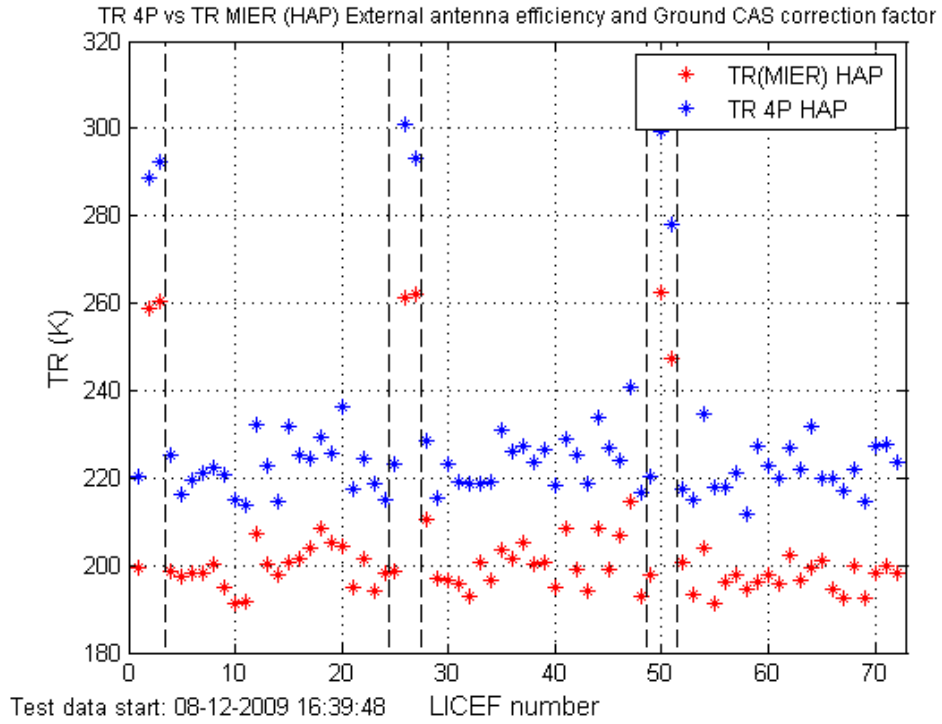

Fig. 6.35 TR 4P vs TR MIER. External antenna efficiency and Ground CAS correction factor (Horizontal)

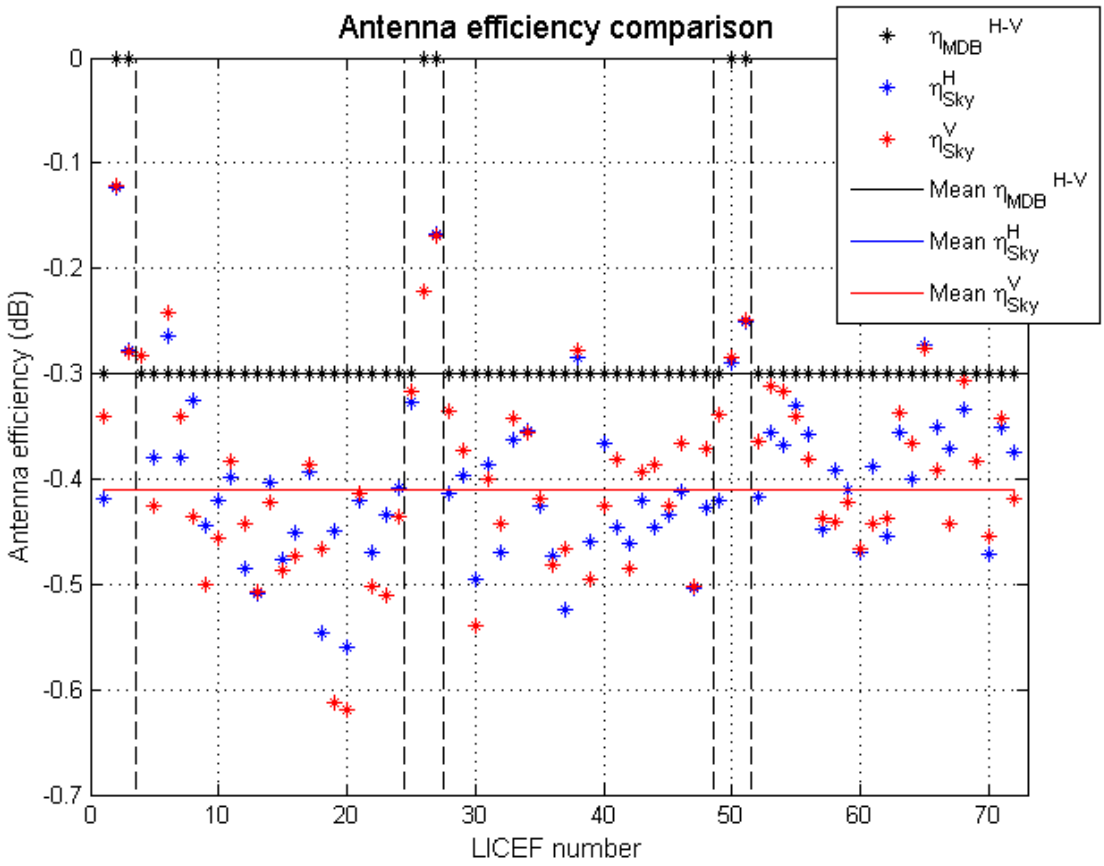

Fig. 6.36 Antenna efficiency comparison (Horizontal vs Vertical) Sky Mean (H)=-0,41047dB Sky Mean (V)=-0,41048dB STD (H)=0.06dB STD (V)=0.07dB

6.7 Case E: External antenna efficiency and external CAS correction factor

E) External CAS correction factor computed after applying the external antenna efficiency correction factor. $$G_{4Pk}^{A} = \frac{v_{2k} - v_{1k}}{T_{CAS_N}^{2} - T_{CAS_N}^{1}} \frac{\left|S_{LA_k}\right|^2}{\left|S_{LC_k}\right|^2} \frac{\left|S_{N0}\right|^2}{\left|S_{k0}\right|^2} \frac{f_{N_{SKY}}^{2}}{f_{k_{SKY}}^{2}} \eta_{A_k} F_{Ak_{SKY}}$$	External TR at VAP/HAP matches ground TR. -G4P matches to G1P to a negligible error. External CAS coefficients in H and V polarizations are very similar, pointing to a good estimation of antenna efficiency in H and V polarization.

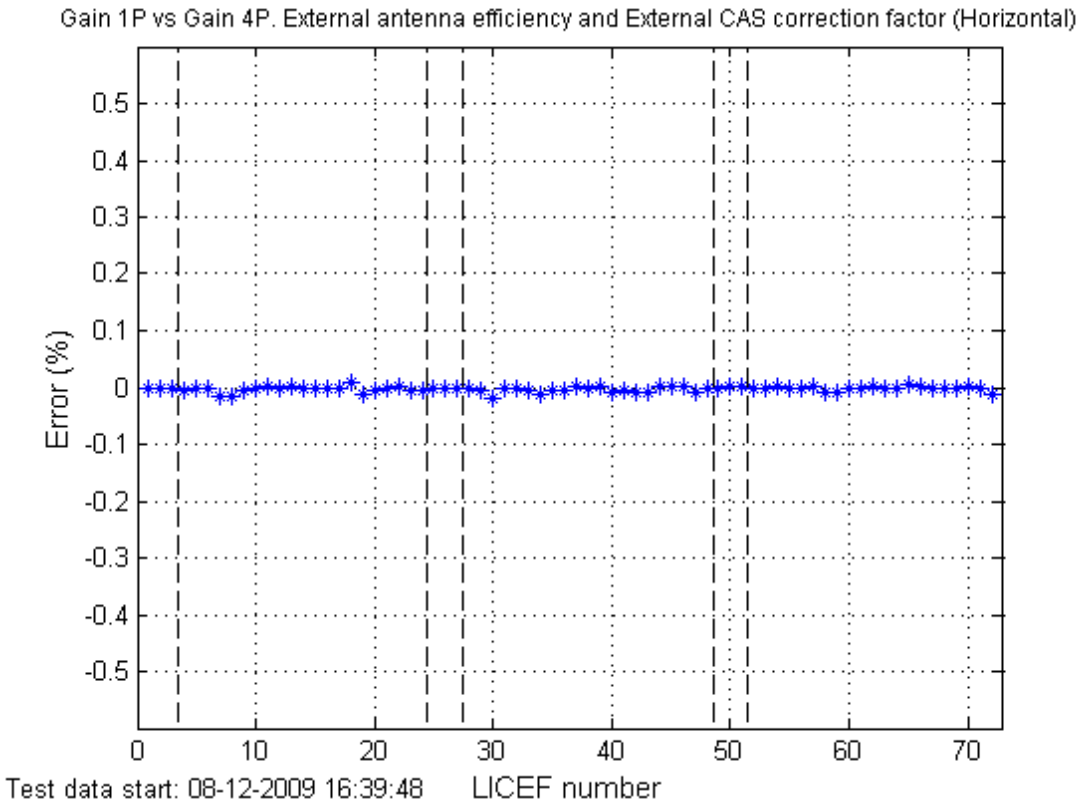

Fig. 6.37 Gain 1P vs Gain 4P. External antenna efficiency and External CAS correction factor (Horizontal)

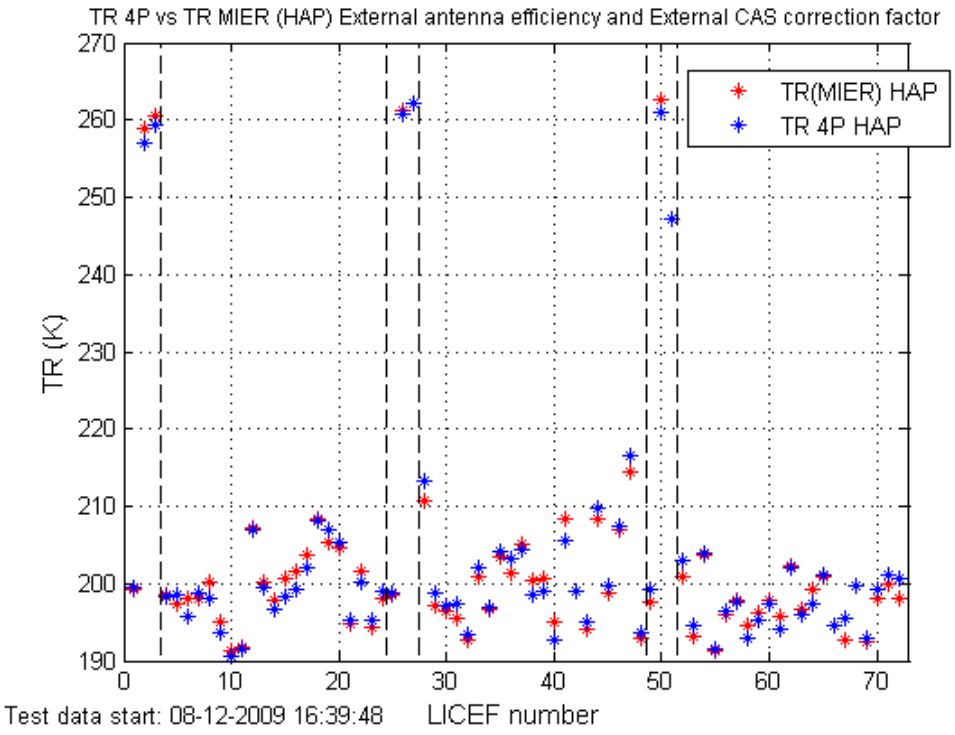

Fig. 6.38 TR 1P vs TR MIER. External antenna efficiency and External CAS correction factor (Horizontal)

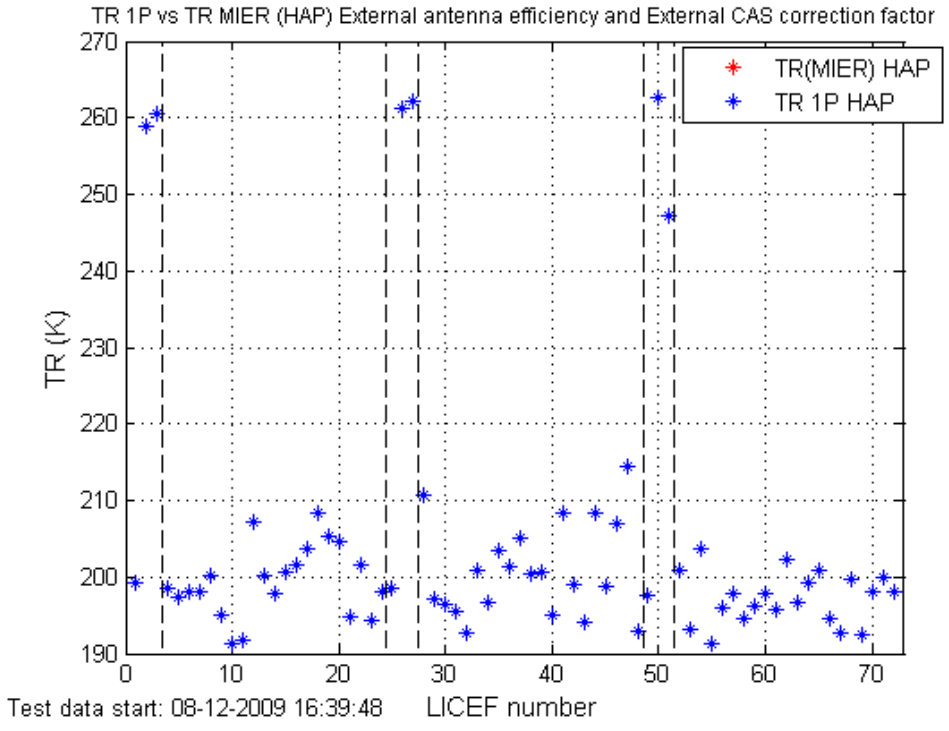

Fig. 6.39 TR 4P vs TR MIER. External antenna efficiency and External CAS correction factor (Horizontal)

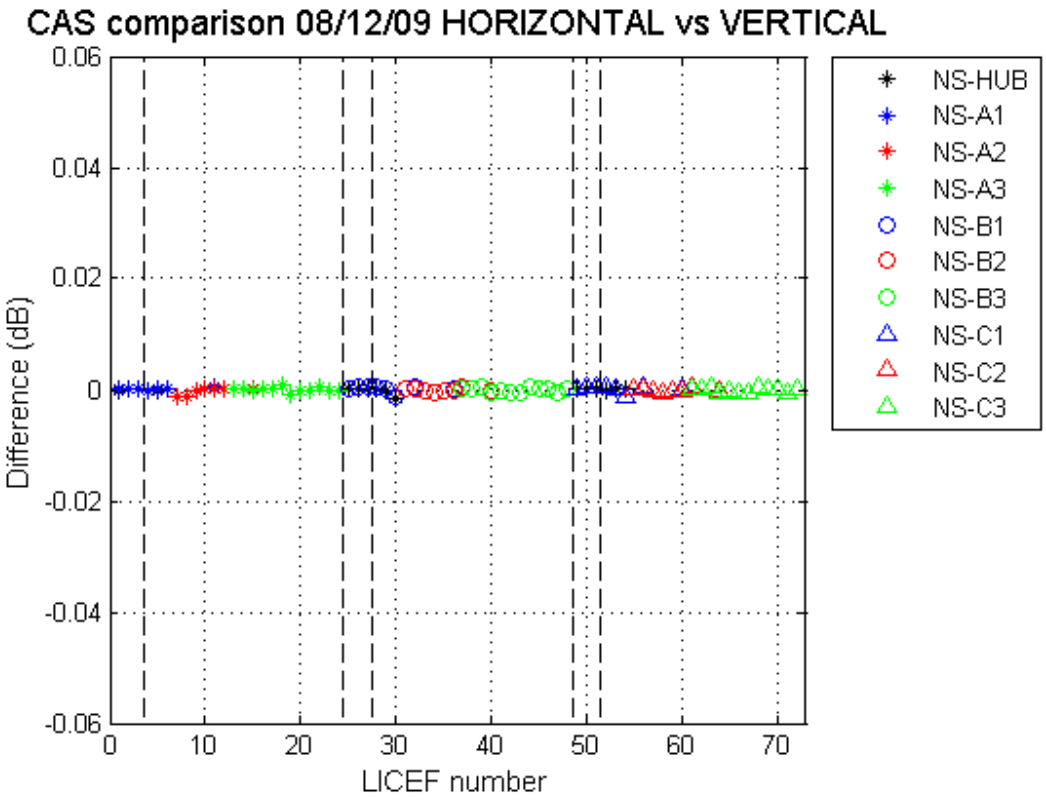

Fig. 6.40 External CAS comparison Horizontal vs Vertical

6.8 Case F: External antenna efficiency and ground CAS correction factor Method 2

F) External antenna efficiency computed to match G4P to G1P when using the ground CAS correction factor. $G_{4Pk}^{A} = \frac{v_{2k} - v_{1k}}{T_{CAS\,N}^{2} - T_{CAS_N}^{1}} \frac{\left\|S_{LA_k}\right\|^2}{\left\|S_{LC_k}\right\|^2} \frac{\left\|S_{N0}\right\|^2}{\left\|S_{k0}\right\|^2} \frac{f_{N_{GND}}^{2}}{f_{k_{GND}}^{2}} \eta_{A_k} F_{Ak_{SKY}}$	Internal G4P matches G1P to a negligible error because there is no need to average H pol and V pol correction coefficients, as done in CASE C Ground TR at VAP/HAP does not match external TR, since the fraction of the correction error related to CAS has been artificially assigned to antenna efficiency.

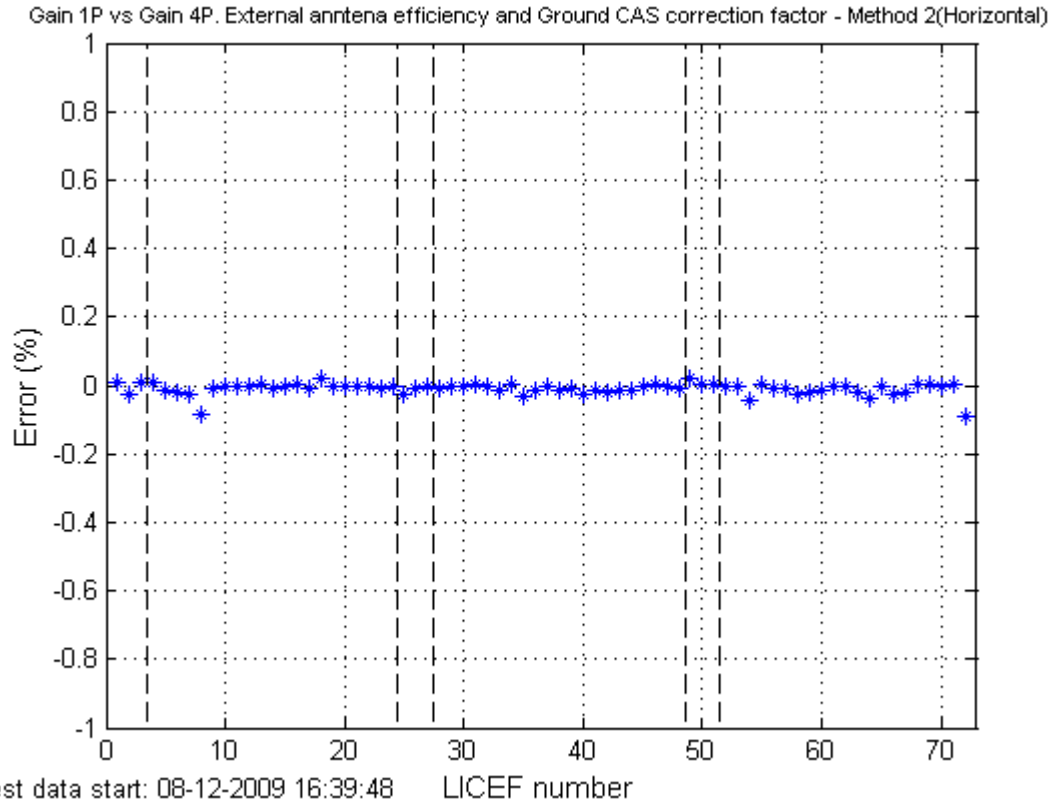

Fig. 6.41 Gain 1P vs Gain 4P. External antenna efficiency and Ground CAS correction factor – Method 2 (Horizontal)

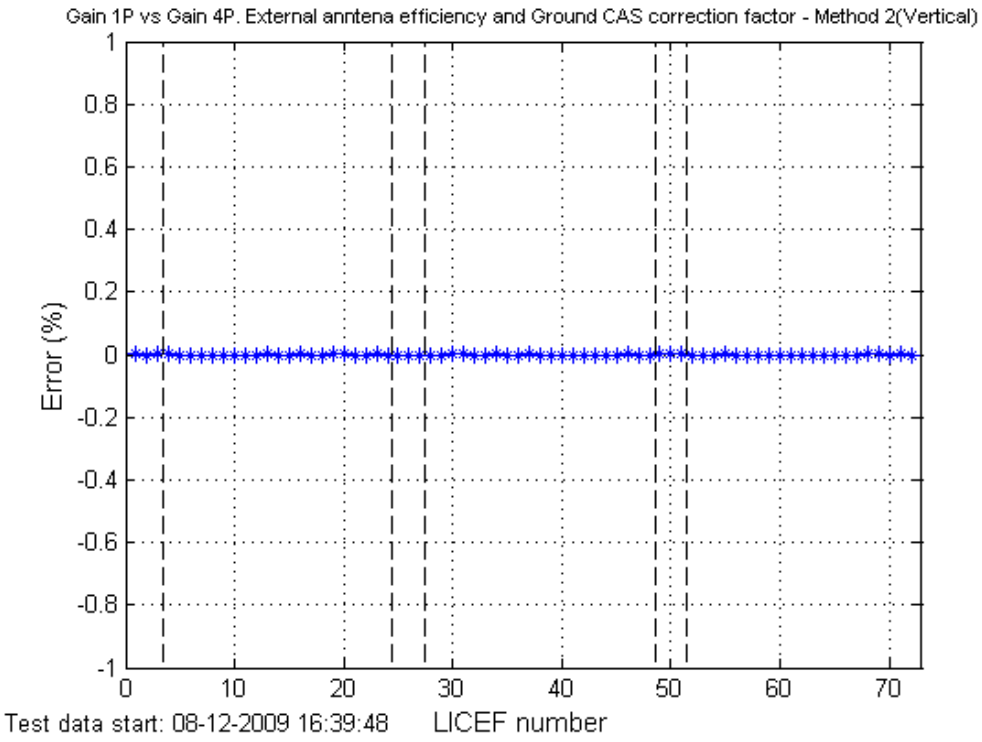

Fig. 6.42 Gain 1P vs Gain 4P. External antenna efficiency and Ground CAS correction factor – Method 2 (Vertical)

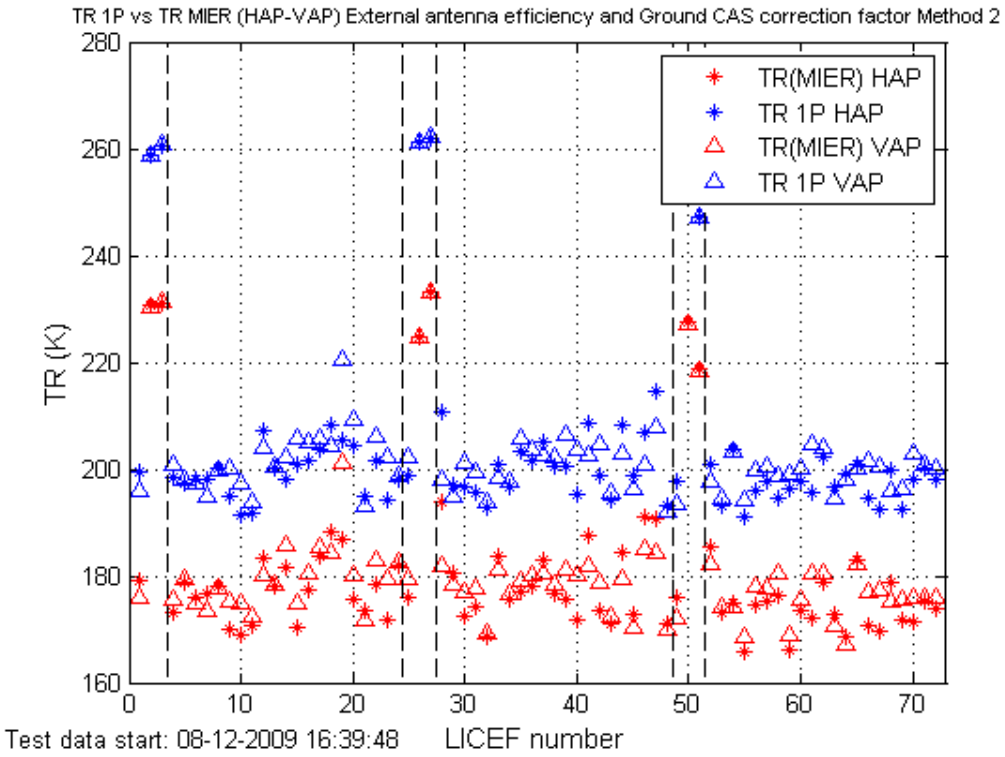

Fig. 6.43 TR 1P vs TR MIER. External antenna efficiency and Ground CAS correction factor – Method 2 (HAP-VAP)

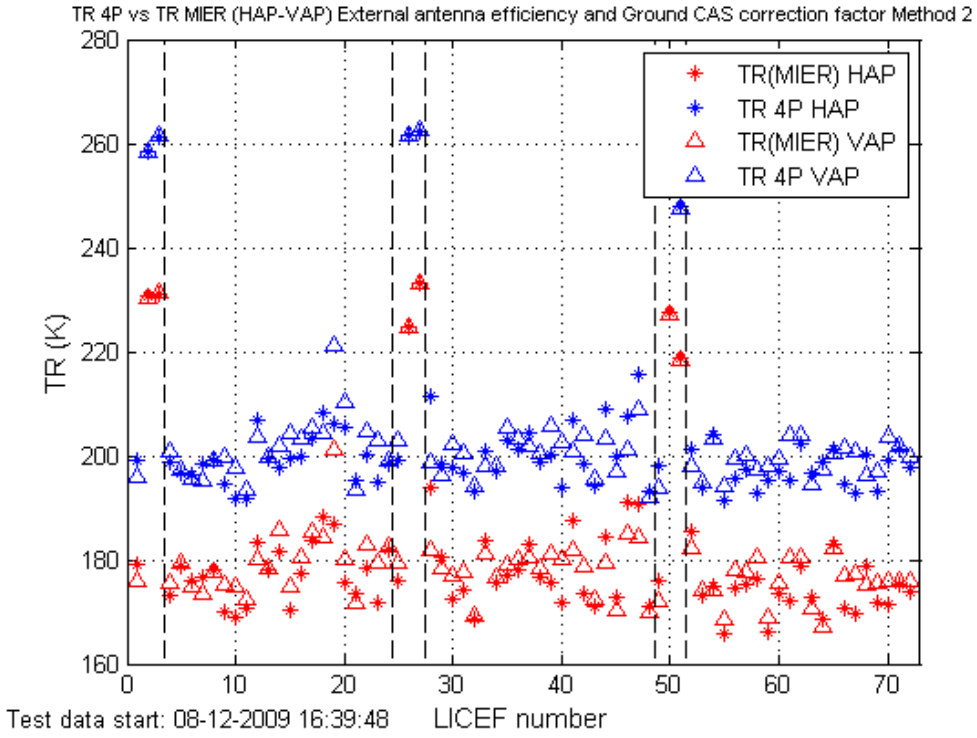

Fig. 6.44 TR 4P vs TR MIER. External antenna efficiency and Ground CAS correction factor – Method 2 (HAP-VAP)

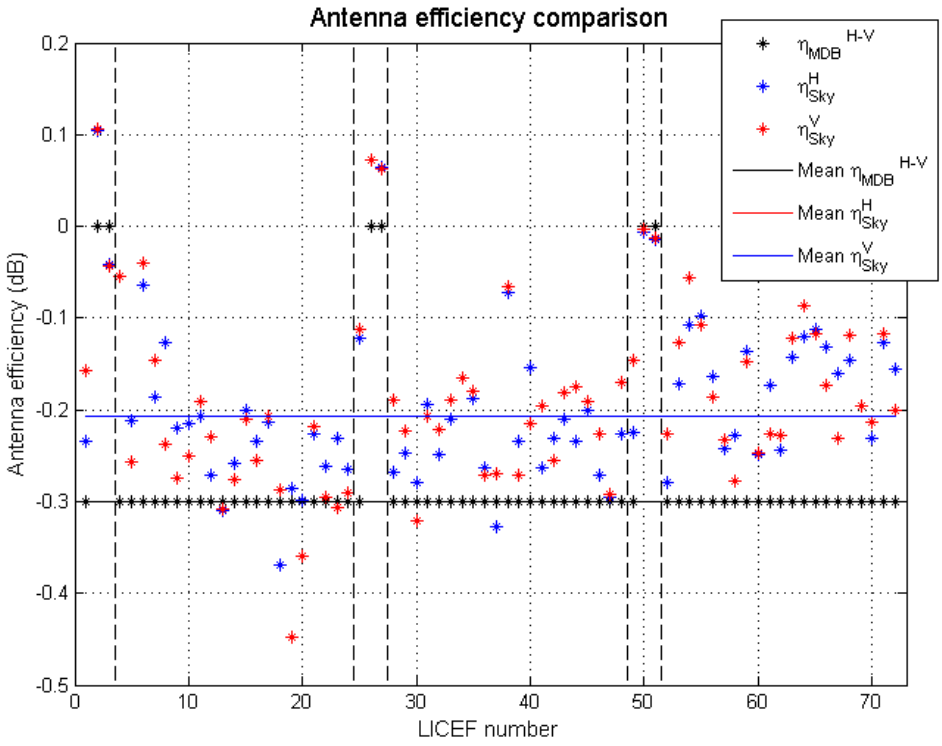

Fig. 6.45 Antenna efficiency comparison (Horizontal vs Vertical) Sky Mean (H)=-0,2074 dB Sky Mean (V)=-0,2072dB STD (H)=0.06 dB STD (V)=0.07 dB

	Tsky=3,6	CASES D-E Tsky=3,43		CASE F Tsky=3,43				
Receiver name	η MDB (H and V) dB	η SKY 1 (H) dB	η SKY 1 (V) dB	η SKY 2 (H) dB	η SKY 2 (V) dB	DIFF H dB	DIFF V dB	DD H-V dB
LCF_AB_03	-0,3000	-0,4180	-0,3404	-0,2348	-0,1573	-0,1833	-0,1831	-0,0001
NIR_AB01_H	0,0000	-0,1235	-0,1219	0,1051	0,1068	-0,2287	-0,2287	0,0000
NIR_AB01_V	0,0000	-0,2778	-0,2802	-0,0415	-0,0439	-0,2363	-0,2363	0,0000
LCF_A_01	-0,3000	-0,2821	-0,2831	-0,0545	-0,0552	-0,2276	-0,2279	0,0004
LCF_A_02	-0,3000	-0,3795	-0,4249	-0,2117	-0,2570	-0,1678	-0,1678	0,0001
LCF_A_03	-0,3000	-0,2643	-0,2418	-0,0634	-0,0407	-0,2009	-0,2011	0,0001
LCF_A_04	-0,3000	-0,3795	-0,3414	-0,1857	-0,1458	-0,1938	-0,1956	0,0018
LCF_A_05	-0,3000	-0,3262	-0,4359	-0,1268	-0,2377	-0,1994	-0,1981	-0,0013
LCF_A_06	-0,3000	-0,4445	-0,5004	-0,2191	-0,2749	-0,2255	-0,2255	0,0001
LCF_A_07	-0,3000	-0,4205	-0,4558	-0,2158	-0,2510	-0,2048	-0,2048	0,0000
LCF_A_08	-0,3000	-0,3987	-0,3838	-0,2065	-0,1916	-0,1922	-0,1922	0,0000
LCF_A_09	-0,3000	-0,4847	-0,4425	-0,2715	-0,2292	-0,2132	-0,2133	0,0002
LCF_A_10	-0,3000	-0,5087	-0,5067	-0,3104	-0,3085	-0,1982	-0,1982	0,0000
LCF_A_11	-0,3000	-0,4043	-0,4222	-0,2577	-0,2757	-0,1466	-0,1466	0,0000
LCF_A_12	-0,3000	-0,4771	-0,4862	-0,2007	-0,2096	-0,2764	-0,2766	0,0002
LCF_A_13	-0,3000	-0,4515	-0,4725	-0,2338	-0,2547	-0,2177	-0,2178	0,0000
LCF_A_14	-0,3000	-0,3939	-0,3873	-0,2137	-0,2069	-0,1802	-0,1804	0,0002
LCF_A_15	-0,3000	-0,5463	-0,4656	-0,3692	-0,2880	-0,1771	-0,1776	0,0005
LCF_A_16	-0,3000	-0,4500	-0,6122	-0,2853	-0,4474	-0,1647	-0,1648	0,0001
LCF_A_17	-0,3000	-0,5592	-0,6199	-0,2987	-0,3590	-0,2605	-0,2608	0,0003
LCF_A_18	-0,3000	-0,4213	-0,4135	-0,2268	-0,2188	-0,1944	-0,1947	0,0003
LCF_A_19	-0,3000	-0,4693	-0,5022	-0,2621	-0,2953	-0,2072	-0,2069	-0,0003
LCF_A_20	-0,3000	-0,4349	-0,5104	-0,2310	-0,3062	-0,2039	-0,2041	0,0002
LCF_A_21	-0,3000	-0,4091	-0,4350	-0,2651	-0,2905	-0,1440	-0,1444	0,0004
LCF_BC_03	-0,3000	-0,3264	-0,3173	-0,1221	-0,1129	-0,2043	-0,2044	0,0002
NIR_BC01_H	0,0000	-0,2221	-0,2225	0,0729	0,0726	-0,2950	-0,2950	0,0000
NIR_BC01_V	0,0000	-0,1681	-0,1697	0,0650	0,0633	-0,2330	-0,2330	0,0000
LCF_B_01	-0,3000	-0,4129	-0,3357	-0,2676	-0,1900	-0,1453	-0,1457	0,0004
LCF_B_02	-0,3000	-0,3974	-0,3732	-0,2479	-0,2234	-0,1495	-0,1498	0,0003
LCF_B_03	-0,3000	-0,4961	-0,5388	-0,2791	-0,3202	-0,2170	-0,2186	0,0015
LCF_B_04	-0,3000	-0,3872	-0,3997	-0,1943	-0,2067	-0,1929	-0,1930	0,0002
LCF_B_05	-0,3000	-0,4698	-0,4432	-0,2484	-0,2217	-0,2214	-0,2215	0,0000
LCF_B_06	-0,3000	-0,3635	-0,3424	-0,2107	-0,1890	-0,1527	-0,1533	0,0006
LCF_B_07	-0,3000	-0,3551	-0,3566	-0,1653	-0,1657	-0,1898	-0,1908	0,0011
LCF_B_08	-0,3000	-0,4259	-0,4185	-0,1883	-0,1803	-0,2376	-0,2382	0,0006
LCF_B_09	-0,3000	-0,4725	-0,4816	-0,2624	-0,2713	-0,2101	-0,2104	0,0003
LCF_B_10	-0,3000	-0,5234	-0,4665	-0,3268	-0,2699	-0,1965	-0,1965	0,0000
LCF_B_11	-0,3000	-0,2853	-0,2784	-0,0729	-0,0660	-0,2123	-0,2124	0,0001
LCF_B_12	-0,3000	-0,4598	-0,4957	-0,2345	-0,2709	-0,2253	-0,2249	-0,0004
LCF_B_13	-0,3000	-0,3660	-0,4265	-0,1543	-0,2148	-0,2117	-0,2117	0,0000
LCF_B_14	-0,3000	-0,4463	-0,3809	-0,2628	-0,1956	-0,1835	-0,1853	0,0018
LCF_B_15	-0,3000	-0,4607	-0,4853	-0,2311	-0,2551	-0,2297	-0,2302	0,0005
LCF_B_16	-0,3000	-0,4204	-0,3938	-0,2096	-0,1820	-0,2109	-0,2118	0,0009
LCF_B_17	-0,3000	-0,4457	-0,3867	-0,2348	-0,1755	-0,2109	-0,2112	0,0002
LCF_B_18	-0,3000	-0,4343	-0,4253	-0,1999	-0,1909	-0,2344	-0,2344	0,0000
LCF_B_19	-0,3000	-0,4112	-0,3668	-0,2715	-0,2270	-0,1397	-0,1397	0,0000
LCF_B_20	-0,3000	-0,5043	-0,5020	-0,2958	-0,2928	-0,2084	-0,2091	0,0007
LCF_B_21	-0,3000	-0,4272	-0,3718	-0,2265	-0,1706	-0,2007	-0,2012	0,0005
LCF_CA_03	-0,3000	-0,4203	-0,3392	-0,2252	-0,1452	-0,1951	-0,1940	-0,0011

NIR_CA01_H	0,0000	-0,2891	-0,2851	-0,0065	-0,0025	-0,2826	-0,2826	0,0000
NIR_CA01_V	0,0000	-0,2499	-0,2481	-0,0148	-0,0130	-0,2351	-0,2351	0,0000
LCF_C_01	-0,3000	-0,4179	-0,3648	-0,2794	-0,2258	-0,1385	-0,1389	0,0004
LCF_C_02	-0,3000	-0,3567	-0,3115	-0,1724	-0,1271	-0,1843	-0,1844	0,0001
LCF_C_03	-0,3000	-0,3672	-0,3161	-0,1072	-0,0556	-0,2600	-0,2605	0,0005
LCF_C_04	-0,3000	-0,3307	-0,3410	-0,0977	-0,1079	-0,2330	-0,2330	0,0001
LCF_C_05	-0,3000	-0,3578	-0,3808	-0,1636	-0,1864	-0,1942	-0,1944	0,0002
LCF_C_06	-0,3000	-0,4472	-0,4373	-0,2429	-0,2331	-0,2043	-0,2042	-0,0001
LCF_C_07	-0,3000	-0,3915	-0,4412	-0,2274	-0,2771	-0,1641	-0,1641	0,0000
LCF_C_08	-0,3000	-0,4097	-0,4217	-0,1368	-0,1480	-0,2729	-0,2737	0,0008
LCF_C_09	-0,3000	-0,4693	-0,4670	-0,2488	-0,2464	-0,2205	-0,2206	0,0001
LCF_C_10	-0,3000	-0,3884	-0,4425	-0,1726	-0,2268	-0,2157	-0,2157	-0,0001
LCF_C_11	-0,3000	-0,4537	-0,4379	-0,2443	-0,2284	-0,2094	-0,2094	0,0000
LCF_C_12	-0,3000	-0,3568	-0,3376	-0,1421	-0,1226	-0,2147	-0,2150	0,0003
LCF_C_13	-0,3000	-0,3994	-0,3663	-0,1196	-0,0860	-0,2797	-0,2802	0,0005
LCF_C_14	-0,3000	-0,2724	-0,2757	-0,1127	-0,1165	-0,1597	-0,1592	-0,0005
LCF_C_15	-0,3000	-0,3513	-0,3923	-0,1323	-0,1736	-0,2190	-0,2187	-0,0003
LCF_C_16	-0,3000	-0,3709	-0,4428	-0,1599	-0,2316	-0,2110	-0,2112	0,0003
LCF_C_17	-0,3000	-0,3341	-0,3069	-0,1465	-0,1193	-0,1876	-0,1877	0,0001
LCF_C_18	-0,3000	-0,3830	-0,3834	-0,1950	-0,1952	-0,1880	-0,1881	0,0002
LCF_C_19	-0,3000	-0,4723	-0,4547	-0,2310	-0,2134	-0,2412	-0,2413	0,0000
LCF_C_20	-0,3000	-0,3508	-0,3419	-0,1262	-0,1171	-0,2245	-0,2248	0,0002
LCF_C_21	-0,3000	-0,3753	-0,4195	-0,1562	-0,2004	-0,2191	-0,2191	0,0000

Table 6.4 Comparison between antenna efficiencies

	Tsky=3,6	CASES D-E Tsky=3,43		CASE F Tsky=3,43				
	η MDB (H and V) dB	η SKY 1 (H) dB	η SKY 1 (V) dB	η SKY 2 (H) dB	η SKY 2 (V) dB	DIFF H dB	DIFF V dB	DD H-V dB
MEAN	-0,300000	-0,410478	-0,410486	-0,207437	-0,207227	-0,203041	-0,203258	0,000217
STD	0,000000	0,062735	0,075441	0,065558	0,075521	0,031794	0,031824	0,000497

Table 6.5 Comparison between antenna efficiencies (Mean and STD)

6.9 Computation of External CAS coefficients from 2nd February 2010

The external coefficients (Antenna efficiency and CAS) are computed by means of method E. Sky temperatures to calibrate each NIR have been provided by EADS-CASA :

$T_{sky}(NIR)$					
AB (H)	**AB (V)**	**BC(H)**	**BC (V)**	**CA (H)**	**CA (V)**
3,590 K	*3,584 K*	*3,593 K*	*3,588 K*	*3,597 K*	*3,594 K*

Table 6.6 Tsky 2 February 2010 values (NIR)

6.9.1 Test 02/02/2010

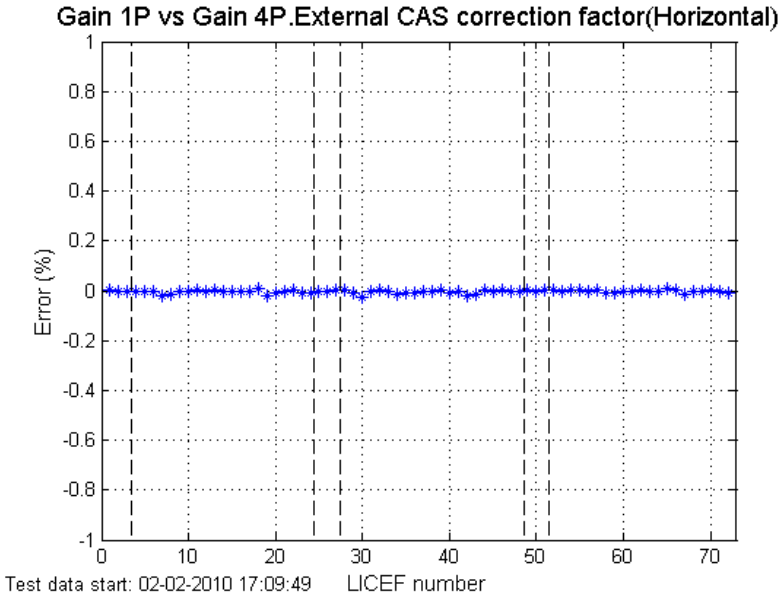

Fig. 6.46 Gain 1P vs Gain 4P. External antenna efficiency and External CAS correction factor (HAP)

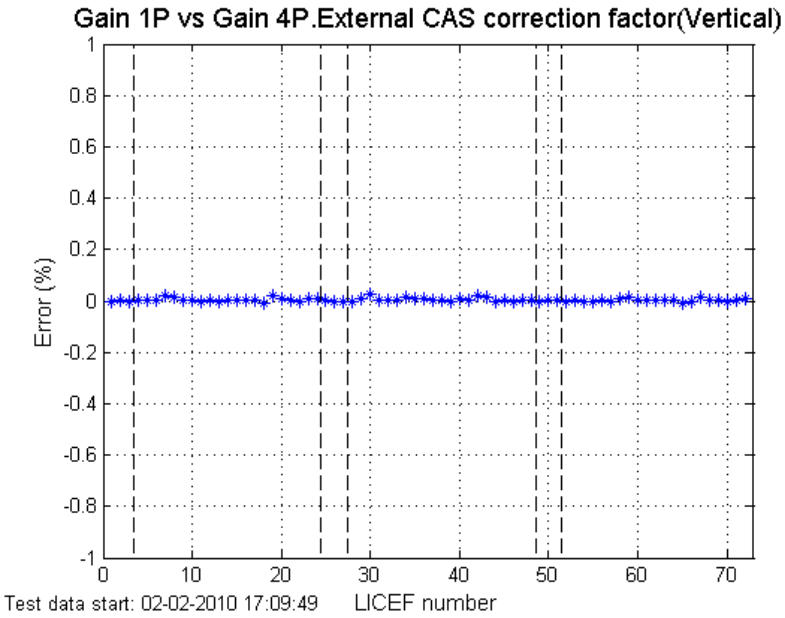

Fig. 6.47 Gain 1P vs Gain 4P. External antenna efficiency and External CAS correction factor (VAP)

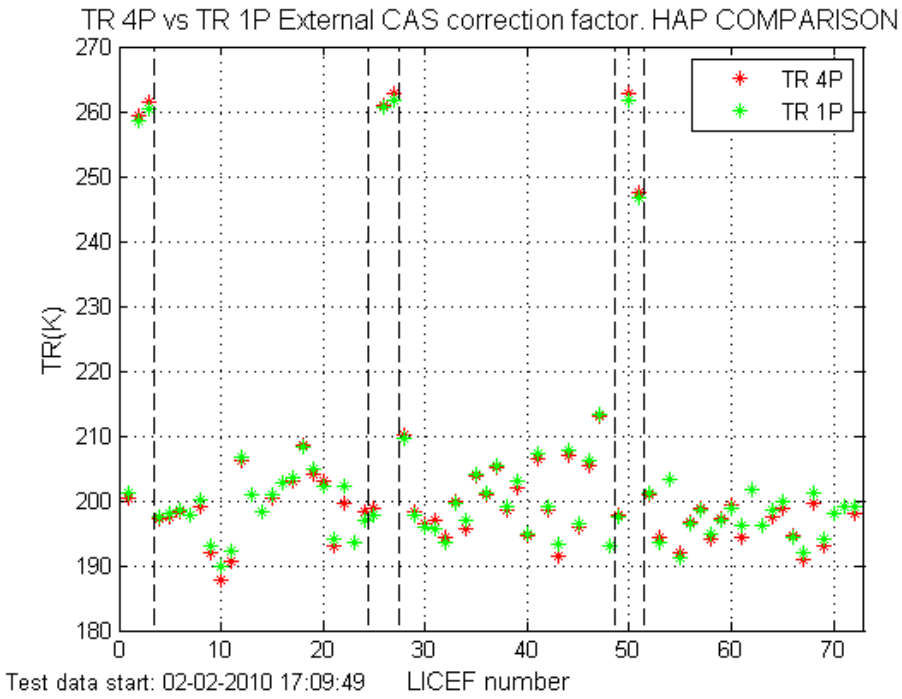

Fig. 6.48 TR 1P vs TR 4P. External antenna efficiency and External CAS correction factor (HAP)

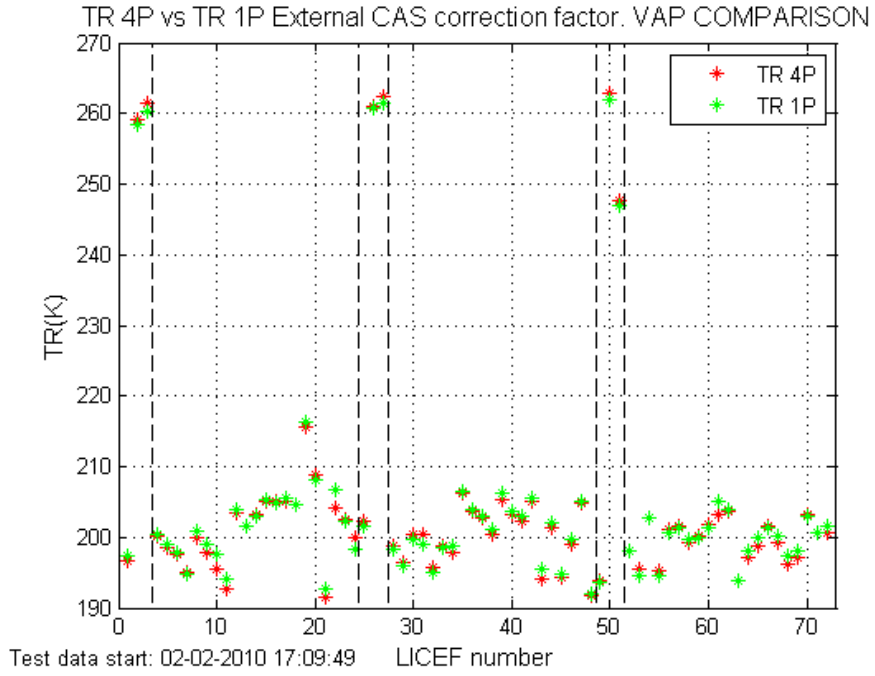

Fig. 6.49 TR 1P vs TR 4P. External antenna efficiency and External CAS correction factor (VAP)

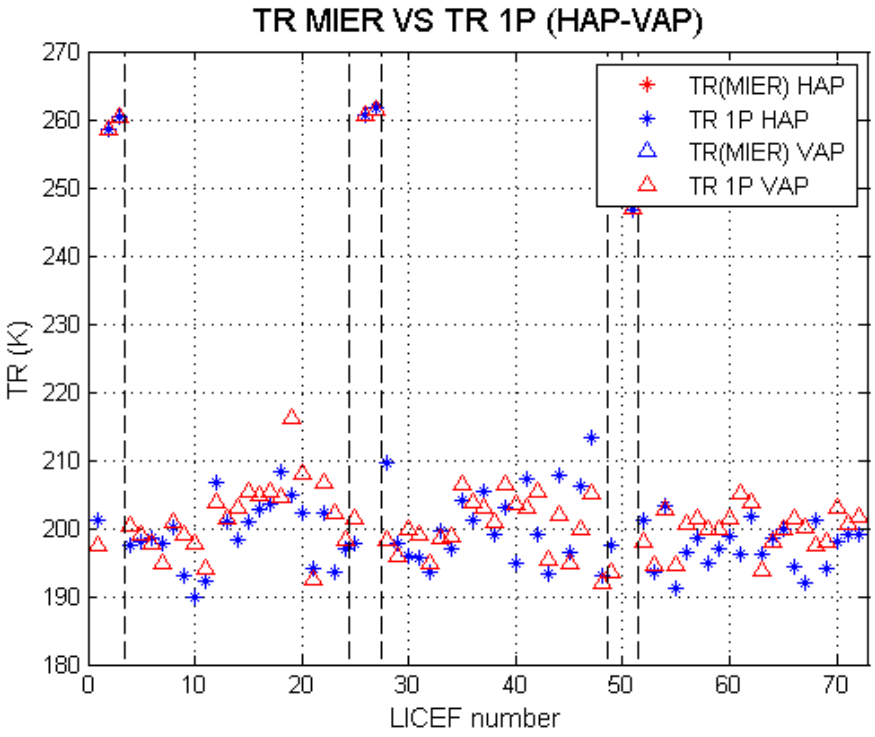

Fig. 6.50 TR MIER vs TR 1P. External antenna efficiency and External CAS correction factor (HAP-VAP)

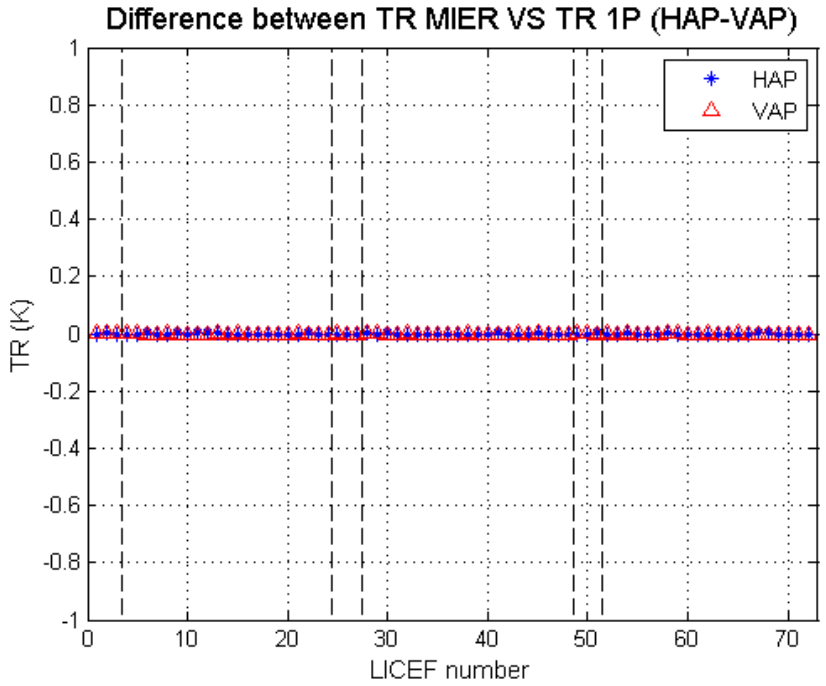

Fig. 6.51 Difference between TR MIER and TR 1P. External antenna efficiency and External CAS correction factor (HAP-VAP)

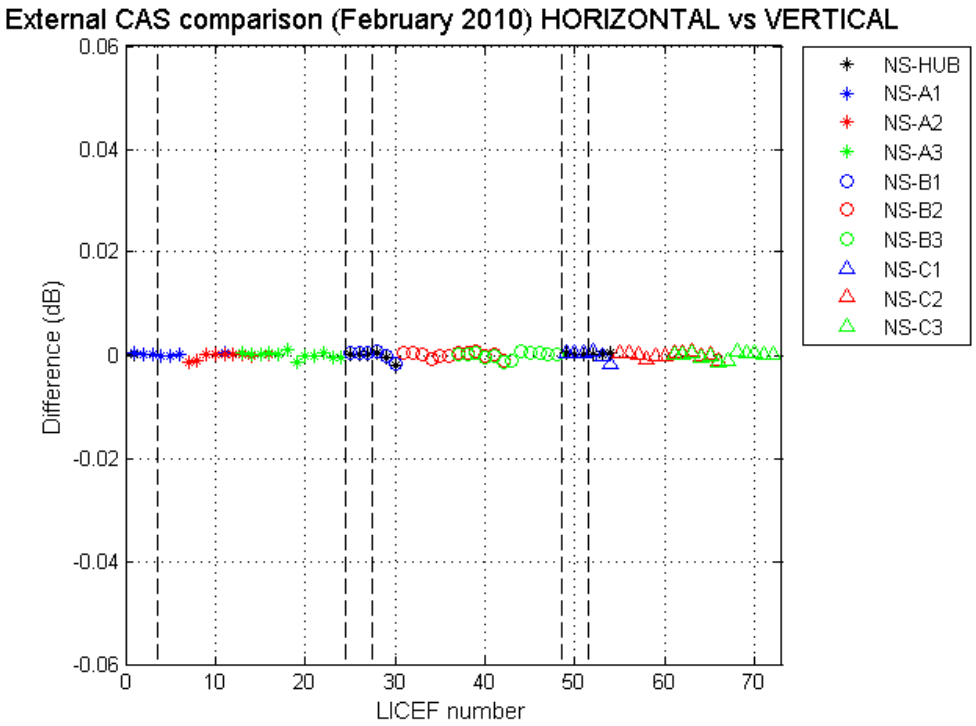

Fig. 6.52 External CAS comparison Horizontal vs Vertical

6.9.2 Comparison between Test 02/02/2010 and Test 02/03/2010

The external calibration on 02/02/2010 is taken as the reference test. In order to perform the comparison, G1P is computed from the external calibration performed on 02/03/2010 using the external antenna efficiency coefficients from 02/02/2010. The G4P is computed using the closest long calibration to 02/03/2010 and the external CAS correction factors from 02/02/2010.

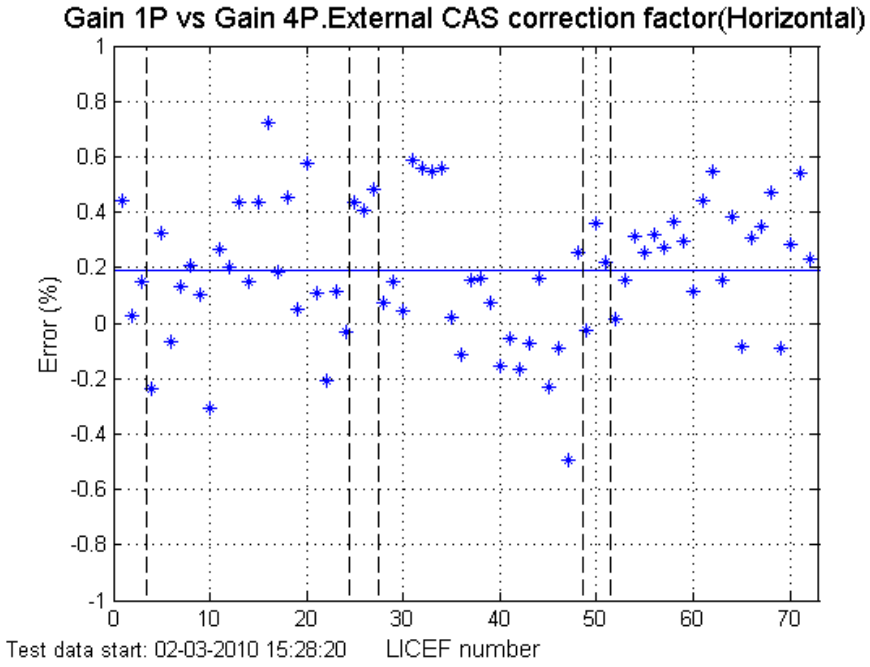

Fig. 6.53 Gain 1P vs Gain 4P. External antenna efficiency and External CAS correction factor from February 2010(HAP)

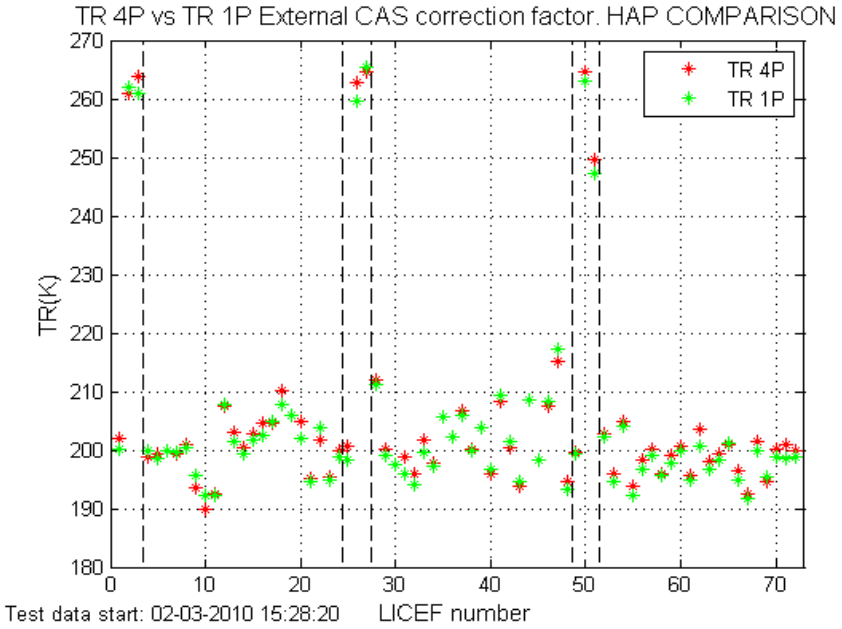

Fig. 6.54 TR 1P vs TR 4P. External antenna efficiency and External CAS correction factor from February 2010 (HAP)

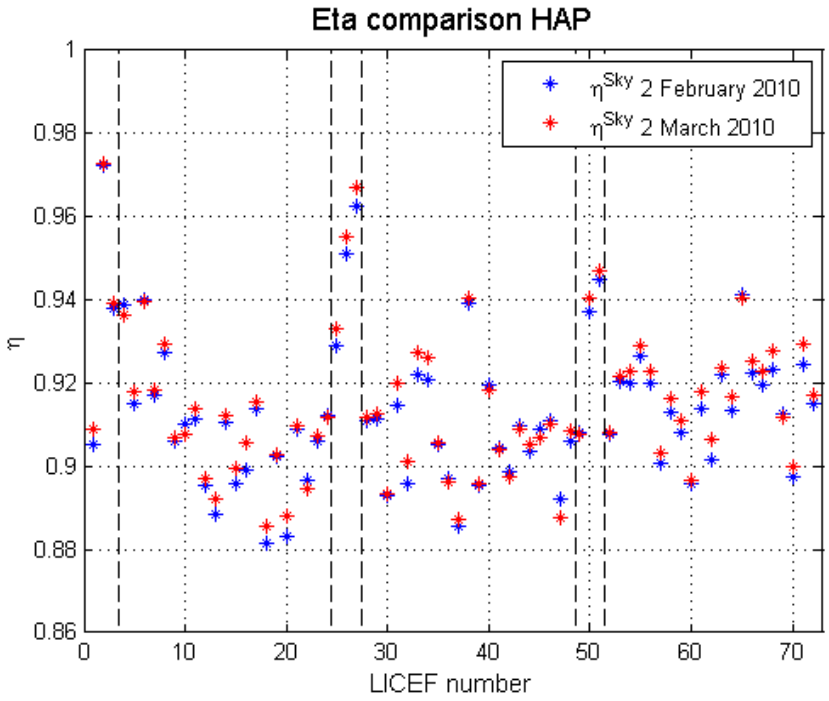

6.55 η comparison 2 February 2010-2 March 2010 (HAP)

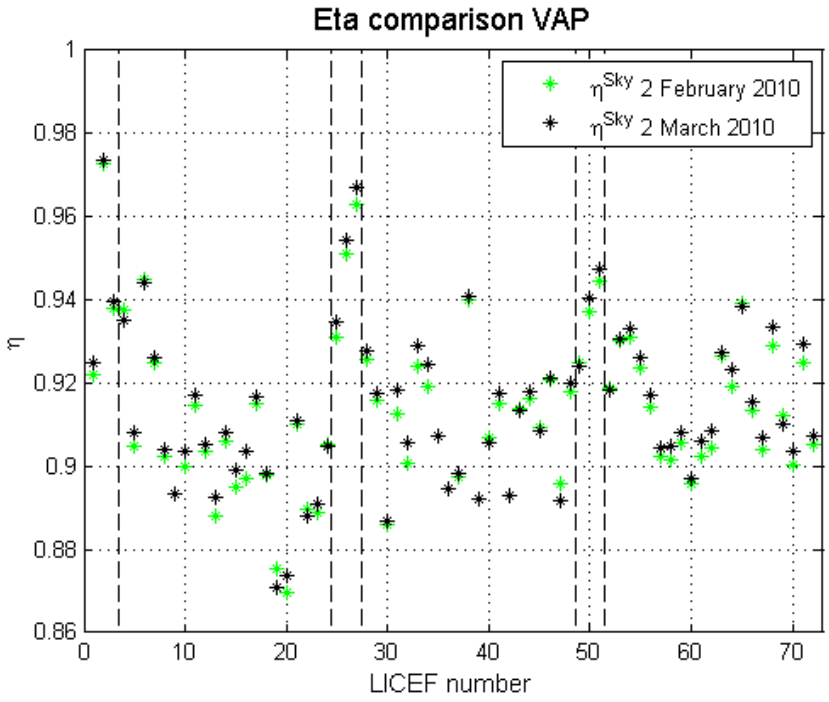

6.56 η comparison 2 February 2010-2 March 2010 (VAP)

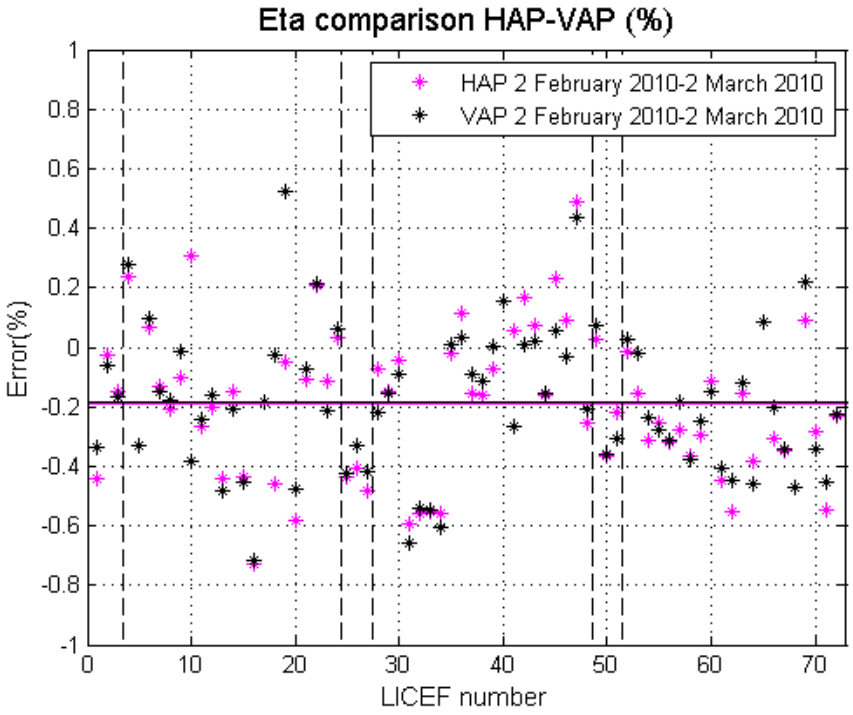

6.57 Difference between η from 2 February 2010-2 March 2010 (HAP-VAP)

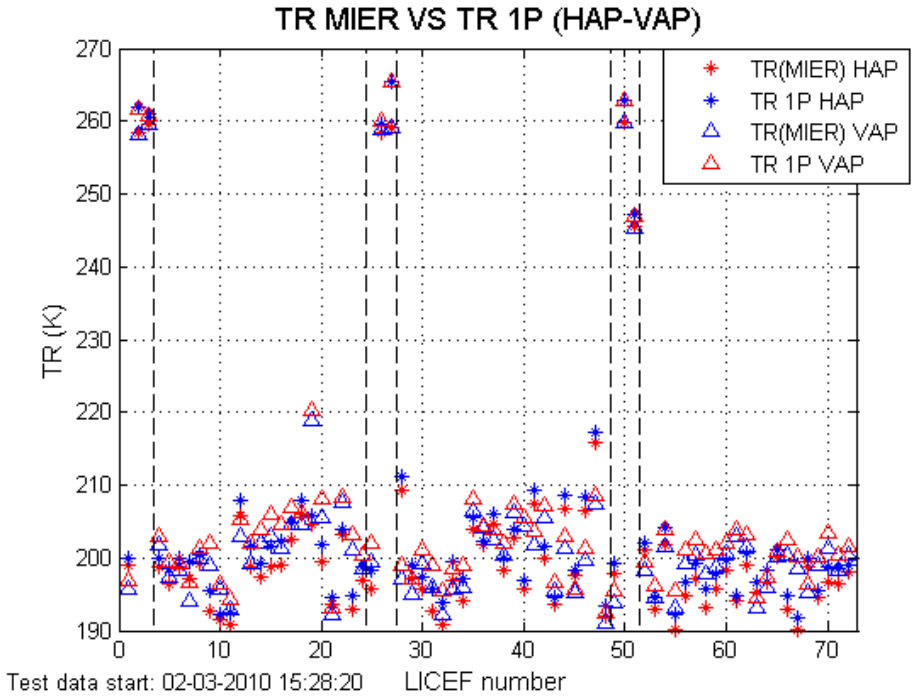

Fig. 6.58 TR MIER vs TR 1P. External antenna efficiency from March 2010 and External CAS correction factor from February 2010 (HAP-VAP)

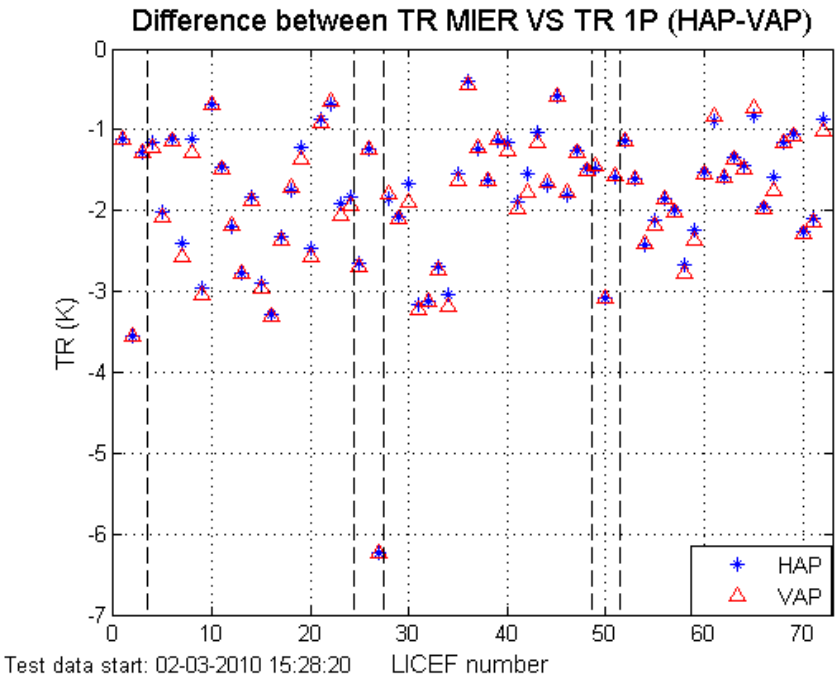

Fig. 6.59 Difference between TR MIER and TR 1P. External antenna efficiency from March 2010 and External CAS correction factor from February 2010 (HAP-VAP)

6.9.3 Comparison between Test 02/02/2010 and Test 16/03/2010

Now, Internal PMS gain G4P is compared to the external PMS gain G1P obtained from the external calibration on 16/03/2010. The external CAS and antenna efficiency coefficients are taken from the external calibration on 02/02/2010. The internal PMS gain G4P is taken from the long calibration closest to the external calibration on 16/03/2010. Comparison is performed at the mean PMS temperature during the internal PMS long calibration.

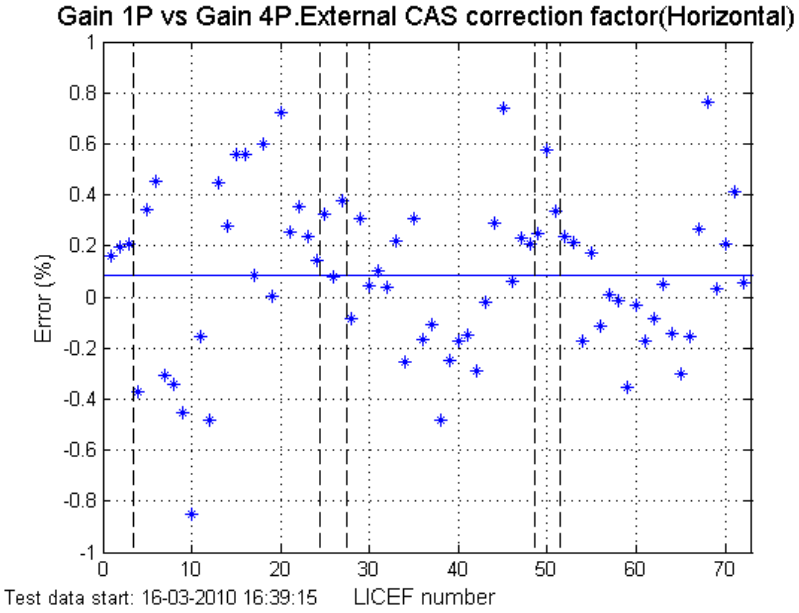

Fig. 6.60 Gain 1P vs Gain 4P. External antenna efficiency and External CAS correction factor from February 2010(HAP)

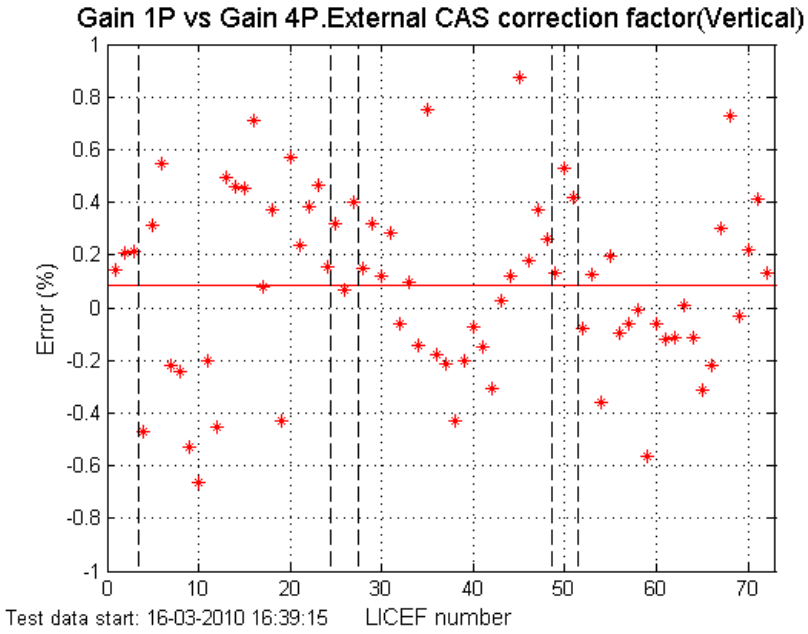

Fig. 6.61 Gain 1P vs Gain 4P. External antenna efficiency and External CAS correction factor from February 2010(VAP)

From now on, in this case, new external antenna efficiency coefficients have been computed by matching PMS gain G4P (using the CAS coefficients from 02/02/2010) to PMS gain G1P (16/03/2010). PMS gain G4P has used the long calibration closest to the external calibration on 16/03/2010. After refreshing the external antenna efficiency coefficients, G1P and G4P matching is very good (*Fig. 6.62* and *Fig. 6.63*).

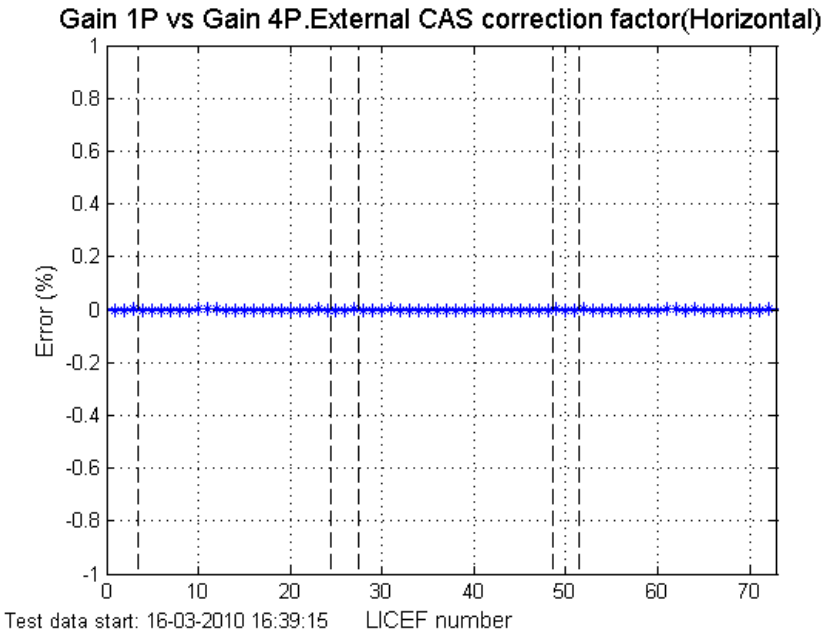

Fig. 6.62 Gain 1P vs Gain 4P. External antenna efficiency from March 2010 and External CAS correction factor from February 2010(HAP)

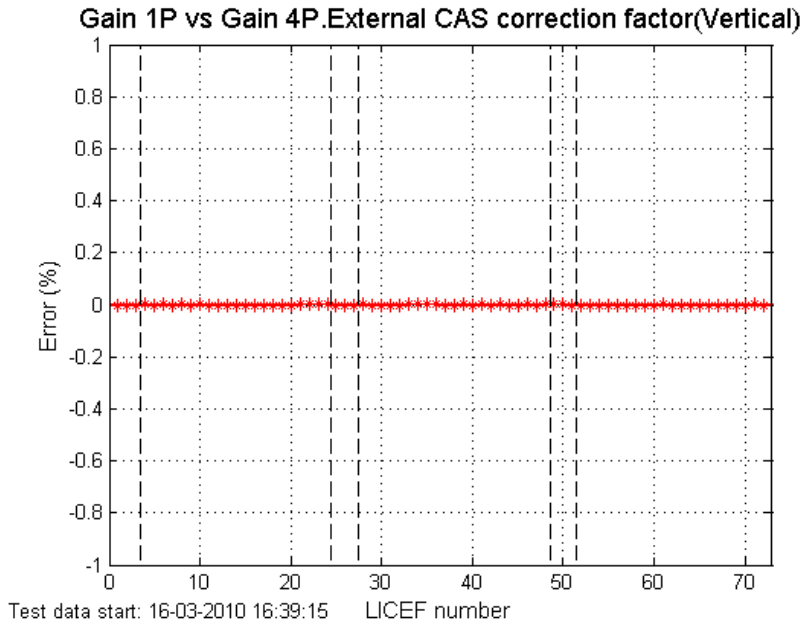

Fig. 6.63 Gain 1P vs Gain 4P. External antenna efficiency from March 2010 and External CAS correction factor from February 2010(VAP)

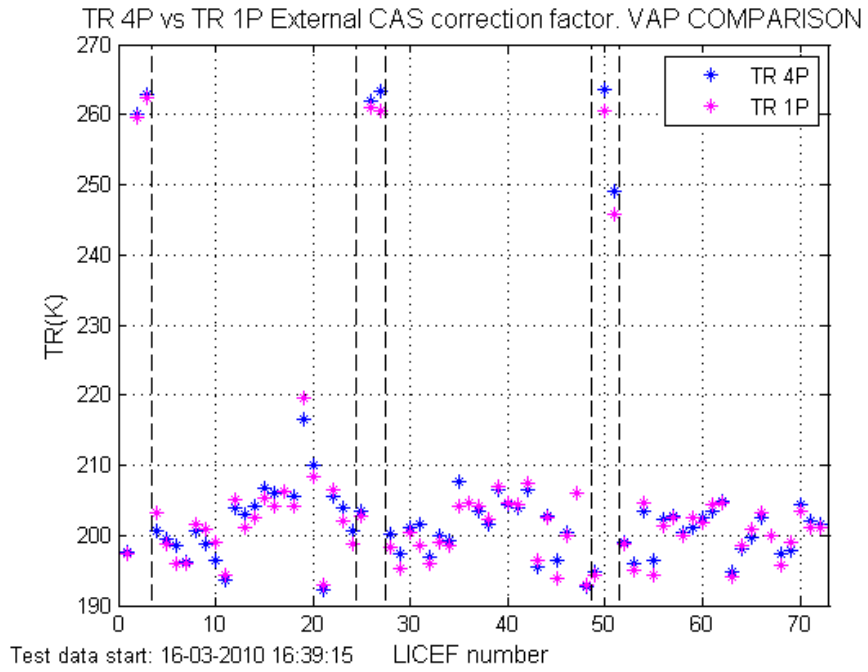

Fig. 6.64 TR 1P vs TR 4P. External antenna efficiency from March 2010 and External CAS correction factor from February 2010 (VAP)

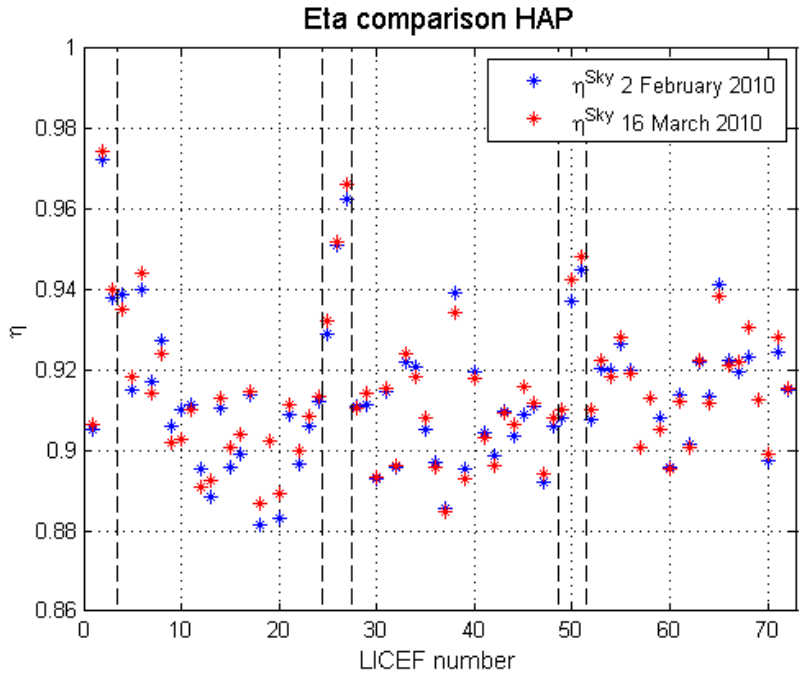

Fig. 6.65 η comparison 2 February 2010-16 March 2010 (HAP)

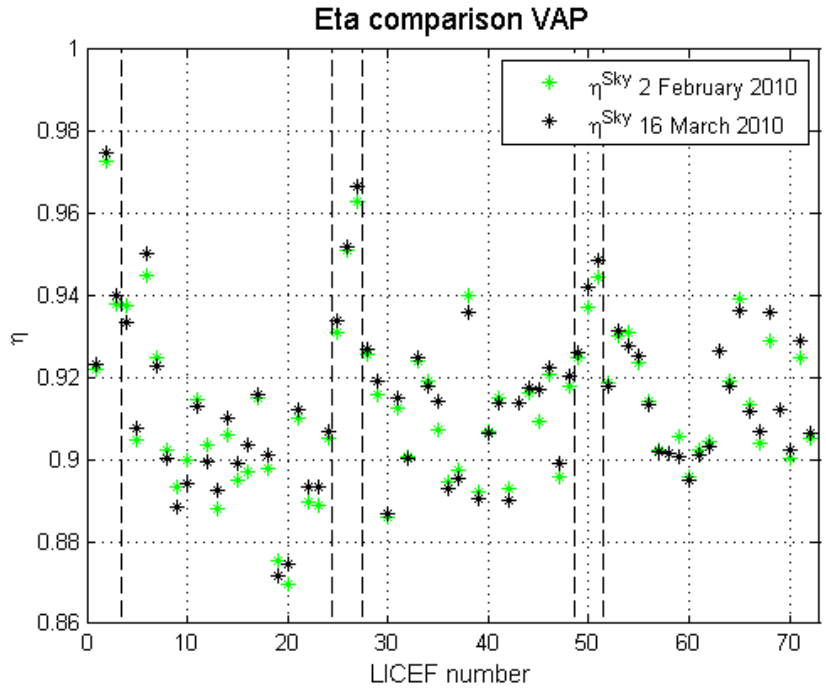

Fig. 6.66 η comparison 2 February 2010-16 March 2010 (VAP)

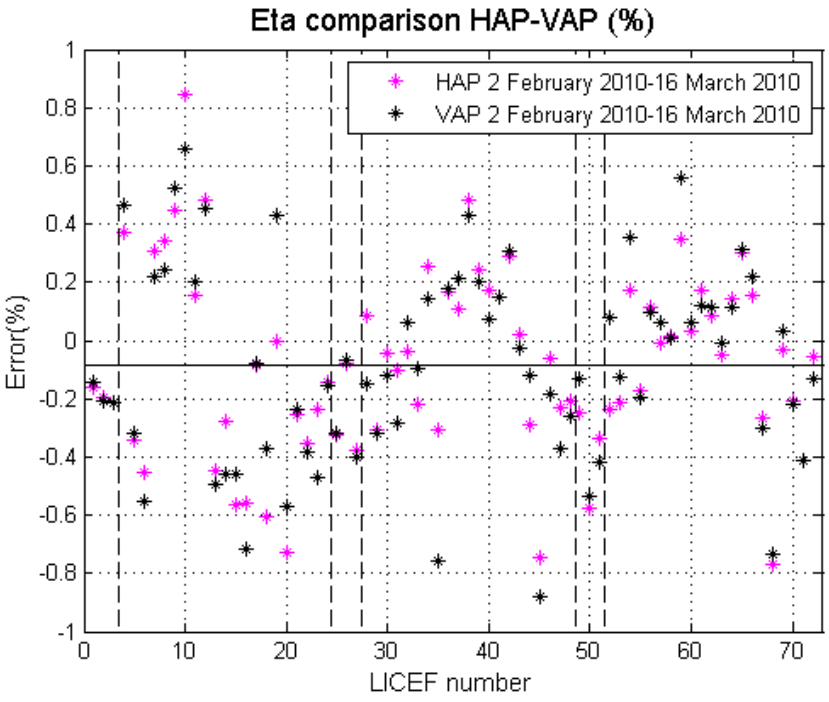

Fig. 6.67 Difference between η from 2 February 2010-16 March 2010 (HAP-VAP)

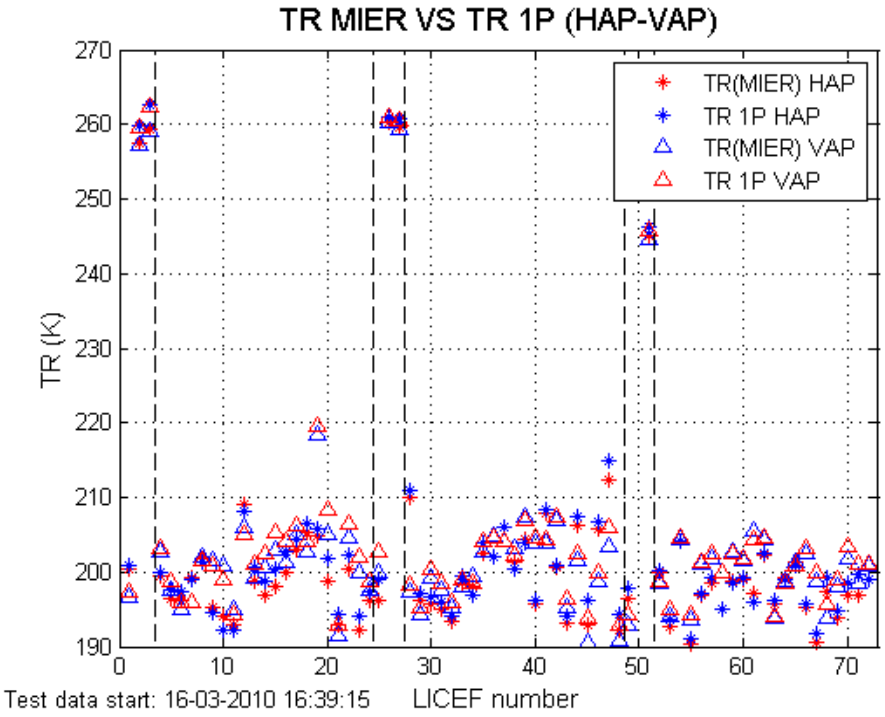

Fig. 6.68 TR MIER vs TR 1P. External antenna efficiency and External CAS correction factor (HAP-VAP)

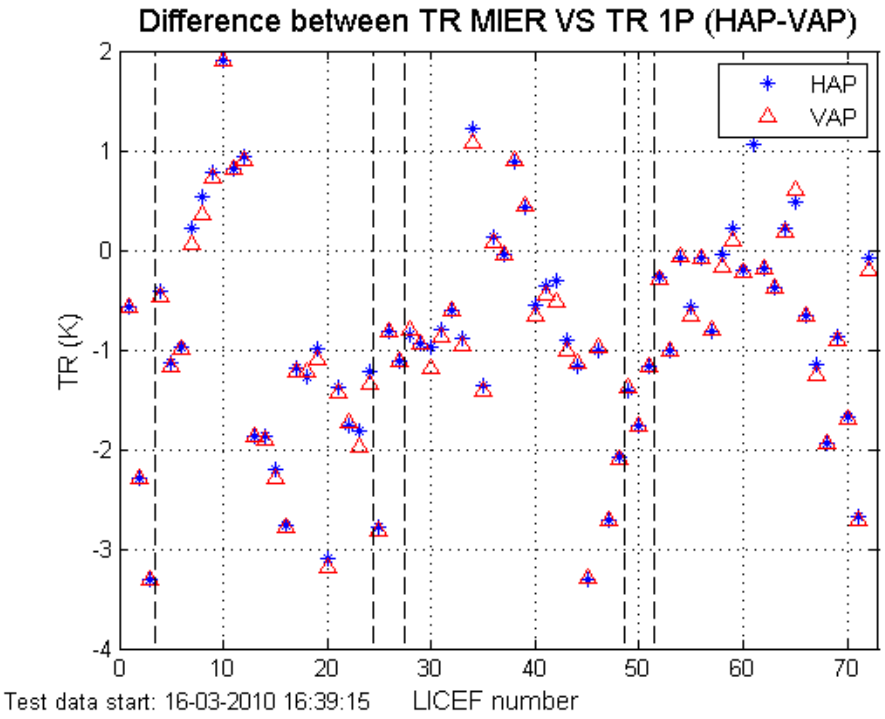

Fig. 6.69 Difference between TR MIER and TR 1P. External antenna efficiency and External CAS correction factor (HAP-VAP)

6.9.4 Comparison between Test 02/02/2010 and Test 06/04/2010

All plots in this section are similar to those given in the previous section.

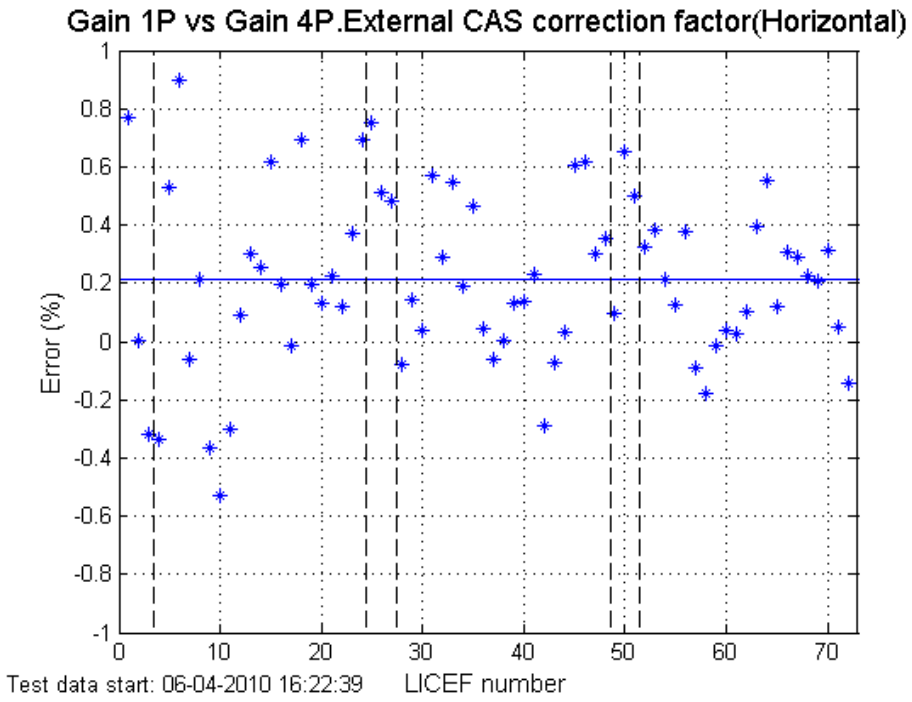

Fig. 6.70 Gain 1P vs Gain 4P. External antenna efficiency and External CAS correction factor from February 2010(HAP)

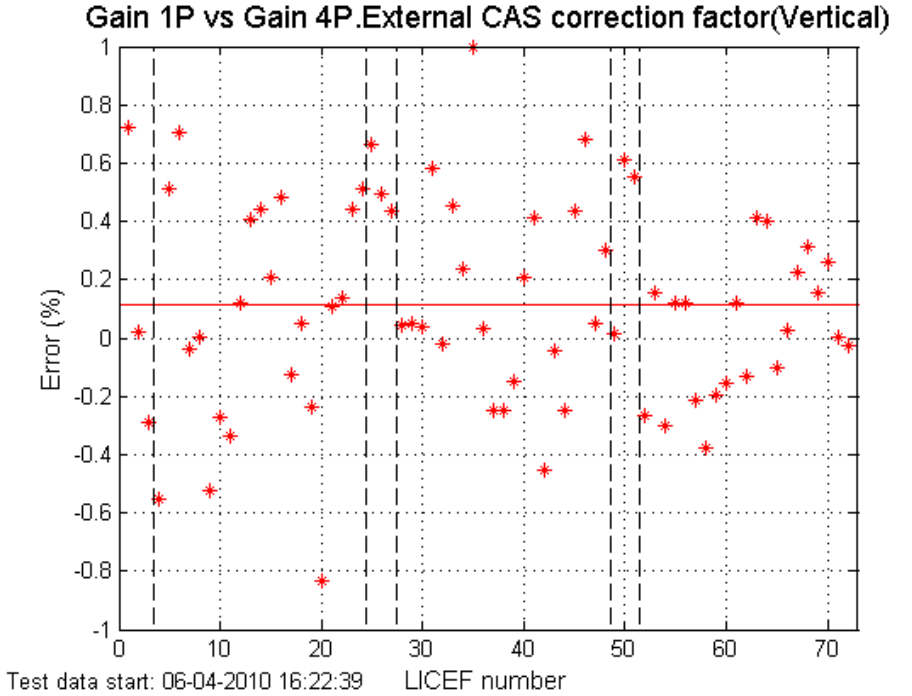

Fig. 6.71 Gain 1P vs Gain 4P. External antenna efficiency and External CAS correction factor from February 2010(VAP)

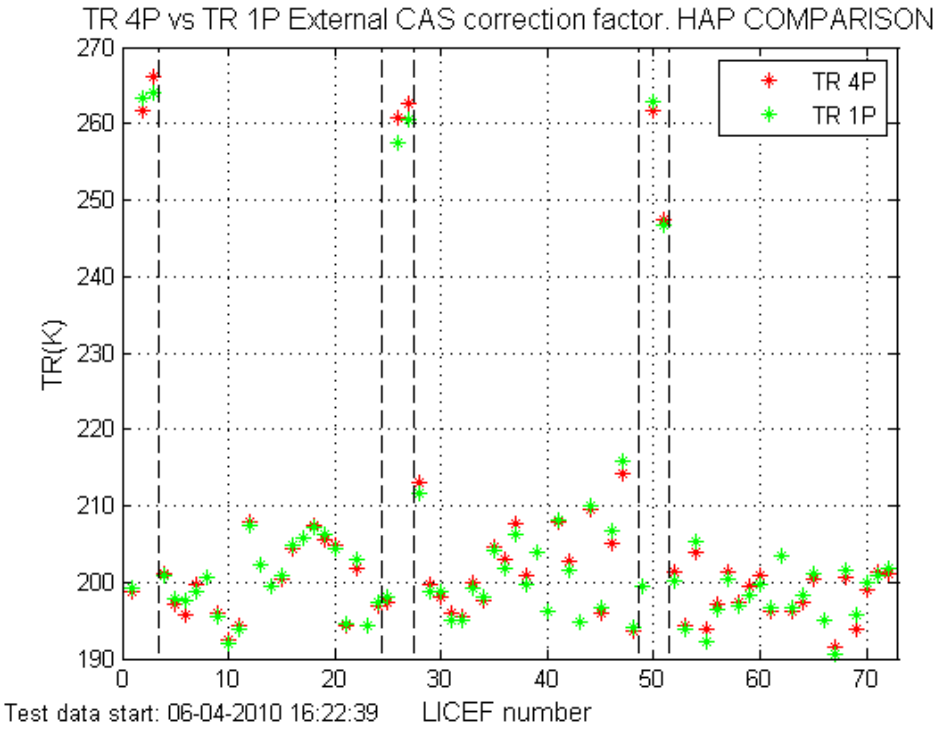

Fig. 6.72 TR 1P vs TR 4P. External antenna efficiency from April 2010 and External CAS correction factor from February 2010 (HAP)

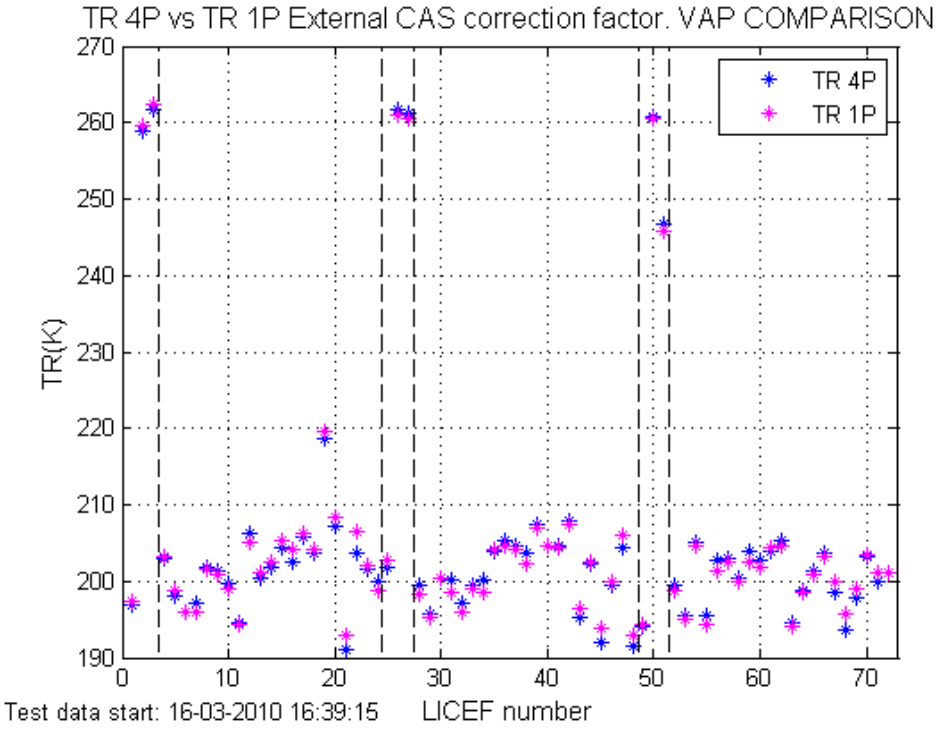

Fig. 6.73 TR 1P vs TR 4P. External antenna efficiency from April 2010 and External CAS correction factor from February 2010 (VAP)

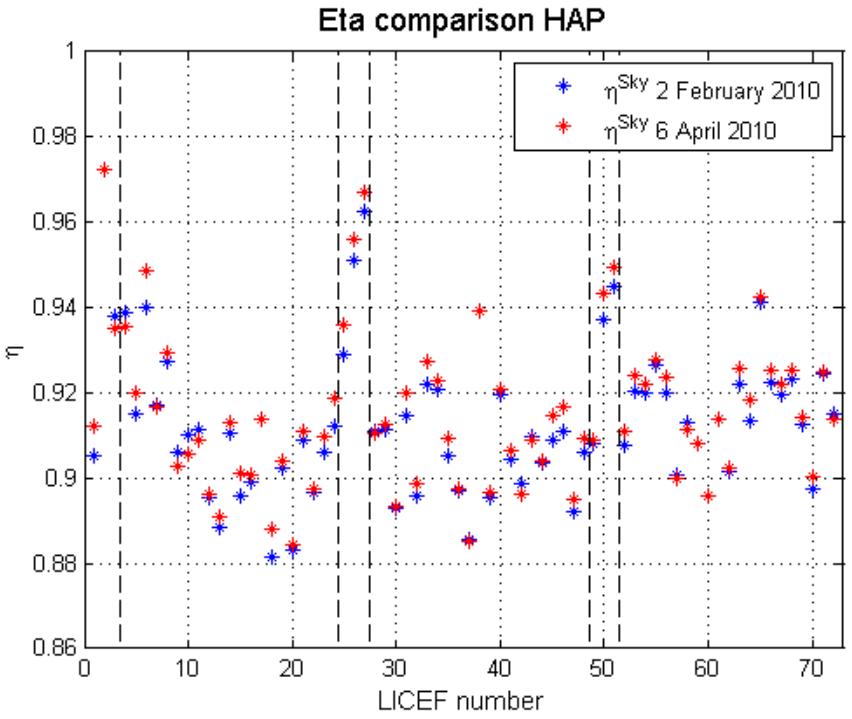

Fig. 6.74 η comparison 2 February 2010-6 April 2010 (HAP)

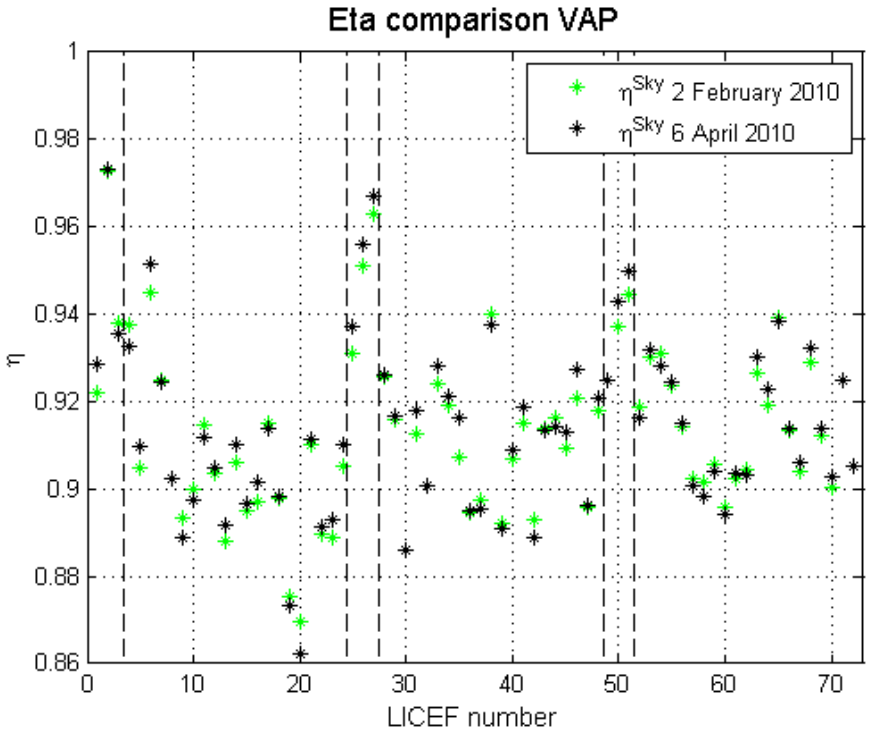

Fig. 6.75 η comparison 2 February 2010-6 April 2010 (VAP)

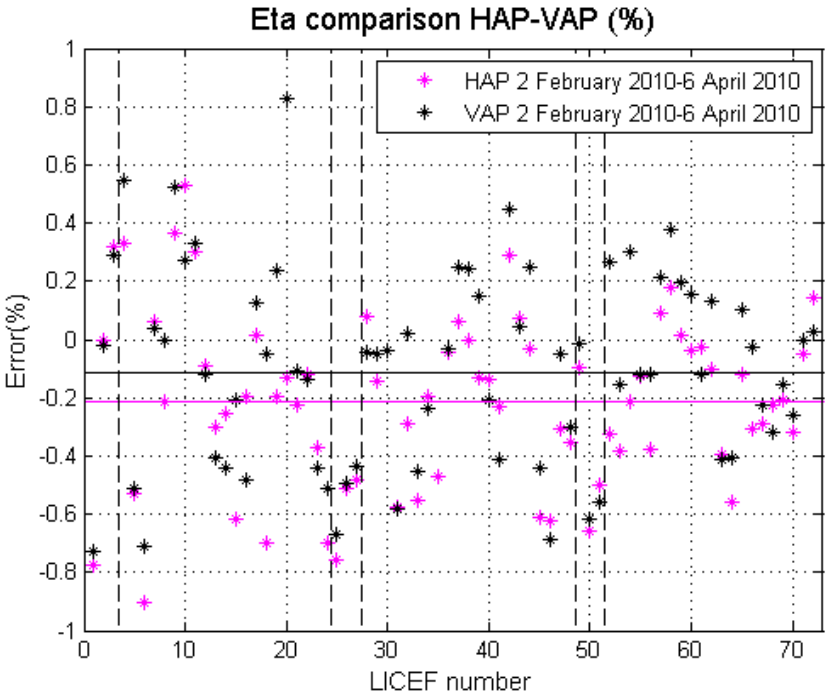

Fig. 6.76 Difference between η from 2 February 2010-6 April 2010 (HAP-VAP))

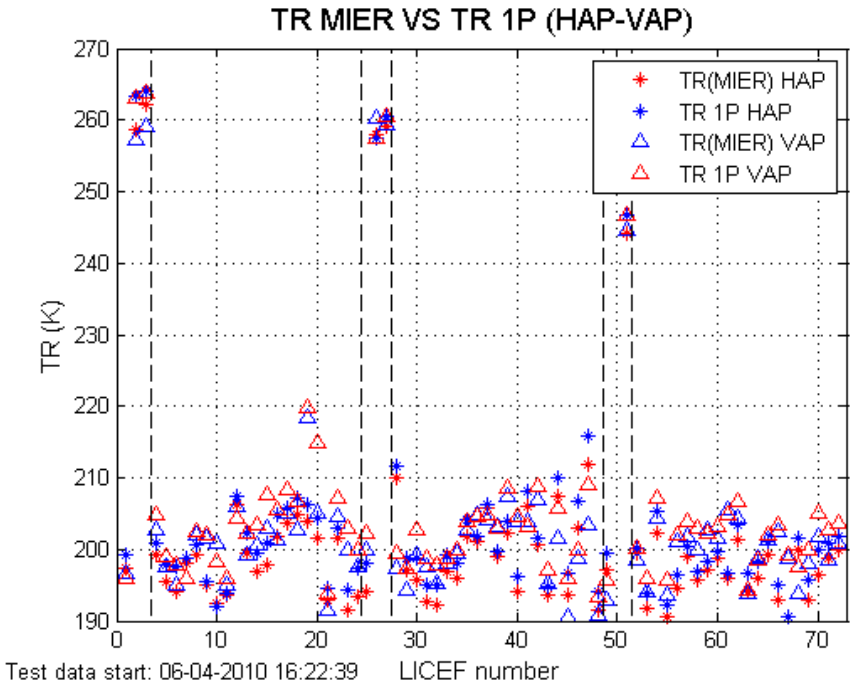

Fig. 6.77 TR MIER vs TR 1P. External antenna efficiency and External CAS correction factor (HAP-VAP)

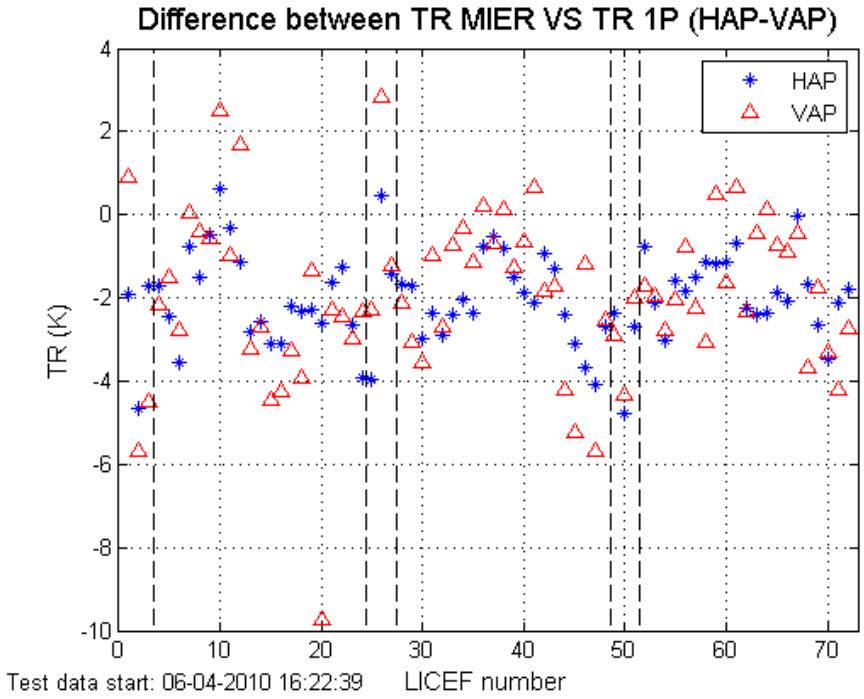

Fig. 6.78 Difference between TR MIER and TR 1P. External antenna efficiency and External CAS correction factor (HAP-VAP)

6.9.5 Comparison between Test 02/02/2010 and Tests 01/12/2010-23/03/2010

All plots in this section as similar to those given in the previous section.

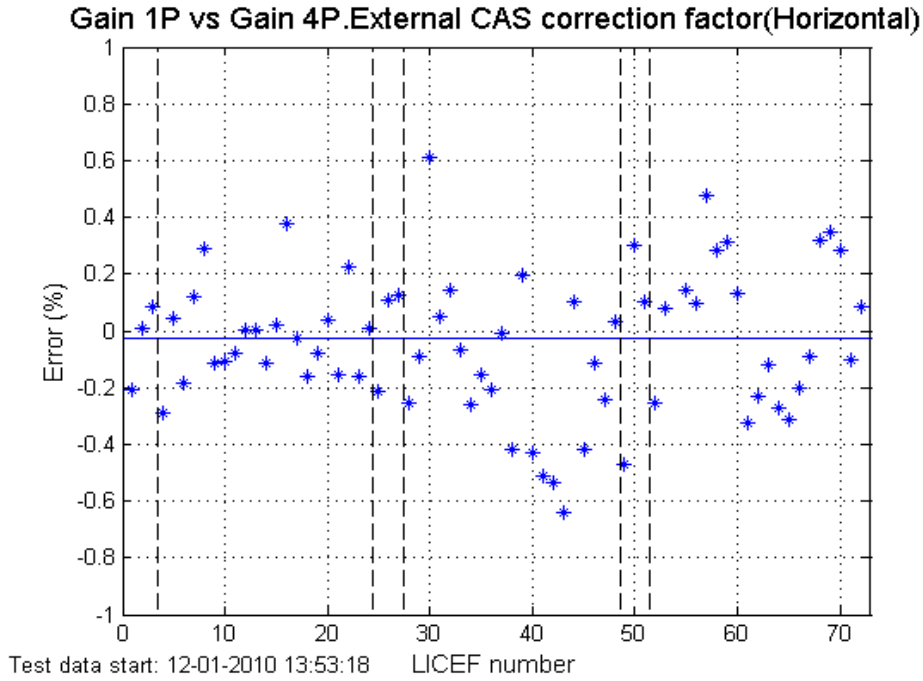

Fig. 6.79 Gain 1P vs Gain 4P. External antenna efficiency and External CAS correction factor from February 2010(HAP)

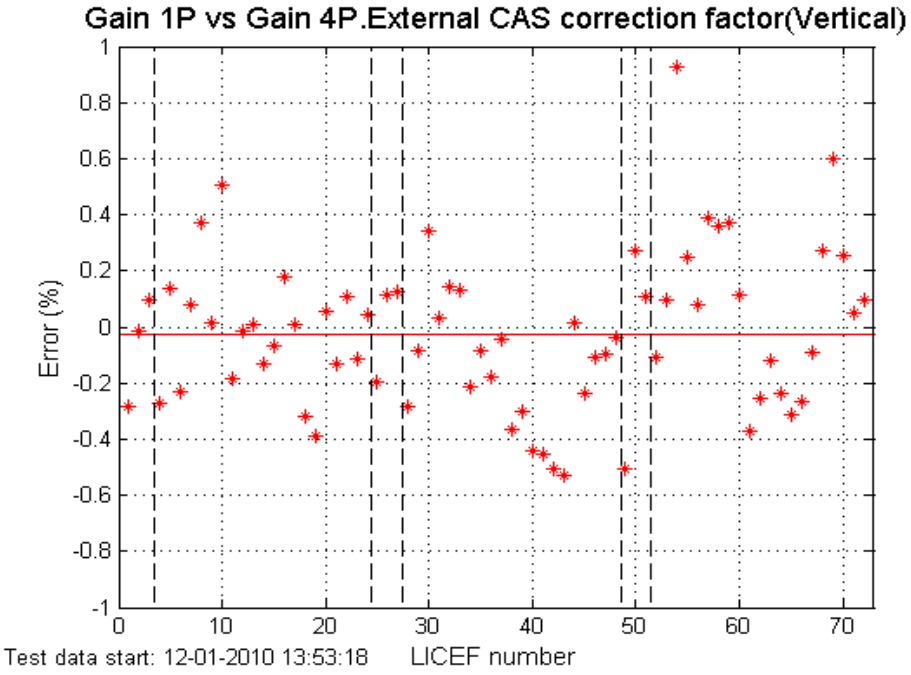

Fig. 6.80 Gain 1P vs Gain 4P. External antenna efficiency and External CAS correction factor from February 2010(VAP)

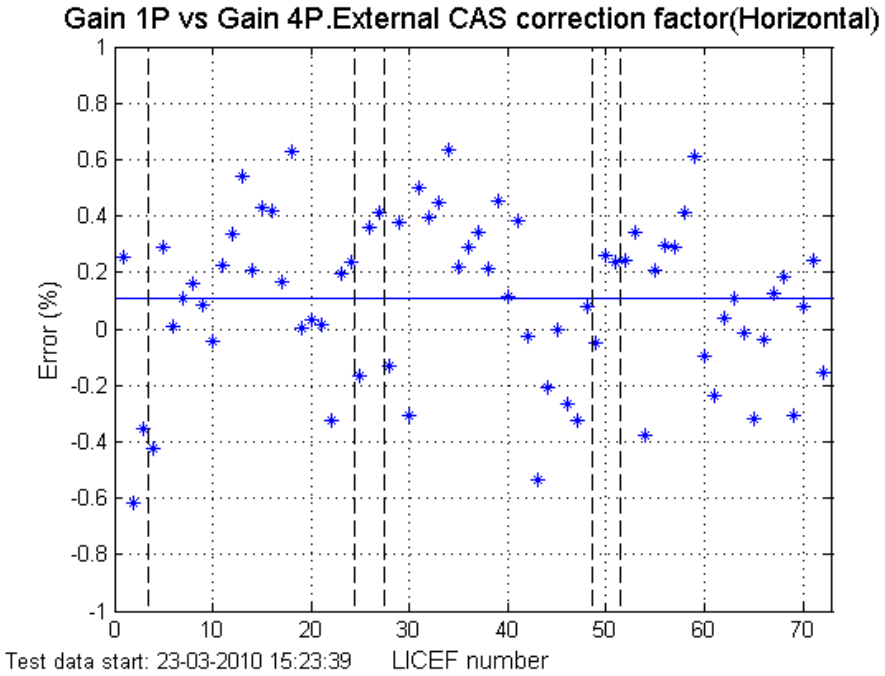

Fig. 6.81 Gain 1P vs Gain 4P. External antenna efficiency and External CAS correction factor from February 2010(HAP)

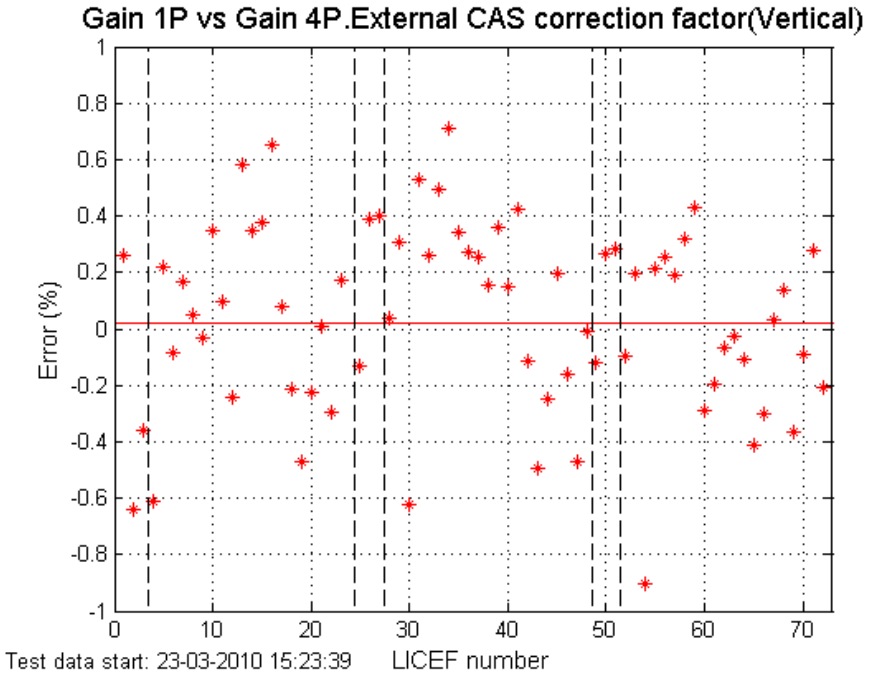

Fig. 6.82 Gain 1P vs Gain 4P. External antenna efficiency and External CAS correction factor from February 2010(VAP)

6.10 Summary of results

In this section all the errors are presented in the same plot (H and V):

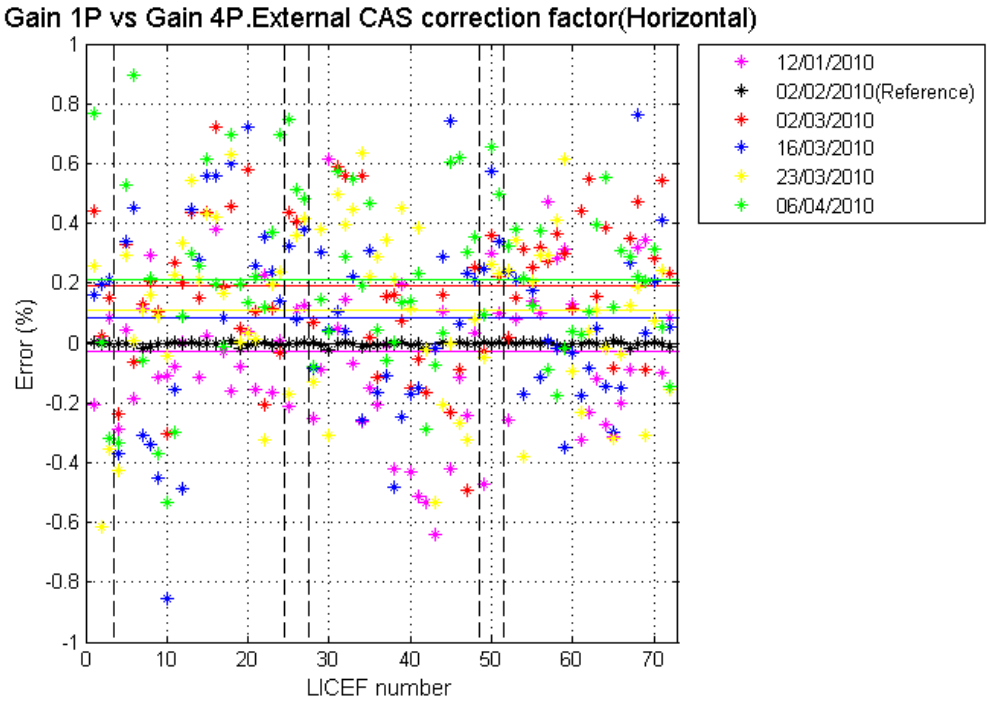

Fig. 6.83 Gain 1P vs Gain 4P. External antenna efficiency and External CAS correction factor from February 2010(HAP)

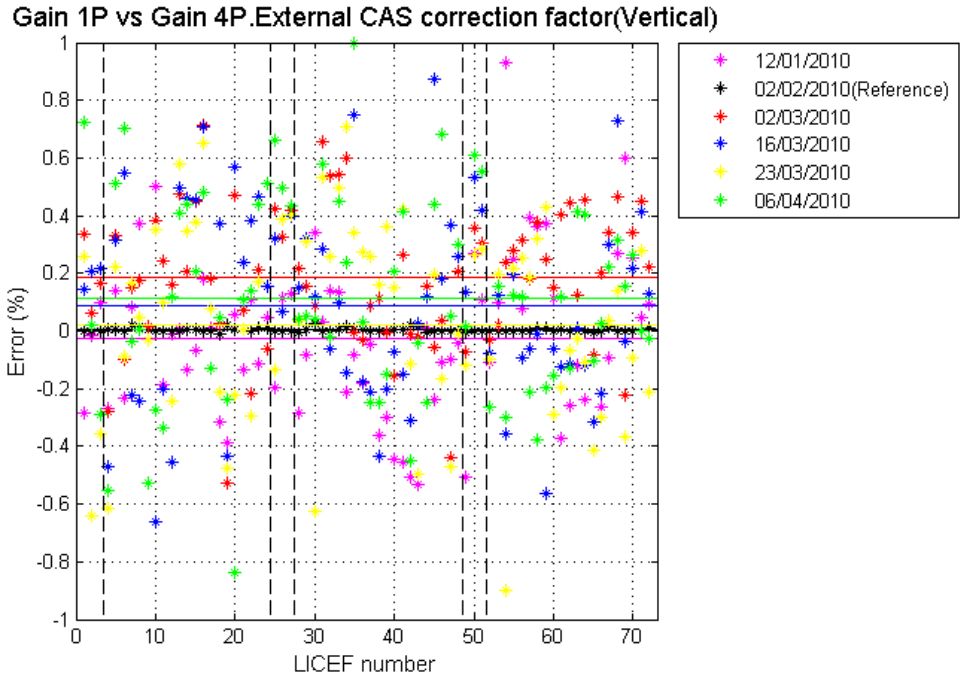

Fig. 6.84 Gain 1P vs Gain 4P. External antenna efficiency and External CAS correction factor from February 2010(VAP)

6.11 Conclusions

A number of methods to display the consistency of the different calibration parameters measured during external calibration have been analyzed in terms of accuracy, advantages and drawbacks.

- Method E is the proposed approach since gives a mathematical match between External G1P and internal PMS gain G4P at VAP/HAP and between ground receiver temperature at VAP/HAP. The correction factor are based on physical assignment of the errors at subsystem level, yielding final values:
    - A set of External CAS correction factors to substitute the current ground CAS correction factors in MDBfactory.xls
    - A set of External Antenna efficiencies: 72 in H and 72 in V
- The computation of the External CAS correction factors is lengthy and not automatic. Since these coefficients are expected to show very low drift, further monitoring of the external correction factor can be done exclusively from the external antenna efficiency by comparison of the internal PMS gain G4P and the external G1P. It can be computed from the error as follows:
    - $\frac{G_{1PA} - G_{4PA}}{G_{1PA}} = x$ where $G4P_A$ is the mean PMS gain at the antenna plane (A=V/H) from a nearby long calibration (at mean temperature T_{ph}^{Long}) and $G1P_A$ is the external PMS gain (A=V/H) translated to T_{ph}^{Long}.
    - A new external antenna efficiency can be computed for each receiver at VAP/HAP planes from the error x and the antenna efficiency used in the external calibration as:

$$\eta_{Ak_{SKY}}^{New} = \frac{\eta_{Ak_{SKY}}^{Old}}{1 - x} \quad \text{(A=V/H)}$$

    - This new value can be used to analyze the stability/repeatability of the correction or to refresh the parameter during each external calibration, as wished.
- A new set of external calibration coefficients has been provided (Annex II) based on the external calibration from 02/02/2010:
    - A set of External CAS correction factors in the same format as given in the MDBfactory. These coefficients are expected to be constant (within amplitude error requirements) for all the operational phase of the SMOS mission.
    - 72 antenna efficiency external coefficients for H and V polarizations: They are linear power gain coefficients: $\eta(dB) = 10 \cdot \log_{10}(\eta_{linear})$. These coefficients are assumed to be very stable, although can be refreshed after each external calibration. In any case, they should be refreshed if the standard deviation of the drift is larger than 0.8%. (Error budget requirement).

Chapter 7

7 Long term stability of calibration parameters

The analysis of the long term stability of calibration parameters is an important task to know if different parameters of the instrument are stable in time. Since current instrument configuration (arm A in nominal source) was settled on January 2010, the calibration events to be compared start on this date and comprise about 5 months of calibration data.

7.1 Summary of results

This section gives a summary of the results regarding the main calibration parameters. The following cases have been analyzed:

- **Case A: Gain 4P stability**: This case shows the stability of the internal PMS gain G4P estimated from the long calibrations. The NIR has been calibrated during the closest external sky calibration, while the external CAS and antenna efficiency factors were retrieved from the external sky calibration on 02/02/2010. For each LICEF, PMS gain for each of the 8 calibrations has been corrected to its mean calibration temperature. All PMS show a clear mean PMS G4P drift, very similar in horizontal and vertical polarizations. This effect is clearly related to the calibration repeatability of the reference, possibly due to an error in the estimation of the sky temperature: MTS uses the NIR antenna temperatures from 02/02/2010 in all calibrations. However, a similar effect is observed in other LICEF parameters pointing to additional sources of error.

  Both internal CAS PMS G4P and external PMS cold sky gain present a similar mean drift trend. This drives to an error in the estimation of sky, temperature. Since CAS PMS G4P drift is slightly larger, it seems that an additional source of error (e.g. temperature correction) is mixed with the sky temperature error.

  RFI does not seem to play a role, since the RMS error dispersion is very similar in all cases.

- **Case B: Gain 1P stability.** In this case, receiver temperature TR is calibrated by means of each external PMS cold sky calibration. Then, internal PMS gain G1P is computed during the long calibration events by means of the U-noise epochs and receiver temperature TR properly corrected in temperature Tph. As shown, mean PMS gain drift/error is smaller than in the case of internal PMS gain G4P (case A), although both cases present a similar trend.

It must be highlighted that PMS gain dispersion (standard deviation) within each calibration is twice larger for the external PMS gain G1P. As first guess, this high dispersion is caused by the large temperature swing of the antenna during the external calibration, to be further investigated during post-commissioning activities.

- **Case C: External Gain stability**. As expected, external PMS cold sky gain presents the same behaviour as given by internal G1P, since it is based in the same external calibration data set and procedure (internal G1P uses, as reference, the external TR estimation from external PMS cold sky calibration)
- **Case D: External gain: new external sequence.** The calibration held on 27th of April is the only new external sequence analyzed so far. It consists of 8 external PMS cold sky calibration events in a time span of approximately 16 minutes. The plots clearly show that the repeatability of the measurement for each PMS is well above the thermal noise estimation. In addition, the PMS gain presents a pk-to-pk drift (after temperature correction) of about 0.2%. This indicates residual front end thermal effects not properly taken into account during the external calibration, to be further assessed during the post-commissioning phase.
- **Case E: TR 1P stability.** TR 1P receiver temperature is the external PMS TR temperature (estimated during external PMS cold sky calibration), translated to the mean temperature during long calibration. The plots show that the drift behaviour of TR1P is the inverse of that for PMS gain (either G1P or G4P). Note that random integration time errors are discarded since horizontal and vertical polarizations show the same behaviour. This clearly points, as a first guess, to an error in the estimation of the sky temperature (Earth contribution, sun, back lobes…). A dynamic front end thermal effect that introduces a residual error in the Friis correction may also be possible, to be further assessed during post-commissioning activities.
- **Case F: L stability.** L (attenuator) presents very good stability. This parameter is not used in calibration (its exact value is irrelevant) and it is plotted just for monitoring. In any case, it is worth to point out that, although very small, L drift presents a clear trend in the 4 months span. So far we do not see any relevant conclusion on this behaviour
- **Case G: Voffset stability.** Voffset has been computed using the heater correction derived from the first set of stability tests. Voffset presents very good stability and very good agreement between external and internal (long cal) estimations. The two last calibrations (06/04/10 and 27/04/10) show an increase on Voffset drift dispersion for the set of 66 LICEF, both for internal and external Voffset estimations. So far, the reason for this behaviour is unknown since more calibration events are required to confirm either a drift or a random effect.
- **Case I: Tph stability.** These plots show that the mean LICEF temperature presents up to 2.7ºC pk-to-pk drift in this 4 months time span. In any case, the absolute mean temperature drift does not seem to play a significant role in the calibration parameters, since it is properly corrected by means of the sensitivity coefficients.

7.1.1 Case A: Gain 4P stability

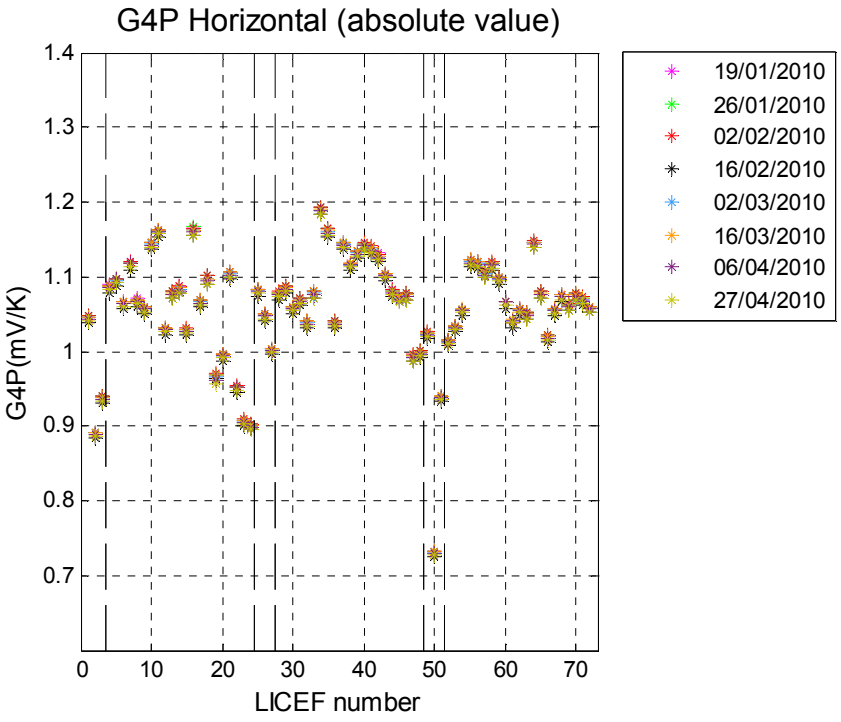

Fig. 7.1 G4P Horizontal (absolute value)

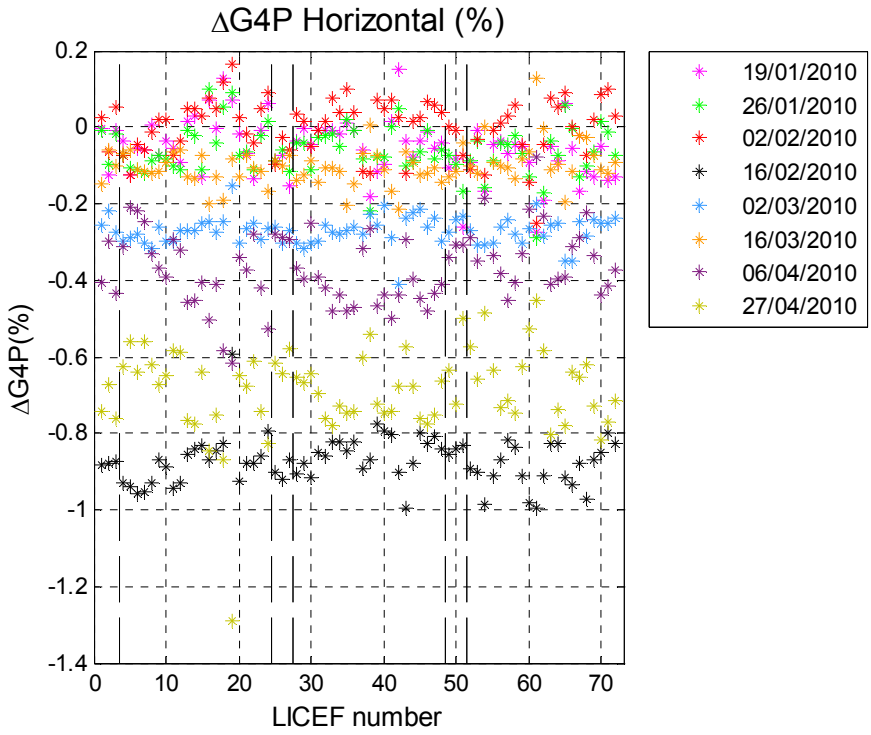

Fig. 7.2 ΔG4P Horizontal (%). Mean gain for all PMS 02/02/2010 calibration taken as reference

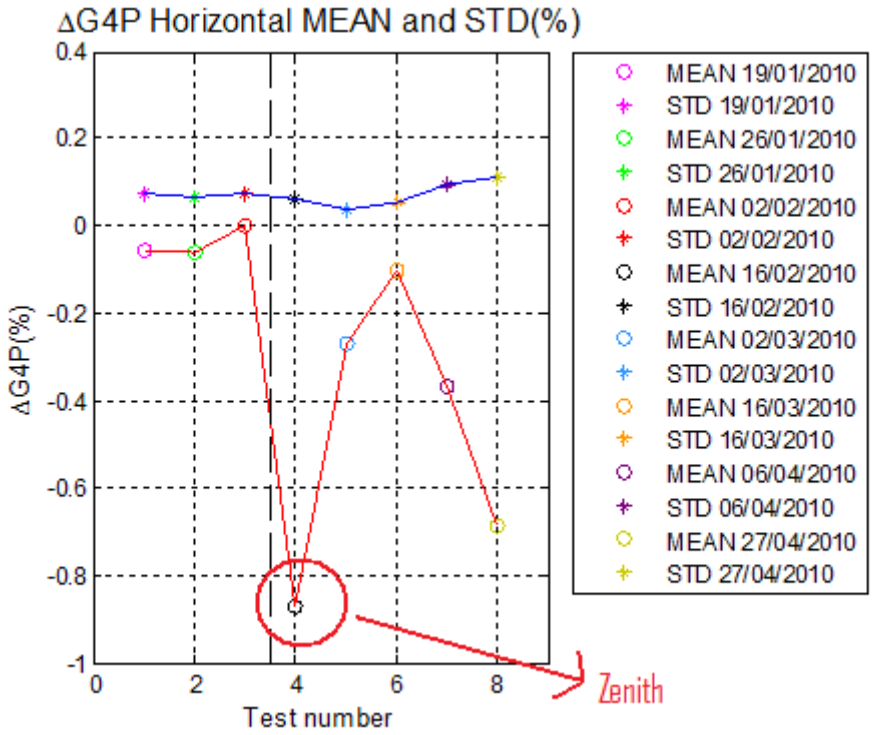

Fig. 7.3 ΔG4P Horizontal MEAN and STD (%).Mean gain for all PMS 02/02/2010 calibration taken as reference

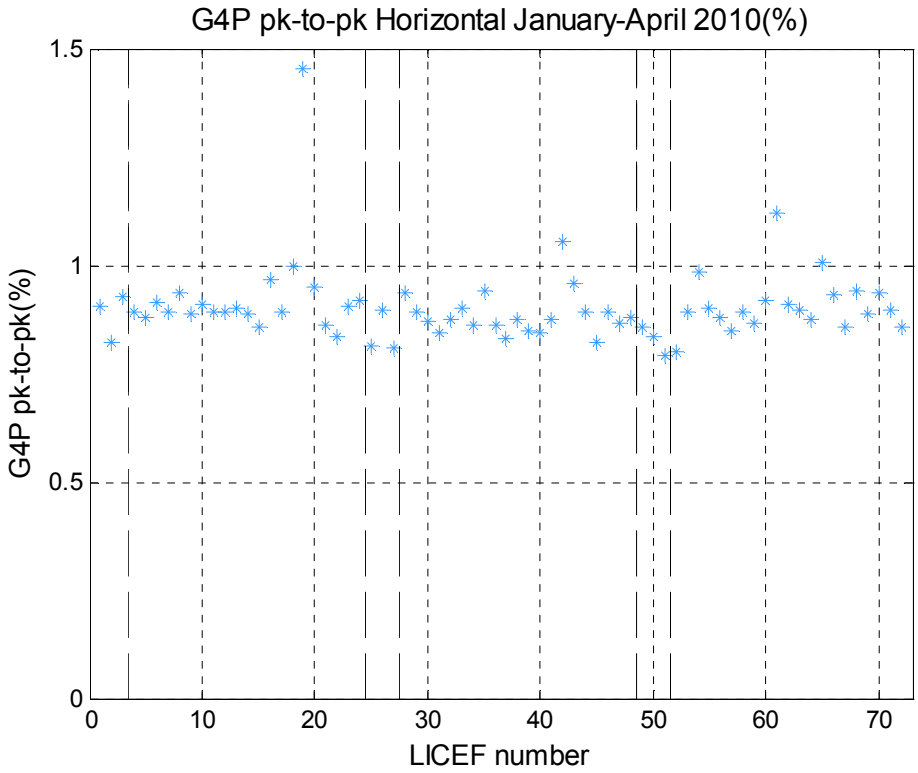

Fig. 7.4 G4P pk-to-pk Horizontal January-April 2010 (%)

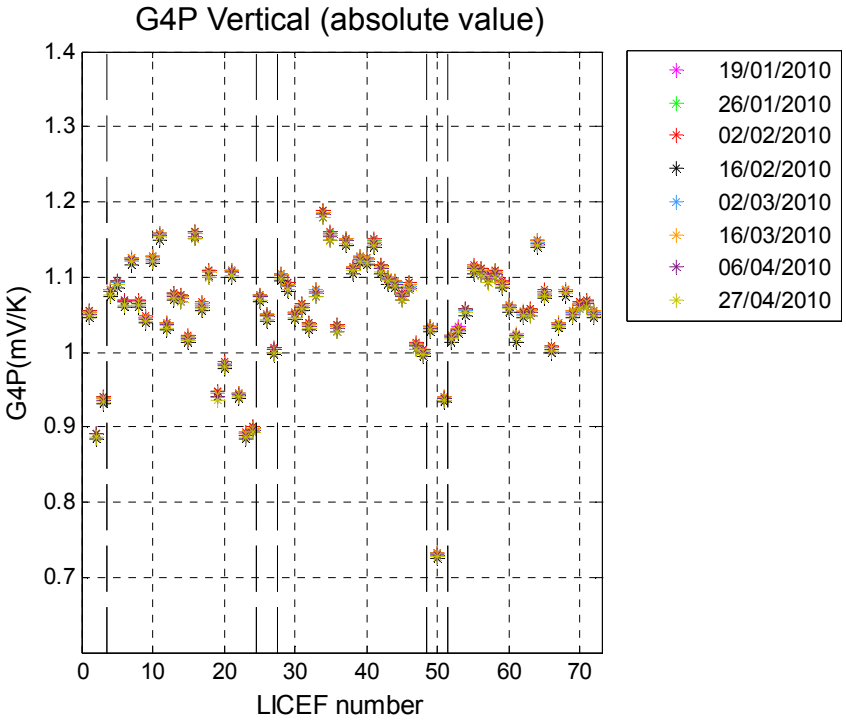

Fig. 7.5 G4P Vertical (absolute value)

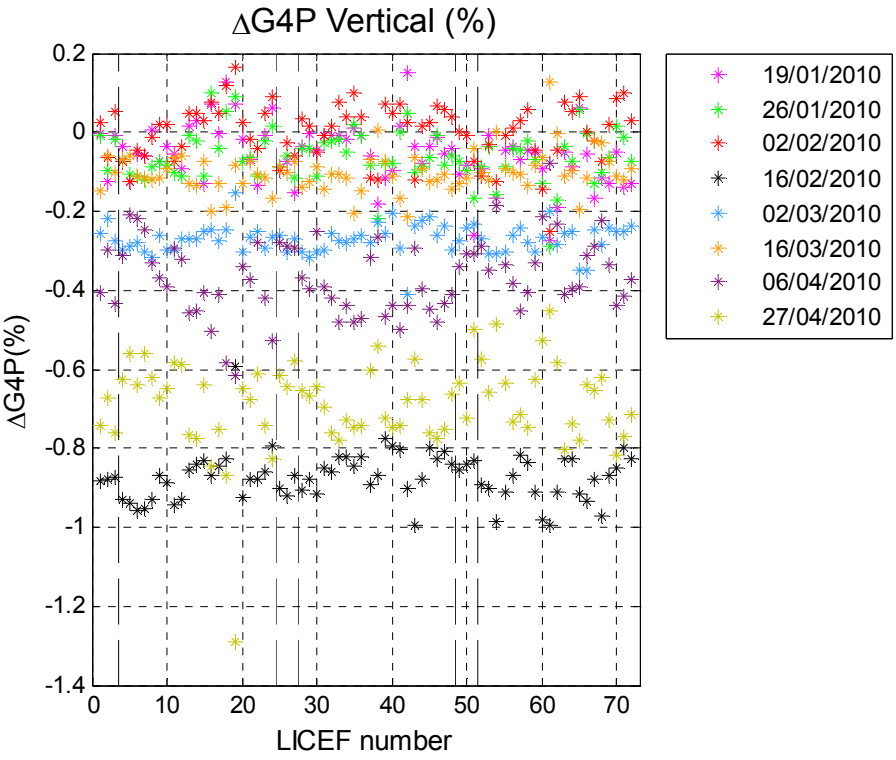

Fig. 7.6 ΔG4P Vertical (%). Mean gain for all PMS 02/02/2010 calibration taken as reference

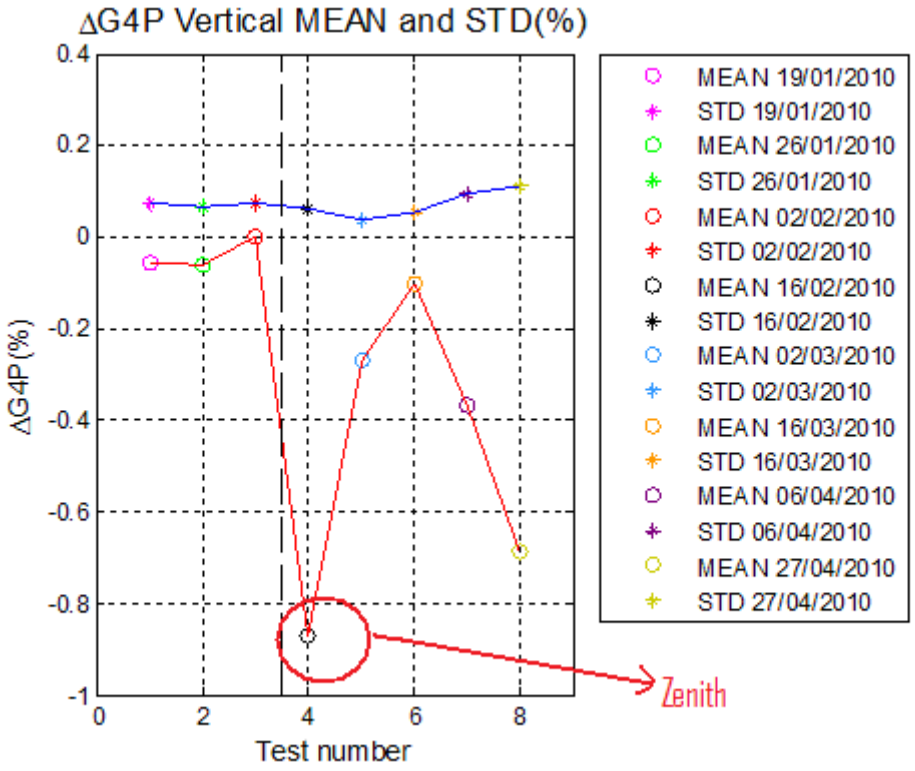

Fig. 7.7 ΔG4P Vertical MEAN and STD (%).Mean gain for all PMS 02/02/2010 calibration taken as reference

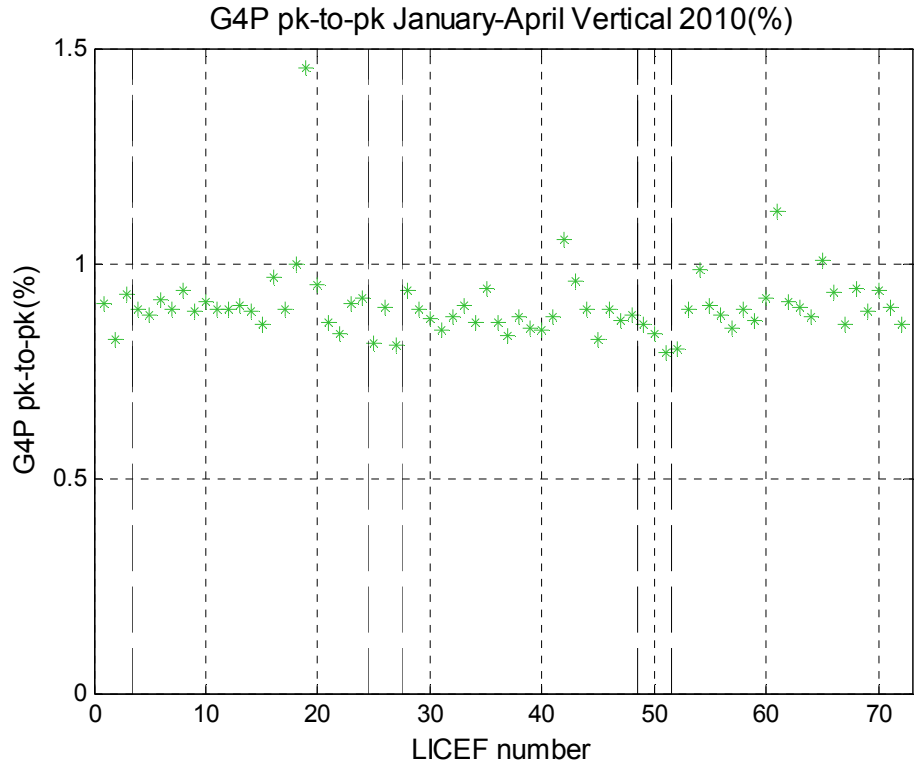

Fig. 7.8 G4P pk-to-pk Vertical January-April 2010 (%)

7.1.2 Case B: Gain 1P stability

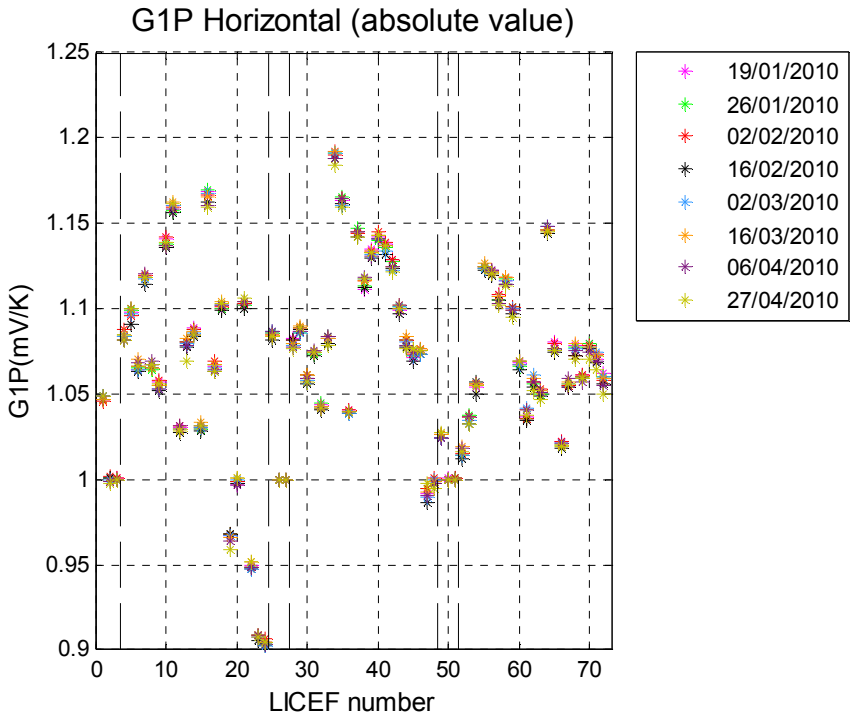

Fig. 7.9 G1P Horizontal (absolute value)

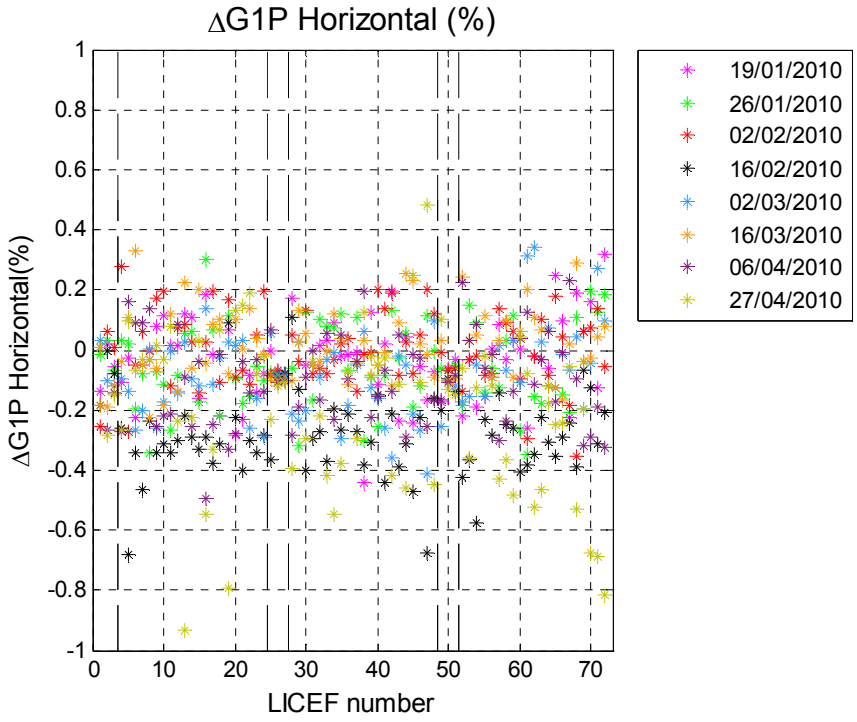

Fig. 7.10 ΔG1P Horizontal (%)

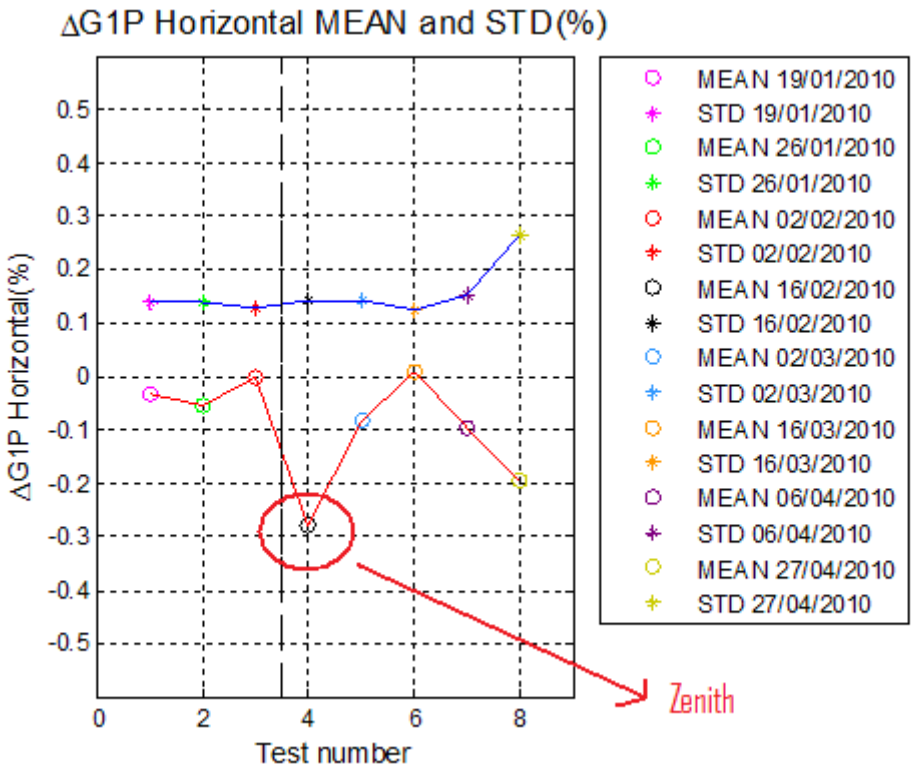

Fig. 7.11 ΔG1P Horizontal MEAN and STD (%)

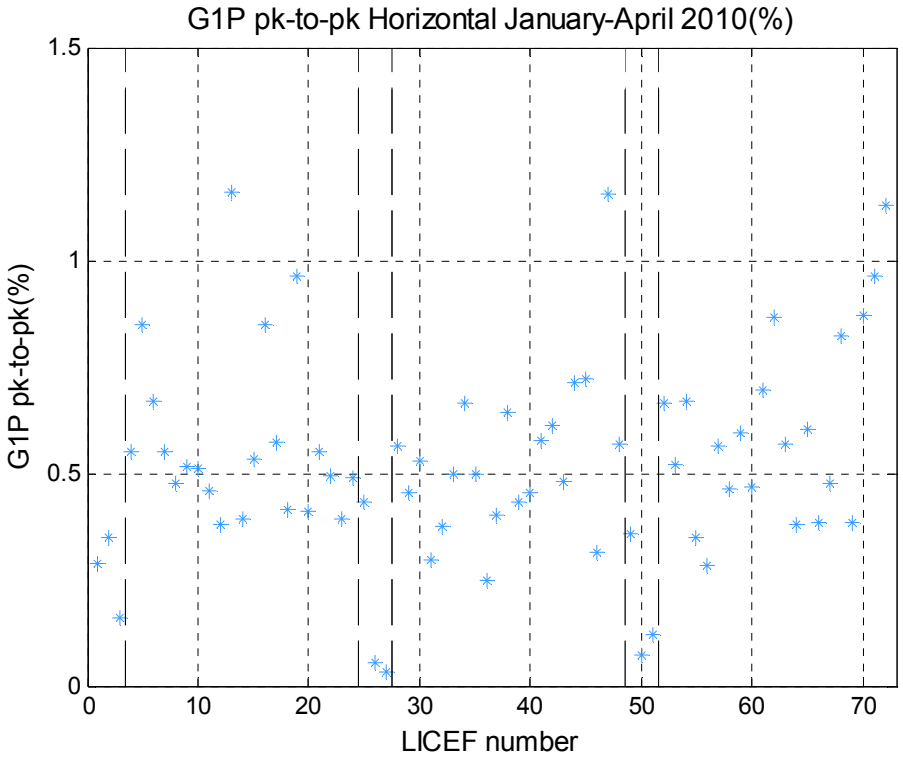

Fig. 7.12 G1P pk-to-pk Horizontal January-April 2010 (%)

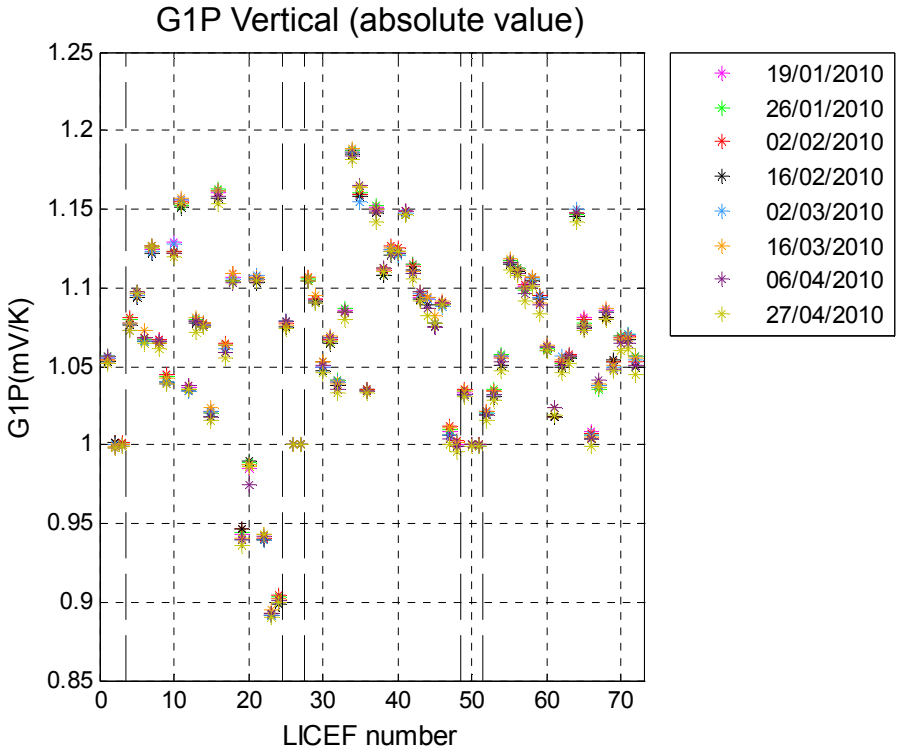

Fig. 7.13 G1P Vertical (absolute value)

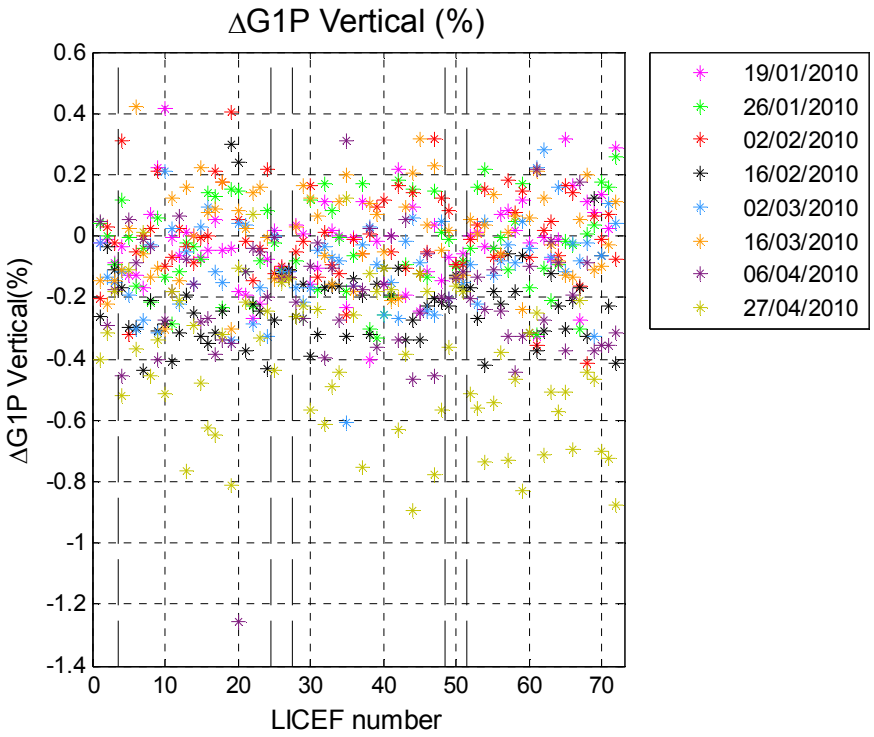

Fig. 7.14 ΔG1P Vertical (%)

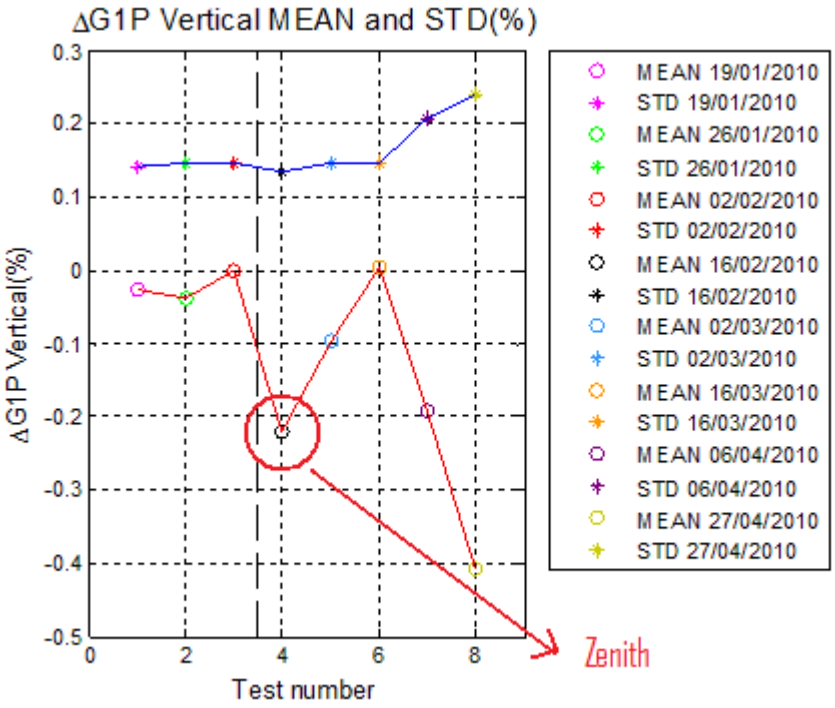

Fig. 7.15 ΔG1P Vertical MEAN and STD (%)

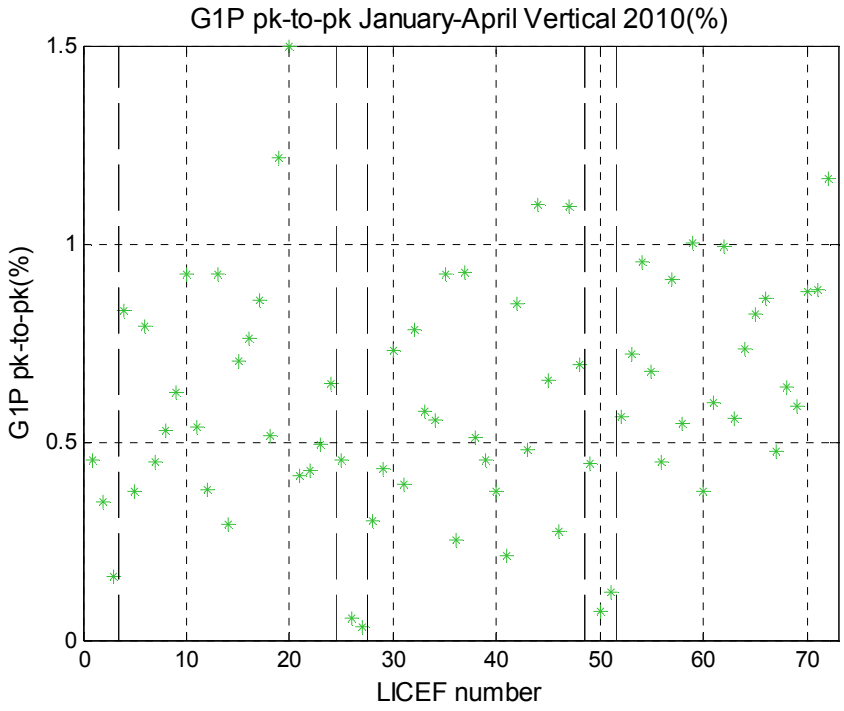

Fig. 7.16 G1P pk-to-pk Vertical January-April 2010 (%)

7.1.3 Case C: External Gain stability

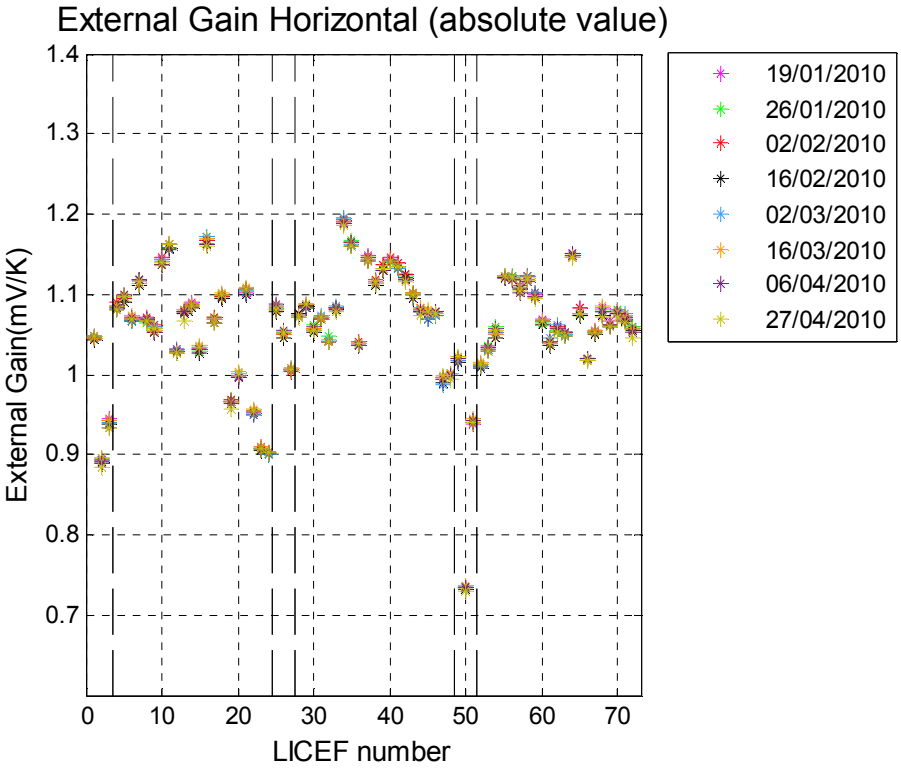

Fig. 7.17 External Gain Horizontal (absolute value)

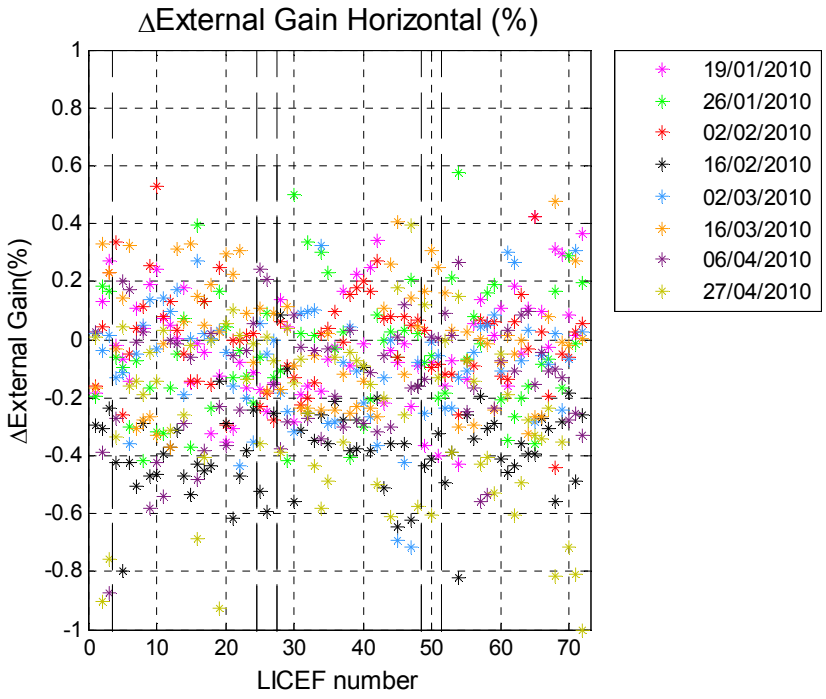

Fig. 7.18 ΔExternal Gain Horizontal(%)

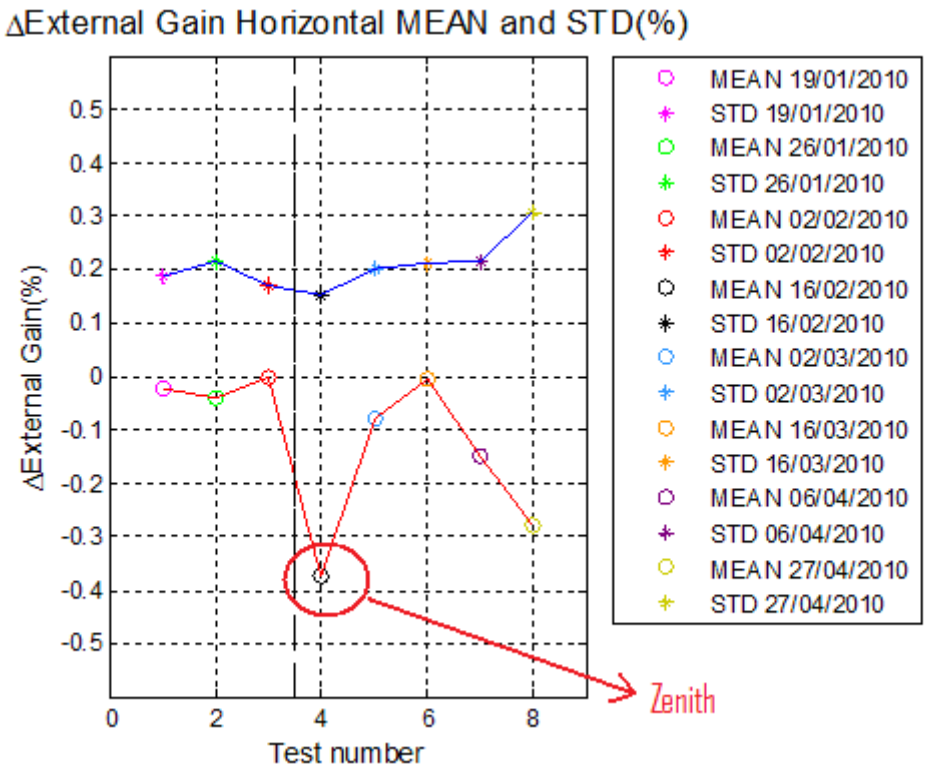

Fig. 7.19 ΔExternal Gain Horizontal MEAN and STD (%)

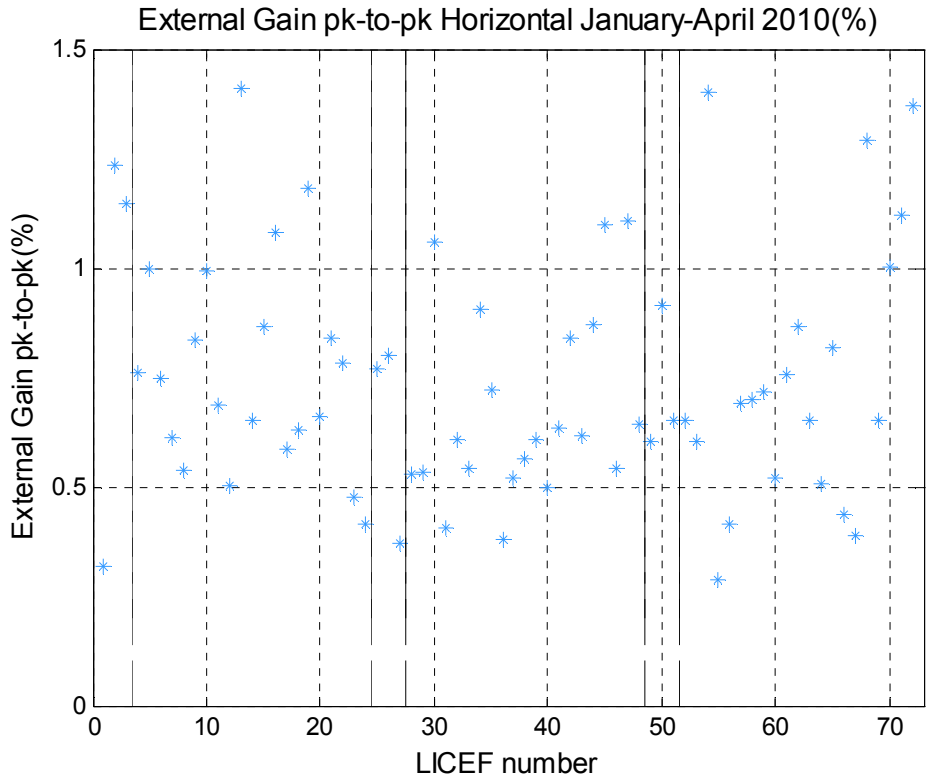

Fig. 7.20 External Gain pk-to-pk Horizontal January-April 2010 (%)

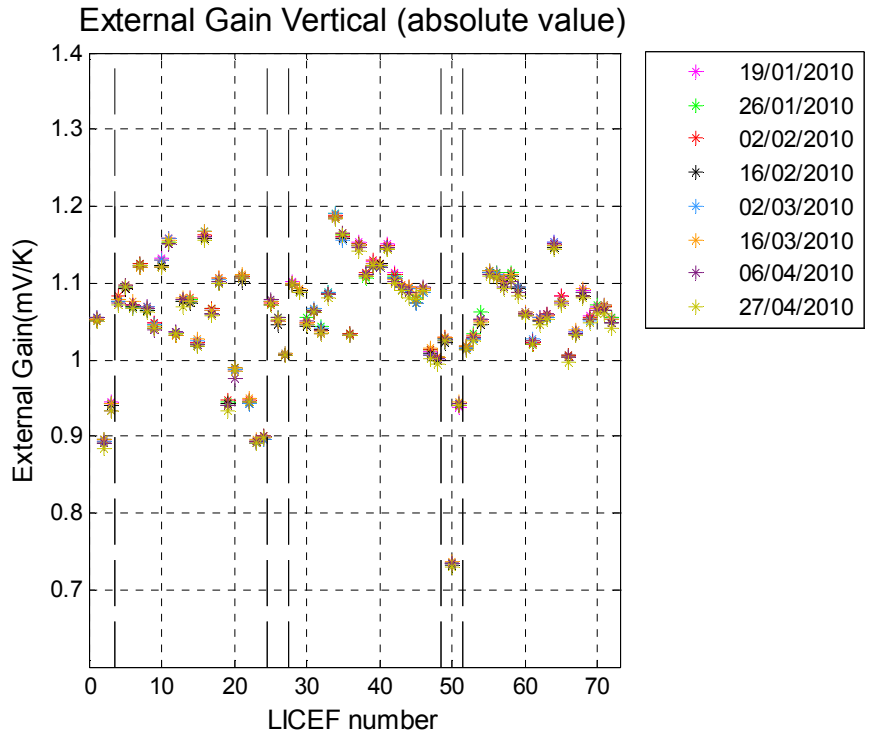

Fig. 7.21 External Gain Vertical (absolute value)

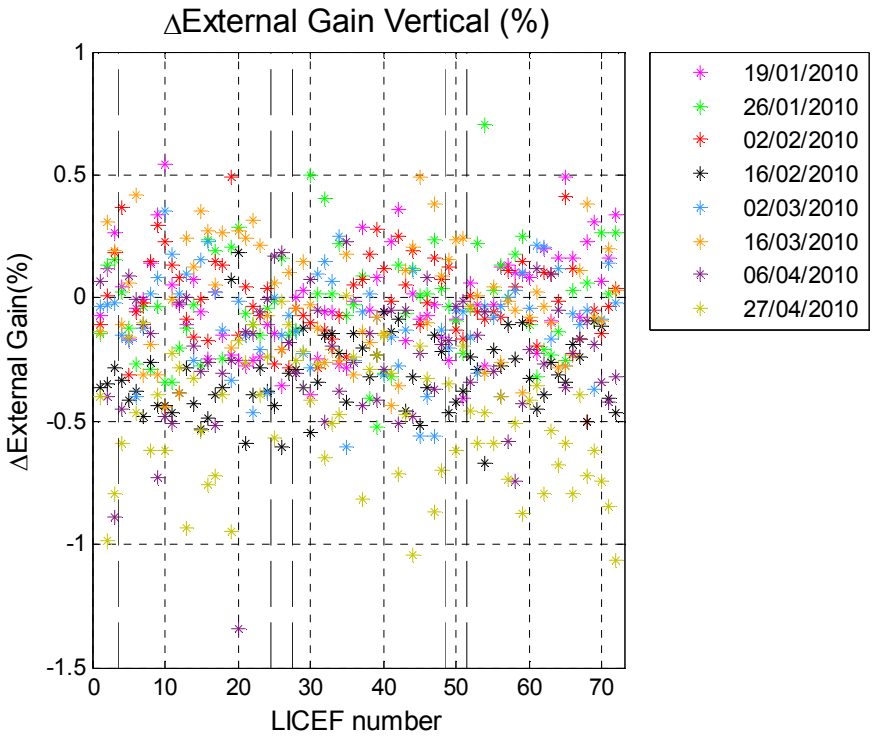

Fig. 7.22 ΔExternal Gain Vertical(%)

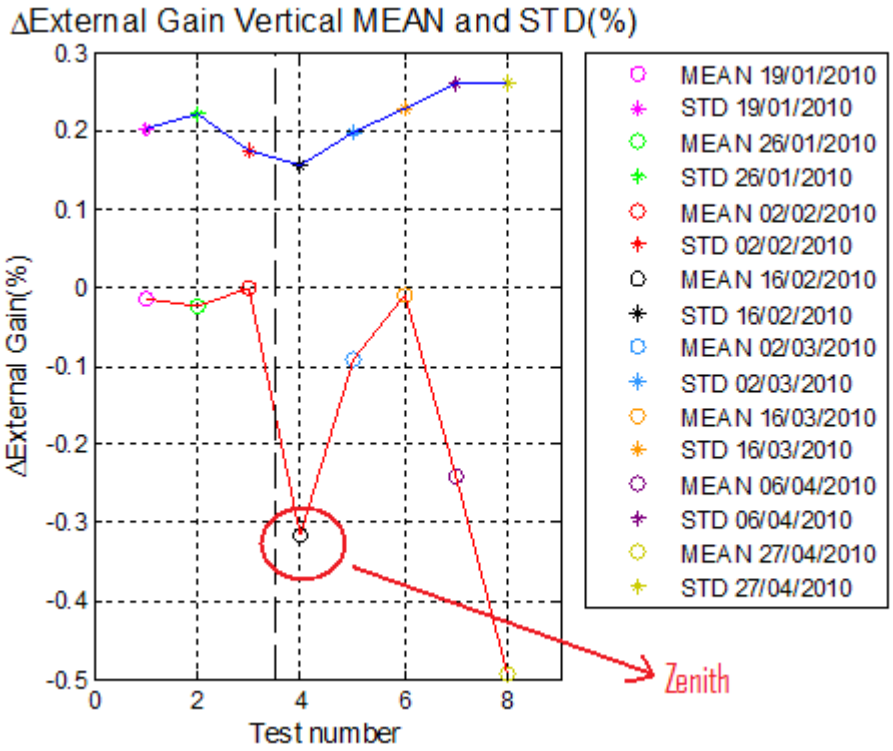

Fig. 7.23 ΔExternal Gain Vertical MEAN and STD (%)

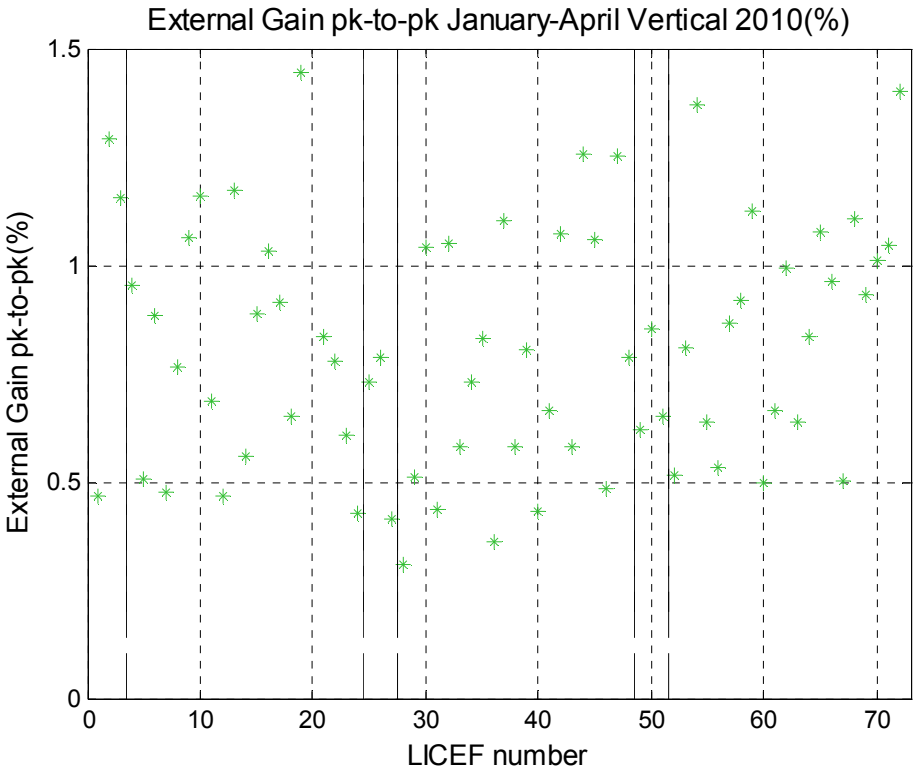

Fig. 7.24 External Gain pk-to-pk Vertical January-April 2010 (%)

7.1.4 Case D: External gain: new external sequence

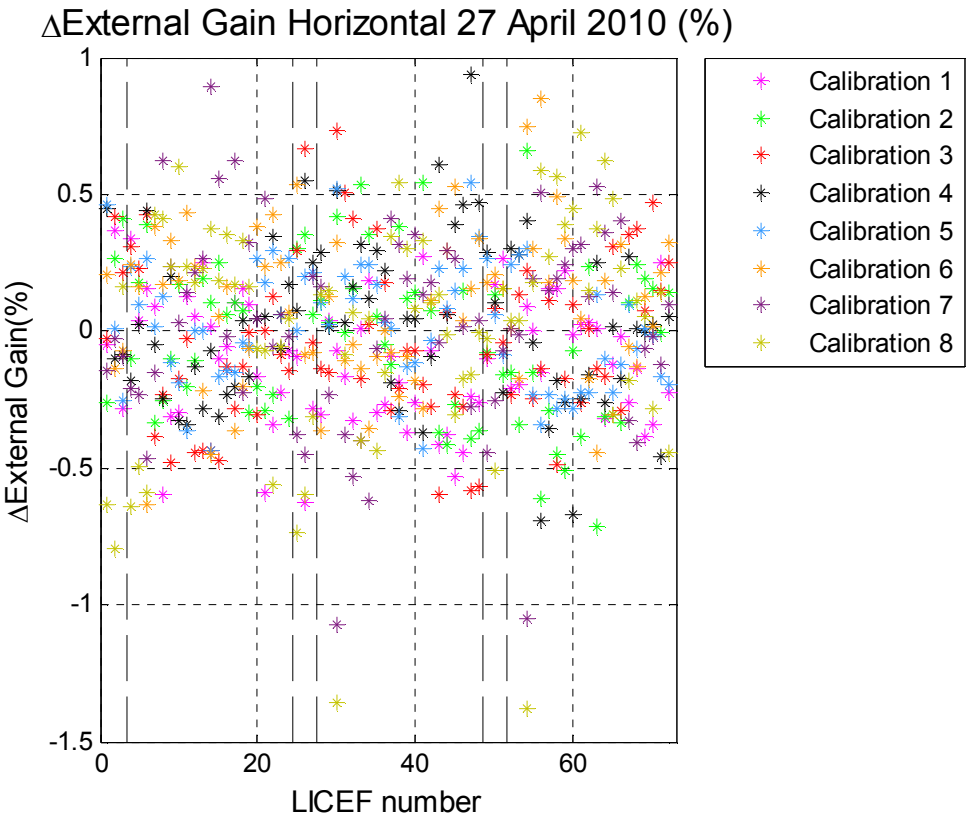

Fig. 7.25 External Gain Horizontal 27 April 2010 (%)

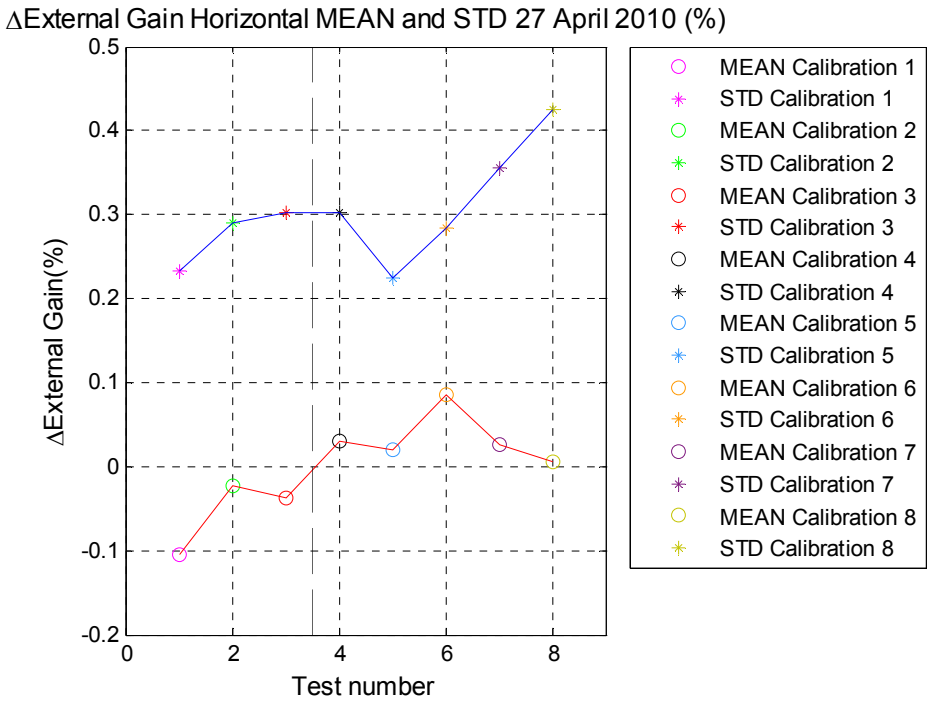

Fig. 7.26 External Gain Horizontal 27 April 2010 MEAN and STD(%)

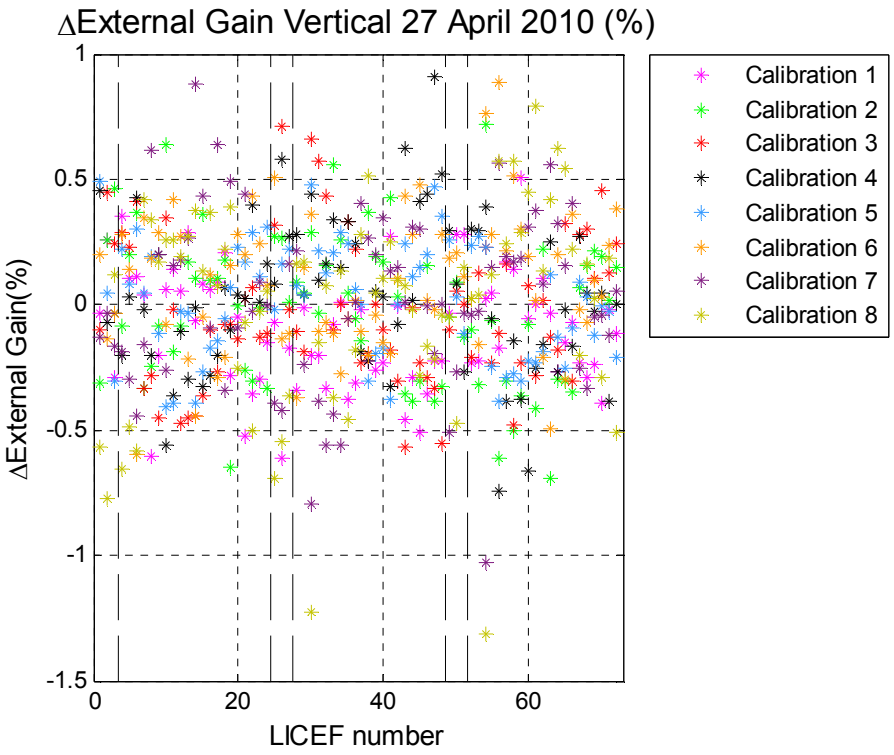

Fig. 7.27 External Gain Vertical 27 April 2010 (%)

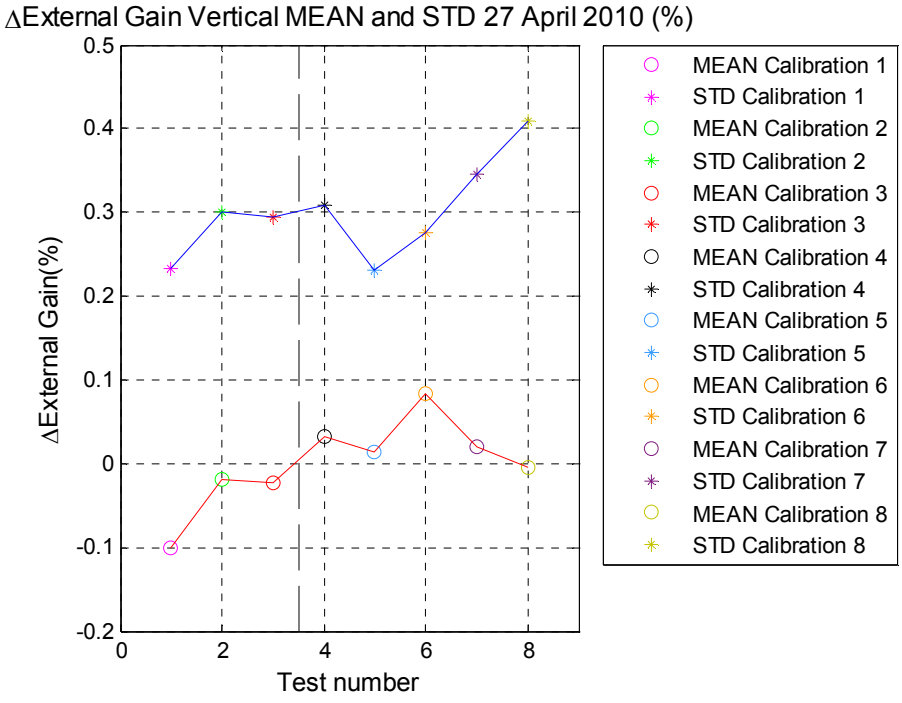

Fig. 7.28 External Gain Vertical 27 April 2010 MEAN and STD (%)

7.1.5 Case E: TR 1P stability

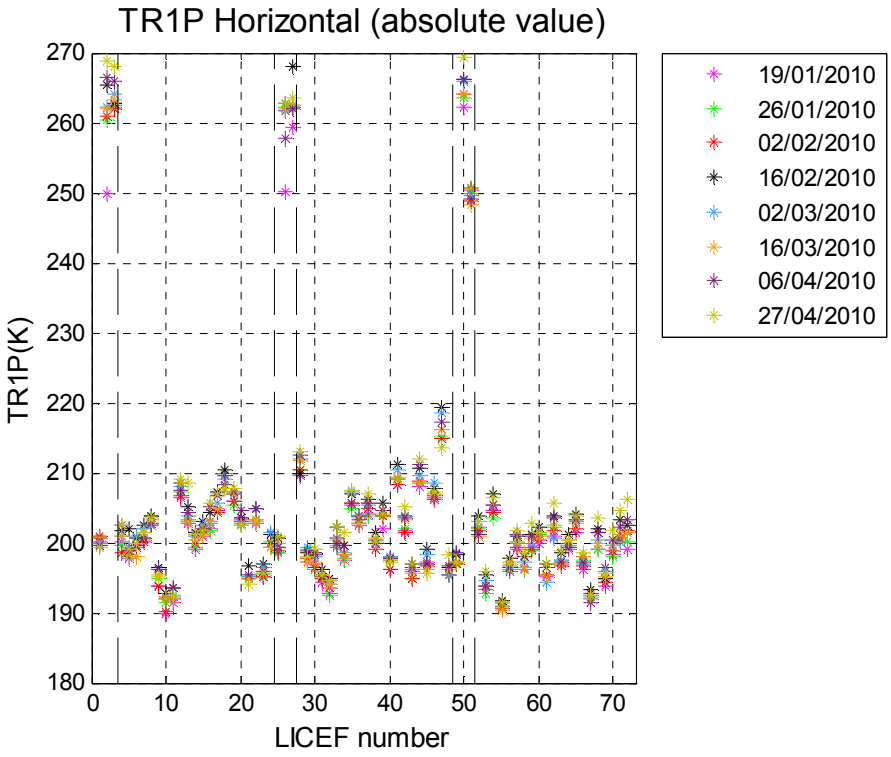

Fig. 7.29 TR 1P Horizontal (absolute value)

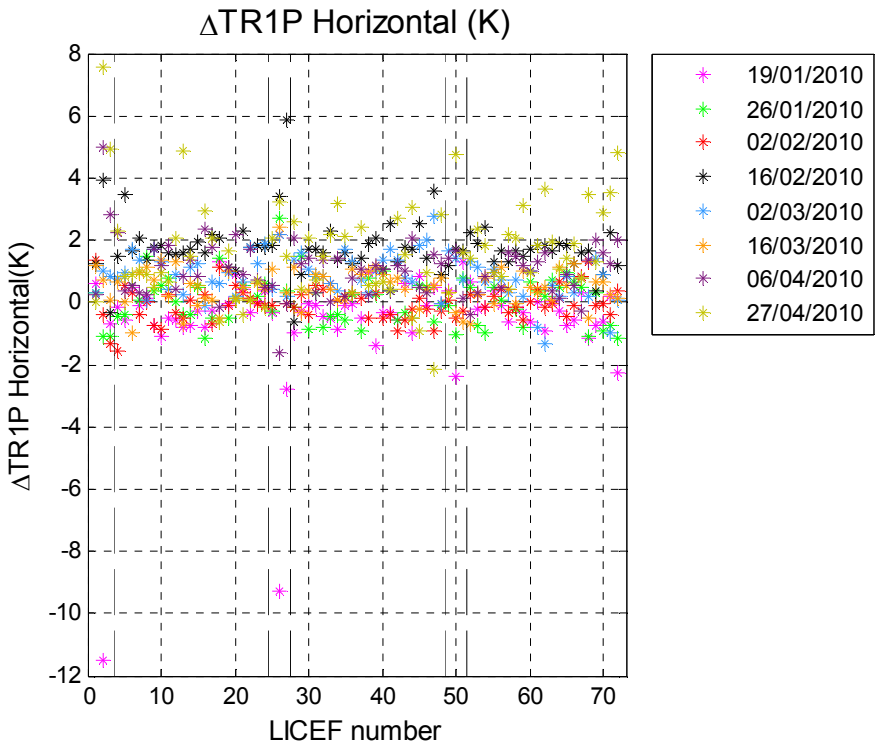

Fig. 7.30 ΔTR1P Horizontal(K)

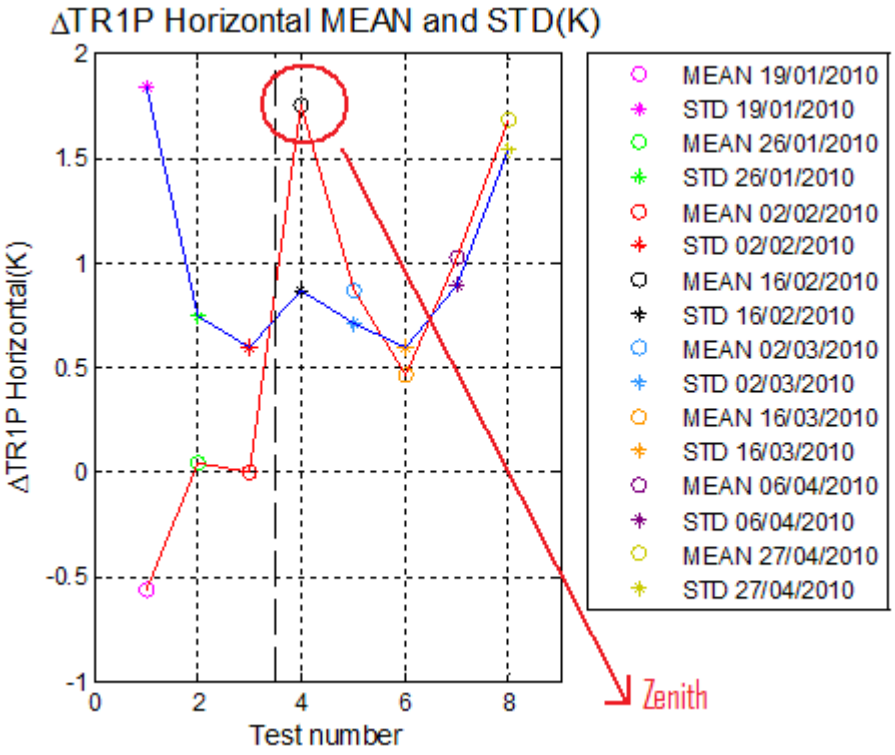

Fig. 7.31 ΔTR1P Horizontal MEAN and STD (K)

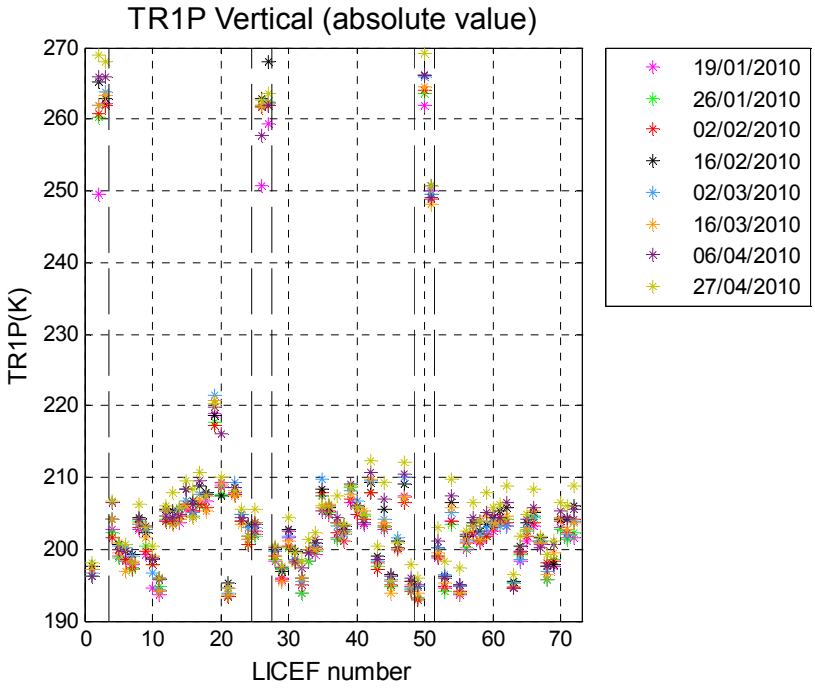

Fig. 7.32 TR 1P Vertical (absolute value)

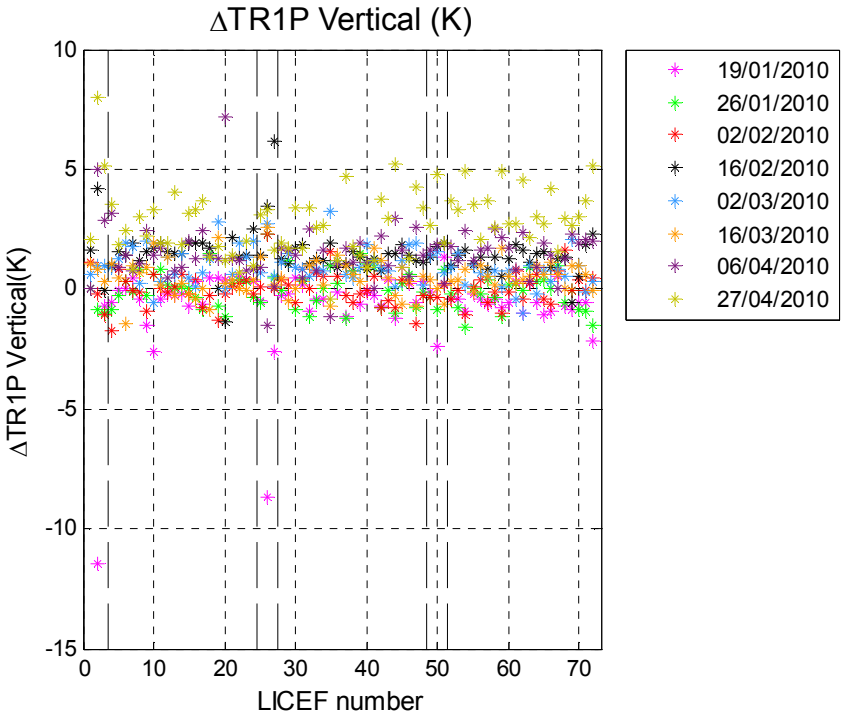

Fig. 7.33 ΔTR1P Vertical(K)

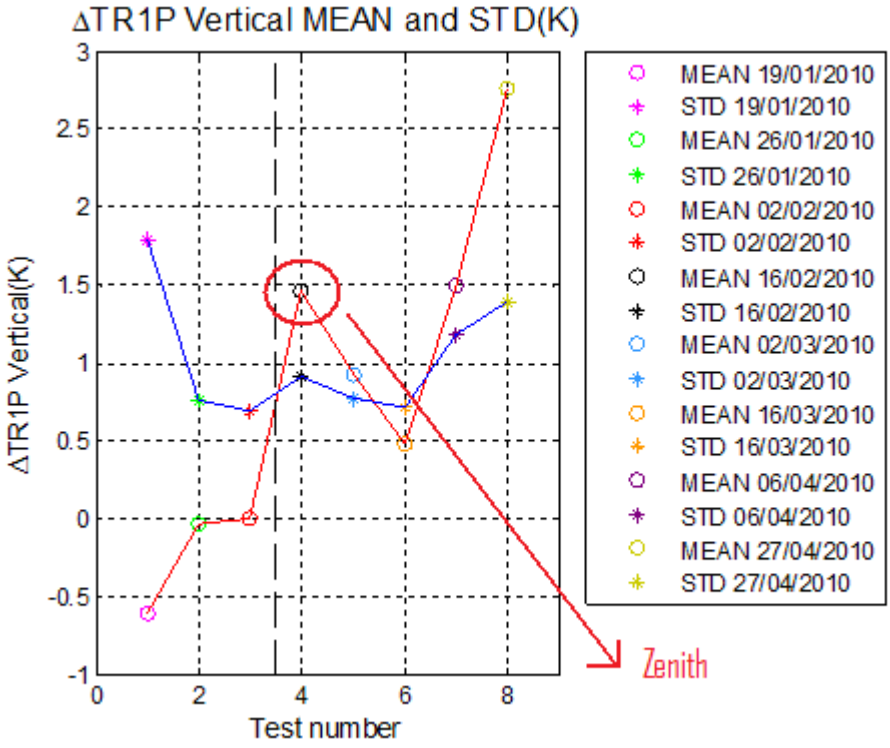

Fig. 7.34 ΔTR1P Vertical MEAN and STD (K)

7.1.6 Case F: L stability

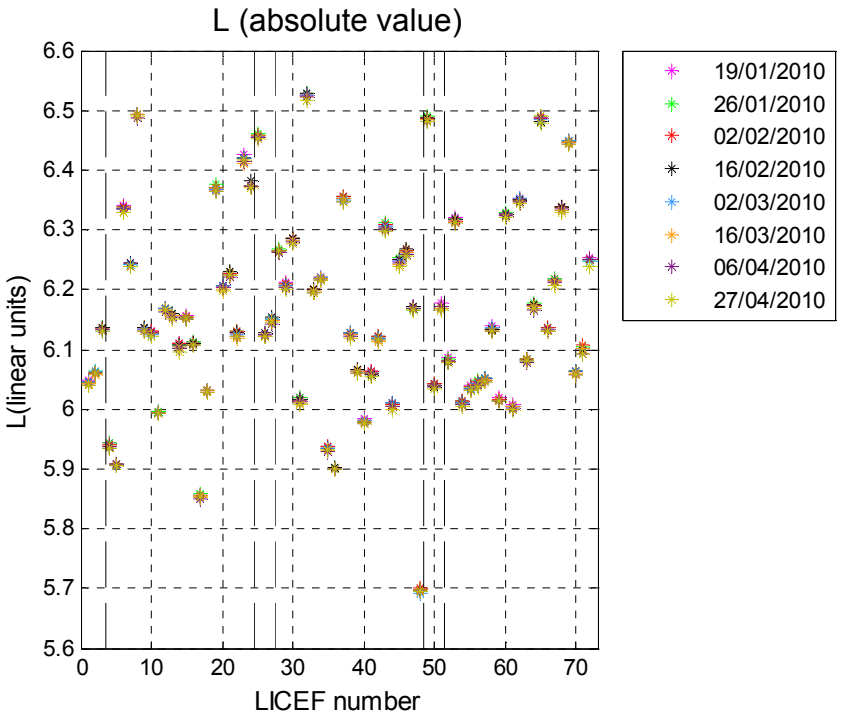

Fig. 7.35 L(absolute value)

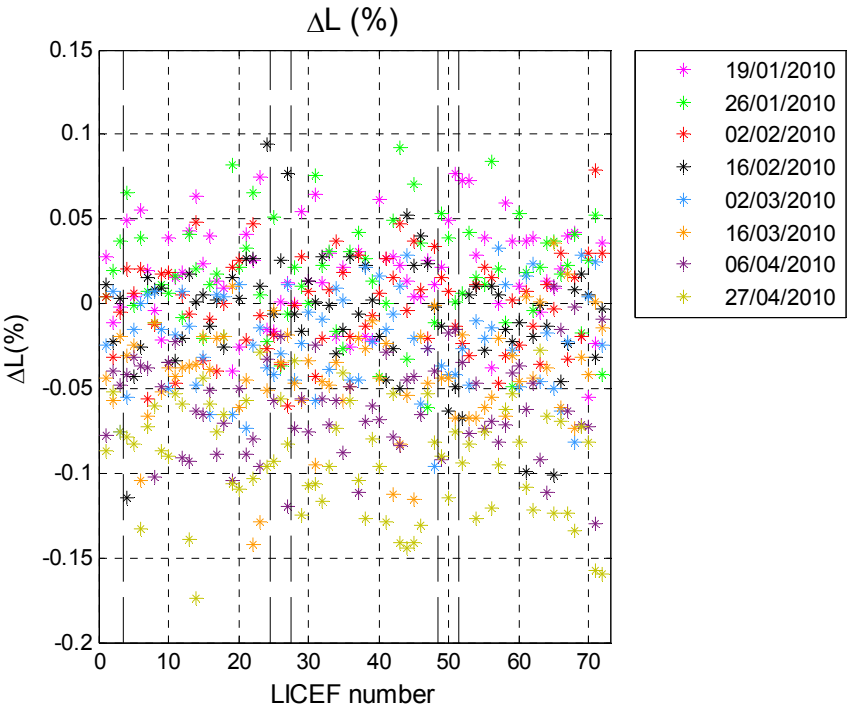

Fig. 7.36 ΔL (%)

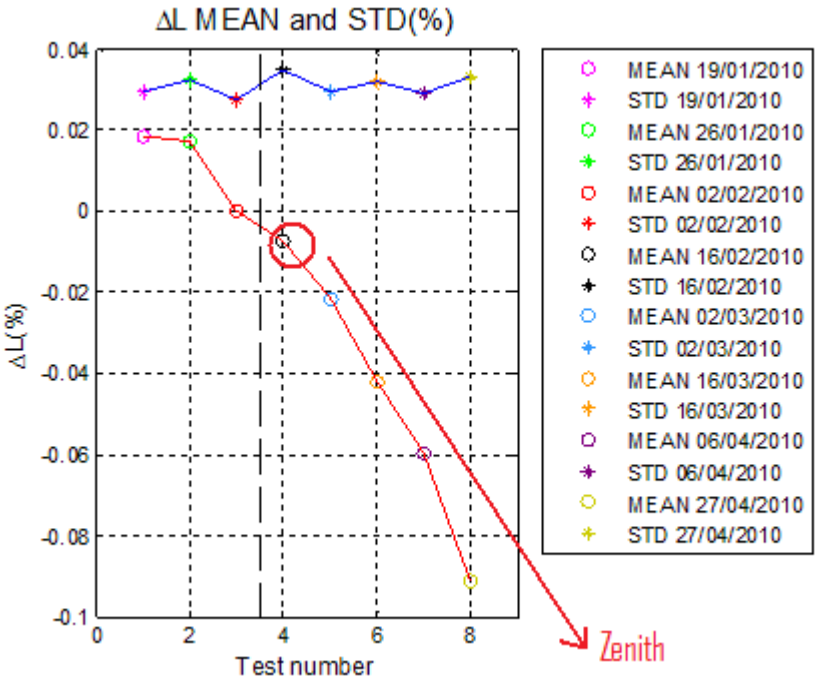

Fig. 7.37 ΔL MEAN and STD (%)

7.1.7 Case G: Voffset stability

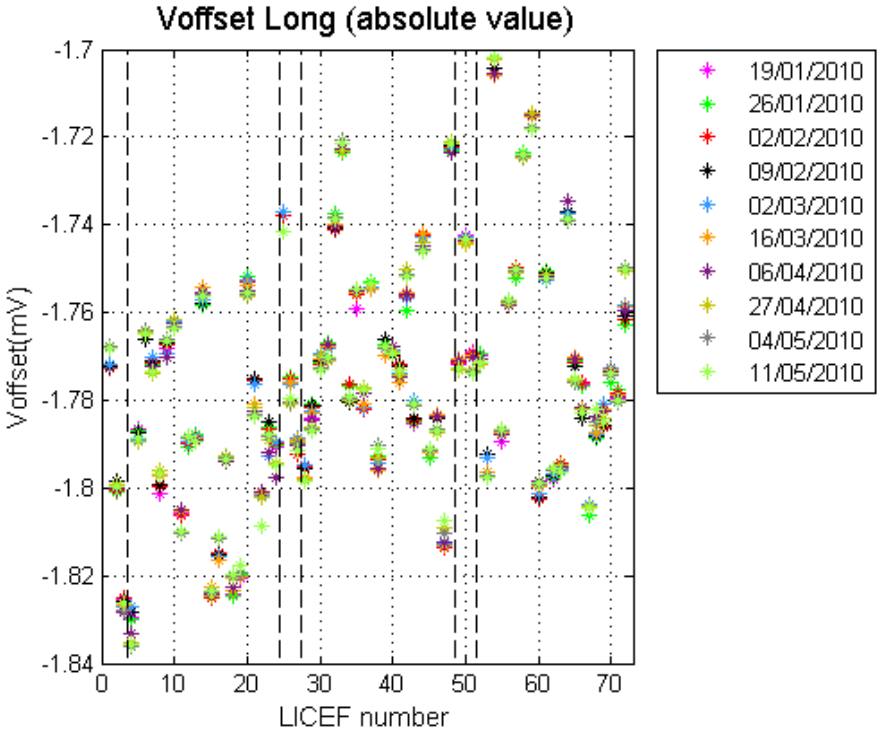

Fig. 7.38 Voffset Long(absolute value)

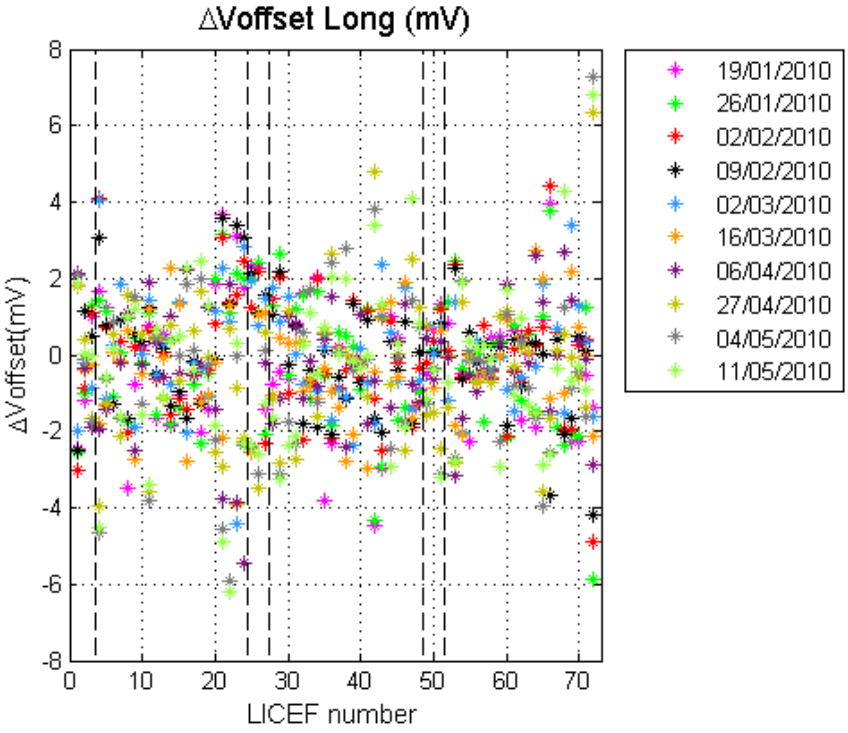

Fig. 7.39 ΔVoffset Long (mV)

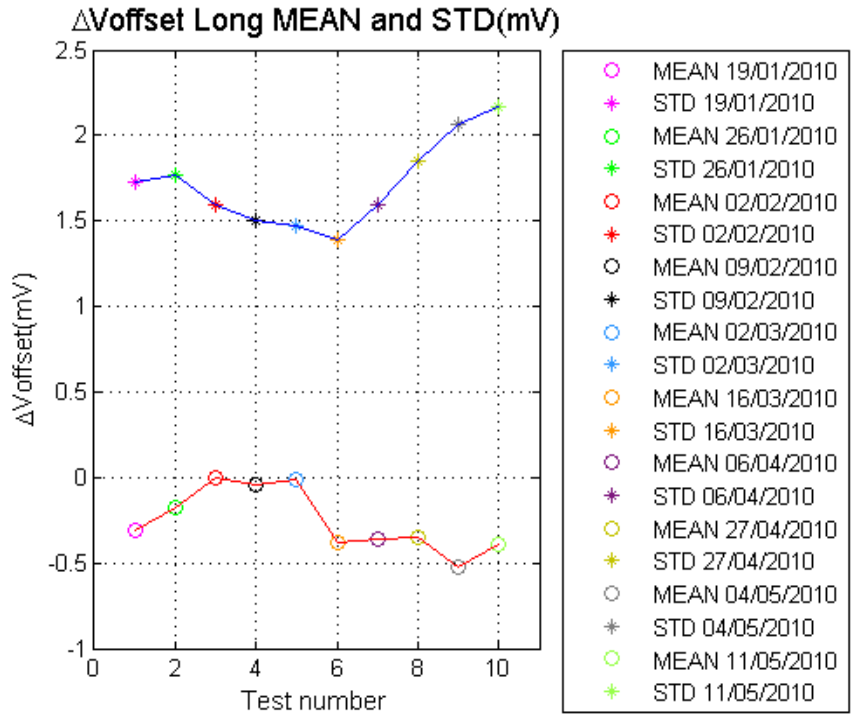

Fig. 7.40 ΔVoffset Long MEAN and STD (mV)

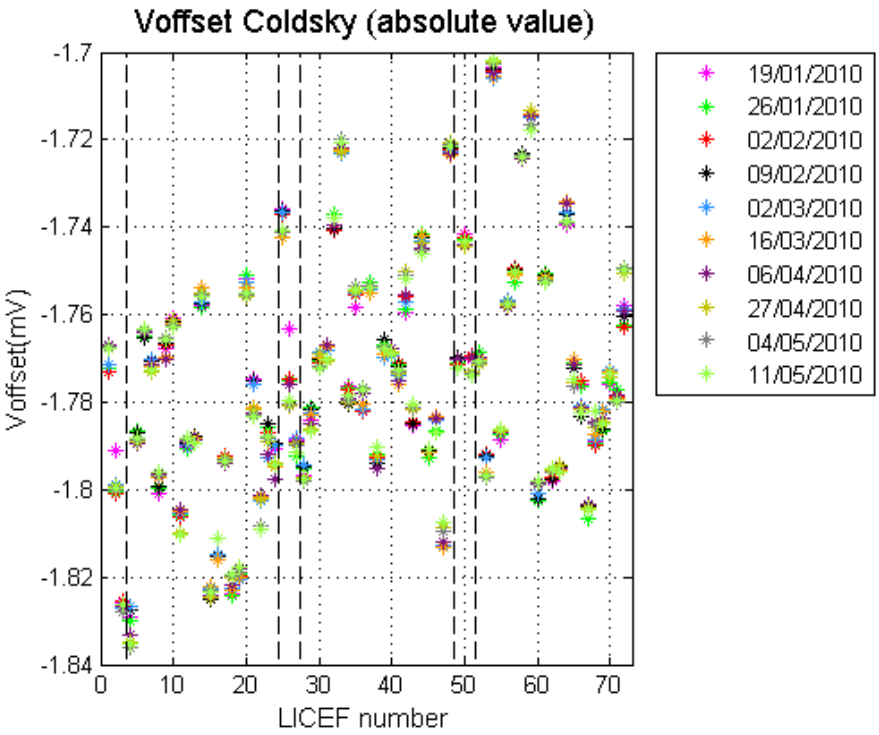

Fig. 7.41 Voffset Coldsky(absolute value)

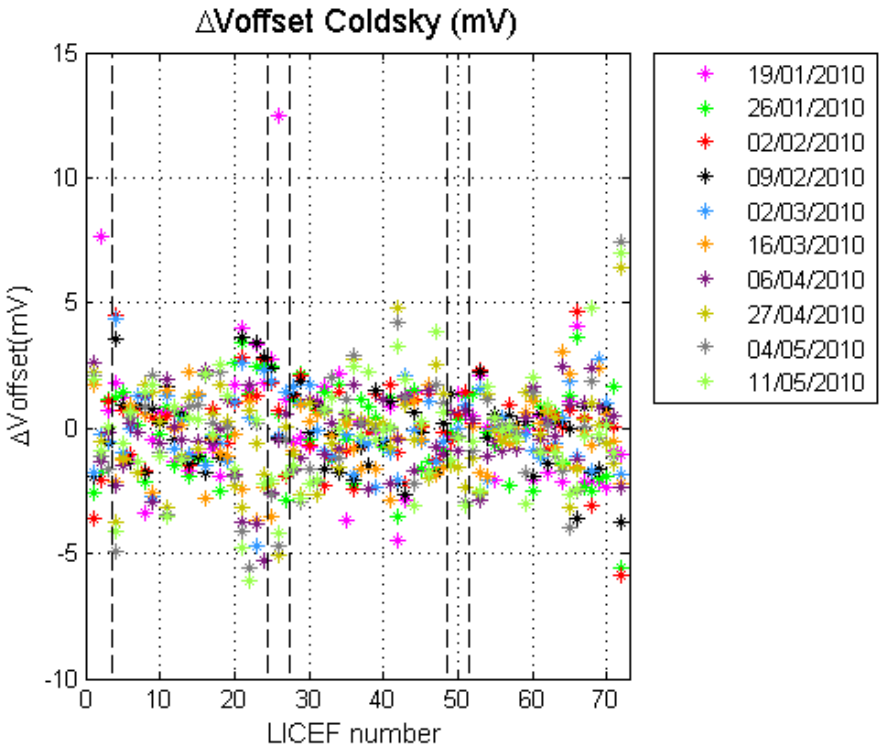

Fig. 7.42 ΔVoffset Coldsky (mV)

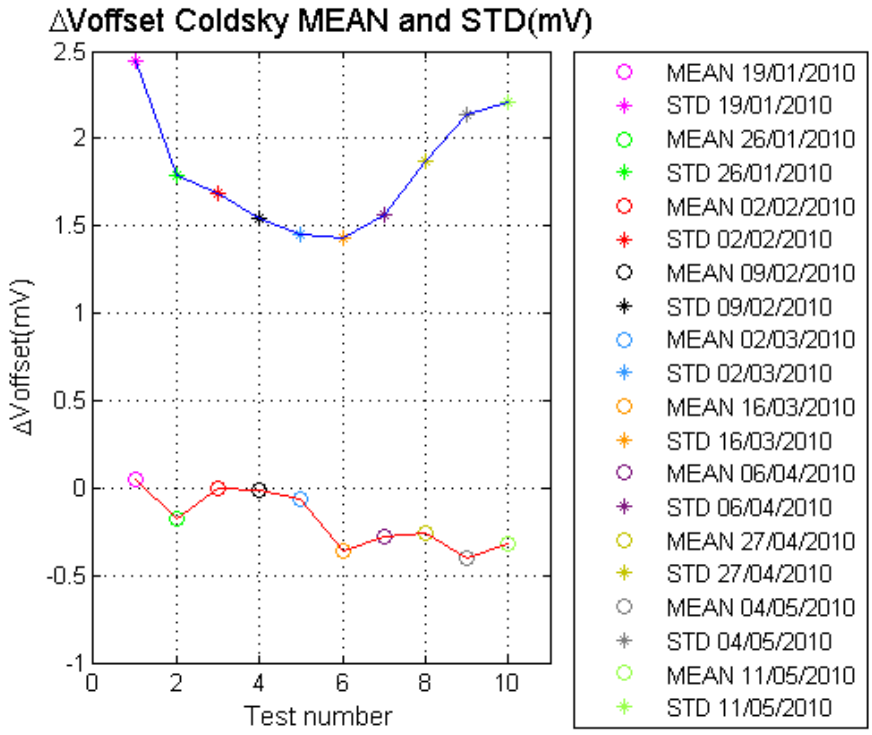

Fig. 7.43 ΔVoffset Coldsky MEAN and STD (mV)

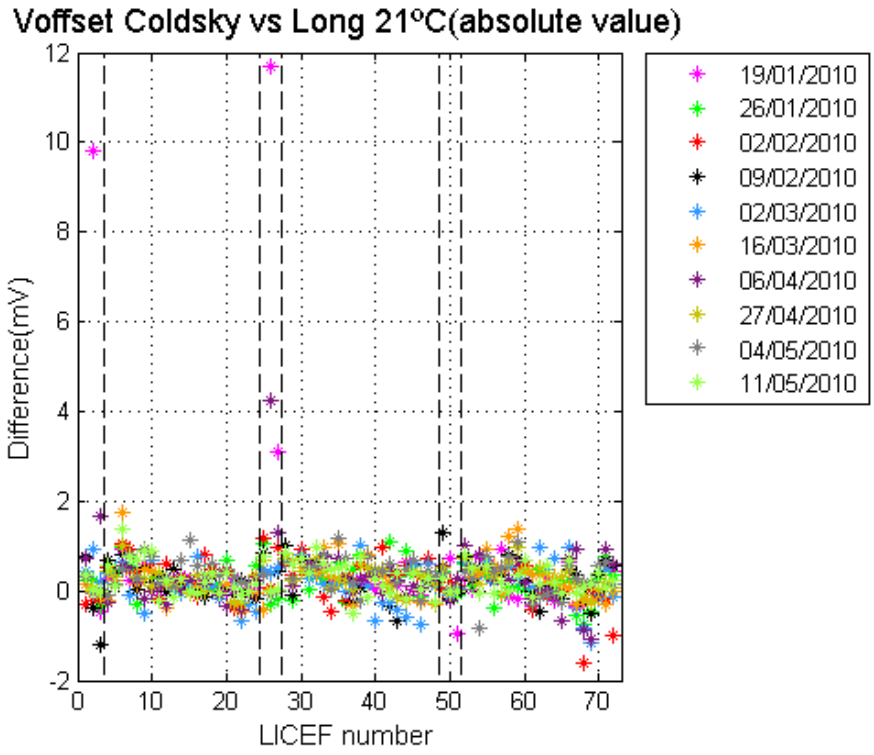

Fig. 7.44 Voffset Coldsky vs Long (mV)

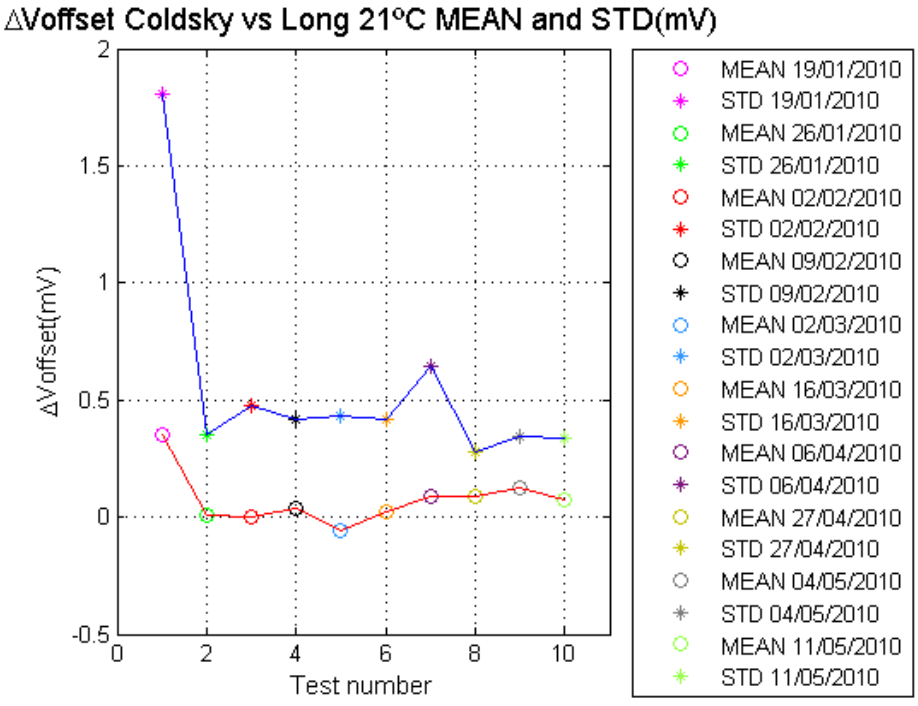

Fig. 7.45 ΔVoffset Coldsky vs Long MEAN and STD(mV)

7.1.8 Case H: Tph stability

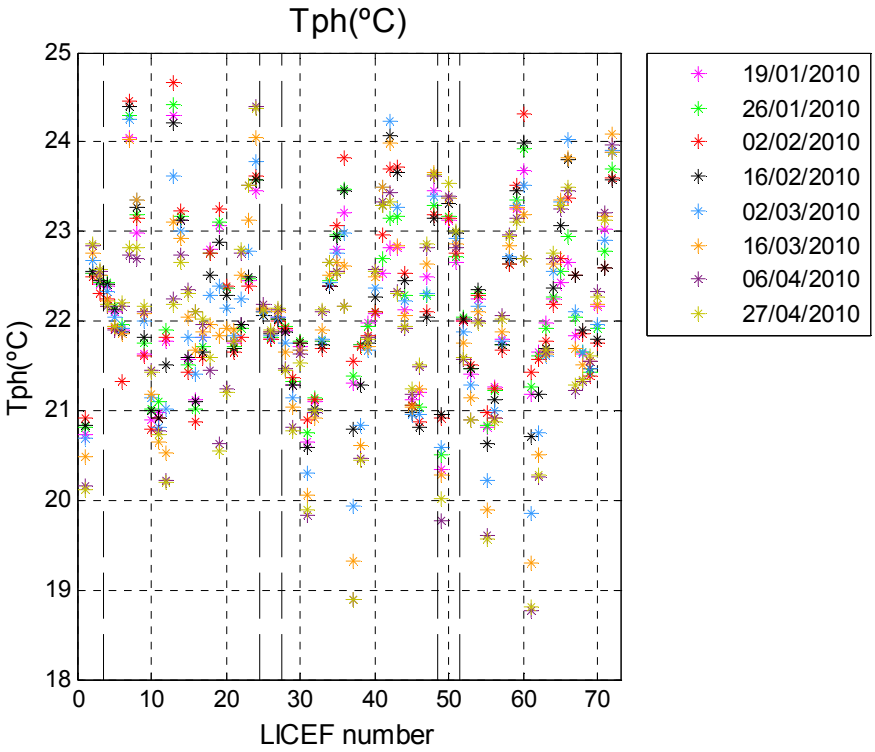

Fig. 7.46 Tph Long (ºC)

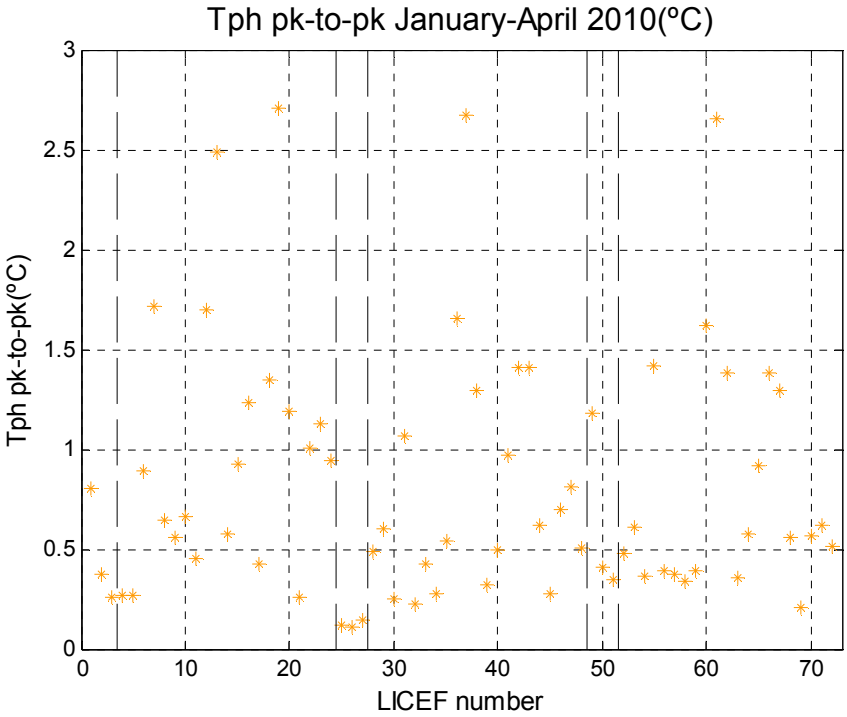

Fig. 7.47 Tph pk-to-pk Long January-April 2010(ºC)

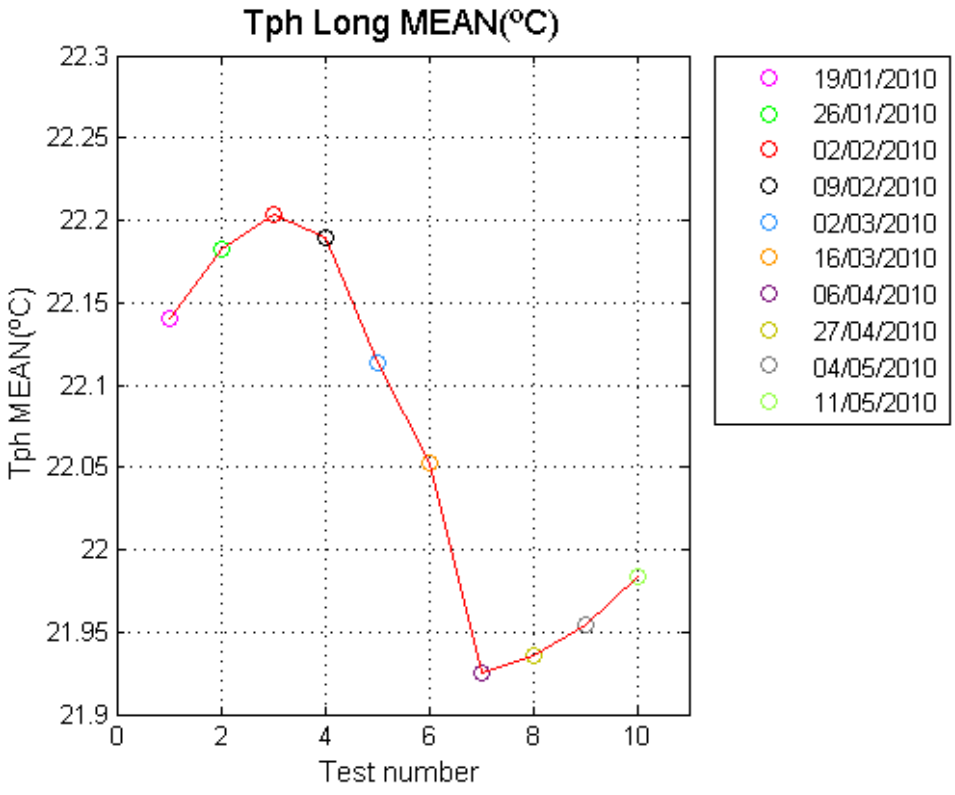

Fig. 7.48 Tph Long MEAN (ºC)

7.1.9 Additional simulations

During simulation it was discovered that the external test on 16/02/2010 was zenithal pointing instead of inertial. This was clearly stated in all plots to identify the outlier.

The following additional simulations were included:

- G1P and G4P MEAN and STD changing zenithal test from 16/02/2010 to 09/02/2010 (inertial). In the case of G1P two new tests from May 2010 were added: 04/05/2010 and 11/05/2010 (External FTR).
- External Gain comparison before/after FTR (Flag Target Response) [9] with data from 04/05/2010 and 11/05/2010.

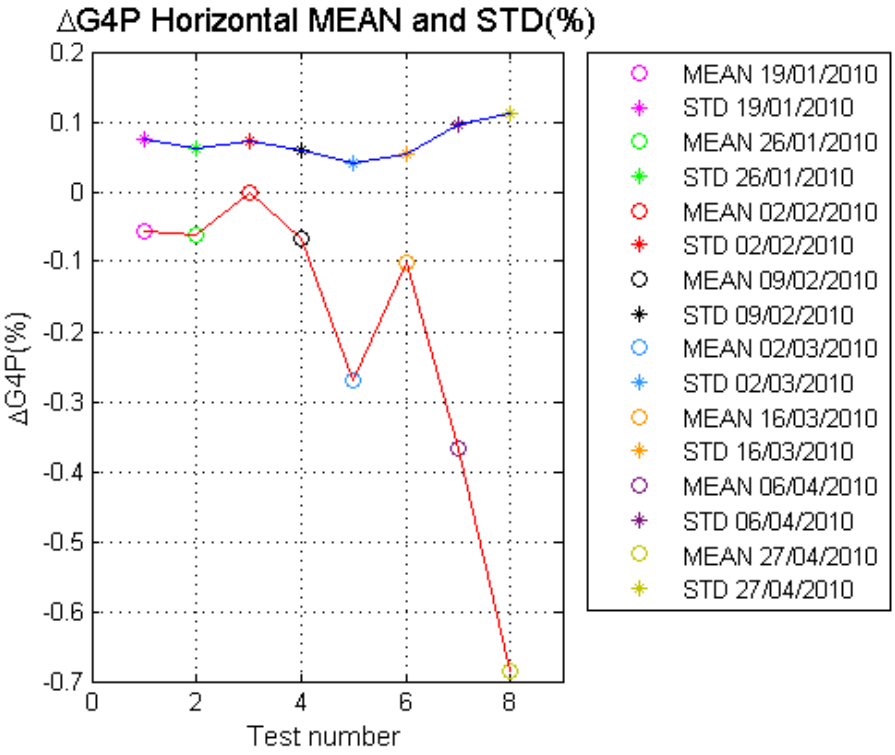

Fig. 7.49 ΔG4P Horizontal MEAN and STD.Mean gain for all PMS. Cal 02/02/2010 calibration taken as reference.

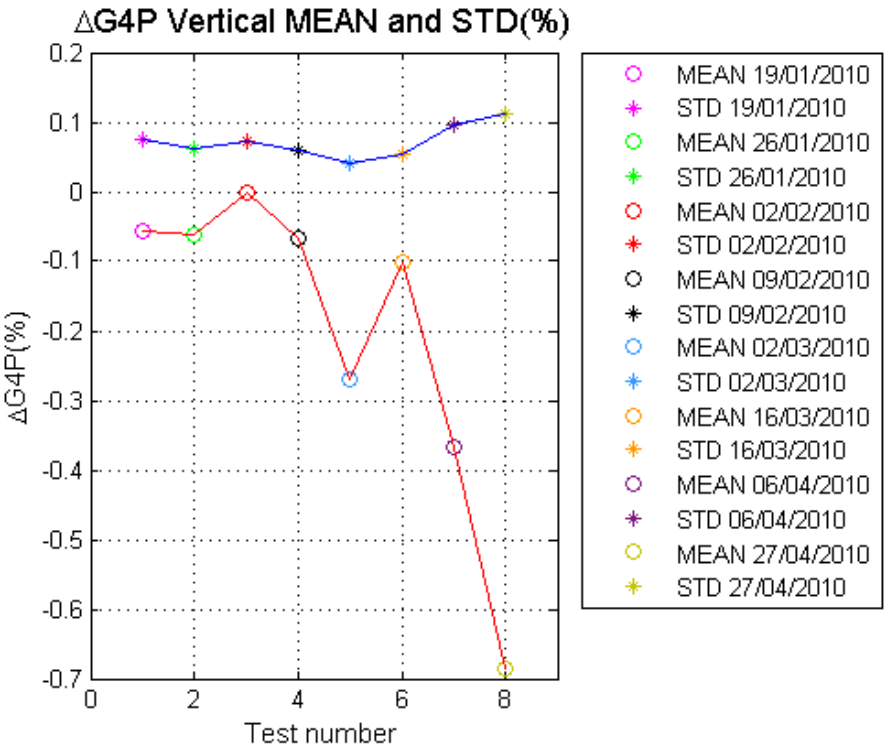

Fig. 7.50 ΔG4P Vertical MEAN and STD (%).Mean gain for all PMS 02/02/2010 calibration taken as reference

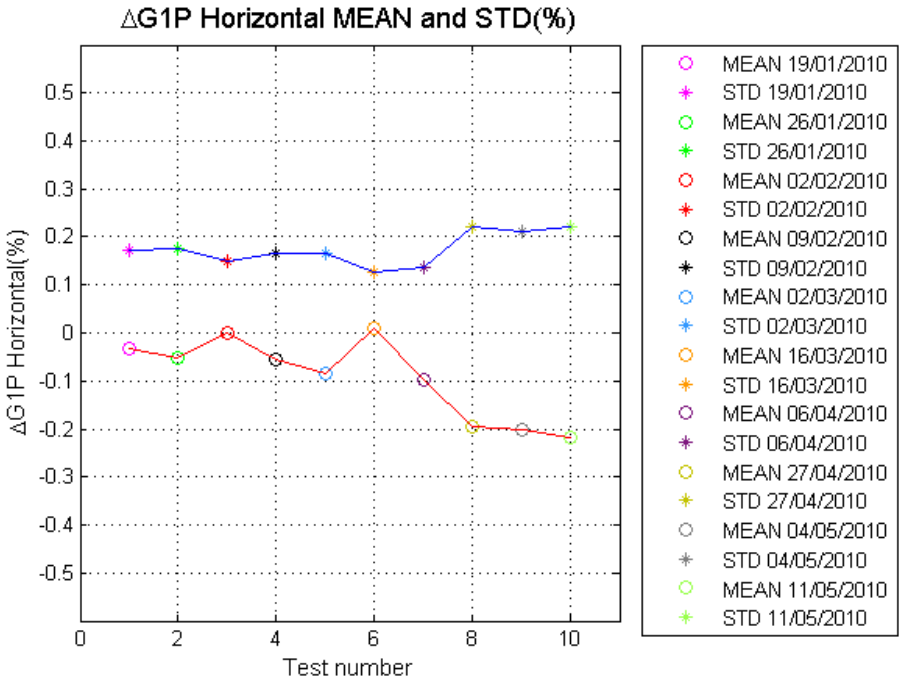

Fig. 7.51 ΔG1P Horizontal MEAN and STD (%).Mean gain for all PMS 02/02/2010 calibration taken as reference

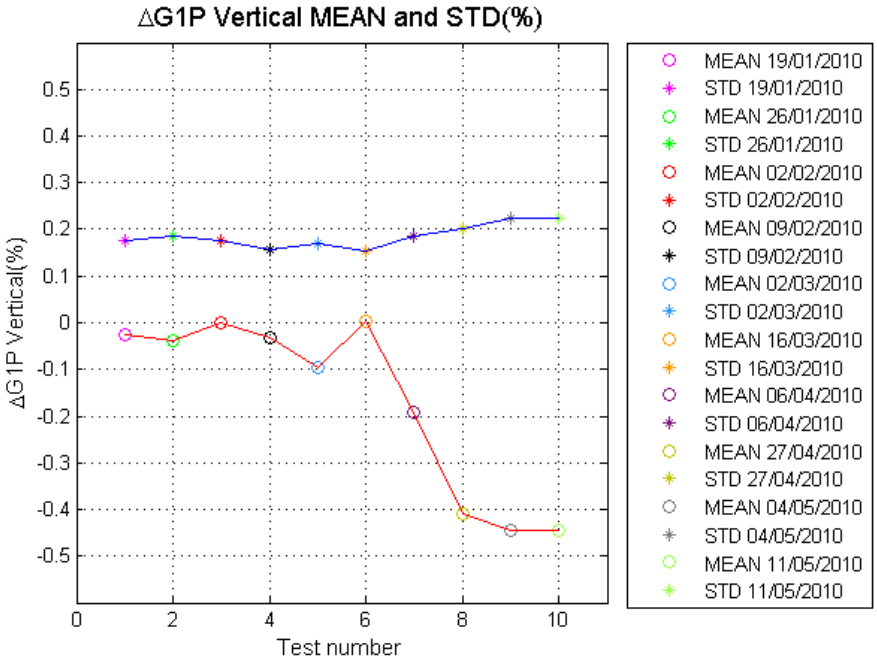

Fig. 7.52 ΔG1P Vertical MEAN and STD (%).Mean gain for all PMS 02/02/2010 calibration taken as reference

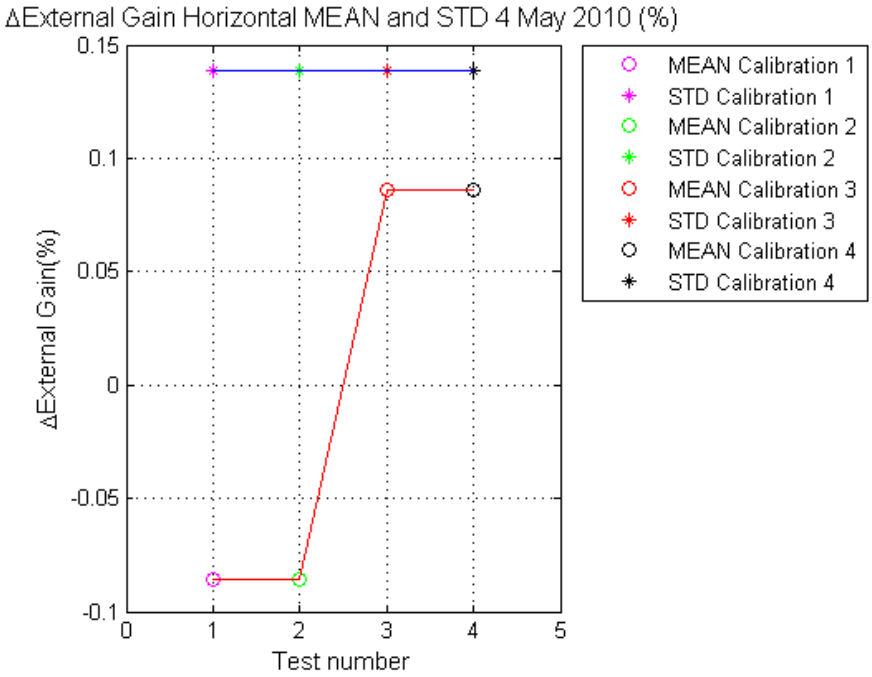

Fig. 7.53 ΔExternal Gain Horizontal MEAN and STD 4 May 2010. Note that the FTR calibration (742 epochs) is performed between PMS cold sky sequences 2 and 3.

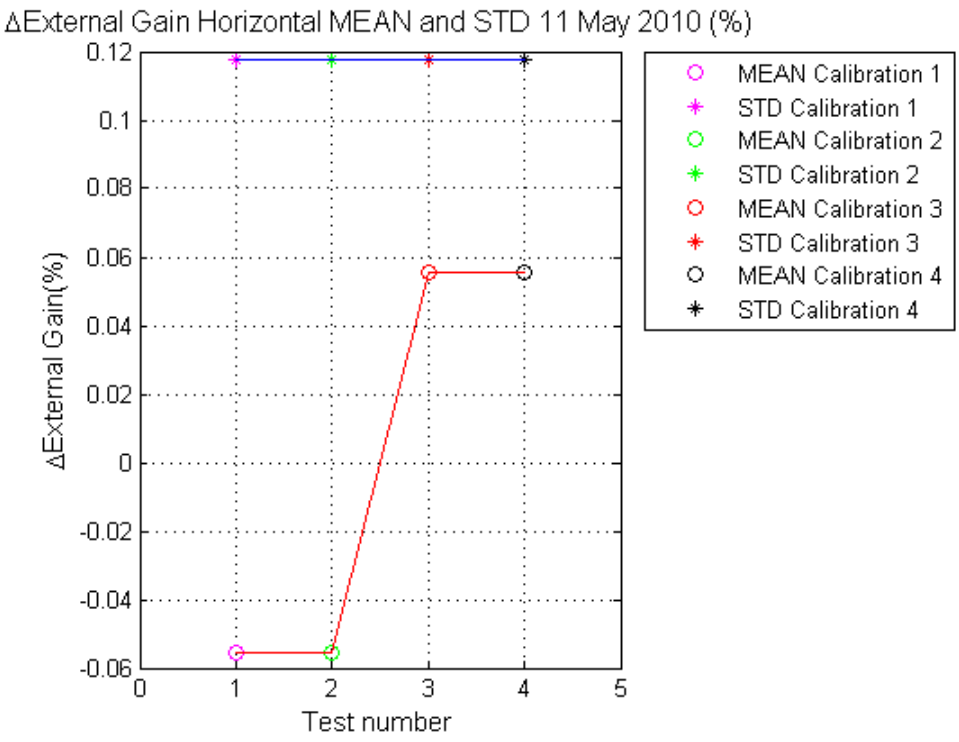

Fig. 7.54 ΔExternal Gain Horizontal MEAN and STD 11 May 2010. Note that the FTR calibration (742 epochs) is performed between PMS cold sky sequences 2 and 3.

7.2 Conclusions

The main conclusions follow:

- **The PMS calibration parameters present a very good stability, well within the expected performance**
- **PMS offset is very stable** and very good agreement is achieved between external and internal (long cal) estimations. Currently PMS offset does not play a significant role in setting the intercalibration period.
- PMS gain presents a very stable and quite predictable behaviour. However **PMS gain drift drives the internal long intercalibration period, to be set to 2 months**. The intercalibration period is mainly contributed by NIR-R drift and/or calibration repeatability.
- **Internal G1P, external G1P, internal G4P and external TR clearly present a correlated behaviour.** This correlation can be assigned, at least partially, to not refreshing sky temperature in each external calibration. The values provided by EADS-CASA for the test on 02/02/2010 have been used for all external calibrations. In the case of PMS cold sky, the mean sky temperature for the 3 NIR in H and 3 NIR in V has been used.
- A preliminary analysis of **the new external NIR-PMS cold sky calibration sequence, shows that residual dynamic thermal effects are present** since the 8 PMS cold sky calibrations within the external calibration on 27/04/10 presents a 0.2% residual drift, after temperature compensation. This change is also present in the two FTR calibrations (Fig*. 7.53* and Fig. *7.54*). This may explain the jump in PMS gain (about 0.15% in H and 0.35% in V) when comparing the OLD and NEW external calibration sequences.

Chapter 8

8 CQC (Calibration Quality Check)

8.1 Program description

CQC (Calibration Quality Check) is a tool implemented in MATLAB to make comparisons between factory and flight data and check the calibration quality.

This tool is basically structured in a main program (CQC) and a sub-function where is possible to fix the maximum error between factory and flight parameters.

First, The Calibration Quality Check computes PMS and FWF (Fringe Washing Function) errors.

Then, all data is saved in separate excel files in two formats:

- Percentage or another necessary magnitude
- Flag format (0 or 1)

Fig. 8.1 shows the output excel file in percentage format and *Fig. 8.2* shows the same results in flag format.

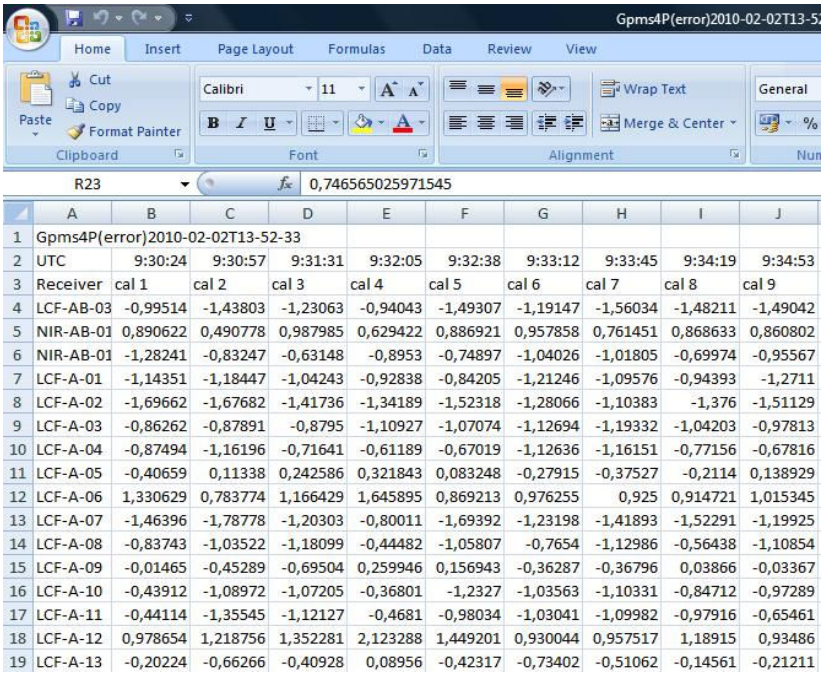

	A	B	C	D	E	F	G	H	I	J
1	Gpms4P(error)2010-02-02T13-52-33									
2	UTC	9:30:24	9:30:57	9:31:31	9:32:05	9:32:38	9:33:12	9:33:45	9:34:19	9:34:53
3	Receiver	cal 1	cal 2	cal 3	cal 4	cal 5	cal 6	cal 7	cal 8	cal 9
4	LCF-AB-03	-0,99514	-1,43803	-1,23063	-0,94043	-1,49307	-1,19147	-1,56034	-1,48211	-1,49042
5	NIR-AB-01	0,890622	0,490778	0,987985	0,629422	0,886921	0,957858	0,761451	0,868633	0,860802
6	NIR-AB-01	-1,28241	-0,83247	-0,63148	-0,8953	-0,74897	-1,04026	-1,01805	-0,69974	-0,95567
7	LCF-A-01	-1,14351	-1,18447	-1,04243	-0,92838	-0,84205	-1,21246	-1,09576	-0,94393	-1,2711
8	LCF-A-02	-1,69662	-1,67682	-1,41736	-1,34189	-1,52318	-1,28066	-1,10383	-1,376	-1,51129
9	LCF-A-03	-0,86262	-0,87891	-0,8795	-1,10927	-1,07074	-1,12694	-1,19332	-1,04203	-0,97813
10	LCF-A-04	-0,87494	-1,16196	-0,71641	-0,61189	-0,67019	-1,12636	-1,16151	-0,77156	-0,67816
11	LCF-A-05	-0,40659	0,11338	0,242586	0,321843	0,083248	-0,27915	-0,37527	-0,2114	0,138929
12	LCF-A-06	1,330629	0,783774	1,166429	1,645895	0,869213	0,976255	0,925	0,914721	1,015345
13	LCF-A-07	-1,46396	-1,78778	-1,20303	-0,80011	-1,69392	-1,23198	-1,41893	-1,52291	-1,19925
14	LCF-A-08	-0,83743	-1,03522	-1,18099	-0,44482	-1,05807	-0,7654	-1,12986	-0,56438	-1,10854
15	LCF-A-09	-0,01465	-0,45289	-0,69504	0,259946	0,156943	-0,36287	-0,36796	0,03866	-0,03367
16	LCF-A-10	-0,43912	-1,08972	-1,07205	-0,36801	-1,2327	-1,03563	-1,10331	-0,84712	-0,97289
17	LCF-A-11	-0,44114	-1,35545	-1,12127	-0,4681	-0,98034	-1,03041	-1,09982	-0,97916	-0,65461
18	LCF-A-12	0,978654	1,218756	1,352281	2,123288	1,449201	0,930044	0,957517	1,18915	0,93486
19	LCF-A-13	-0,20224	-0,66266	-0,40928	0,08956	-0,42317	-0,73402	-0,51062	-0,14561	-0,21211

Fig. 8.1 CQC Excel file (percentage format)

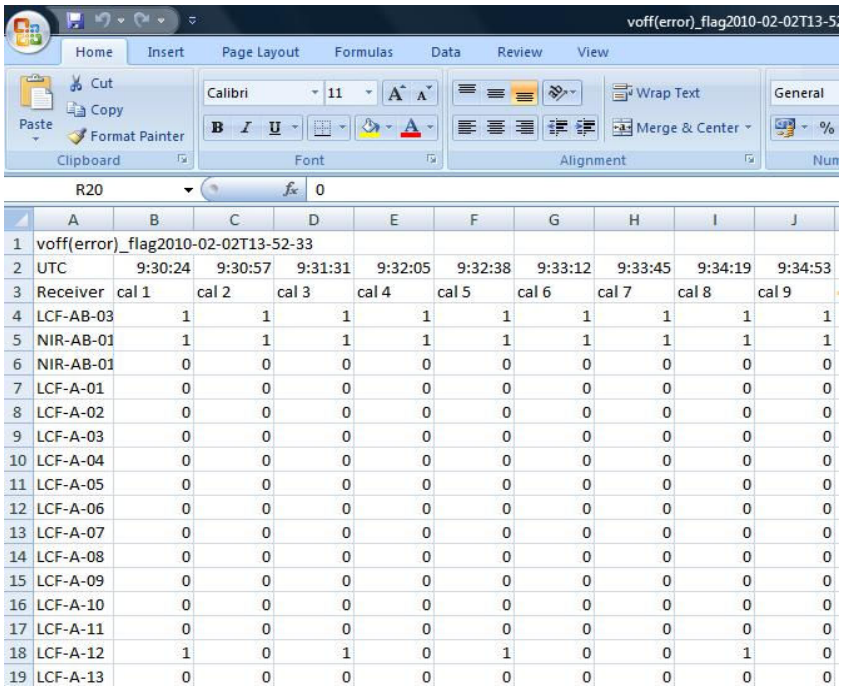

	A	B	C	D	E	F	G	H	I	J
1	voff(error)_flag2010-02-02T13-52-33									
2	UTC	9:30:24	9:30:57	9:31:31	9:32:05	9:32:38	9:33:12	9:33:45	9:34:19	9:34:53
3	Receiver	cal 1	cal 2	cal 3	cal 4	cal 5	cal 6	cal 7	cal 8	cal 9
4	LCF-AB-03	1	1	1	1	1	1	1	1	1
5	NIR-AB-01	1	1	1	1	1	1	1	1	1
6	NIR-AB-01	0	0	0	0	0	0	0	0	0
7	LCF-A-01	0	0	0	0	0	0	0	0	0
8	LCF-A-02	0	0	0	0	0	0	0	0	0
9	LCF-A-03	0	0	0	0	0	0	0	0	0
10	LCF-A-04	0	0	0	0	0	0	0	0	0
11	LCF-A-05	0	0	0	0	0	0	0	0	0
12	LCF-A-06	0	0	0	0	0	0	0	0	0
13	LCF-A-07	0	0	0	0	0	0	0	0	0
14	LCF-A-08	0	0	0	0	0	0	0	0	0
15	LCF-A-09	0	0	0	0	0	0	0	0	0
16	LCF-A-10	0	0	0	0	0	0	0	0	0
17	LCF-A-11	0	0	0	0	0	0	0	0	0
18	LCF-A-12	1	0	1	0	1	0	0	1	0
19	LCF-A-13	0	0	0	0	0	0	0	0	0

Fig. 8.2 CQC Excel file (flag format)

A threshold is chosen to fix if a value is correct or not, for instance, if it is necessary that error between Gain (factory) vs Gain (flight) would be 5%, all bigger values will have a '1' and the other '0' in the output excel file.

Finally, all data is represented in the flag format, being a green square a correct value and a red square an incorrect value (exceeds the threshold). Next figure illustrates an example of this kind of representation:

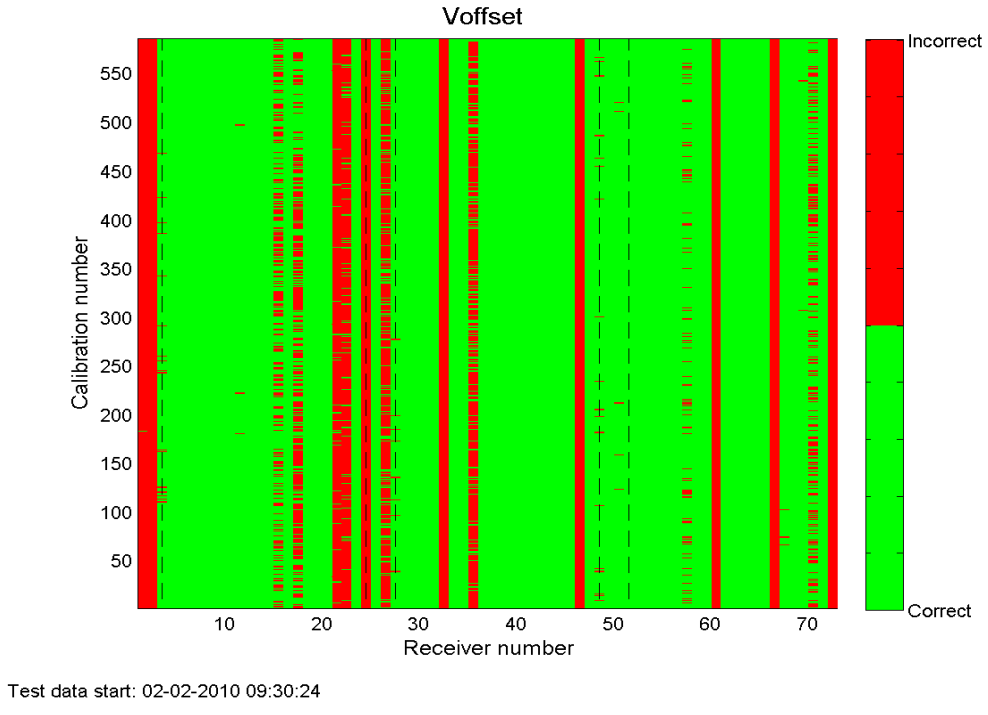

Fig. 8.3 CQC Flag representation

8.2 Results with flight data

CQC has been used to analyze flight data from different months. The calibration quality check shows that the instrument is well-calibrated because most of the parameters has a '0' flag (using an appropriate threshold), and therefore a green square.

G4P	G1P(H)	G1P(V)	Voffset	TR	TR1P(H)	TR1P(V)
5 %	5 %	5 %	7 mV	25 K	25 K	25 K
L	**Gkj**	**A**	**B**			
5 %	5 %	5 %	1 MHz			

Table 8.1 CQC threshold

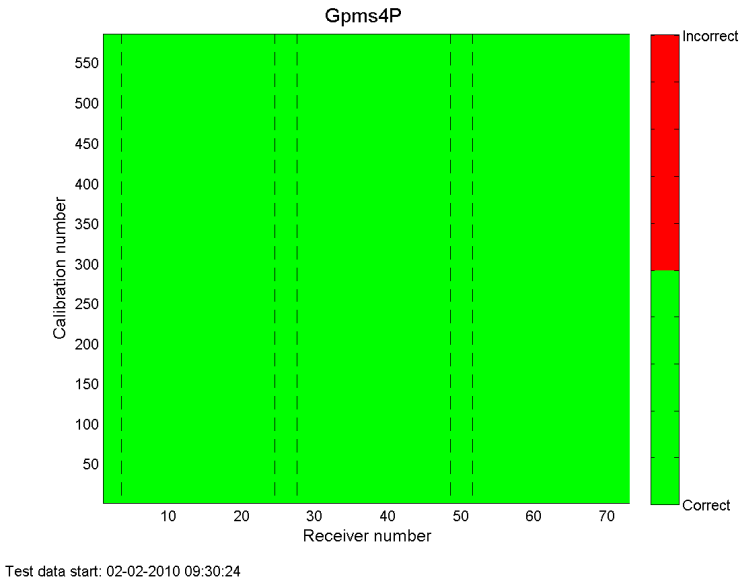

Fig. 8.4 CQC representation - Gain 4P Error <5% Test 02/02/2010

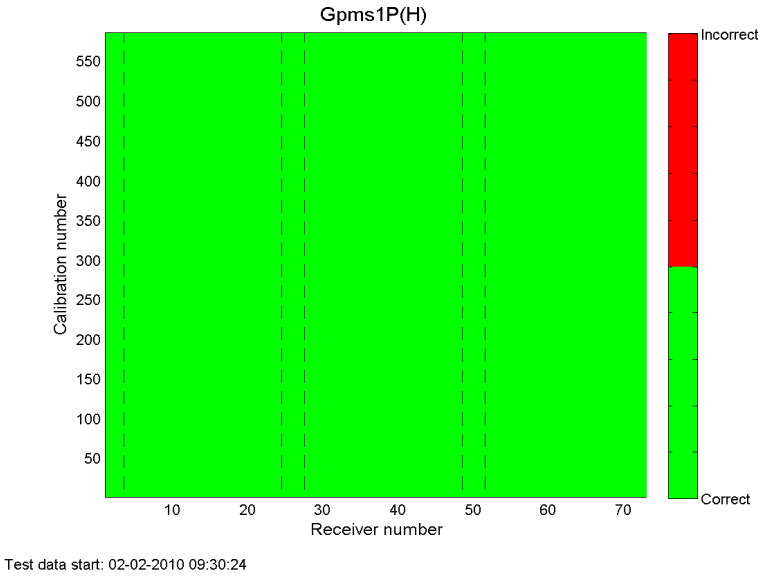

Fig. 8.5 CQC representation - Gain 1P Horizontal Error <5% Test 02/02/2010

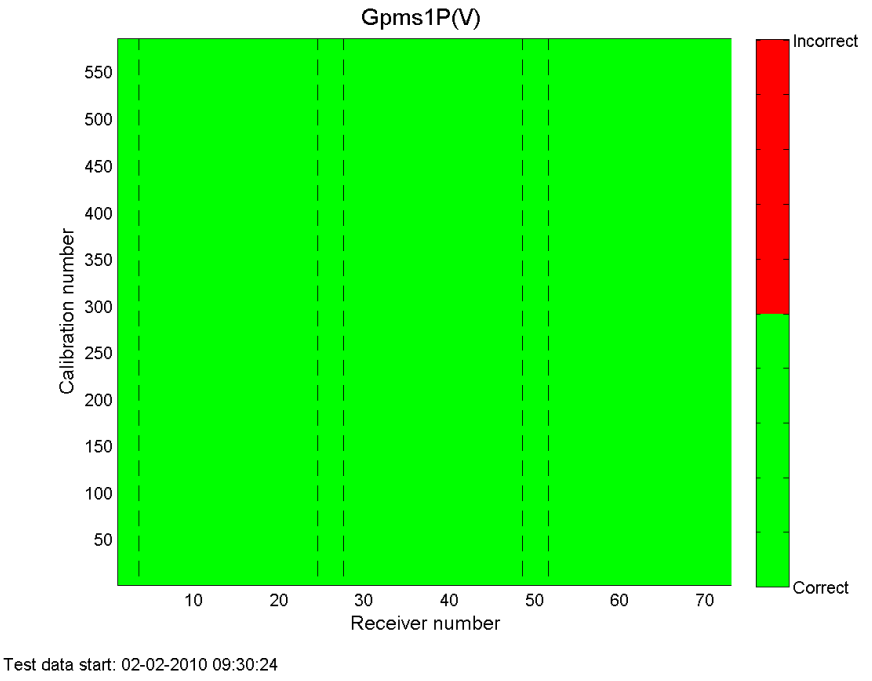

Fig. 8.6 CQC representation - Gain 1P Vertical Error <5% Test 02/02/2010

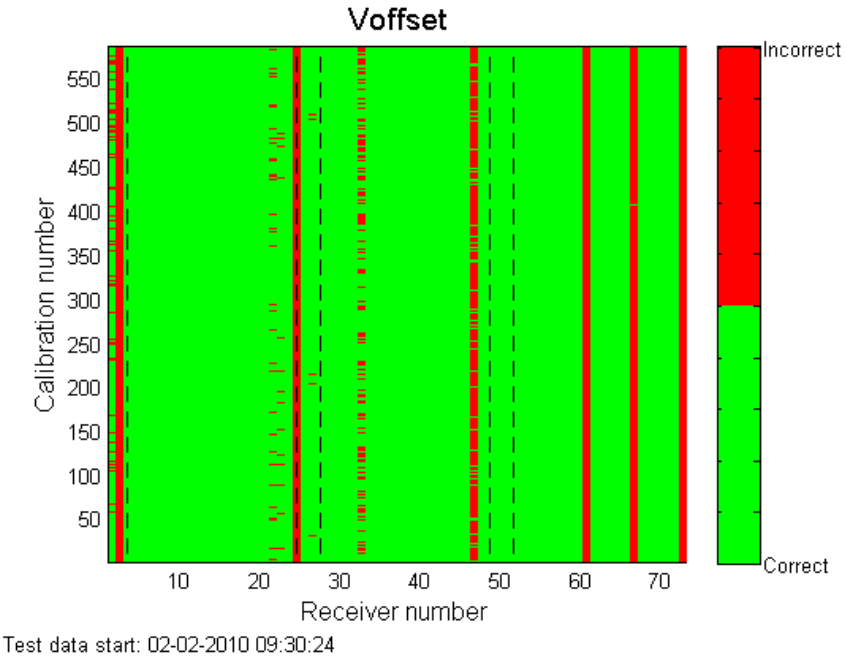

Fig. 8.7 CQC representation - Voffset Error <7 mV Test 02/02/2010

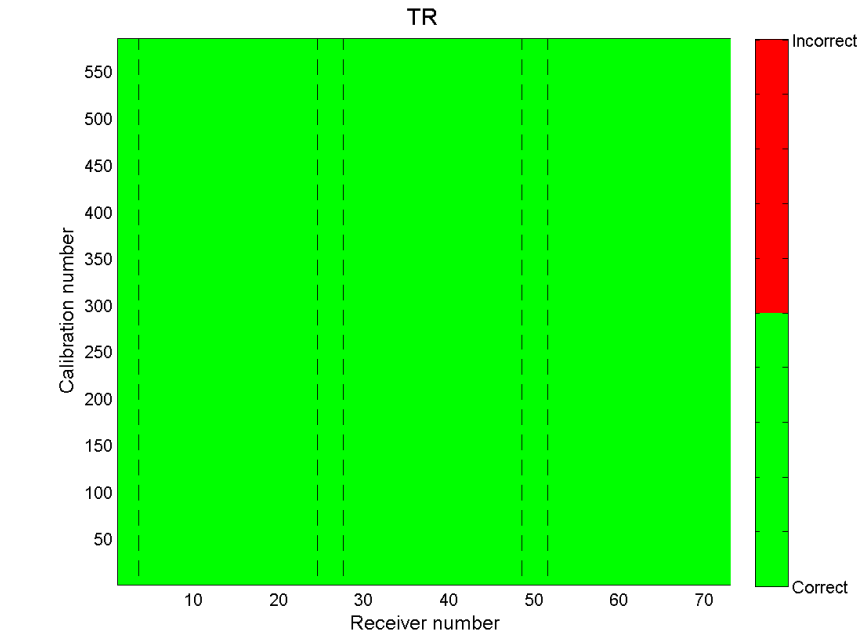

Fig. 8.8 CQC representation – TR 4P Error <25 K Test 02/02/2010

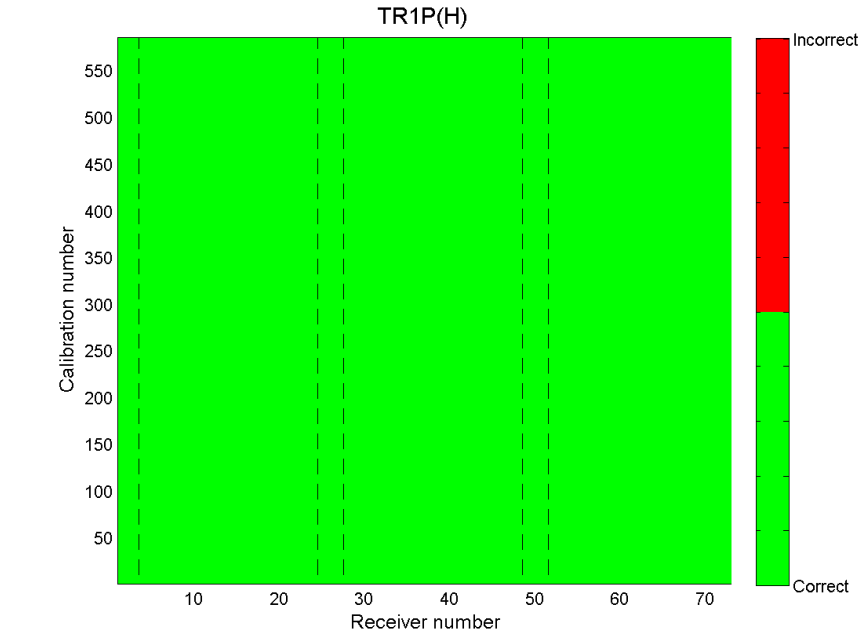

Fig. 8.9 CQC representation – TR 1P (Horizontal) Error <25 K Test 02/02/2010

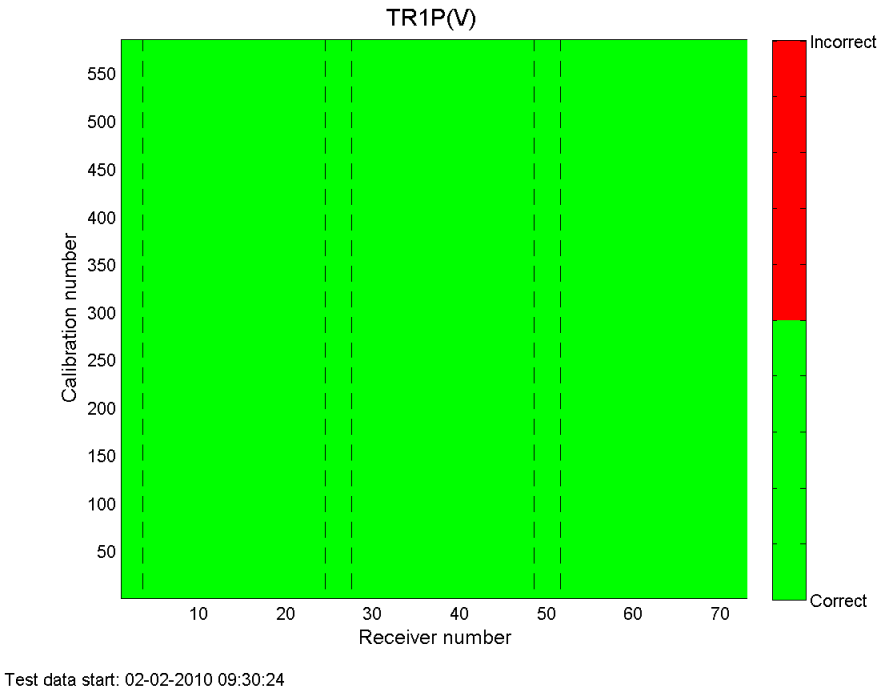

Fig. 8.10 CQC representation – TR 1P (Vertical) Error <25 K Test 02/02/2010

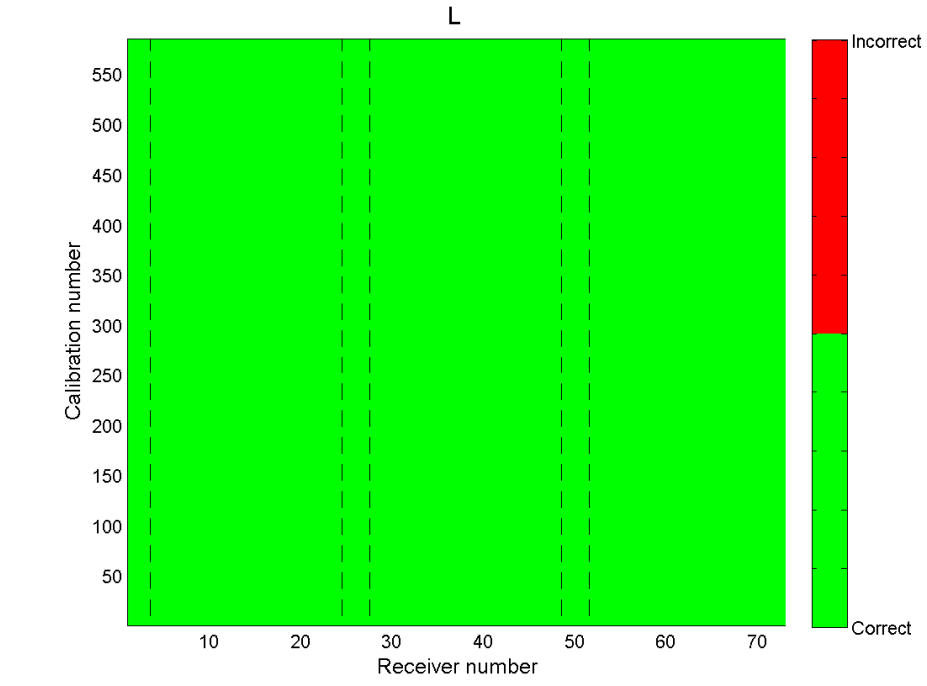

Fig. 8.11 CQC representation - L Error <5% Test 02/02/2010

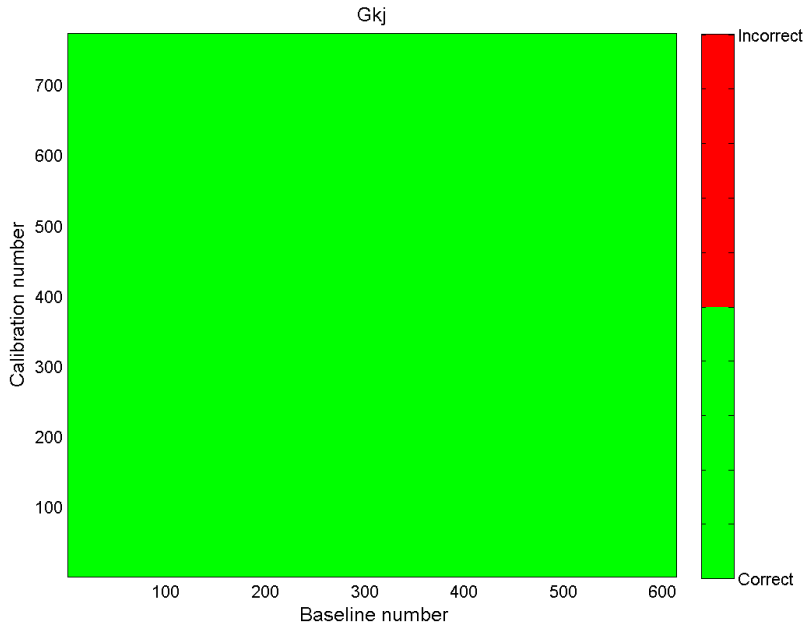

Fig. 8.12 CQC representation Gkj Error <5% Test 02/02/2010

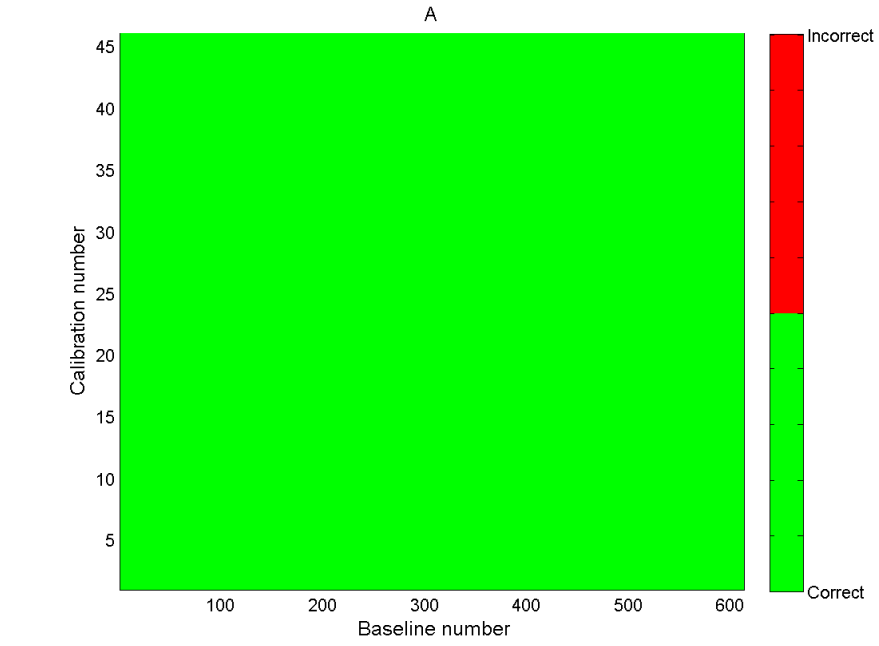

Fig. 8.13 CQC representation - A Error <5% Test 02/02/2010

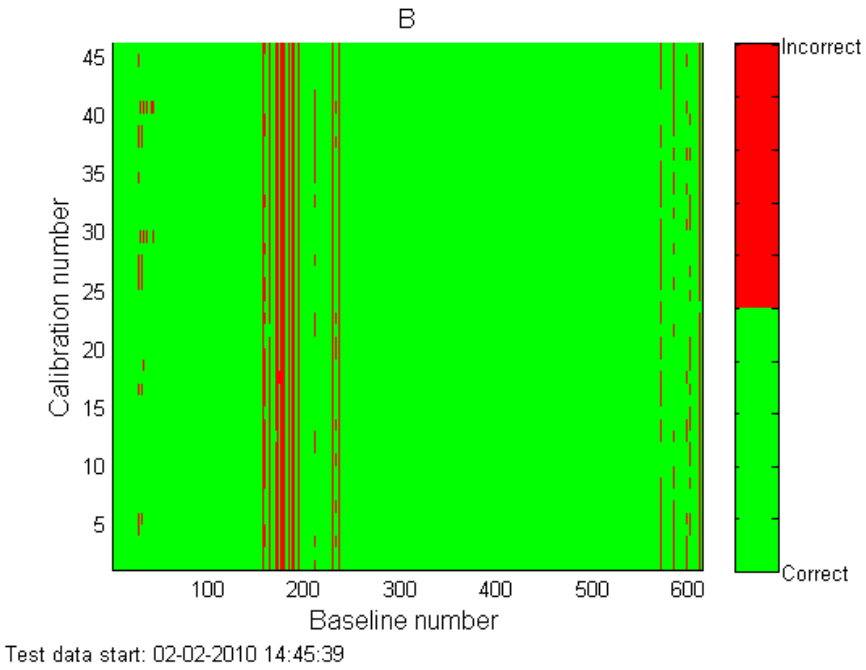

Fig. 8.14 CQC representation – B Error <1 MHz Test 02/02/2010

8.3 Conclusions

- CQC is a powerful tool to analyze the main calibration parameters of the instrument.
- Calibration Quality Check has very clear representation of each parameter being a green square a good result and a red square a bad one.
- This tool has the possibility to fix the reference (for example a flight test) to compare with recent tests.
- All parameters matches very well in flight (Test 02/02/2010) with the results obtained in tests measured before launch.

Chapter 9

9 Conclusions and further work

The main conclusions obtained after carrying out this project are:

- CAS S-parameters validation by means of deep sky views is a powerful tool to analyze the performance of the internal CAS calibration system. It basically works by comparison of PMS gain at VAP/HAP for two different methods: a) Internal CAS calibration and b) one-point PMS sky calibration.

- The proposed approach to compute CAS S-parameters gives a mathematical match between External G1P and internal PMS gain G4P at VAP/HAP and between ground receiver temperature at VAP/HAP. The correction factor are based on physical assignment of the errors at subsystem level, yielding final values:
    - A set of External CAS correction factors to substitute the ground CAS correction factors
    - A set of External Antenna efficiencies: 72 in H and 72 in V

- The computation of the External CAS correction factors is lengthy and not automatic. Since these coefficients are expected to show very low drift, further monitoring of the external correction factor can be done exclusively from the external antenna efficiency by comparison of the internal PMS gain G4P and the external G1P.

- The PMS calibration parameters present a very good stability, well within the expected performance.

- PMS offset is very stable and very good agreement is achieved between external and internal (long cal) estimations. Currently PMS offset does not play a significant role in setting the intercalibration period.

- PMS gain presents a very stable and quite predictable behaviour. However PMS gain drift drives the internal long intercalibration period, to be set to 2 months. The intercalibration period is mainly contributed by NIR-R drift and/or calibration repeatability. It must be pointed out that in this assessment the recently proposed NIR correction in temperature (Tp7 mean orbital temperature) has not been taken into account.

- CQC is a powerful tool to analyze the main calibration parameters of the instrument.

- All parameters matches very well in flight (Test 02/02/2010) with the results obtained in tests measured before launch.

A list of further work is described as follows:

- The limited number of calibrated data sets that have been analyzed so far show a small mean value drift that may have an impact on the mean value of the brightness temperature retrievals. This drift need further assessment to:
  - Assess the feasibility to develop additional correction techniques.
  - Systematic and periodic analysis of all calibrations to check for correlation between instrument and physical parameter drifts/changes.

- Improve MTS external calibration accuracy by computing the sky temperature during external calibration. In addition the impact on calibration repeatability of external sources (sun, earth, moon,…) should be assessed.

- Assessment on the slight drift/repeatability differences between the external PMS gain G1P and the internal PMS gain G4P.

Bibliography

[1] European Space Agency web: http://www.esa.int/esaLP/LPsmos.html

[2] Eurorockot Launch Service Provider web: http://www.eurockot.com/alist.asp?cnt=20040811&main=3&subm=97

[3] Remote sensing laboratory group web: http://www.tsc.upc.edu/rslab/index.php?option=com_content&view=article&id=79&Itemid=165

[4] Barcelona Expert Centre on Radiometric Calibration and Ocean Salinity web: http://www.smos-bec.icm.csic.es

[5] McMullan, K.D., Brown, M.A.; Martín-Neira, M.; Rits, W.; Ekholm, S.; Martí, J., Lemanczyk, J., "SMOS: The payload", Geoscience and Remote Sensing, vol. 46, Pages: 594-605, IEEE Transactions March 2008.

[6] González-Gambau, V.; "Caracterización y calibración de radiómetros interferométricos por Síntesis de Apertura", Master Thesis, Barcelona June 2006, Universitat Politècnica de Catalunya.

[7] Camps, A.; Corbella, I.; Duffo, N.; "Temas de formación SMOS", Training course for INDRA Espacio, San Fernando de Henares March 2006, Universitat Politècnica de Catalunya.

[8] Brown, M.A.; Torres, F.; Corbella, I.; Colliander, A.; "SMOS Calibration", Geoscience and Remote Sensing, vol. 46, Pages: 646-658, IEEE Transactions March 2008.

[9] Corbella, I.; Torres, F.; Duffo, N.; Camps, A.; Vall-llossera, M.; González-Gambau, V.; "MIRAS In-Orbit Calibration", Geoscience and Remote Sensing Shymposium, IGARSS 2007, IEEE International, Universitat Politécnica de Catalunya.

[10] González-Haro, C.; "Power detector of second order correction stydy applied to MIRAS/SMOS mission", MERIT Master Thesis, Barcelona, February 2010, Universitat Politécnica de Catalunya.

[11] Torres, F.; González-Gambau, V.; González-Haro, C.; "One point calibration in interferometric radiometers devoted to Earth observation", SPIE Europe Remote Sensing 2008, Barcelona, Universitat Politècnica de Catalunya, SMOS Barcelona Expert Centre.

[12] Torres, F;Corbella, I.;Duffo, N.;González-Gambau,V;Durán,I;Pablos,M;Martín-Neira,M.;"One point calibration in interferometric radiometers: MIRAS/SMOS preliminary results", European Space Agency, European Space Research and Technology Centre (ESTEC), The Netherlands

[13] Internal technical note: SO-TN-UPC-PLM-0076 IOCP summary of equations Phase C/D v3.0 17/09/09.

[14] Internal technical note: SO-TN-UPC-PLM-0069 Calibration consistency tool v1.13 12/03/09.

[15] Internal technical note: SO-TN-UPC-PLM-0007 EB v7_3 Error budget map to SRD (PRS) 23/03/07

[16] Internal technical note: SO-TN-UPC-PLM-0019 v1.5. SMOS in-orbit calibration plan. Phase C-D. 17th of January 2007.

ANNEX I: CAS coefficients error

In each page: CAS in-orbit validation results

TOP:	without CAS correction factor
MIDDLE:	with ON-GROUND CAS correction factor (consistency tool)
BOTTOM:	with External CAS correction factor

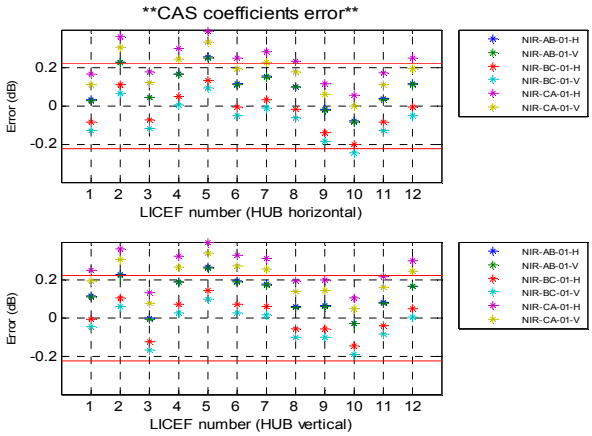

Figure 1 CAS coefficients error in the HUB (without using CAS S-parameter correction)

Representation 1: LICEFs to calibrate on the x-axis

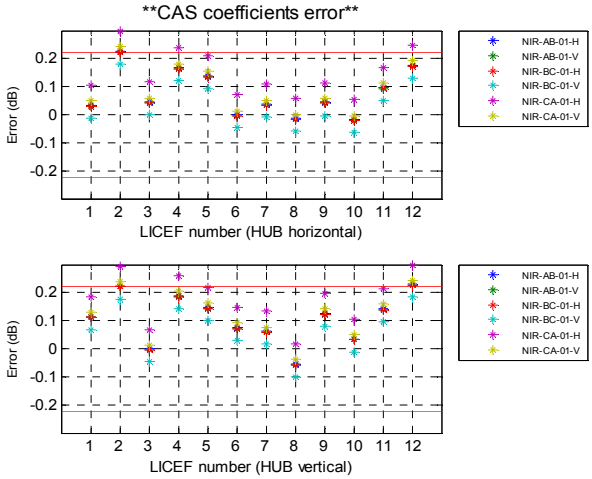

Figure 2 CAS coefficients error in the HUB (using ON-GROUND CAS S-parameter correction)

Representation 1: LICEFs to calibrate on the x-axis

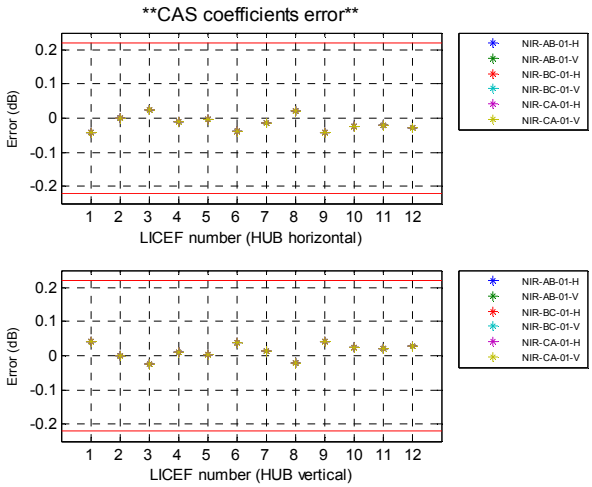

Figure 3 CAS coefficients error in the HUB (using External CAS S-parameter correction)

Representation 1: LICEFs to calibrate on the x-axis

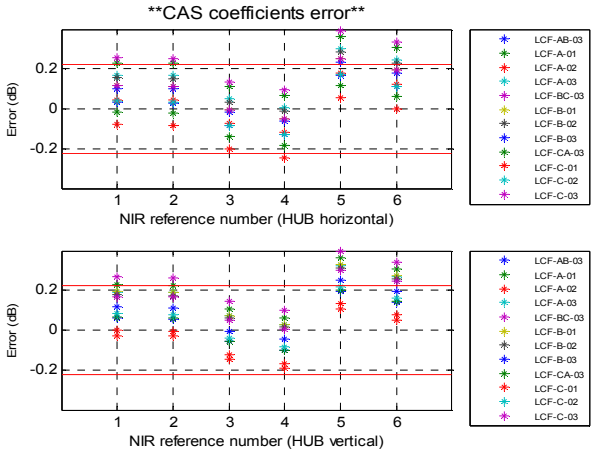

Figure 4 CAS coefficients error in the HUB (without using CAS S-parameter correction)

Representation 2: References on the x-axis

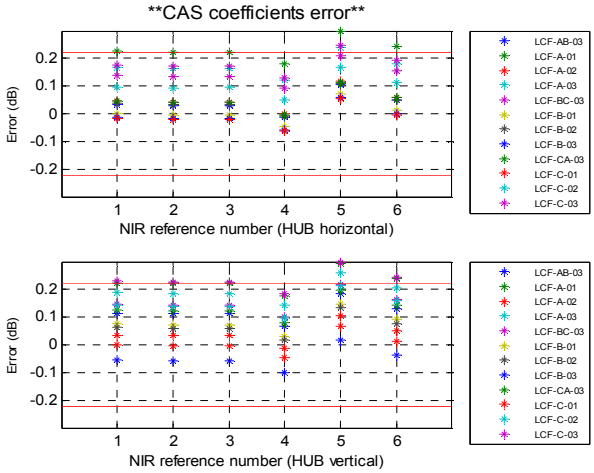

Figure 5 CAS coefficients error in the HUB (using ON-GROUND CAS S-parameter correction)

Representation 2: References on the x-axis

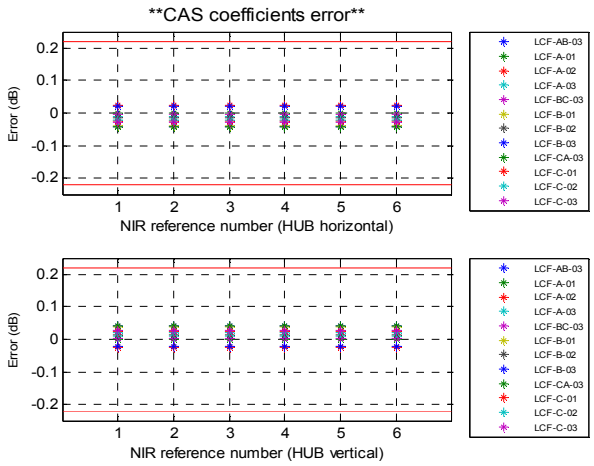

Figure 6 CAS coefficients error in the HUB (using External CAS S-parameter correction)

Representation 2: References on the x-axis

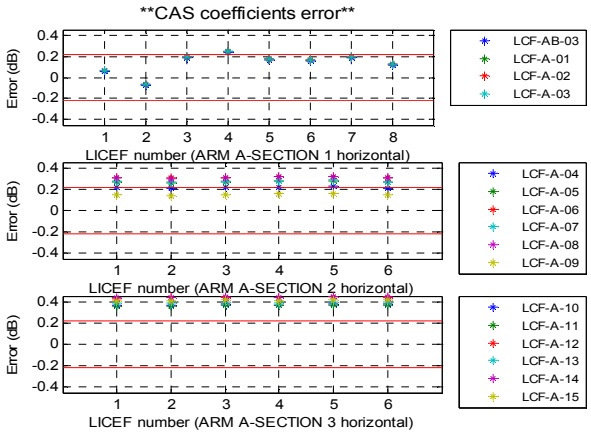

Figure 7 CAS coefficients error in ARM A –horizontal polarization (without using CAS S-parameter correction)

Representation 1: LICEFs to calibrate on the x-axis

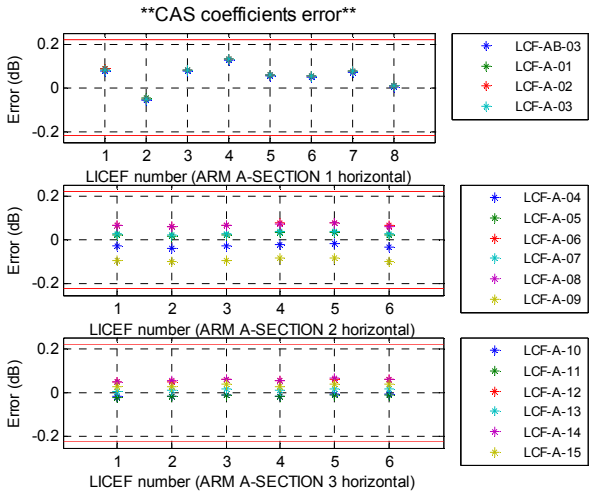

Figure 8 CAS coefficients error in ARM A - horizontal polarization(using ON- GROUND CAS S-parameter correction)

Representation 1: LICEFs to calibrate on the x-axis

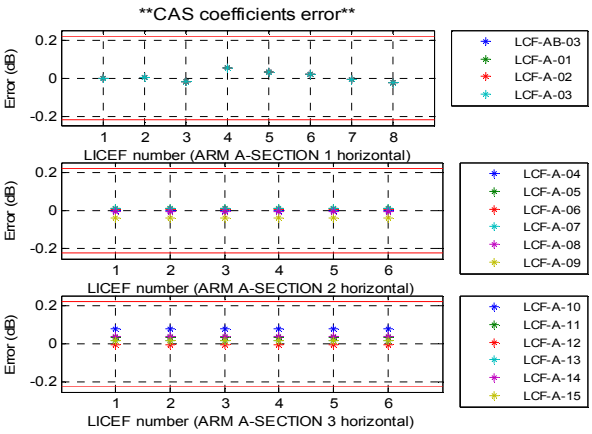

Figure 9 CAS coefficients error in ARM A - horizontal polarization(using External CAS S-parameter correction)

Representation 1: LICEFs to calibrate on the x-axis

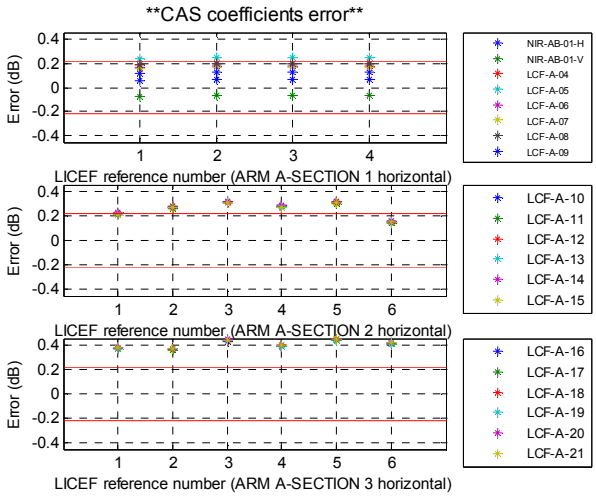

Figure 10 CAS coefficients error in ARM A – horizontal polarization (without using CAS S-parameter correction)

Representation 2: References on the x-axis

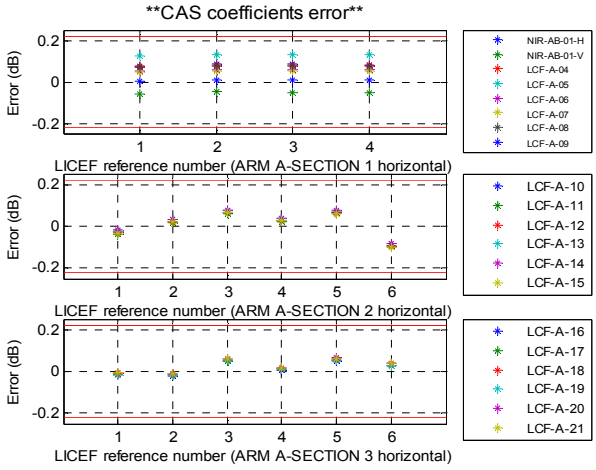

Figure 11 CAS coefficients error in ARM A - horizontal polarization(using ON-GROUND CAS S-parameter correction)

Representation 2: References on the x-axis

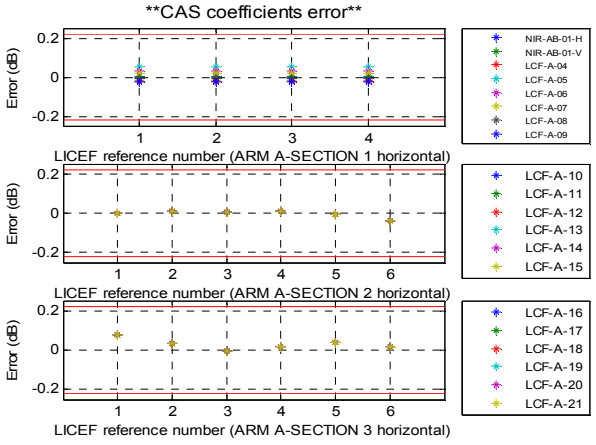

Figure 12 CAS coefficients error in ARM A - horizontal polarization(using External CAS S-parameter correction)

Representation 2: References on the x-axis

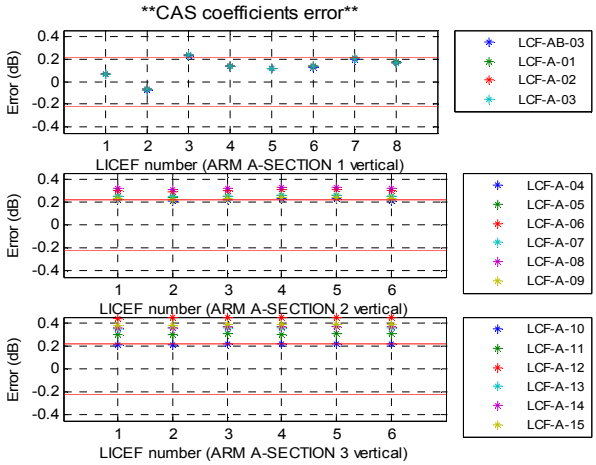

Figure 13 CAS coefficients error in ARM A – vertical polarization (without using CAS S-parameter correction)

Representation 1: LICEFs to calibrate on the x-axis

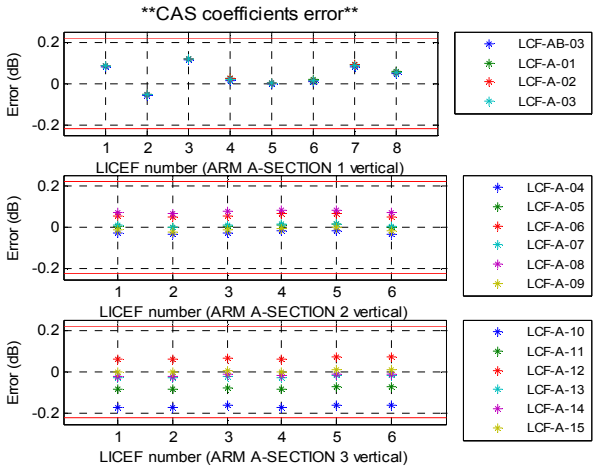

Figure 14 CAS coefficients error in ARM A – vertical polarization (using ON-GROUND CAS S-parameter correction)

Representation 1: LICEFs to calibrate on the x-axis

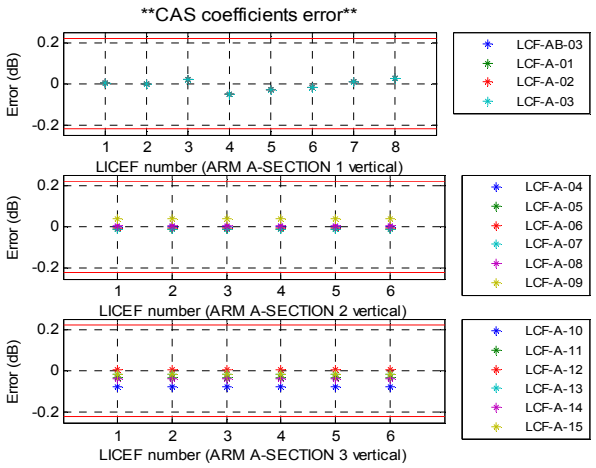

Figure 15 CAS coefficients error in ARM A – vertical polarization (using External CAS S-parameter correction)

Representation 1: LICEFs to calibrate on the x-axis

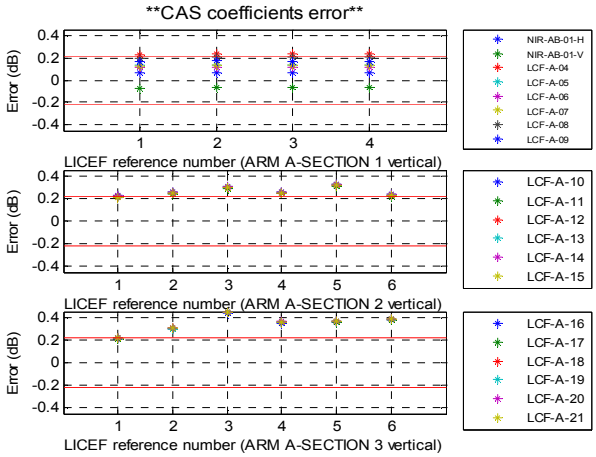

Figure 16 CAS coefficients error in ARM A – vertical polarization (without using CAS S-parameter correction)

Representation 2: References on the x-axis

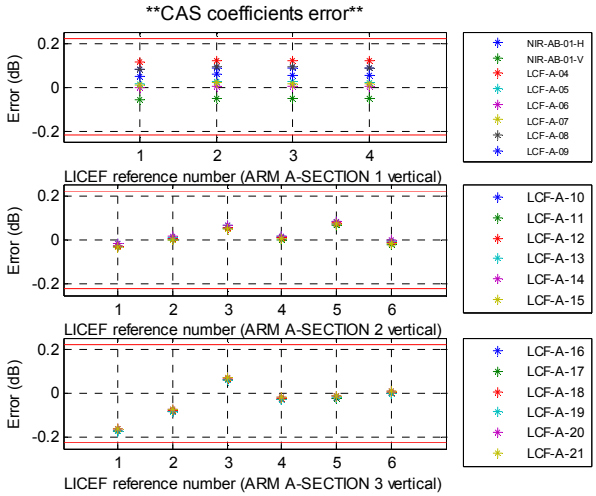

Figure 17 CAS coefficients error in ARM A – vertical polarization (using ON-GROUND CAS S-parameter correction)

Representation 2: References on the x-axis

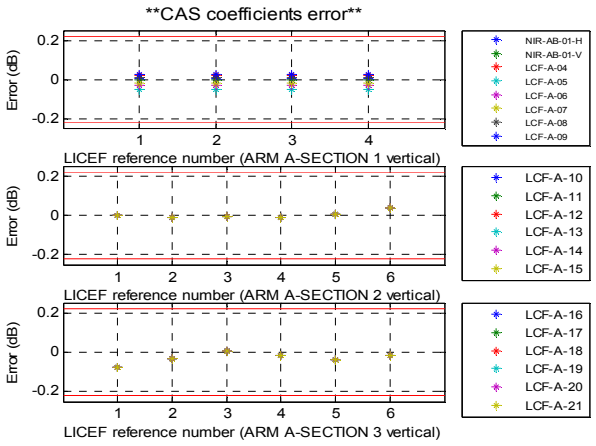

Figure 18 CAS coefficients error in ARM A – vertical polarization (using External CAS S-parameter correction)

Representation 2: References on the x-axis

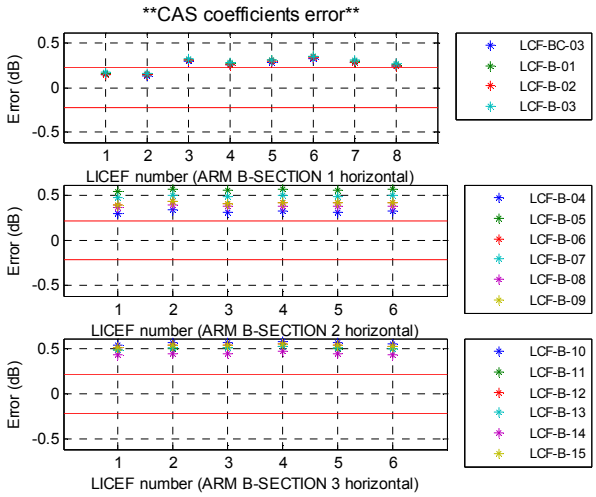

Figure 19 CAS coefficients error in ARM B – horizontal polarization (without using CAS S-parameter correction)

Representation 1: LICEFs to calibrate on the x-axis

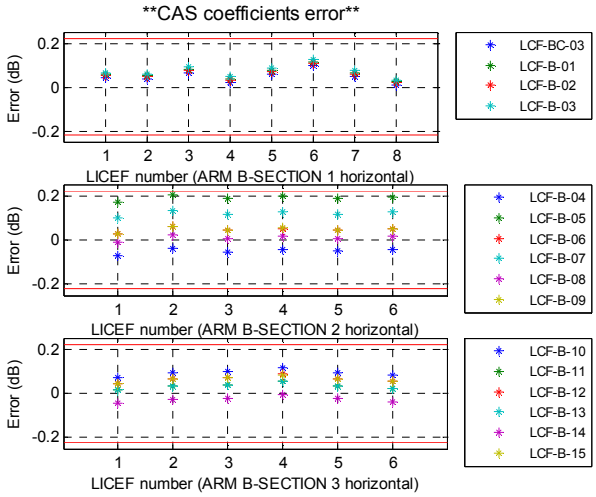

Figure 20 CAS coefficients error in ARM B – horizontal polarization (using ON-GROUND CAS S-parameter correction)

Representation 1: LICEFs to calibrate on the x-axis

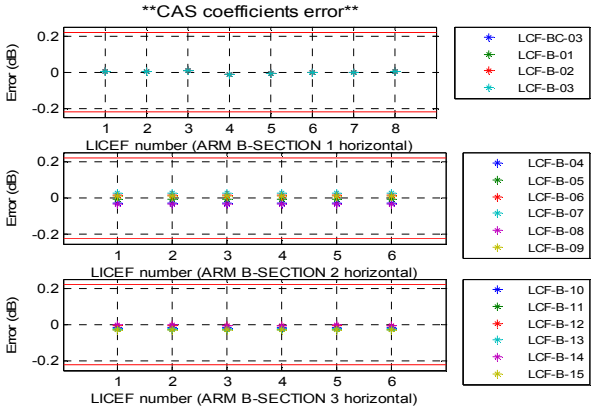

Figure 21 CAS coefficients error in ARM B – horizontal polarization (using External CAS S-parameter correction)

Representation 1: LICEFs to calibrate on the x-axis

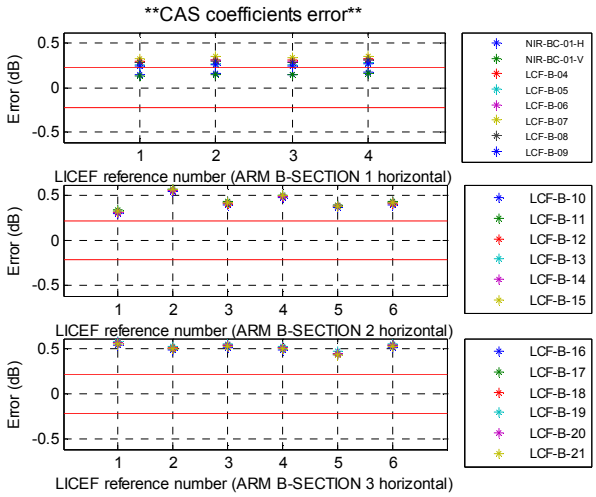

Figure 22 CAS coefficients error in ARM B – horizontal polarization (without using CAS S-parameter correction)

Representation 2: References on the x-axis

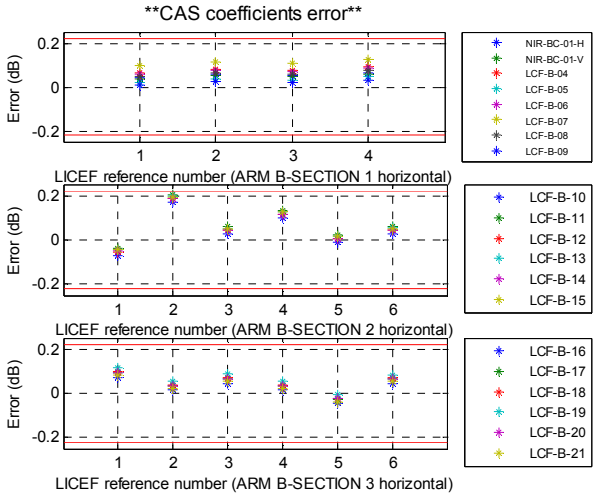

Figure 23 CAS coefficients error in ARM B – horizontal polarization (using ON-GROUND CAS S-parameter correction)

Representation 2: References on the x-axis

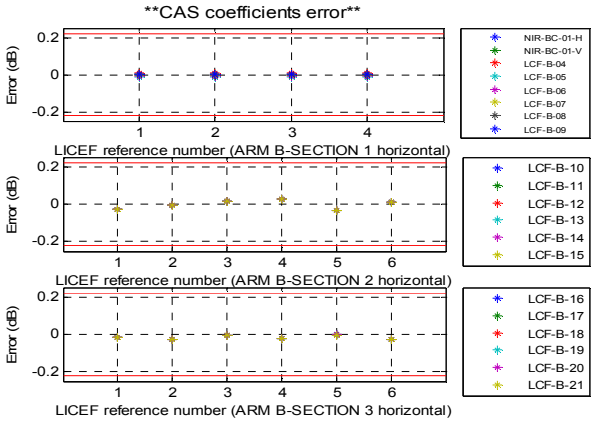

Figure 24 CAS coefficients error in ARM B – horizontal polarization (using External CAS S-parameter correction)

Representation 2: References on the x-axis

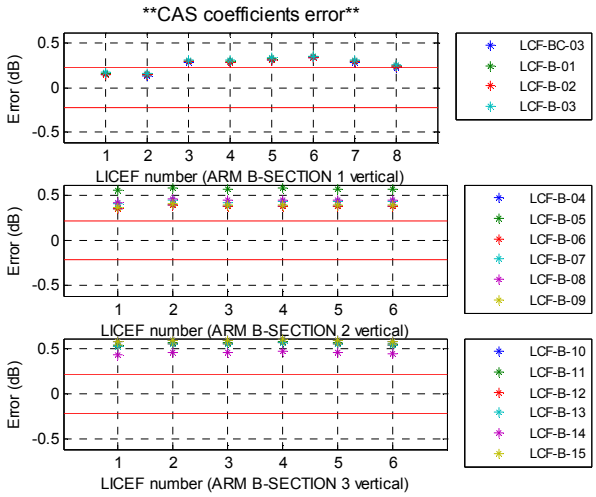

Figure 25 CAS coefficients error in ARM B – vertical polarization (without using CAS S-parameter correction)

Representation 1: LICEFs to calibrate on the x-axis

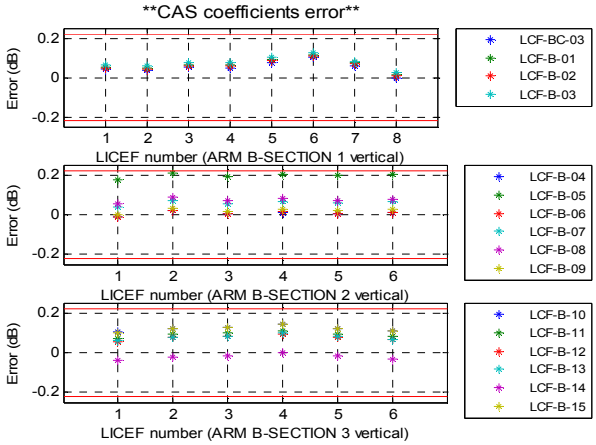

Figure 26 CAS coefficients error in ARM B – vertical polarization (using ON-GROUND CAS S-parameter correction)

Representation 1: LICEFs to calibrate on the x-axis

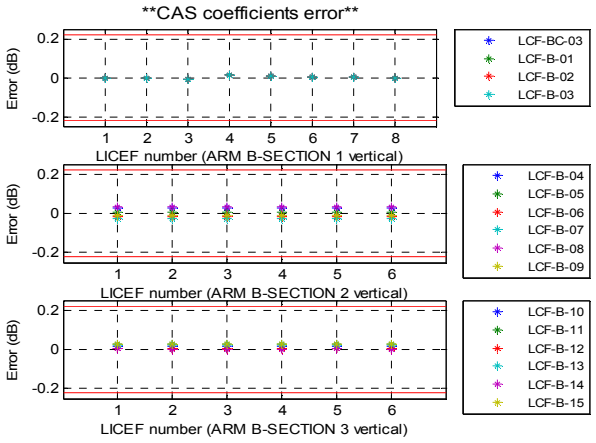

Figure 27 CAS coefficients error in ARM B – vertical polarization (using External CAS S-parameter correction)

Representation 1: LICEFs to calibrate on the x-axis

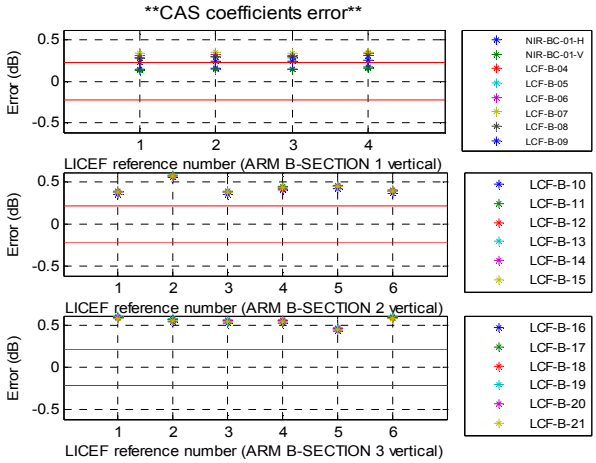

Figure 28 CAS coefficients error in ARM B – vertical polarization (without using CAS S-parameter correction)

Representation 2: References on the x-axis

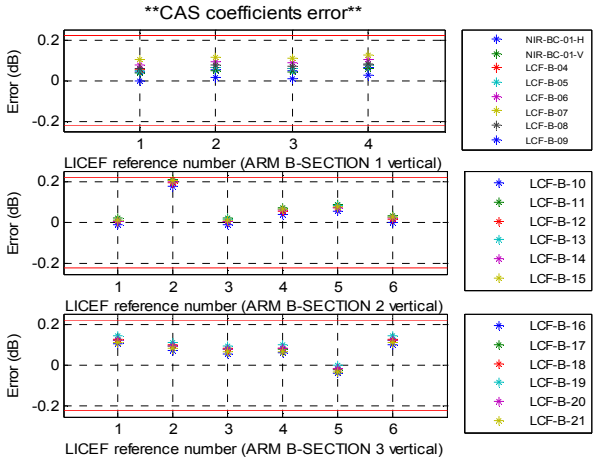

Figure 29 CAS coefficients error in ARM B – vertical polarization (using ON-GROUND CAS S-parameter correction)

Representation 2: References on the x-axis

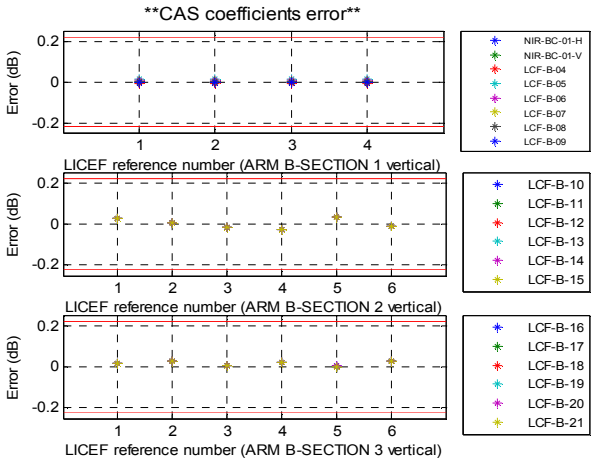

Figure 30 CAS coefficients error in ARM B – vertical polarization (using External CAS S-parameter correction)

Representation 2: References on the x-axis

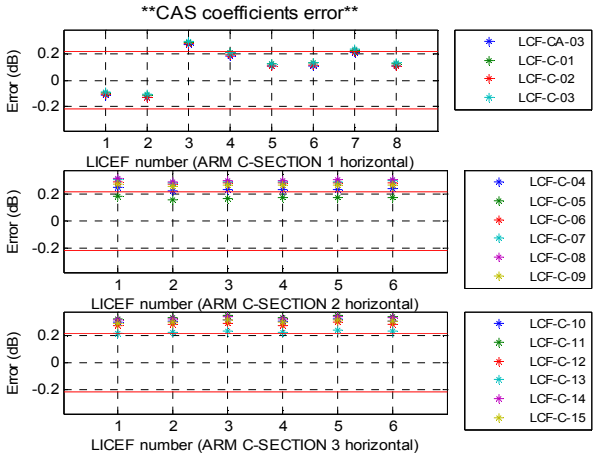

Figure 31 CAS coefficients error in ARM C– horizontal polarization (without using CAS S-parameter correction)

Representation 1: LICEFs to calibrate on the x-axis

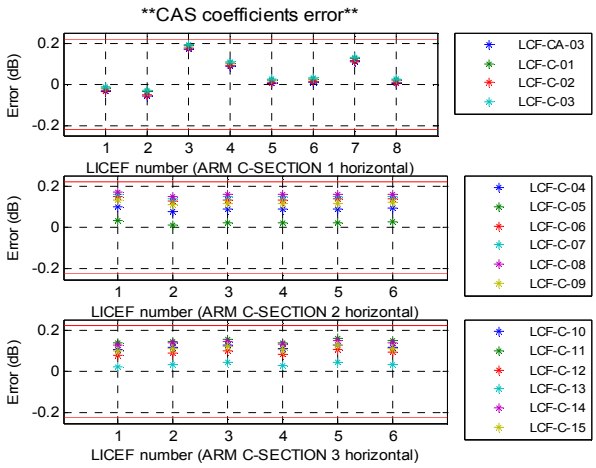

Figure 32 CAS coefficients error in ARM C– horizontal polarization (using ON-GROUND CAS S-parameter correction)

Representation 1: LICEFs to calibrate on the x-axis

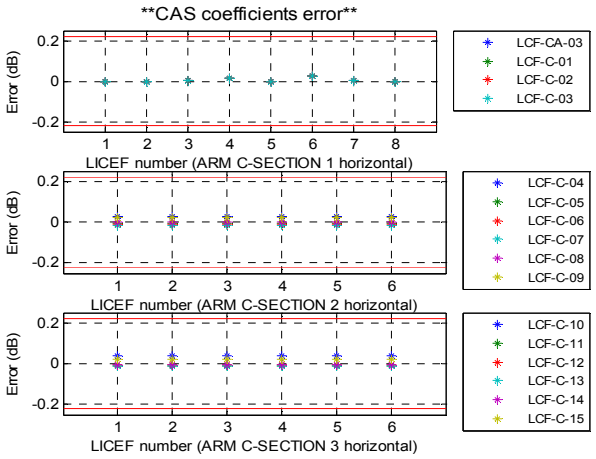

Figure 33 CAS coefficients error in ARM C– horizontal polarization (using External CAS S-parameter correction)

Representation 1: LICEFs to calibrate on the x-axis

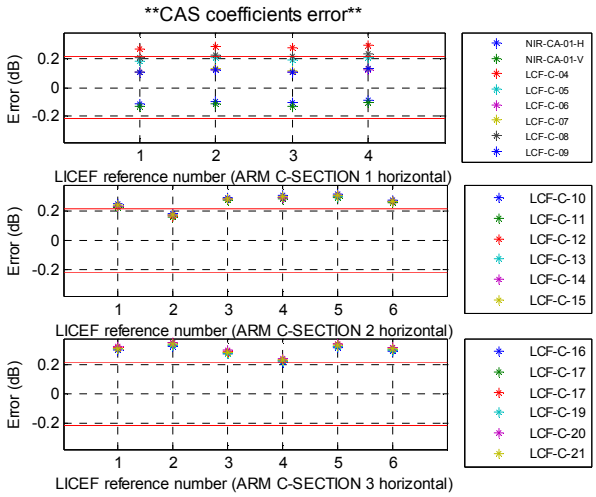

Figure 34 CAS coefficients error in ARM C– horizontal polarization (without using CAS S-parameter correction)

Representation 2: References on the x-axis

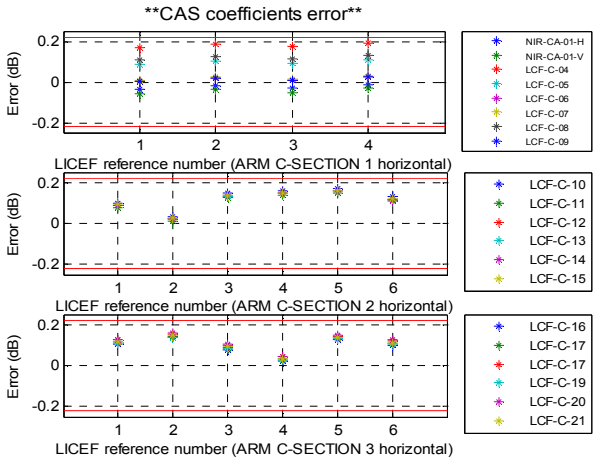

Figure 35 CAS coefficients error in ARM C– horizontal polarization (using ON-GROUND CAS S-parameter correction)

Representation 2: References on the x-axis

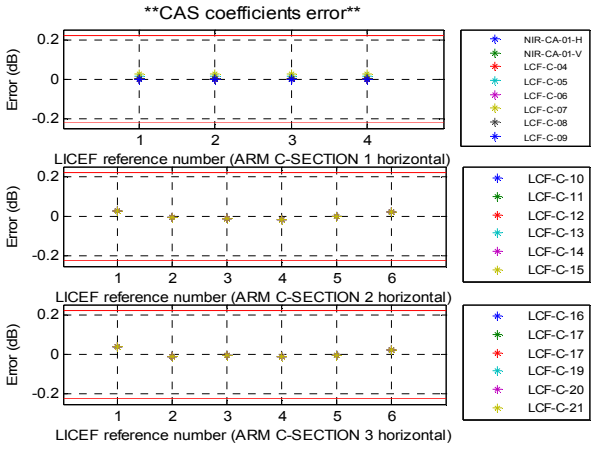

Figure 36 CAS coefficients error in ARM C– horizontal polarization (using External CAS S-parameter correction)

Representation 2: References on the x-axis

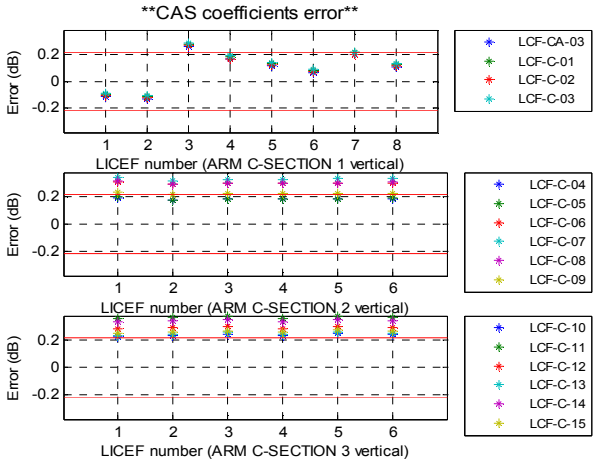

Figure 37 CAS coefficients error in ARM C– vertical polarization (without using CAS S-parameter correction)

Representation 1: LICEFs to calibrate on the x-axis

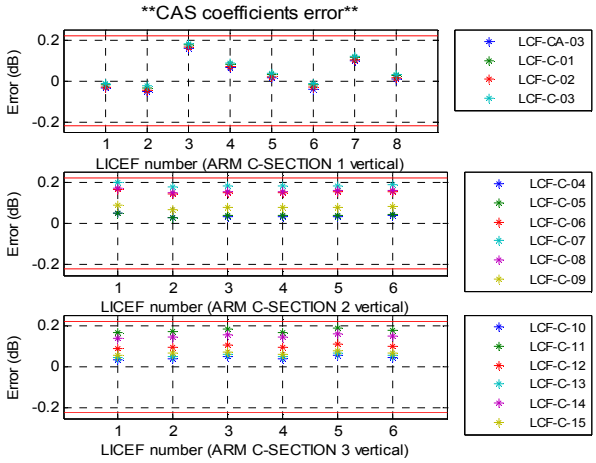

Figure 38 CAS coefficients error in ARM C– vertical polarization (using ON-GROUND CAS S-parameter correction)

Representation 1: LICEFs to calibrate on the x-axis

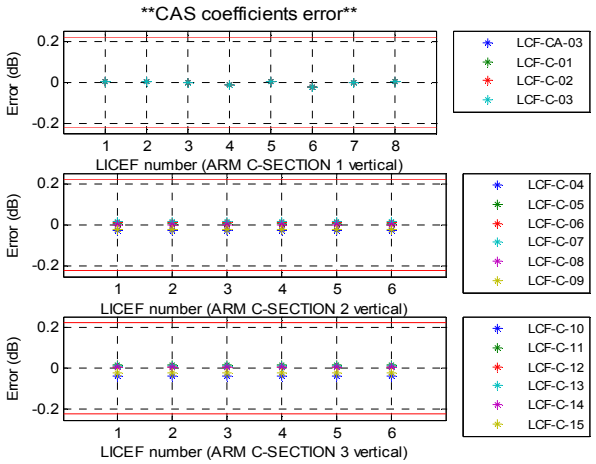

Figure 39 CAS coefficients error in ARM C– vertical polarization (using External CAS S-parameter correction)

Representation 1: LICEFs to calibrate on the x-axis

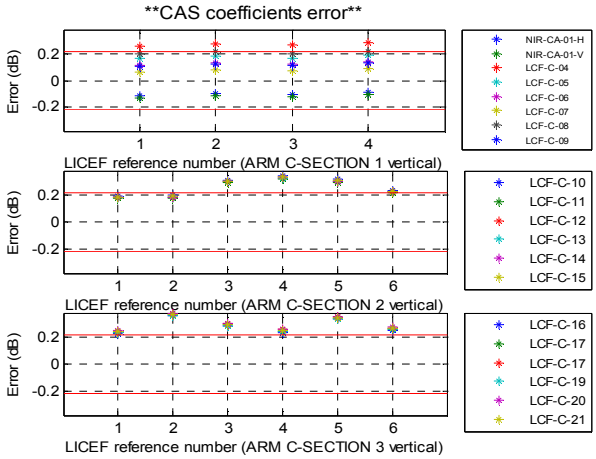

Figure 40 CAS coefficients error in ARM C– vertical polarization (without using CAS S-parameter correction)

Representation 2: References on the x-axis

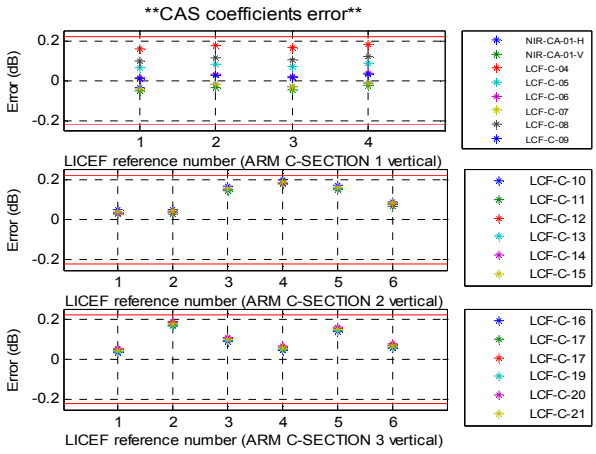

Figure 41 CAS coefficients error in ARM C– vertical polarization (using ON-GROUND CAS S-parameter correction)

Representation 2: References on the x-axis

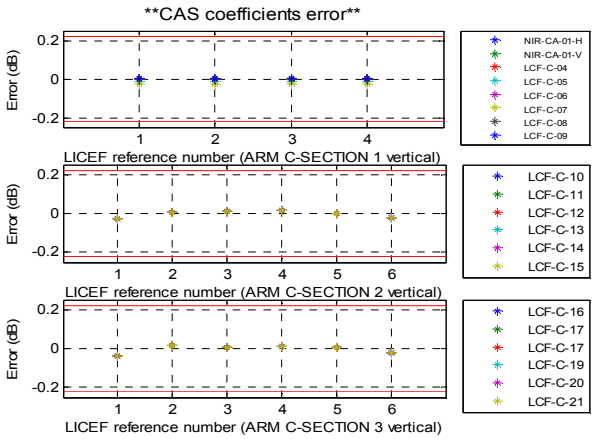

Figure 42 CAS coefficients error in ARM C– vertical polarization (using External CAS S-parameter correction)

Representation 2: References on the x-axis

ANNEX II: Official External CAS and antenna efficiency correction

External CAS coefficients 02/02/2010

Nominal

HUB	ARM A			ARM B			ARM C		
NS-HUB	NS-A1	NS-A2	NS-A3	NS-B1	NS-B2	NS-B3	NS-C1	NS-C2	NS-C3
	1,00066473	0,9950333	0,99742886						
	0,99710016	0,99563908	1,00269275						
	0,99592086	0,99224495	0,98867275						
	0,99554908	0,99273254	0,99617081						
	1,00348323	0,99545481	0,99928953						
	1,00113472	0,9945147	0,99899384						
	1,00234519	1,00645225	1,00556664						
	1,00227916	1,01142035	0,99606352						
	0,99900838	0,99717024	1,00178974						
	0,9993385	1,00454062	1,00177212						
	1,00174512	1,00767356	1,00195709						
	1,00062647	1,00748802	1,00974864						

Table n. 1 Official External CAS coefficients (Nominal)

Redundant

HUB	ARM A			ARM B			ARM C		
NS-HUB	NS-A1	NS-A2	NS-A3	NS-B1	NS-B2	NS-B3	NS-C1	NS-C2	NS-C3
0,98611317				1,00480456	1,0090976	1,00722904	1,00863315	1,00118788	1,00240177
1,00812995				0,99472357	1,00586645	1,00608382	1,00060551	1,00547147	1,00382657
1,00701247				1,00263234	1,01440064	1,00319517	1,00499602	1,00483276	1,00326563
0,98103259				1,01222112	1,00863849	1,00619566	1,01621937	1,00962343	0,99555828
0,98846741				1,01077468	1,00516208	1,00958611	1,01002621	0,99709319	1,00855859
0,98576649				1,00256295	1,0077496	1,00302638	1,00176676	1,00253137	1,0030433
0,98773022				0,99153569	0,99307669	0,99282392	0,98506398	0,9960794	0,99705121
1,01054106				0,9881353	0,99204706	0,99269944	0,989121	0,99775443	0,99943552
1,00561423				0,99616352	0,98898877	0,99085498	0,98851993	0,99711065	0,99967205
0,99448911				0,99073052	0,99194676	1,00100596	0,99291373	0,98934233	0,9944435
0,99332962				0,98688145	0,99464852	0,99311611	0,98076683	1,00232651	0,99625057
0,98505375				0,98914626	0,9888194	0,99446917	0,98598651	0,99680513	0,99652614
0,99099957									
1,02122138									
1,01519711									
0,99745946									
0,99200925									
0,9838524									

Table n. 2 Official External CAS coefficients (Redundant)

Antenna efficiency from February 2010 and other consecutive tests

	REFERENCE MDB FLIGHT 02/02/2010		02/03/2010		16/03/2010		06/04/2010	
Receiver name	η H	η V	η H	η V	η H	η V	η H	η V
LCF_AB_03	0,905043015	0,921889873	0,909054553	0,924994149	0,906480617	0,92321394	0,912049067	0,92321394
NIR_AB01_H	0,972513627	0,972799339	0,972747872	0,973408354	0,974429875	0,974798803	0,972549901	0,974798803
NIR_AB01_V	0,938006148	0,938091343	0,939409635	0,939638207	0,939984565	0,940118724	0,935032403	0,940118724
LCF_A_01	0,938702967	0,93774881	0,936465471	0,935132945	0,93523366	0,933378023	0,935582996	0,933378023
LCF_A_02	0,915063708	0,904913234	0,918062694	0,90792437	0,918198997	0,907776905	0,919928514	0,907776905
LCF_A_03	0,940058355	0,944920319	0,939447489	0,944005983	0,944319523	0,950139722	0,948571972	0,950139722
LCF_A_04	0,917173236	0,924739675	0,918378742	0,926137756	0,914347033	0,922698281	0,916618695	0,922698281
LCF_A_05	0,927416168	0,902476196	0,929331572	0,904068526	0,92426473	0,900298083	0,929418138	0,900298083
LCF_A_06	0,905990105	0,89333407	0,906937174	0,893479435	0,901918937	0,888632893	0,902664761	0,888632893
LCF_A_07	0,910305046	0,89996988	0,907535817	0,903404978	0,902613723	0,894054247	0,905492798	0,894054247
LCF_A_08	0,91152064	0,91471778	0,913956912	0,916963515	0,91011117	0,912893343	0,908798402	0,912893343
LCF_A_09	0,895377589	0,903730689	0,897167729	0,905178255	0,891056564	0,899656676	0,896180536	0,899656676
LCF_A_10	0,888363832	0,888137535	0,892264043	0,892397873	0,892350766	0,892543817	0,891029382	0,892543817
LCF_A_11	0,910644161	0,906169096	0,912013511	0,908033849	0,913182439	0,910335097	0,912976973	0,910335097
LCF_A_12	0,895614827	0,894915461	0,899525476	0,89898028	0,900642921	0,898999116	0,90115447	0,898999116
LCF_A_13	0,899053705	0,897140962	0,905589582	0,903563535	0,904098724	0,903545881	0,900821776	0,903545881
LCF_A_14	0,913790352	0,915094309	0,915495649	0,916758745	0,914563593	0,915800615	0,913661562	0,915800615
LCF_A_15	0,881681888	0,897982938	0,885709168	0,898232199	0,887003239	0,901328189	0,887856153	0,901328189
LCF_A_16	0,902429549	0,875504311	0,902853662	0,870900205	0,902468115	0,871738105	0,904200995	0,871738105
LCF_A_17	0,883035498	0,869490155	0,888172634	0,873616947	0,889466148	0,874452942	0,884216009	0,874452942
LCF_A_18	0,908843562	0,910203027	0,909803504	0,910883206	0,911176384	0,91235498	0,910883855	0,91235498
LCF_A_19	0,896533186	0,889873664	0,894678224	0,887964937	0,899726951	0,893288282	0,897608015	0,893288282
LCF_A_20	0,906200831	0,889052077	0,907256116	0,890955583	0,908335711	0,893214055	0,90958218	0,893214055
LCF_A_21	0,912273993	0,905388567	0,911985557	0,904833153	0,913576353	0,906800217	0,918666214	0,906800217
LCF_BC_03	0,929025485	0,930881609	0,933099333	0,934855036	0,932047995	0,93386508	0,936042492	0,93386508
NIR_BC01_H	0,951093544	0,951143083	0,954980233	0,954260522	0,951823397	0,95178008	0,955984412	0,95178008
NIR_BC01_V	0,962543208	0,962976668	0,967199424	0,9670106	0,966193026	0,966835878	0,967186042	0,966835878
LCF_B_01	0,911161581	0,925569387	0,911804141	0,927578834	0,910406305	0,926943957	0,910441193	0,926943957
LCF_B_02	0,911398695	0,916068291	0,912739744	0,917500857	0,914195152	0,919000138	0,912722683	0,919000138
LCF_B_03	0,893123146	0,88581776	0,893519237	0,886613451	0,893515855	0,886864237	0,893447755	0,886864237
LCF_B_04	0,914695667	0,912416188	0,920108914	0,918444086	0,915642346	0,915030543	0,91995529	0,915030543
LCF_B_05	0,896018405	0,900760677	0,901032537	0,905642301	0,89635512	0,900182	0,898625084	0,900182
LCF_B_06	0,922138908	0,923892578	0,927229846	0,928922508	0,924175341	0,924781944	0,927227024	0,924781944
LCF_B_07	0,920852406	0,919081896	0,926003583	0,924630666	0,918498984	0,91775182	0,922631792	0,91775182
LCF_B_08	0,905272565	0,907289526	0,905447271	0,907219982	0,908059756	0,914139128	0,909514712	0,914139128
LCF_B_09	0,897240025	0,894719205	0,896213594	0,89442859	0,895769428	0,8931473	0,897626493	0,8931473
LCF_B_10	0,885676777	0,897492701	0,887060159	0,898286198	0,884696611	0,895579948	0,885136046	0,895579948

LCF_B_11	0,939007858	0,93998041	0,940529266	0,941026557	0,934491625	0,935930846	0,939049033	0,935930846
LCF_B_12	0,895242355	0,892128463	0,895905972	0,892094666	0,893046524	0,890334327	0,896434719	0,890334327
LCF_B_13	0,919586606	0,906935467	0,918185565	0,905533045	0,917999374	0,906278546	0,920873301	0,906278546
LCF_B_14	0,904458436	0,915135148	0,903978135	0,91754636	0,9031138	0,913771114	0,906552222	0,913771114
LCF_B_15	0,898833323	0,892851243	0,897356331	0,892753365	0,896242664	0,890093038	0,896251891	0,890093038
LCF_B_16	0,909548292	0,91378988	0,908876764	0,913580812	0,909380539	0,914018817	0,908875541	0,914018817
LCF_B_17	0,903713438	0,91636493	0,905181369	0,91780951	0,906320756	0,917457422	0,904017572	0,917457422
LCF_B_18	0,909115395	0,909141293	0,906999849	0,908614142	0,915910715	0,917168286	0,914644729	0,917168286
LCF_B_19	0,911096042	0,920844344	0,910295262	0,921159975	0,911675358	0,922514791	0,916766628	0,922514791
LCF_B_20	0,892199984	0,895798035	0,887818696	0,891872561	0,894260664	0,899111294	0,894920565	0,899111294
LCF_B_21	0,906011049	0,917933858	0,908309277	0,919830991	0,90791776	0,920325836	0,909218362	0,920325836
LCF_CA_03	0,907918875	0,924717246	0,907678536	0,924048287	0,91015563	0,925960829	0,90879809	0,925960829
NIR_CA01_H	0,936991143	0,936994501	0,940392532	0,940353886	0,942399311	0,941991438	0,943160896	0,941991438
NIR_CA01_V	0,944902796	0,944617814	0,946982486	0,947490496	0,948098171	0,94858953	0,949646044	0,94858953
LCF_C_01	0,907836809	0,918780405	0,907988707	0,918518718	0,910006127	0,918050473	0,910772983	0,918050473
LCF_C_02	0,920384952	0,93033495	0,92178835	0,930521292	0,922342534	0,931497257	0,923918836	0,931497257
LCF_C_03	0,919879608	0,930888306	0,922779799	0,933089096	0,918298125	0,927568766	0,921860419	0,927568766
LCF_C_04	0,926609731	0,923462358	0,928976782	0,926026584	0,92823181	0,925265649	0,927783416	0,925265649
LCF_C_05	0,920093157	0,914115531	0,923039575	0,916991411	0,919019783	0,913244109	0,923556852	0,913244109
LCF_C_06	0,900761637	0,902558596	0,903237973	0,904211386	0,900816562	0,901989786	0,899970272	0,901989786
LCF_C_07	0,913016996	0,901593684	0,916355678	0,904999175	0,912871434	0,901488263	0,911393933	0,901488263
LCF_C_08	0,908294796	0,905705851	0,911001951	0,907979406	0,905111803	0,900636746	0,908143447	0,900636746
LCF_C_09	0,89562284	0,895723512	0,89663749	0,897077943	0,895347608	0,895183676	0,895977885	0,895183676
LCF_C_10	0,91369364	0,902425436	0,917766628	0,906089872	0,912095781	0,901321227	0,913956053	0,901321227
LCF_C_11	0,901498473	0,904383612	0,906473987	0,908418996	0,900733214	0,903353827	0,902439607	0,903353827
LCF_C_12	0,922141421	0,926338544	0,923581346	0,927467904	0,922601458	0,926431893	0,925792396	0,926431893
LCF_C_13	0,913292088	0,91897942	0,916800817	0,92319278	0,911985936	0,917910703	0,918384901	0,917910703
LCF_C_14	0,941266956	0,939164968	0,940483738	0,938381252	0,9384573	0,936225072	0,942420827	0,936225072
LCF_C_15	0,922607412	0,913604211	0,925459858	0,915442869	0,921200145	0,911604612	0,925452456	0,911604612
LCF_C_16	0,919447927	0,90397291	0,922665561	0,90706257	0,921899168	0,906685005	0,922111981	0,906685005
LCF_C_17	0,92332633	0,929123847	0,92769649	0,933481156	0,93041767	0,935942908	0,925391119	0,935942908
LCF_C_18	0,912441212	0,912297875	0,911612469	0,910297013	0,912758152	0,911990093	0,914339289	0,911990093
LCF_C_19	0,89731384	0,900437548	0,899853881	0,903512649	0,899177551	0,902418964	0,900147963	0,902418964
LCF_C_20	0,924345158	0,925039608	0,929382064	0,929207826	0,928169326	0,928880217	0,924826448	0,928880217
LCF_C_21	0,915141254	0,905380322	0,917271692	0,907418079	0,915653765	0,906556552	0,913832413	0,906556552

Table n. 3 External antenna efficiency from February 2010 and other consecutive tests

ANNEX III: Publications

SMOS-MIRAS CALIBRATION AND PERFORMANCE

Ignasi Corbella[1], Francesc Torres[1], Veronica Gonzalez-Gambau[1], Nuria Duffo[1], Miriam Pablos[1], Israel Duran[1], Josep Closa[2], and Manuel Martin-Neira[3]

[1]*Remote Sensing Laboratory, Universitat Politècnica de Catalunya (UPC). C/ Jordi Girona 1-3. 08034 Barcelona, Spain.*
[2]*EADS-CASA Espacio*
[3]*ESA-ESTEC, 2200 AG Noordwijk, The Netherlands*

ABSTRACT

An intense activity has been carried out during the in-orbit commissioning phase of the SMOS (Soil Moisture and Ocean Salinity) mission. Concerning the payload MIRAS (Microwave Imaging Radiometer with Aperture Synthesis) it has been fully characterized using specific orbits dedicated to check all instrument modes. The procedures, already defined during the on-ground characterization, have been repeated so as to obtain realistic temperature characterization and updated internal calibration parameters. External calibration maneuvers have been tested for the first time and have provided absolute instrument calibration, as well as corrections to improve the internal calibration data.

Key words: SMOS; MIRAS; Interferometric Radiometers; Calibration; Imaging.

1. INTRODUCTION

The ESA SMOS satellite was successfully launched on the 2nd November 2009. The six-month long in-orbit commissioning phase started just after launch and included a complete and systematic check of the payload MIRAS, the retrieval of all calibration parameters and a thorough thermal characterization. The mission is now in the operational phase and data products are continuously being generated by the data processing ground segment using the selected algorithms and payload modes of operation.

This paper is focused on the work performed during the payload commissioning. It describes some tests carried out during this phase and the results obtained. All results have been obtained using the MIRAS-Testing Software (MTS) [1], an independent processing tool able to ingest SMOS raw data and produce calibration parameters, calibrated visibility (compatible with level 1A SMOS data) and geolocated brightness temperature (equivalent to the SMOS level 1C).

2. MIRAS CALIBRATION OVERVIEW

A complete description of the MIRAS calibration system can be found in [2]. In general, calibration of an interferometric radiometer such as MIRAS is needed to provide accurate values of visibility for all receiver pairs and antenna temperature (zero baseline visibility) for at least one element. Besides, image reconstruction algorithms [3, 4] need additional calibration parameters, such as the fringe washing function shape and the flat target response [5]. MIRAS uses a combination of both external and internal calibration procedures to estimate all the time varying parameters. On the other hand, stable parameters such as antenna patterns, S-parameters of noise distribution network and others, are directly used from on-ground characterization.

The visibility is derived by the level 1 processor using the following equation

$$V_{kj} = \frac{M_{kj}\sqrt{T_{sys_k}T_{sys_j}}}{G_{kj}} \text{ where } T_{sys_k} = \frac{v_k - v_{off_k}}{G_k} \quad (1)$$

where v_k is the measured voltage of the PMS (power measurement system) and M_{kj} the normalized correlation measured by the on-board digital correlator. On the other hand, antenna temperature is measured by three noise-injection radiometers (NIR's) [6] located near the center of the array using

$$T_A = T_U - \eta T_{NA} \quad (2)$$

where T_U is the physical temperature in kelvin measured by a sensor placed in a reference resistor near the antenna, η is the measured Dicke pulse fraction (raw NIR measurement) and T_{NA} the noise equivalent temperature of the internal noise source.

The brightness temperature is computed out of the calibrated visibility (1) by inverting the visibility equation [7].

$$V_{kj} = \iint_{\xi^2+\eta^2\leq 1} T'_{kj}(\xi,\eta)\,\overline{\tilde{r}}_{kj}\left(-\tfrac{u\xi+v\eta}{f_0}\right) e^{-j2\pi(u\xi+v\eta)}\,d\xi\,d\eta \quad (3)$$

where $\bar{\bar{r}}_{kj}(\ )$ is the fringe washing function normalized to its value at the origin and T'_{kj} the *modified* brightness temperature:

$$T'_{kj}(\xi,\eta) = \frac{\sqrt{D_k D_j}}{4\pi} \frac{T_B(\xi,\eta) - T_r}{\sqrt{1-\xi^2-\eta^2}} F_{n_k}(\xi,\eta) F^*_{n_j}(\xi,\eta) \tag{4}$$

where T_B is the brightness temperature to be retrieved. In this equation, the only parameter that has eventually to be updated is the normalized fringe washing function, which is approximated by the following analytical expression.

$$\bar{\bar{r}}_{kj} \approx A\,\mathrm{sinc}(B(\tau - C))\, e^{j(D\tau^2 + E\tau)} \tag{5}$$

In summary, the outcome of the MIRAS calibration procedure is made of the following parameters: the PMS gain G_k and offset v_{off}, the correlation complex gain G_{kj} in amplitude and phase, the NIR source noise temperature T_{NA} and the five parameters A to E of the fringe washing function. All calibration parameters are planned to be periodically updated during the mission to account for possible instrumental drifts. Additionally, the Flat Target Response, which is essentially the calibrated visibility measured when the instrument is pointing to the cold sky, is also considered a calibration parameter.

3. INTERNAL AND EXTERNAL CALIBRATION

External calibration is performed by commanding the platform to go into inertial attitude. In this case, the instrument starts to rotate with respect to the earth-fixed coordinate system until the earth disappears from the field of view of the antenna. At this point, the radiometer is measuring the brightness temperature of a fixed point of the sky, which is chosen to be near the galactic pole to avoid influence from the Galactic emission. Since the sky brightness temperature at L-band is known [8], the calibration parameters of the instrument are adjusted so as to match the measurements to this absolute reference.

External calibration provides the best quality of calibration and it is the only way to obtain the absolute accuracy of the instrument. However, the pointing maneuvers cannot be performed too often and the impact in terms of percentage of time dedicated to calibration is high.

Internal calibration, on the other hand, is carried out by periodically injecting noise to all receivers using an internal source and a distribution network [9]. It tracks fast variations of parameters, but for those requiring a known calibration standard, it cannot provide their absolute values. In this case, the accuracy of the internal calibration relies on the quality of a secondary standard, which has to be previously calibrated using the external view. On the other hand, noise injection is very fast and is easily interspersed between normal measurement operation.

The calibration method utilized for each of the parameters is the following

- PMS gain: External calibration with periodic tracking by internal calibration
- PMS offset: Internal calibration.
- Correlator gain (amplitude and phase): Internal calibration.
- NIR internal noise temperature: External calibration
- Fringe washing function parameters: Internal calibration

4. CALIBRATION RATE

Most of the calibration procedures and measurement sequences were precisely defined during the on-ground characterization of the instrument [10]. The in-orbit commissioning phase has been essential to adjust the timing of calibration events in accordance with the real instrument operation. Particularly, the following general trends have been observed:

- Flat Target Response: Stable, to be corrected only twice a year.
- Fringe washing function shape: The same stability as the Flat Target Response
- Visibility amplitude: To be updated once every 8 weeks
- Antenna temperature: Needs to be calibrated every 2 weeks
- Visibility phase. A calibration is needed every 10 minutes.

Some parameters, as the PMS gain and offsets have been accurately characterized in terms of temperature variation though the computation of sensitivity parameters. This, in combination with a very low physical temperature drift of the whole instrument, has allowed to reduce the need for their frequent calibration updates. New sensitivity parameters have been derived during the in-orbit commissioning phase and they are very well in agreement with the ones obtained during the ground characterization.

As a general rule, the percentage of total time devoted to calibration must be the minimum, just to ensure that the quality of the measurements is according to the requirements. In SMOS, about one percent of the time is used in calibration. This has been achieved by minimizing the number of external calibration maneuvers, using accurate thermal characterization and agreeing a compromise value for the parameters changing the fastest (phase of visibility)

5. CORRELATOR CALIBRATION

Calibrating the corrrelator gain means measuring the complex parameter G_{kj} and its evolution with time and

temperature. This is achieved by processing the internal calibration data using a straightforward method described in [9, 11]. The absolute value of G_{kj} is nearly one by definition and it has been observed having negligible variation from one calibration event to the other. However, the phase of G_{kj} for some baselines shows large and relatively fast variations with time that must be tracked by frequent calibration events. The reason is that the G_{kj} phase for two receivers not sharing a common local oscillator is roughly equal to the phase difference between the signals generated by the oscillators, which vary independently as a function of their local temperature variation. This effect is the main driver for the intercalibration period: every ten minutes a short burst of correlated noise is injected during 1.2 seconds to all receivers just to compute this phase. Figure 1 shows a plot of the amplitude stability of G_{kj} and the large phase variation in a baseline having two different local oscillators.

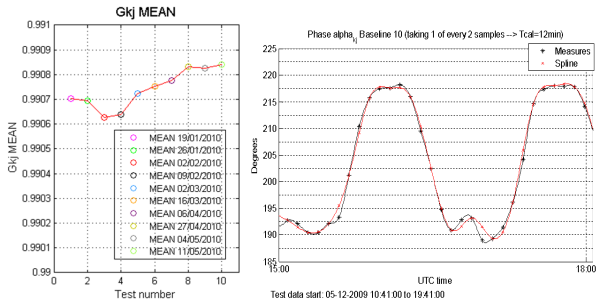

Figure 1. Left: Stability of the amplitude of G_{kj} along time. Right: phase of G_{kj} variation due to local oscillator phase drift

6. PMS CALIBRATION

According to (1), the PMS parameters (gain and offset) are directly responsible of the amplitude of the calibrated visibility. For this reason, accurate PMS calibration has a strong impact on the quality of the final brightness temperature image. In general, errors in the PMS gains and offsets increase the pixel bias, defined as the spatial standard deviation of an image in the director cosines coordinates [12, 13].

The measurements carried out during the commissioning phase have shown that the PMS offset has a periodic variation linked to a control signal used to drive the heaters of the instrument thermal control system. This effect is general but particularly noticeable in some receivers, and has been solved by applying a software correction based on a meticulous process of characterization. The results are given in figure (2) where plots of the offset and the heater signal are drawn superimposed to demonstrate this effect. At the right the same plot after applying the software correction is given. The effect of the correction is apparent.

On the other hand, the PMS gain is extremely stable and very well characterized in temperature. In fact, several

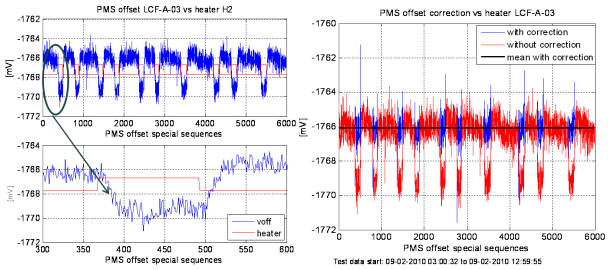

Figure 2. Effect of heater signal in the PMS offset and its correction

retrievals made in different calibration events show high consistency among them. It is calibrated by external calibration using the sky as cold standard and an internal resistor at known physical temperature as hot standard [11]. Independently, their values are monitored by internal calibration using the method described in [9, 11, 14], based on using the NIR, working in a specific mode of operation, to measure the noise power injected to the receivers. This implies that the NIR has to be previously calibrated during the cold sky views. One key result of the in-orbit payload characterization is the computation of correction factors to be applied to internal noise distribution network parameters and antenna efficiencies so as to make these two PMS gain measurements consistent with each other.

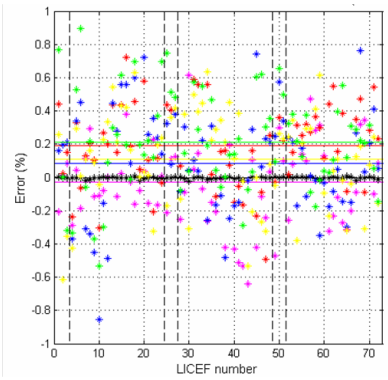

Figure 3. PMS gain calibration. Difference between external and internal calibrations once correction factors applied. The results are for H-pol and for six calibration events spanning three months

Figure 3 shows the difference in percentage between gain retrievals from both external and internal calibration, once the correction factors have been applied. The different traces correspond to six calibration events carried out respectively on 12th January, 2nd February, 2nd, 16th and 23rd March, and 6th April 2010, that is spanning about three months. The peak to peak differences in individual gains is always lower than $\pm 1\%$ and the drift of the average values is as low as 0.2%.

The PMS gain variation between calibration events is very well tracked by means of the measured physical temperature and the sensitivity parameter derived during the in-orbit commissioning phase. Figure 4 shows the measurements of gain during a specific test carried out to

derive this sensitivity. During this test, several orbits of continuous gain retrievals using internal calibration were commanded. The gain sensitivity parameter to temperature was computed by using linear regression of the data acquired. The figure shows a comparison between the measured gain and the one derived using the sensitivity parameter and the physical temperature, so demonstrating that the gain can be accurately tracked just by measuring the temperature sensors, and there is no need for frequent calibration updates.

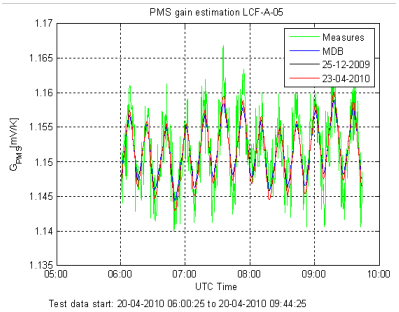

Figure 4. PMS gain tracking using the sensitivity parameter

Finally, figure 5 shows the long-term stability of both PMS gain and offset. It shows the difference of the averaged values retrieved during ten calibration events distributed regularly between 12th January to 11th May 2010. It turns out that the long-term drift is lower than 0.5 mV for the offset and 0.2% for the gain, which has led the the proposal of a PMS intercalibration period of eight weeks to be conservative.

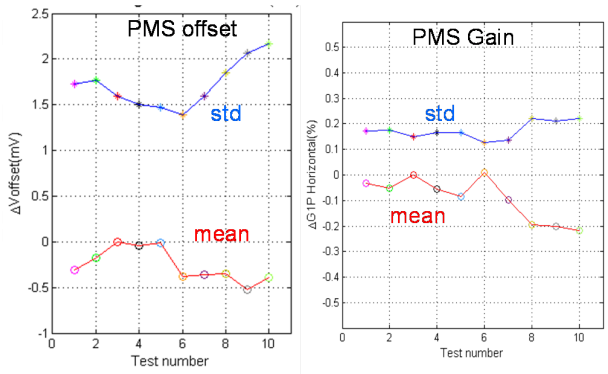

Figure 5. Long term PMS calibration. The test numbers correspond to different calibration events carried out in a 4-month span, from 19th January 2010 to 11th May 2010. Left: Offset, Right: Gain

7. CONCLUSIONS

Calibration and performance of MIRAS, the SMOS payload, has been accurately assessed during the in-orbit commissioning phase. By careful analysis of the measurements performed in specific tests, all the parameters related to internal and external calibration have been retrieved and found to be very well in consistency with the ones obtained during the on-ground characterization. The rate of calibration events, both internal and external, has been established as a result of the analysis made during the commissioning phase.

ACKNOWLEDGMENTS

The work was supported by the European Space Agency and EADS-CASA Space Division under ESTEC contract 17950/03/NL/FF-SMOS; and by the Spanish Ministry of Science and Innovation and FEDER under projects TEC2008-06764-C02-01 and MIDAS-5 ESP2007-65667-C04-0

REFERENCES

1. I. Corbella, F. Torres, N. Duffo, V. González, A. Camps, and M. Vall-llossera, "Fast processing tool for SMOS data," in *International Geoscience and Remote Sensing Symposium, IGARSS 2008*, no. II. Boston(Ma), USA: IEEE, 7 - 11 July 2008, pp. 1152–1155.

2. M. Brown, F. Torres, I. Corbella, and A. Colliander, "SMOS calibration," *IEEE Transactions on Geoscience and Remote Sensing*, vol. 46, no. 3, pp. 646–658, March 2008.

3. I. Corbella, F. Torres, A. Camps, N. Duffo, and M. Vall-llossera, "Brightness temperature retrieval methods in synthetic aperture radiometers," *IEEE Transactions on Geoscience and Remote Sensing*, vol. 47, no. 1, pp. 285–294, January 2009.

4. A. Camps, M. Vall-llossera, I. Corbella, N. Duffo, and F. Torres, "Improved image reconstruction algorithms for aperture synthesis radiometers," *IEEE Transactions on Geoscience and Remote Sensing*, vol. 46, no. 1, pp. 146–158, January 2008.

5. M. Martín-Neira, M. Suess, and J. Kainulainen, "The flat target transformation," *IEEE Transactions on Geoscience and Remote Sensing*, vol. 46, no. 3, pp. 613–620, March 2008.

6. A. Colliander, L. Ruokokoski, J. Suomela, K. Veijola, J. Kettunen, V. Kangas, A. Aalto, M. Levander, H. Greus, M. T. Hallikainen, and J. Lahtinen, "Development and calibration of SMOS reference radiometer," *IEEE Transactions on Geoscience and Remote Sensing*, vol. 45, no. 7, pp. 1967–1977, July 2007.

7. I. Corbella, N. Duffo, M. Vall-llossera, A. Camps, and F. Torres, "The visibility function in interferometric aperture synthesis radiometry," *IEEE Transactions on Geoscience and Remote Sensing*, vol. 42, no. 8, pp. 1677–1682, August 2004.

8. D. M. Le Vine and S. Abraham, "Galactic noise and passive microwave remote sensing from space at L-band," *IEEE Transactions on Geoscience and Remote Sensing*, vol. 42, no. 1, pp. 119–129, January 2004.

9. I. Corbella, F. Torres, A. Camps, A. Colliander, M. Martín-Neira, S. Ribó, K. Rautiainen, N. Duffo, and M. Vall-llossera, "MIRAS end-to-end calibration. Application to SMOS L1 processor," *IEEE Transactions on Geoscience and Remote Sensing*, vol. 43, no. 5, pp. 1126–1134, May 2005.

10. I. Corbella, F. Torres, N. Duffo, M. Martín-Neira, V. González-Gambau, A. Camps, and M. Vall-llossera, "On-ground characterization of the SMOS payload," *IEEE Transactions on Geoscience and Remote Sensing*, vol. 47, no. 9, pp. 3123–3133, September 2009.

11. F. Torres, I. Corbella, A. Camps, N. Duffo, M. Vall-llossera, S. Beraza, C. Gutierrez, and M. Martín-Neira, "Denormalization of visibilities for in-orbit calibration of interferometric radiometers," *IEEE Transactions on Geoscience and Remote Sensing*, vol. 44, no. 10, pp. 2679–2686, October 2006.

12. F. Torres, A. Camps, J. Bará, and I. Corbella, "Impact of receiver errors on the radiometric resolution of large 2d aperture synthesis radiometers. study applied to MIRAS," *Radio Science*, vol. 32, no. 2, pp. 629–642, March-April 1997.

13. I. Corbella, F. Torres, A. Camps, J. Bará, N. Duffo, and M. Vall-llossera, "L-band aperture synthesis radiometry: hardware requirements and system performance," in *International Geoscience and Remote Sensing Symposium, IGARSS 2000*, vol. 7. Honolulu (Hw), USA: IEEE, 24-28 July 2000, pp. 2975 – 2977.

14. F. Torres, A. Camps, J. Bará, I. Corbella, and R. Ferrero, "On-board phase and modulus calibration of large aperture synthesis radiometers: Study applied to MIRAS," *IEEE Transactions on Geoscience and Remote Sensing*, vol. GRS-34, no. 4, pp. 1000–1009, July 1996.

15. A. Camps, "Application of interferometric radiometry to Earth observation," Ph.D. dissertation, Universitat Politècnica de Catalunya, November 1996.

MIRAS Calibration and Performance. Results From the SMOS In-Orbit Commissioning Phase

Ignasi Corbella, *Senior Member, IEEE,* Francesc Torres, *Senior Member, IEEE* Nuria Duffo, *Member, IEEE,* Verónica González-Gambau, Miriam Pablos, Israel Duran, Manuel Martín-Neira, *Senior Member, IEEE,*

Abstract

After the successful launching of the SMOS satellite in November 2009, continuous streams of data started to be regularly downloaded and made available to be processed. The first six months of operation were fully dedicated to the In Orbit Commissioning Phase, with an intense activity aimed at bringing the satellite and instrument into a fully operational condition. Concerning the payload MIRAS (Microwave Imaging Radiometer with Aperture Synthesis) it was fully characterized using specific orbits dedicated to check all instrument modes. The procedures, already defined during the on-ground characterization, were repeated so as to obtain realistic temperature characterization and updated internal calibration parameters. External calibration maneuvers were tested for the first time and provided absolute instrument calibration, as well as corrections to internal calibration data. Overall performance parameters, such as stability, radiometric sensitivity and radiometric accuracy were evaluated. The main results of this activity are presented in this paper, showing that the instrument delivers stable and well calibrated data thanks to the combination of external and internal calibration and to an accurate thermal characterization. Finally, the quality of the visibility calibration is demonstrated by producing brightness temperature images in

The work was supported by the European Space Agency and EADS-CASA Space Division under ESTEC contract 17950/03/NL/FF-SMOS; and by the Spanish Ministry of Science and Innovation and FEDER under projects TEC2008-06764-C02-01 and MIDAS-5 ESP2007-65667-C04-0

I. Corbella, F. Torres, N. Duffo V. González-Gambau, I. Duran and M. Pablos are with the Remote Sensing Laboratory, Universitat Politècnica de Catalunya and with the SMOS Barcelona Expert Centre. Barcelona-Spain (e-mail: corbella@tsc.upc.edu).

M. Martín-Neira, is with the European Space Agency (ESA-ESTEC) Noordwijk. The Nederlands (e-mail: Manuel.Martin-Neira@esa.int)

the alias-free field of view using standard inversion techniques. Images of ocean, ice and land are given as examples.

Index Terms

SMOS, interferometric synthetic aperture radiometry, calibration, imaging

I. INTRODUCTION

SMOS (acronym of Soil Moisture and Ocean Salinity) is a European Space Agency (ESA) mission designed to provide global maps of soil moisture over land and sea surface salinity over oceans [1]. It consists of a satellite in a sun-synchronous orbit at about 770 km height carrying a passive L-band sensor called MIRAS (Microwave Imaging Radiometer with Aperture Synthesis) [2], [3]. The satellite was successfully launched the 2nd November 2009 from the Plesestz cosmodrome in northern Russia and the payload was switched on on 17th November 2009. Since then, continuous data is regularly received by the ground segment data acquisition station located in Villafranca del Castillo, near Madrid (E).

The SMOS In-Orbit Commissioning Phase (IOCP) started just after the 3-week long Switch-On and Data Acquisition Phase (SODAP), which was mainly focused at testing low level processes for data acquisition and handling. The IOCP had an overall duration of 6 months and the first half part comprised the characterization, calibration, validation and verification of the instrument. The main goal was to provide a fine tune of MIRAS by means of: Systematic check of all instrument modes, retrieval of internal and external calibration parameters, computation of temperature sensitivity coefficients, assessment on imaging capability, assessment on calibration rate requirements, and instrument overall performance evaluation: Stability, Radiometric sensitivity, Radiometric accuracy and Absolute accuracy.

Most of the goals were successfully achieved on time thanks to the combined effort of a team formed by EADS-CASA Espacio (E) as instrument manufacturer; Deimos Enginheria (P) developer of the Level 1 Prototype Processor (L1PP); the ESA Calibration Expert Center (CEC) dedicated to analyze the quality of the calibration data; and the Universitat Politecnica de Catalunya (UPC) responsible of the definition and implementation of calibration and processing algorithms. All of them were efficiently led by the ESA's principal engineer of the instrument.

The following sections provide a brief description of the activities carried out by UPC in the frame of the SMOS IOCP and shows the main results achieved, including determination of calibration parameters and their stability, as well as retrieval of brightness temperature images of ocean, ice and land. Everything has been processed using the MIRAS Testing Software, an independent software tool developed by UPC, capable of producing geolocated brightness temperature out of the raw data downloaded from the payload [4].

II. MIRAS CALIBRATION

A complete description of the MIRAS calibration system can be found in [5]. In general, calibration of an interferometric radiometer such as MIRAS is needed to provide accurate values of visibility for all receiver pairs and antenna temperature (zero baseline visibility) for at least one element. Besides, image reconstruction algorithms [6], [7] need additional calibration parameters, such as the fringe washing function shape and the flat target response [8]. MIRAS uses a combination of both external and internal calibration to estimate all the time varying parameters. On the other hand, stable parameters such as antenna patterns, S-parameters of noise distribution network and others, are directly used from on-ground characterization.

The visibility is derived by the level 1 processor using the following equation

$$V_{kj} = \frac{M_{kj}\sqrt{T_{sys_k}T_{sys_j}}}{G_{kj}} \text{ where } T_{sys_k} = \frac{v_k - v_{off_k}}{G_k} \tag{1}$$

where v_k is the measured voltage of the PMS (power measurement system) and M_{kj} the normalized correlation measured by the on-board digital correlator. On the other hand, antenna temperature is measured by three noise-injection radiometers (NIR's) [9] located near the center of the array using

$$T_A = T_U - \eta T_{NA} \tag{2}$$

where T_U is the physical temperature in kelvin measured by a sensor placed in a reference resistor near the antenna, η is the measured Dicke pulse fraction (raw NIR measurement) and T_{NA} the noise equivalent temperature of the internal noise source.

The brightness temperature is computed out of the calibrated visibility (1) by inverting the visibility equation [10].

$$V_{kj} = \iint\limits_{\xi^2+\eta^2\leq 1} T'_{kj}(\xi,\eta)\ \overline{\overline{r}}_{kj}\Big(-\tfrac{u\xi+v\eta}{f_0}\Big)\ e^{-j2\pi(u\xi+v\eta)} d\xi d\eta \tag{3}$$

where $\overline{\tilde{r}}_{kj}(\ )$ is the fringe washing function normalized to its value at the origin and T'_{kj} the *modified* brightness temperature:

$$T'_{kj}(\xi,\eta) = \frac{\sqrt{D_k D_j}}{4\pi} \frac{T_B(\xi,\eta) - T_r}{\sqrt{1-\xi^2-\eta^2}} F_{n_k}(\xi,\eta) F^*_{n_j}(\xi,\eta) \tag{4}$$

with T_B is the brightness temperature to be retrieved. In this equation, the only parameter that needs eventually to be updated is the normalized fringe washing function, which is approximated by the following analytical expression.

$$\overline{\tilde{r}}_{kj} \approx A\,\mathrm{sinc}(B(\tau - C))\, e^{j(D\tau^2 + E\tau)} \tag{5}$$

In summary, the outcome of the MIRAS calibration procedure is made of the following parameters: the PMS gain G_k and offset v_{off}, the correlation complex gain G_{kj} in amplitude and phase, the NIR source noise temperature T_{NA}, and the five parameters A to E of the fringe washing function. All calibration parameters are planned to be periodically updated during the mission to account for possible instrumental drifts. Additionally, the Flat Target Response, which is essentially the calibrated visibility measured when the instrument is pointing to the cold sky, is also considered a calibration parameter.

III. INTERNAL CALIBRATION

Internal calibration is carried out by periodically injecting noise to all receivers using an internal source and a power distribution network. Two-levels of power are injected so as to cancel the internal noise coming from the distribution network [11], [12]. Also, in order to simplify this network, a distributed approach is used [13].

Internal calibration is used to monitor the power measurement system (PMS) (gain G_k and offset v_{off}), the correlator complex gain (G_{kj}), both in amplitude and phase and the fringe washing function parameters. It is also used to measure the residual visibility offset by switching all receivers' inputs to internal resistors, so producing uncorrelated noise injection. This offset is very small and was very well characterized on ground [14].

A. PMS gain

Figure 1 shows the relative PMS gain variation in percentage with respect to the average value for all 72 receivers. Both the standard deviation and the peak to peak deviation are shown. It

is computed after analyzing a total of 2499 samples measured during more than 24 hours with the instrument continuously in internal calibration mode. Most of the receivers have PMS gain variations below 0.5% rms and all of them are well below the specified 1%. These variations are dominated by the thermal noise inherent to the measurements due to the limited integration time.

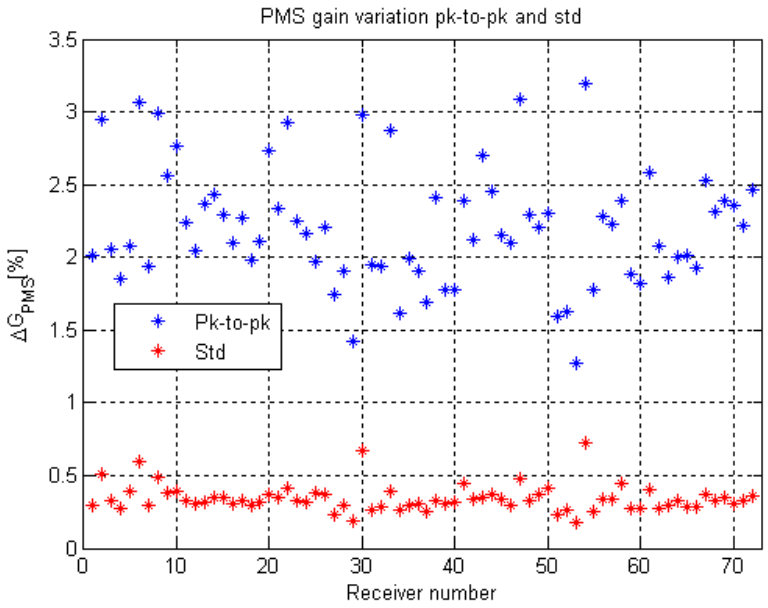

Fig. 1. Relative PMS gain variation in 24 hours of continuous measurements

Nevertheless, there is still a small dependance of the PMS gain with temperature. To characterize this behavior, plots of PMS gains as a function of temperature have been produced and sensitivity coefficients have been computed from linear regression. An example of such plots is given in figure 2 along with a comparison between the measured gain and the one predicted from the temperature measurement. Two values of sensitivity are shown, one in blue corresponding to on ground measurement [14] and other in red obtained from flight data in the frame of the In Orbit Commissioning Phase.

Figure 3 shows the long-term stability of the gain. It represents the difference in the measured gain at six different calibration events spanning more than three months. At each event, the gain is computed by averaging 45 individual retrievals, saving the result as a calibration product to be used during the measurement mode (see section III-D). To make the plot of figure 3 all

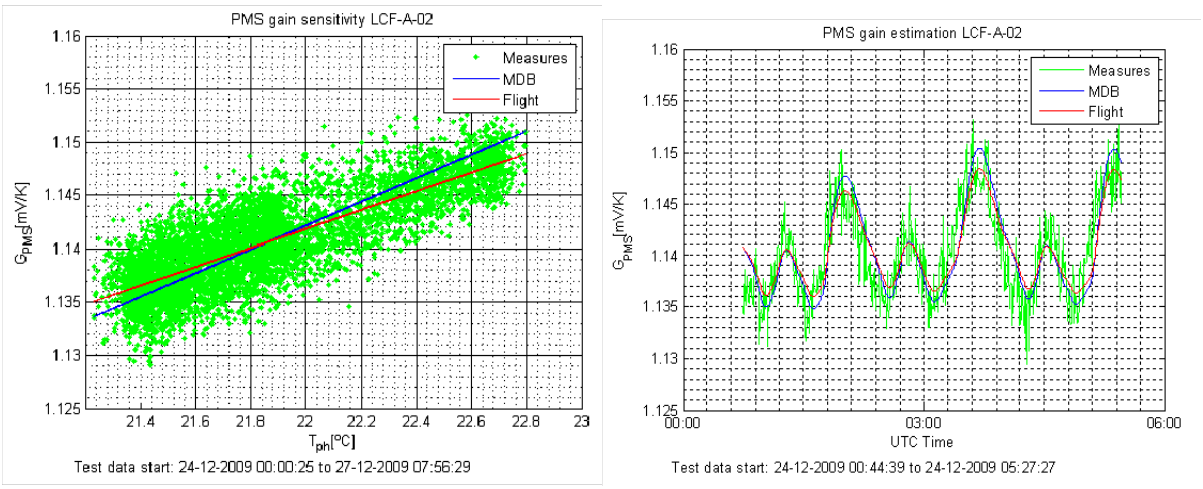

Fig. 2. PMS Gain sensitivity and estimation from physical temperature.

gains were corrected in temperature as described above. The main result is that the overall PMS gain is stable within 0.4% peak to peak in a period of three months, provided the temperature correction is applied.

B. PMS offset

The PMS offset voltages showed small jumps linked to the signal controlling the heaters in the payload temperature stabilization circuitry. Some receivers are more affected than others, but the effect is general. Plots of the offset voltage and the heater signal are drawn superimposed in figure 4 (left) to demonstrate this effect. To cancel this variation, a software correction was implemented based on an accurate characterization carried out with the data acquired during a test sequence specifically designed for it. It consisted of continuously driving the voltage detectors at four levels, so as to make continuous measurements of PMS offsets using the four-point technique [15]. The result is seen in the plot at the right of figure 4, showing the offset once the correction is applied. There are still some points where it is not perfect, but in general most of the points show only the random fluctuation due to thermal noise. A better insight on the quality of this correction is given in figure 5 where for all the receivers, the standard deviation of the measured offset is plot as a function of the receiver number. Three traces are given: without heater correction and with two different retrievals of the correction parameters measured at two different operations of the special sequence of calibration. The correction clearly reduces the

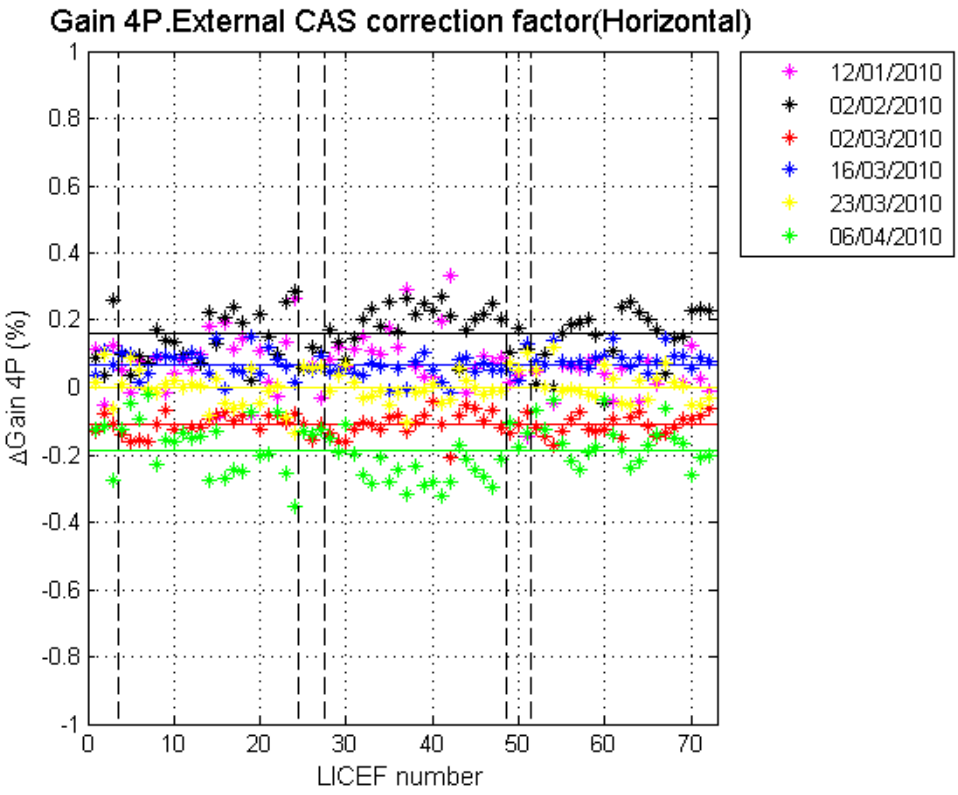

Fig. 3. PMS gain differences between separated calibration events

rms values of the offset and the results are very consistent with each other for both retrievals. The residual offset rms error is well below the 1 mV specification.

C. Correlator complex gain

The correlator gain G_{kj} is a complex valued parameter. Its amplitude is always around unity and very stable: only a negligible variation with time has been detected (see the plot at the left of figure 6). On the other hand, in baselines formed by two receivers not sharing a common local oscillator, the phase of G_{kj} has a significant variation. This phase is roughly equal to the phase difference between the signals generated by the oscillators, which vary independently as a function of their local temperature variation [16]. To account for this dependance, frequent phase calibration events must be carried out interspersed with the normal measurement operation. Several strategies were studied within the commissioning phase in order to decide the best phase calibration rate. To this end the payload was programmed to acquire data with different LO

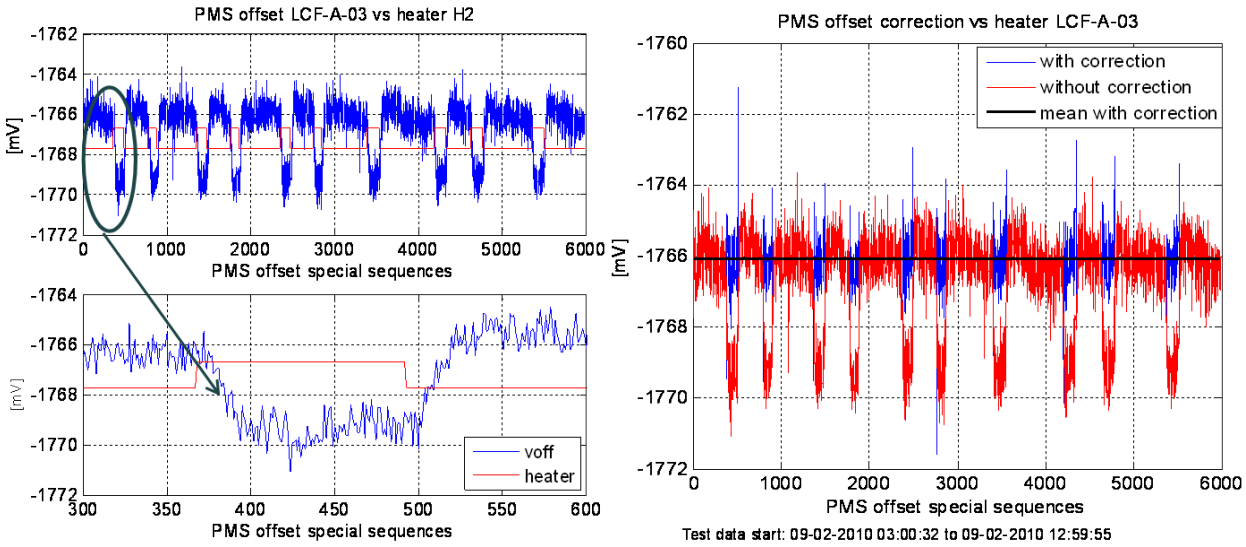

Fig. 4. Left: PMS offset and heater signal showing the high correlation between both. Right: Offset voltage after correction for heater signal dependance.

calibration rates, ranging from 2 minutes to 14 minutes. The final value was fixed after a complete analysis of the data acquired, bearing in mind that the final goal is to provide the maximum quality of the geophysical parameters retrievals. It was finally established in ten minutes to keep residual rms phase error below the 1 deg requirement. Figure 6 shows an example of the phase of G_{kj} along with its estimation based on a spline interpolation.

D. Internal calibration strategy

Two different sequences are used for internal calibration purposes. The so-called "LOcal" consists of injecting a short burst of noise (1.2s duration) just to record the phase of the correlation, which is equal to the phase of G_{kj}. Due to the distributed approach of the network [13], this is actually done twice, one with the "even" sources and other with the "odd" sources. For baselines not sharing noise source, their phases are estimated by solving a system of equations. The LOcal sequence is repeated once every ten minutes and has a total duration of 6 seconds to allow for signals to stabilize after changing the input power so drastically. This is the main contribution to an overall ratio of calibration to measurement slightly above 1%.

The second internal calibration sequence is the "Long-cal". As described in [17] it uses a whole orbit (actually two half-orbits) continuously dedicated to internal calibration alternating between

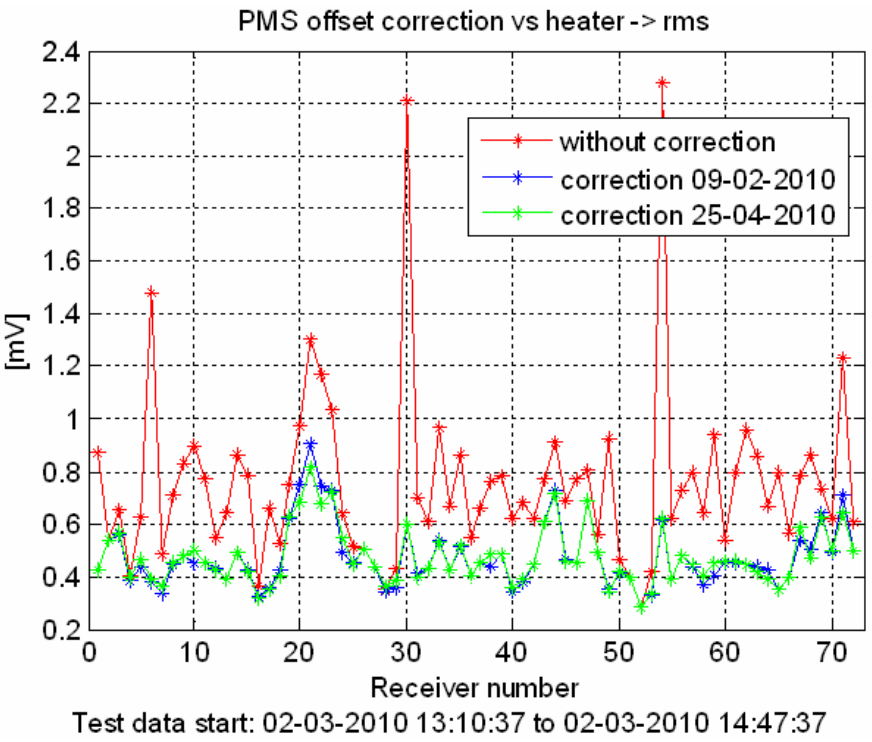

Fig. 5. PMS offset standard deviation of all receivers. After correction, the RMS is reduced well below the 1 mV specification.

two-level correlated noise and uncorrelated noise injection. Figure 7 shows the schematic time line of this sequence. The whole orbit of 5000 seconds is divided into 15 segments of about 400 seconds each. Each one includes three subsegments of correlated noise injection and a longer one of uncorrelated noise injection (abbreviated "U-noise"). This provides a total of 45 individual measurements of PMS gain, offset and amplitude of G_{kj} (its phase is ignored). All of them are averaged to obtain a calibration product that is saved and used later for correcting the science measurements as explained below. All the U-noise measurements are averaged together to estimate the visibility offset to be subtracted to all the subsequent measurements. Finally, using part of the correlated noise injection with time delays, the parameters of the fringe washing function are estimated. The long calibration sequence is performed once every eight weeks, which is enough to track the small variation of the retrieved parameters.

During science measurement operation, the PMS gain is estimated from the calibration product just described but corrected in temperature using the temperature sensitivity coefficients derived during the commissioning phase (see figure 2). The offset is estimated from the calibration product and the correction of the heater signal. The amplitude of the correlator gain is just the

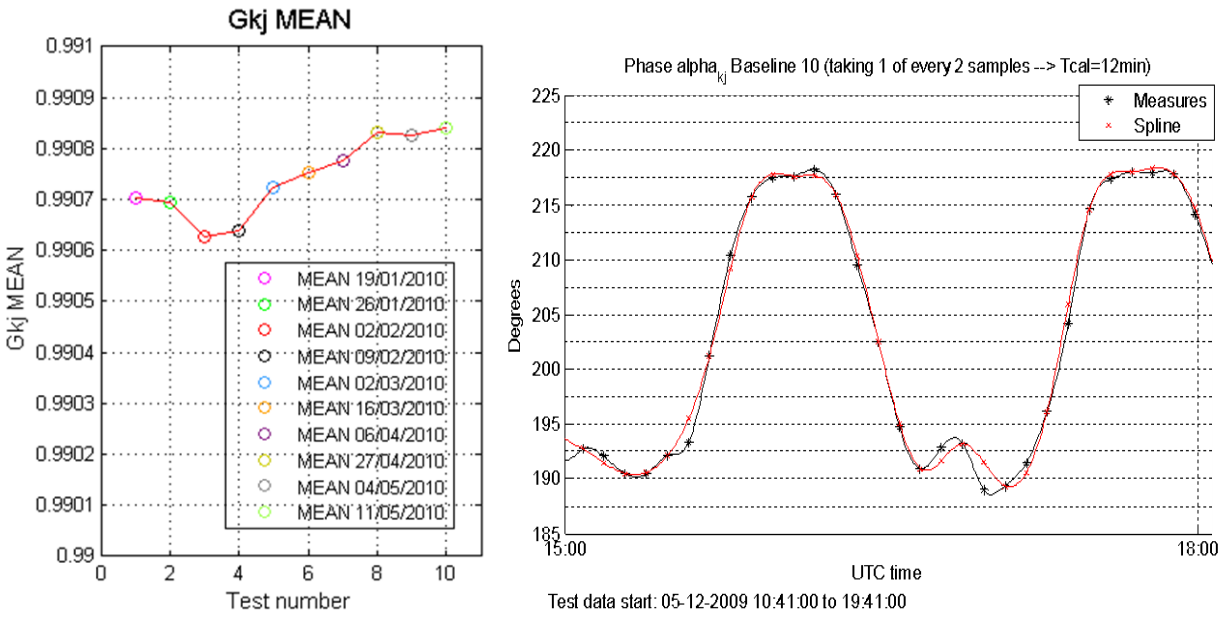

Fig. 6. Correlator complex gain G_{kj}: left: Stability of amplitude along time showing high stability in four-month span. Right: Fast phase variation due to local oscillator phase drift

one measured and its phase is estimated by spline interpolation between measurements of the LOcal sequence.

IV. External Calibration

External calibration is performed by commanding the platform to go into inertial attitude. When this command is received, the instrument starts to rotate with respect to the earth-fixed coordinate system until the earth disappears from the field of view of the antenna. At this point, the radiometer is measuring the brightness temperature of a fixed point of the sky, which is chosen to be near the galactic pole to avoid influence from the Galactic emission. Since the sky brightness temperature at L-band is known [18], the calibration parameters of the instrument are adjusted so as to match the measurements to this absolute reference.

External calibration is used to calibrate the Noise Injection Radiometers (NIRs), which means computing the equivalent noise temperature of their internal source [9]. For each NIR, two parameters are obtained (T_{NA} and T_{NR}), the first one used in equation (2) to measure the antenna temperature and the second one as a secondary standard for the PMS gain calibration in the internal calibration procedure [12].

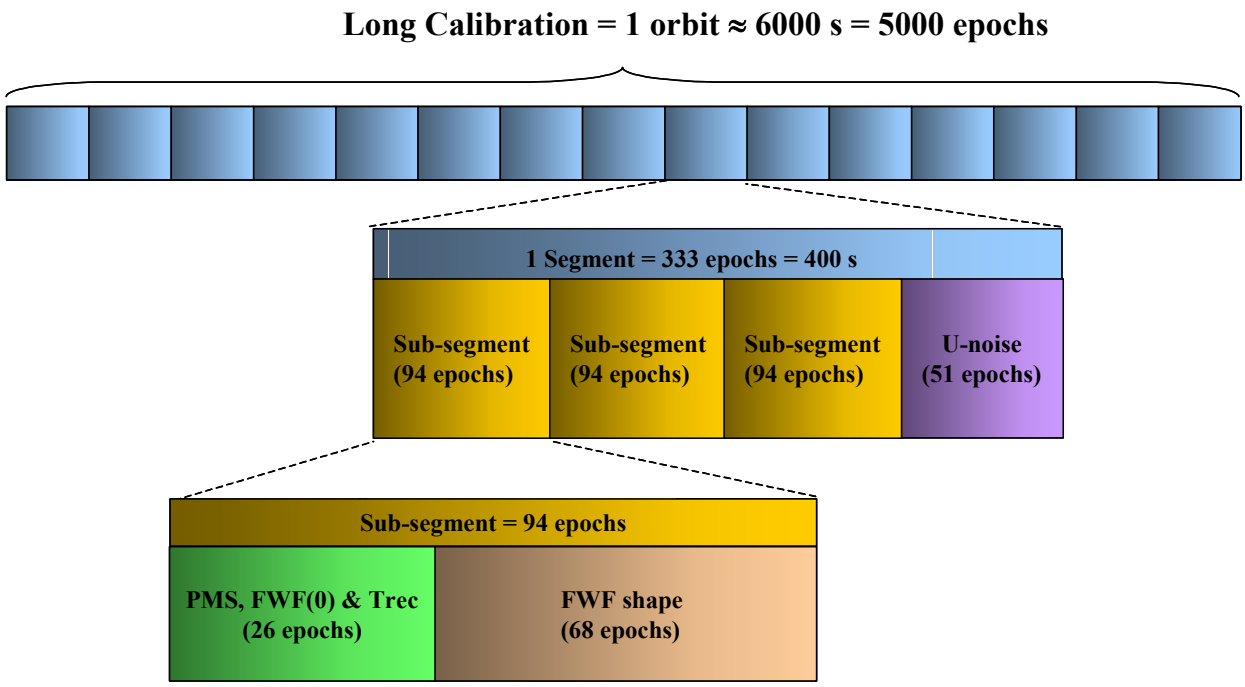

Fig. 7. Long calibration sequence

External calibration is also used to correct for the term of the PMS gain not included in the internal calibration, namely the overall loss between the antenna plane and the noise input port. This is achieved by comparing the PMS gain derived from internal calibration with the one obtained using the one-point approach described in [12], [19] and using the sky as cold standard and an internal resistor at known physical temperature as hot standard. Figure 8 shows the measured difference in percentage between both PMS gains. The comparison is made by translating the internal gain to the antenna reference plane using the S-parameters of the switches measured on ground and a rough estimation of the antenna ohmic efficiencies. The plot shows that the gains have a discrepancy of about 4%, which is completely out of requirements.

Correction factors were computed during the in-orbit payload characterization to be applied to internal noise distribution network parameters, switches and antenna efficiencies so as to make these two PMS gain measurements consistent with each other. The correction factors were computed once for a particular external calibration data set and saved as fixed parameters to use in subsequent calibrations. Eventually, during the mission lifetime these parameters could be updated. Figure 9 shows the difference in percentage between gain retrievals from both

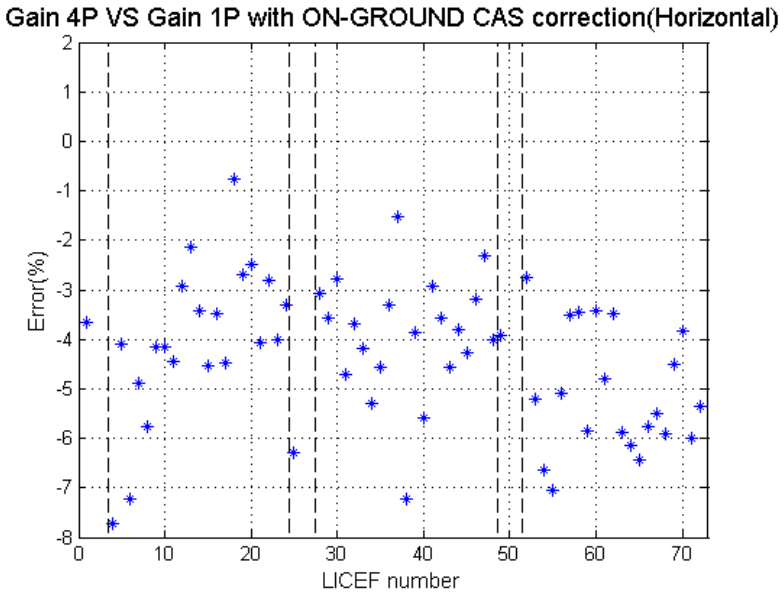

Fig. 8. Comparison between PMS gain retrieved with internal calibration and with external calibration.

external and internal calibration, once the correction factors have been applied. The different traces correspond to eight calibration events carried out at the dates specified in the figure, that is spanning about five months. The peak to peak differences in individual gains is always lower than $\pm 1\%$ and the drift of the average values is as low as 0.6%.

The gain derived from external calibration is more accurate than the one from internal calibration since it uses directly well known standards. The gain from internal calibration is based on using the NIR working in a specific mode of operation to measure the noise power injected to the receivers, which is then used as a secondary standard. This implies that the NIR has to be previously calibrated during the cold sky views. Figure 14 shows the long term stability of the PMS gain derived from external calibration using the one-point approach.

V. System performance

Two parameters have been used to define the overall system performance of the instrument [20]. The first is the radiometric sensitivity, defined as the temporal standard deviation of the brightness temperature, a function of the spatial direction. The second is the pixel bias, defined as the spatial standard deviation across the image in the director cosines coordinates. Both of them have been obtained after analyzing in detail the data retrieved from ocean scenes. Figure

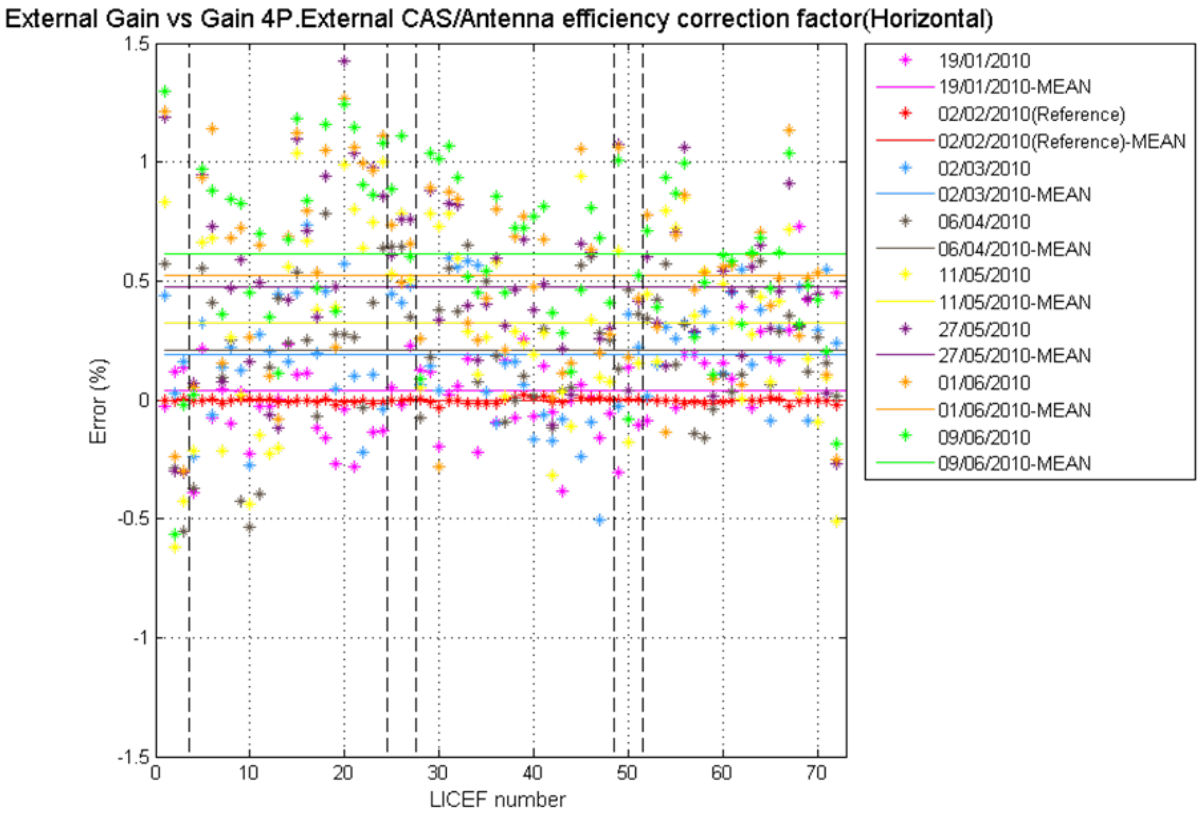

Fig. 9. PMS gain calibration. Difference between external and internal calibrations once correction factors applied. The results are for H-pol and for six calibration events spanning three months

(11) at the left shows an image of the radiometric sensitivity as a function of the director cosines coordinates. At the right of the figure there is a plot of a cut for $\xi = 0$ and a comparison between the measured values and those predicted by the following theoretical formula derived in [21]:

$$\Delta T_B(\xi,\eta) = \frac{\sqrt{3}d^2}{2}\frac{T_A + T_R}{\sqrt{B\tau_{eff}}}\frac{\Omega_a}{t(\xi,\eta)}\sqrt{1-\xi^2-\eta^2}\alpha_w\sqrt{N} \tag{6}$$

where T_A is the antenna temperature measured by the NIRs, T_R is the average receiver noise temperature measured while in external calibration, B is the noise equivalent bandwidth measured through the B parameter of the fringe washing function, τ_{eff} is the effective integration time taking into account the one-bit correlator [20], α_w is a coeficient that depends on the window used in the inversion process (0.45 for Blackmann window), Ω_a is the antenna equivalent solid angle and $t(\xi,\eta)$ is the normalized antenna power pattern, these last two obtained from the accurate antenna measurements carried out on ground. The plot shows an excellent agreement between

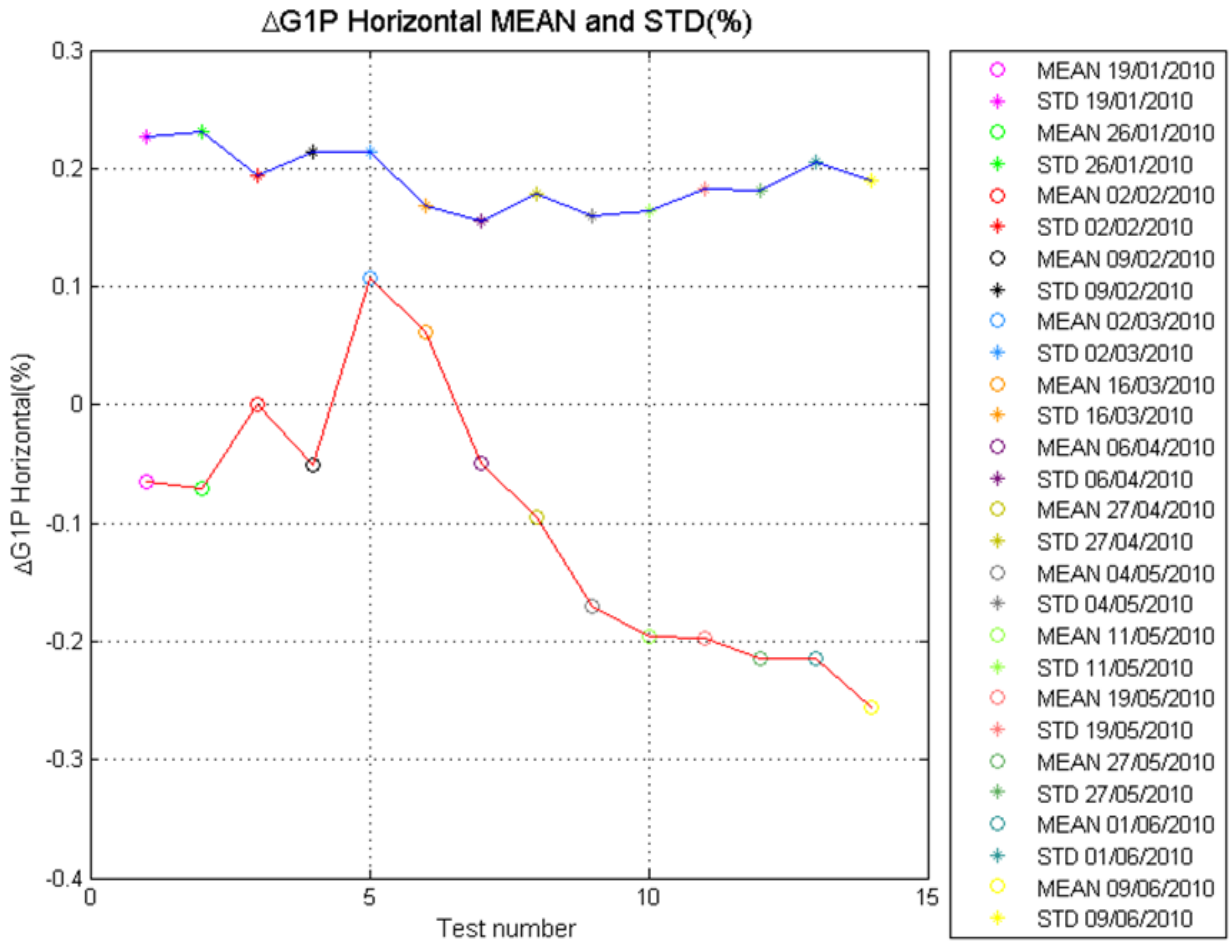

Fig. 10. Stability of the PMS gain derived from external calibration.

the measurement results and the theoretical predictions.

Figure 12 gives the same results but for the measurement of the cold sky during an external calibration maneuver. The agreement is also good, although not as perfect as for the ocean scenes. One of the reasons for this discrepancy might be associated to the back lobes of the antennas that when the instrument is looking upwards are collecting the power emitted by the Earth and are thus contaminating the measurements.

Figure (13) shows an image corresponding to the average of about 60 consecutive snapshots of pure ocean after compensating for the incidence angle dependance. The pixel bias is estimated by the spatial standard deviation of this image in a circle of radius 0.3 inside the alias-free field of view. According to the labels of the images, this turns out to be 1.2 K and 1.35 K respectively

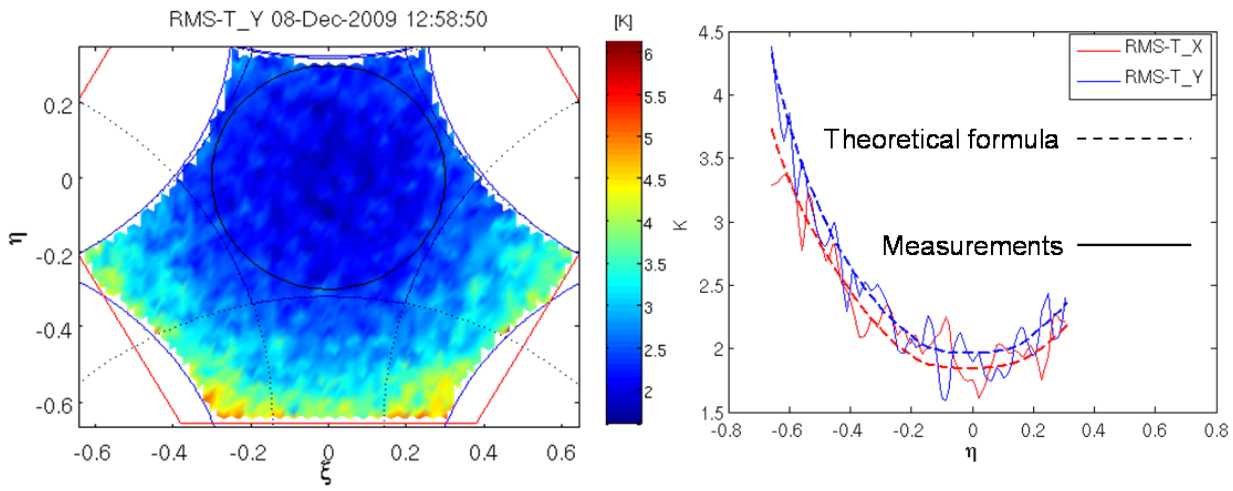

Fig. 11. Radiometric sensitivity in ocean scenes. Left: as a function of pixel position for H-pol. Right: comparison with theoretical formula

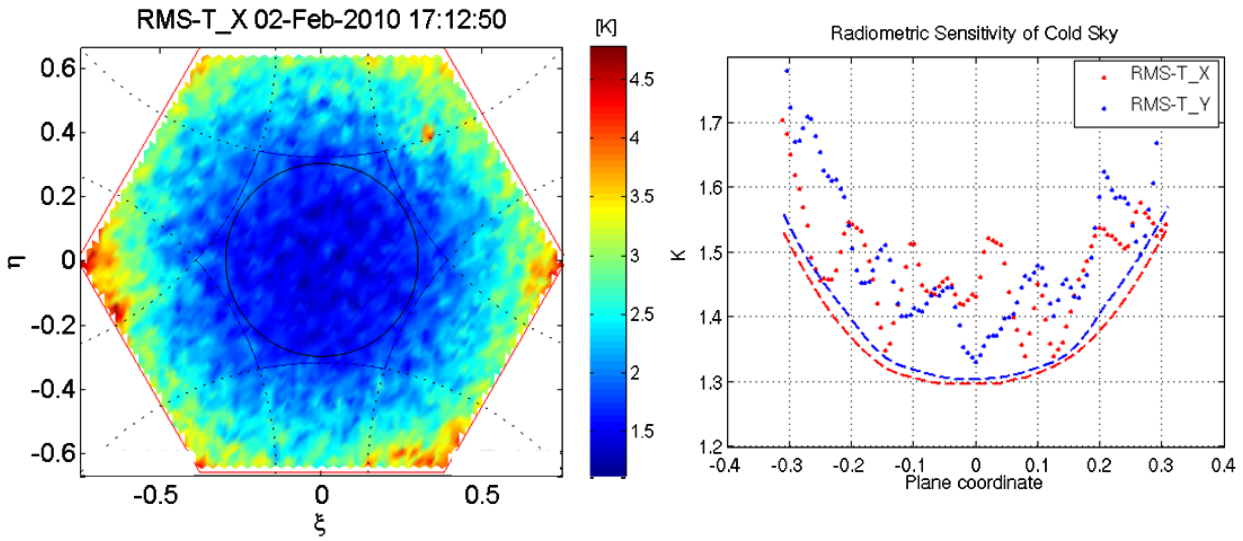

Fig. 12. Radiometric sensitivity during sky looks. Left: as a function of pixel position for H-pol. Right: comparison with theoretical formula

for horizontal and vertical polarization. It should be noted that the predicted value given in [20] was of 1.8K in the worst case, well in line with the values obtained with the real instrument, and it is a good indicator of the quality of the calibration and the inversion. The structure of the image and thus the corresponding standard deviation, is highly increased if the extended alias-free region is considered, although it is not shown here.

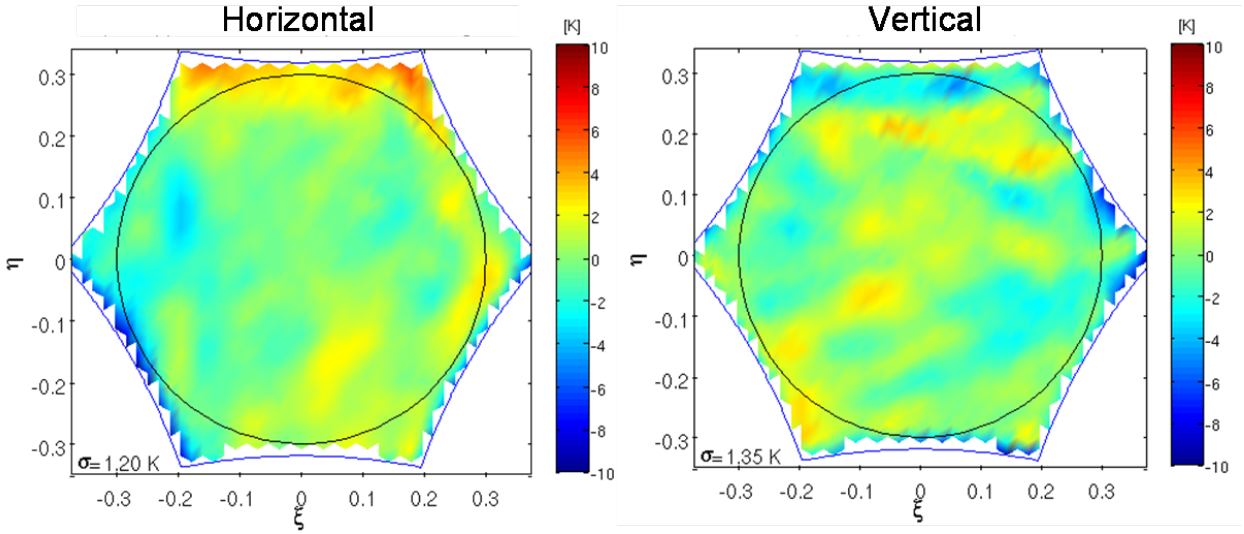

Fig. 13. Pixel bias derived from the brightness temperature of the ocean corrected to compensate the incidence angle dependency

VI. Brightness temperature images

Brightness temperature images are obtained by inverting the calibrated visibility using equation (5). Examples are presented here for ocean, land and ice using the inversion approach number 3 defined in [6] and implemented in the MIRAS Testing software [4]. The images correspond to maps of half the first Stokes parameter, that is $(T_H + T_V)/2$ to make them independent of the rotation angles between the instrument frame at each pixel and the ground frame. In the case of ocean images, the theoretical variation due to specular reflection, directly computed from the fresnel reflection coefficients, has been compensated so as to obtain fairly constant images in all the field of view. Only the data in the true alias-free zone is considered since it is the one of which its quality depends only on the quality of the visibility calibration.

Figure (14) shows a four-days cumulated image over ocean corresponding to data from 6th to 9th June 2010 using both ascending and descending orbits. The image shows low brightness temperature values on the Atlantic compatible with a known increase of salinity in this area. Other stable spatial structures are observed at certain locations over the globe, particularly at high latitudes, although no scientific assessment has been made about them in the frame of this work. They could be caused by RFI sources, particularly in Southern Greenland and North of Canada. What is apparent from this figure is the increase of brightness temperature at the Amazon river plume, which is due to the mixing of fresh water. This is confirmed by a zoom

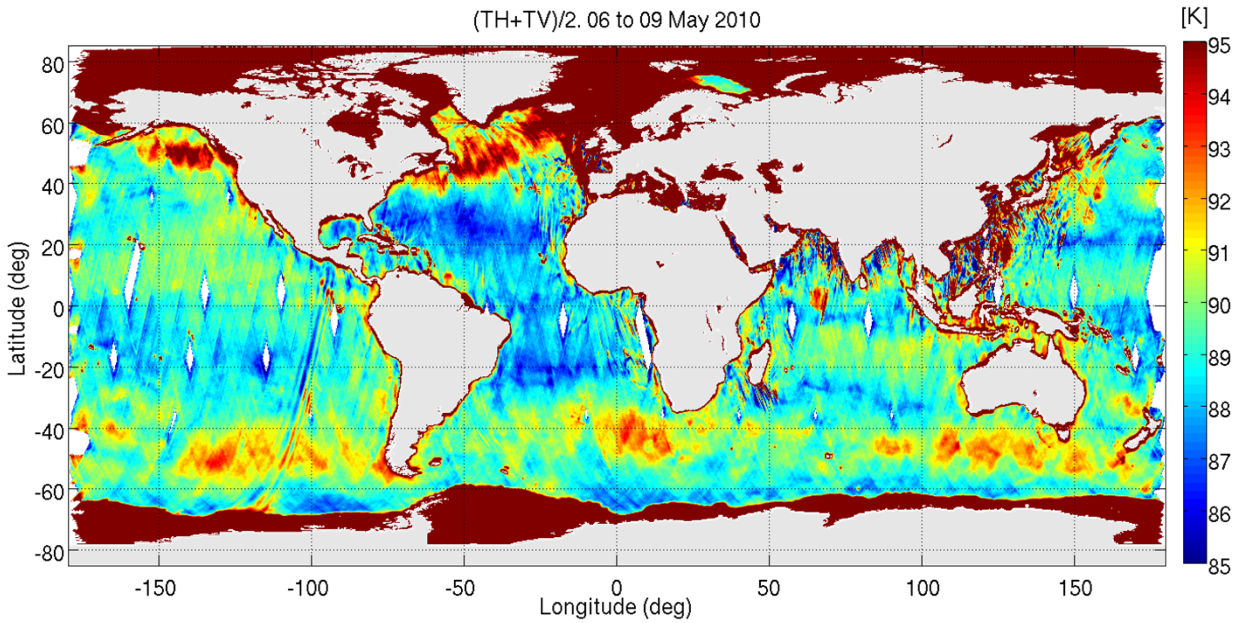

Fig. 14. Cumulated brightness temperature in ocean from 6th to 9th May 2010 for both ascending and descending orbits

of the image shown in figure 15. There is a clear negative gradient of brightness temperature that enters to the ocean just at the point where the river Amazon flows into the Atlantic ocean.

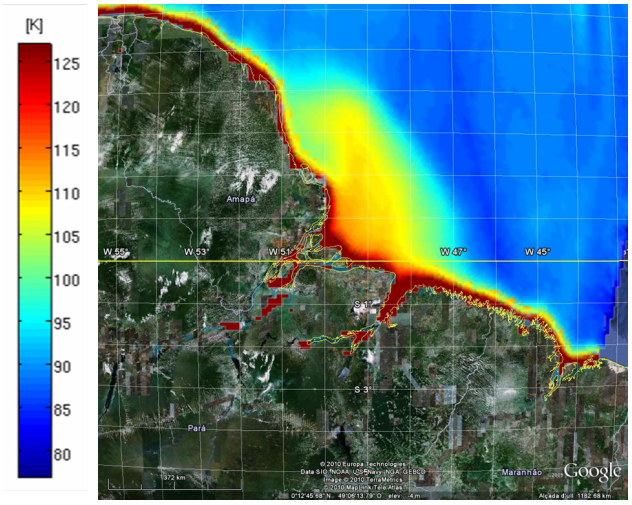

Fig. 15. Zoom of the Amazon river plume showing the influence of higher brightness temperature of fresh water entering into the ocean.

Figure 16 shows the retrieved brightness temperature over Antarctica. A fairly constant value of about 200K is seen at the right of the image and in particular at the Dome-C area, but higher

values are measured in other zones.

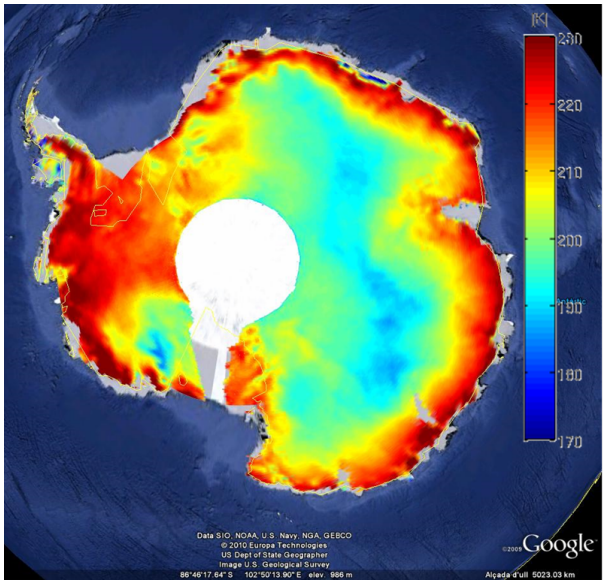

Fig. 16. Brightness temperature image over the Antarctica in 9th May 2010

Brightness temperature over land is expected to be more variable in time since it depends on the amount of water in the soil, which can have important variations when strong rain events are present. Also, differences from ascending to descending orbits are expected since they correspond respectively to the dawn and dusk times of the day. In any case, in order to have a global view of the L-band brightness temperature of the land areas, Figure 17 shows the cumulated brightness temperature for the same four days (6th to 9th May 2010), but separating ascending and descending orbits. Clear features are observed, which in general coincide with the zones of the planet where there are changes in soil moisture. However, there are zones of the planet, particularly in Europe and Asia, that are highly contaminated by RFI, making the brightness temperature images to saturate.

VII. Conclusions

MIRAS provides accurately calibrated visibility as a result of using a combination of internal and external calibration. During the in-orbit commissioning phase, all calibration parameters were measured and found consistent with the ones obtained during the on-ground characterization of the instrument. The visibility amplitude shows a high degree of stability both in short- and long terms, which allows to space apart the external calibration events. On the other hand, the

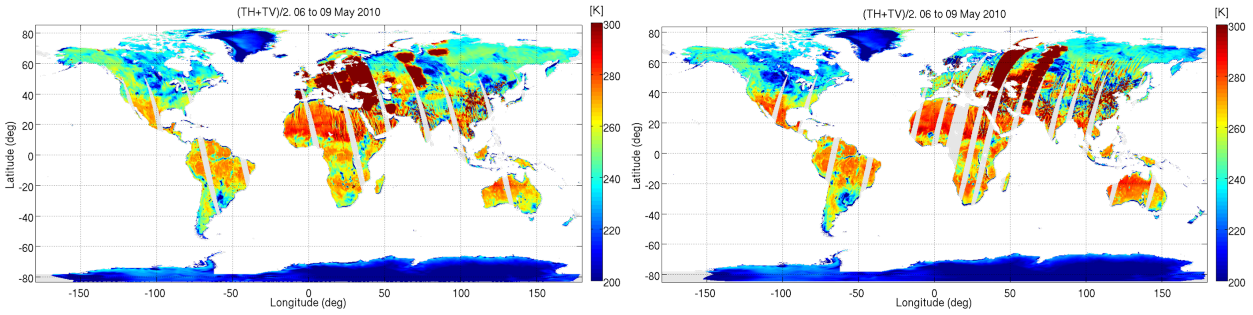

Fig. 17. Global brightness temperature for land regions in ascending (left) and descending (right) orbits

phase has significant variations, requiring to perform updates every ten minutes using internal calibration. The main overall system performance parameters, such as radiometric accuracy and pixel bias have been found well in accordance with the expected values. Brightness Temperature images of good quality in the alias-free field of view have been demonstrated using the UPC's MIRAS testing software, an independent processing tool able to ingest SMOS raw data and provide calibrated visibility and geo-located brightness temperature. Examples over sea, ice and land are given. As a general conclusion: SMOS mission is a success and good global maps of Soil Moisture and Ocean Salinity are expected to be produced in the years to come

REFERENCES

[1] H. Barré, B. Duesmann, and Y. Kerr, "SMOS. the mission and the system," *IEEE Transactions on Geoscience and Remote Sensing*, vol. 46, no. 3, pp. 587–593, March 2008.

[2] M. Martín-Neira and J. M. Goutoule, "MIRAS a two-dimensional aperture-synthesis radiometer for soil moisture and ocean salinity observations," *ESA Bulletin*, no. 92, pp. 95–104, November 1997.

[3] K. McMullan, M. Brown, M. Martín-Neira, W. Rits, S. Ekholm, J. Marti, and J. Lemanzyk, "SMOS: The payload," *IEEE Transactions on Geoscience and Remote Sensing*, vol. 46, no. 3, pp. 594–605, March 2008.

[4] I. Corbella, F. Torres, N. Duffo, V. González, A. Camps, and M. Vall-llossera, "Fast processing tool for SMOS data," in *International Geoscience and Remote Sensing Symposium, IGARSS 2008*, no. II. Boston(Ma), USA: IEEE, 7 - 11 July 2008, pp. 1152–1155.

[5] M. Brown, F. Torres, I. Corbella, and A. Colliander, "SMOS calibration," *IEEE Transactions on Geoscience and Remote Sensing*, vol. 46, no. 3, pp. 646–658, March 2008.

[6] I. Corbella, F. Torres, A. Camps, N. Duffo, and M. Vall-llossera, "Brightness temperature retrieval methods in synthetic aperture radiometers," *IEEE Transactions on Geoscience and Remote Sensing*, vol. 47, no. 1, pp. 285–294, January 2009.

[7] A. Camps, M. Vall-llossera, I. Corbella, N. Duffo, and F. Torres, "Improved image reconstruction algorithms for aperture synthesis radiometers," *IEEE Transactions on Geoscience and Remote Sensing*, vol. 46, no. 1, pp. 146–158, January 2008.

[8] M. Martín-Neira, M. Suess, and J. Kainulainen, "The flat target transformation," *IEEE Transactions on Geoscience and Remote Sensing*, vol. 46, no. 3, pp. 613–620, March 2008.

[9] A. Colliander, L. Ruokokoski, J. Suomela, K. Veijola, J. Kettunen, V. Kangas, A. Aalto, M. Levander, H. Greus, M. T. Hallikainen, and J. Lahtinen, "Development and calibration of SMOS reference radiometer," *IEEE Transactions on Geoscience and Remote Sensing*, vol. 45, no. 7, pp. 1967–1977, July 2007.

[10] I. Corbella, N. Duffo, M. Vall-llossera, A. Camps, and F. Torres, "The visibility function in interferometric aperture synthesis radiometry," *IEEE Transactions on Geoscience and Remote Sensing*, vol. 42, no. 8, pp. 1677–1682, August 2004.

[11] I. Corbella, F. Torres, A. Camps, A. Colliander, M. Martín-Neira, S. Ribó, K. Rautiainen, N. Duffo, and M. Vall-llossera, "MIRAS end-to-end calibration. Application to SMOS L1 processor," *IEEE Transactions on Geoscience and Remote Sensing*, vol. 43, no. 5, pp. 1126–1134, May 2005.

[12] F. Torres, I. Corbella, A. Camps, N. Duffo, M. Vall-llossera, S. Beraza, C. Gutierrez, and M. Martín-Neira, "Denormalization of visibilities for in-orbit calibration of interferometric radiometers," *IEEE Transactions on Geoscience and Remote Sensing*, vol. 44, no. 10, pp. 2679–2686, October 2006.

[13] F. Torres, A. Camps, J. Bará, I. Corbella, and R. Ferrero, "On-board phase and modulus calibration of large aperture synthesis radiometers: Study applied to MIRAS," *IEEE Transactions on Geoscience and Remote Sensing*, vol. GRS-34, no. 4, pp. 1000–1009, July 1996.

[14] I. Corbella, F. Torres, N. Duffo, M. Martín-Neira, V. González-Gambau, A. Camps, and M. Vall-llossera, "On-ground characterization of the SMOS payload," *IEEE Transactions on Geoscience and Remote Sensing*, vol. 47, no. 9, pp. 3123–3133, September 2009.

[15] F. Torres, N. Duffo, I. Corbella, A. Camps, M. Vall-llossera, and L. Sagués, "Dynamic range and linearity tradeoff in detectors for interferometric radiometers," *IEE Electronics Letters*, vol. 39, no. 25, pp. 1852–1854, 11th December 2003.

[16] V. González-Gambau, F. Torres, and N. Duffo, "Phase calibration temperature track in interferometric radiometers devoted to earth observation," in *Proceedings of SPIE Europe Remote Sensing 2008*. Cardiff. Wales, United Kingdom: SPIE Europe Remote Sensing 2008. Sensors, Systems, and Next-Generation Satellites XII., 15-18 september 2008.

[17] I. Corbella, F. Torres, N. Duffo, A. Camps, M. Vall-llossera, and V. González, "MIRAS in-orbit calibration," in *International Geoscience and Remote Sensing Symposium, IGARSS 2007*, no. ISBN DVD-ROM: 1-4244-1212-9. Barcelona, Spain: IEEE, 23 - 27 July 2007, pp. 3622–3625.

[18] D. M. Le Vine and S. Abraham, "Galactic noise and passive microwave remote sensing from space at L-band," *IEEE Transactions on Geoscience and Remote Sensing*, vol. 42, no. 1, pp. 119–129, January 2004.

[19] F. Torres, V. González-Gambau, and C. González-Haro, "One-point calibration in interferometric radiometers devoted to earth observation," in *Proceedings of SPIE Europe Remote Sensing 2008.* Cardiff. Wales, United Kingdom: SPIE Europe Remote Sensing 2008. Sensors, Systems, and Next-Generation Satellites XII., 15-18 september 2008.

[20] I. Corbella, F. Torres, A. Camps, J. Bará, N. Duffo, and M. Vall-llossera, "L-band aperture synthesis radiometry: hardware requirements and system performance," in *International Geoscience and Remote Sensing Symposium, IGARSS 2000*, vol. 7. Honolulu (Hw), USA: IEEE, 24-28 July 2000, pp. 2975 – 2977.

[21] A. Camps, "Application of interferometric radiometry to Earth observation," Ph.D. dissertation, Universitat Politècnica de Catalunya, November 1996.

SOME RESULTS ON SMOS-MIRAS CALIBRATION AND IMAGING

Ignasi Corbella[(1)], Francesc Torres[(1)], Nuria Duffo[(1)], Verónica González-Gambau[(1)], Israel Duran[(1)], Miriam Pablos[(1)], Manuel Martín-Neira[(2)]

(1) Remote Sensing Laboratory, Universitat Politècnica de Catalunya (UPC).
C/ Jordi Girona 1-3. 08034 Barcelona, Spain.
(2) European Space Agency (ESA-ESTEC) Noordwijk. The Nederlands
contact e-mail: corbella@tsc.upc.edu

ABSTRACT

After the six-month long In-Orbit Commissioning Phase (IOCP) the SMOS satellite started to work in its fully operational mode. During the IOCP, the payload MIRAS was completely characterized, both in short- and long-term, and the optimum calibration rate for in-flight operation was established. The results show that the amplitude of the visibility is very stable, thus allowing a very low calibration rate, and that the phase has a systematic and periodic variation, easily tracked with short but frequent internal calibration sequences. Absolute calibration for antenna temperature is carried out by external maneuvers to account for drift in the reference Noise Injection Radiometer. Brightness temperature images of good quality are obtained by inverting the calibrated visibility. The images show features compatible with ocean salinity over ocean and soil moisture over land.

1. INTRODUCTION

SMOS (acronym of Soil Moisture and Ocean Salinity) is an European Space Agency (ESA) mission aimed at providing global maps of soil moisture over land and sea surface salinity over oceans [1]. The mission payload is the Microwave Imaging Radiometer with Aperture Synthesis (MIRAS) [2, 3], an L-band, Y-shape 2D interferometric radiometer manufactured by EADS-CASA Espacio (ES) and integrated to a generic PROTEUS platform manufactured by Thales Alenia Space. SMOS was successfully launched on 2nd November 2009 from the Plesestz cosmodrome by a launcher from Eurockot. The payload was switched on on 17th November and since then raw data measurements are being received regularly by the ground segment data acquisition station, located near Madrid (ES). After due processing, they provide the first-ever global brightness temperature maps at L-band.

The work was supported by the European Space Agency and EADS-CASA Space Division under ESTEC contract 17950/03/NL/FF-SMOS; and by the Spanish Ministry of Science and Innovation and FEDER under projects TEC2008-06764-C02-01 and MIDAS-5 ESP2007-65667-C04-0

The first six months of operation were dedicated to make a complete and systematic check of the payload, including the retrieval of all calibration parameters and their temperature dependance [4]. Good brightness temperature images can be produced by inverting the calibrated visibility, which is a good indicator of the quality of the calibration. This paper shows some of the results, especially those dealing with the main calibration parameters and their stability; and the brightness temperature imaging. All the results have been obtained using the MIRAS testing software [5], developed by the UPC team.

2. CALIBRATION

Calibration is needed to provide accurate values of visibility for all receiver pairs and antenna temperature for at least one element. Besides, image reconstruction algorithms [6, 7] need the fringe washing function shape and the flat target response [8]. MIRAS uses a combination of both external and internal calibration to estimate all the time varying parameters [9]. Stable parameters such as antenna patterns, S-parameters of noise distribution network and others, are directly used from on-ground characterization [10].

The outcome of the MIRAS calibration system consists of the following parameters: the PMS (power monitoring system) gain G_k and offset v_{off}, the correlation complex gain G_{kj} in amplitude and phase, the NIR source noise temperature T_{NA} and the the normalized fringe washing function [11]. All of them are periodically updated during the mission to account for instrumental drifts. Additionally, the Flat Target Response [8] is also considered a calibration parameter.

2.1. Internal and External calibration

External calibration is performed by commanding the platform to go into inertial attitude. In this case, the instrument starts to rotate with respect to the earth-fixed coordinate system until the earth disappears from the field of view of the antenna. At this point, the radiometer is measuring the brightness temperature of a fixed point of the sky, which is chosen

to be near the galactic pole to avoid influence from the Galactic emission. Since the sky brightness temperature at L-band is known [12], the calibration parameters of the instrument are adjusted so as to match the measurements to this absolute reference. External calibration provides the best quality of calibration and it is the only way to obtain the absolute accuracy of the instrument. However, the pointing maneuvers cannot be performed too often and the impact in terms of percentage of time dedicated to calibration is high.

Internal calibration is carried out by periodically injecting noise to all receivers using an internal source and a distribution network [11]. It tracks fast variations of parameters, but for those requiring a known calibration standard, it cannot provide their absolute values. In this case, the accuracy of the internal calibration relies on the quality of a secondary standard, which has to be previously calibrated using the external view. On the other hand, noise injection is very fast and is easily interspersed between normal measurement operation.

The calibration method utilized for each of the parameters is the following

- PMS gain: External calibration with periodic tracking by internal calibration
- PMS offset: Internal calibration.
- Correlator gain (amplitude and phase): Internal calibration.
- NIR internal noise temperature: External calibration
- Fringe washing function parameters: Internal calibration

2.2. Calibration rate

Most of the calibration procedures and measurement sequences were precisely defined during the on-ground characterization of the instrument [10]. Then, the in-orbit commissioning phase has been essential to adjust the timing of calibration events in accordance with the real in-flight instrument operation [4]. Particularly, the following general trends have been observed:

- Flat Target Response: Stable, to be corrected only twice a year.
- Fringe washing function shape: The same stability as the Flat Target Response
- Visibility amplitude: To be updated once every 8 weeks
- Antenna temperature: Needs to be calibrated every 2 weeks
- Visibility phase. A calibration is needed every 10 minutes.

Some parameters, as the PMS gain and offsets have been accurately characterized in terms of temperature variation though the computation of sensitivity parameters. This, in combination with a very low physical temperature drift of the whole instrument, has allowed to reduce the need for their frequent calibration updates. New sensitivity parameters have been derived during the in-orbit commissioning phase and they are very well in agreement with the ones obtained during the ground characterization.

As a general rule, the percentage of total time devoted to calibration must be the minimum, just to ensure that the quality of the measurements is according to the requirements. In SMOS, about one percent of the time is used in calibration. This has been achieved by minimizing the number of external calibration maneuvers, using accurate thermal characterization and agreeing a compromise value for the parameters changing the fastest (phase of visibility).

2.3. Calibration parameters trend

Figure 1 shows a plot of the long-term stability of the amplitude of correlator gain (G_{kj}), along with the short-term variation of its phase for a baseline having two different local oscillators. As seen, the amplitude has negligible variation from one calibration event to another. On the other hand, the phase variation is large, but can be easily tracked by frequent internal calibration sequences: every ten minutes a short burst of correlated noise is injected during 1.2 seconds to all receivers to measure this phase.

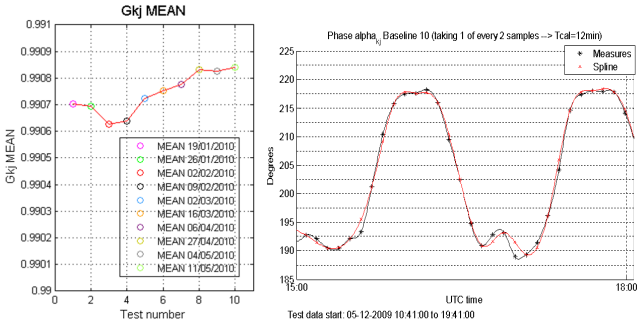

Fig. 1. Left: Stability of the amplitude of G_{kj} along time. Right: phase of G_{kj} variation due to local oscillator phase drift

Figure 2 shows the measurements of PMS gain during a specific test carried out to derive its thermal sensitivity. The figure shows a comparison between the measured gain and the one derived from the physical temperature and the sensitivity, demonstrating that the gain can be accurately tracked just by measuring the temperature sensors.

Figure 3 shows the long-term stability of both PMS gain and offset. It shows the difference of the averaged values retrieved during ten calibration events distributed regularly between 12th January to 11th May 2010. It turns out that the long-term drift is lower than 0.5 mV for the offset and 0.2% for the gain, which has led the the proposal of a PMS intercalibration period of eight weeks to be conservative.

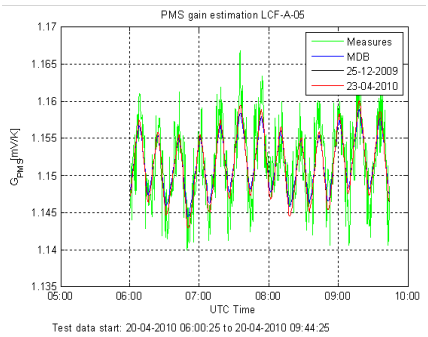

Fig. 2. PMS gain tracking using the sensitivity parameter

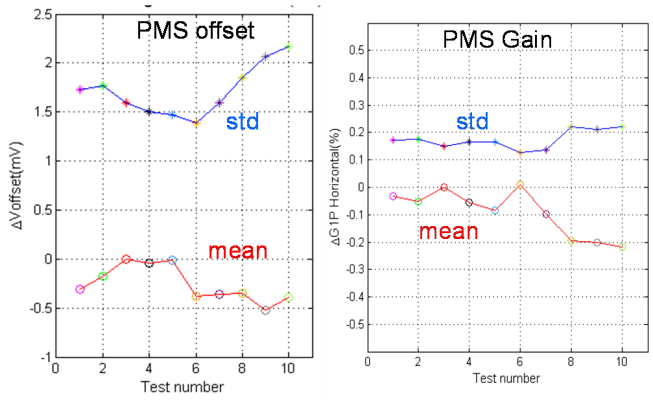

Fig. 3. Long term PMS calibration. The test numbers correspond to different calibration events carried out in a 4-month span, from 19th January 2010 to 11th May 2010. Left: Offset, Right: Gain

3. IMAGING

Figure 4 shows an example of several snapshots in a pass over Australia in dual polarization mode. Since the polarization is mixed in the field of view, the definitions Horizontal and Vertical refer to the sub-satellite track. These images were obtained just two weeks after the payload switch-on with still uncomplete calibration. Nevertheless, they already show that the instrument is capable of producing good brightness temperature images. Improved images were obtained after the instrument was fully characterized and calibrated. Figure 5 shows two images corresponding to four-day cumulated data over Australia acquired in January 2010 and in February 2010. Between both dates there were strong rain events in the eastern part of Australia due to the pass of the tropical storm "Olga". This is clearly visible in the images, where lower britghtness temperatures are measured after the pass of the storms.

Over the ocean the brightness temperature is lower than in land and has also a much smaller dynamic range than in land. On the other hand its spatial variation is much smoother, allowing to perform spatial averages. Figure 6 shows the averages of 150 consecutive snapshots over the ocean both

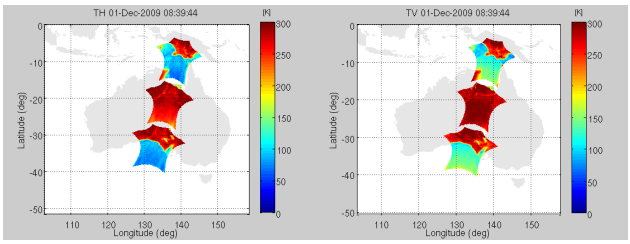

Fig. 4. L-Band brightness temperature maps at instrument reference frame retrieved over Australia in a descending orbit Left: H-polarization at satellite track. Right: V-polarization at satellite track

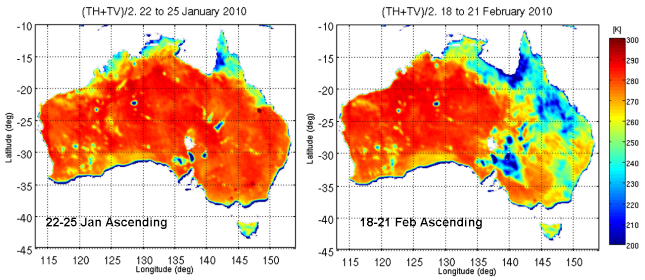

Fig. 5. Average of horizontal and vertical L-Band brightness temperature. Four-day cumulated data for ascending orbits. Left: 22nd to 25th January 2010. Right 18th to 21th February 2010.

for horizontal and vertical channel. The strong dependance with the incidence angle, characteristic of the ocean brightness temperature is clearly visible in these images. Also, some artifacts can be seen in the extended alias-free zone, in which a model is used to estimate the brightness temperature of the sky alias zone and the result subtracted to the images. This procedure is not eliminating all the errors in the sky alias zone. To assess the instrument capability of making brightness temperature images, only the strict alias-free zone has been considered in subsequent processing.

As an example, figure 7 shows the image of four-day cumulated first Stokes parameter over the Atlantic. As expected, it has lower values in those regions where the salinity is known to be larger according to the NOAA climatological data.

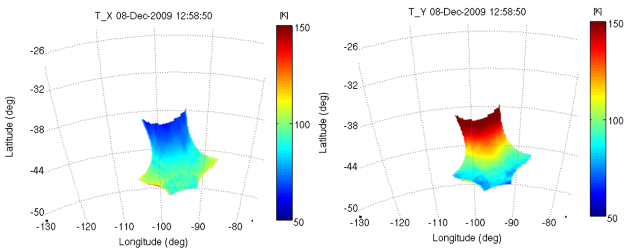

Fig. 6. Average of 150 snapshots in for a region of pure ocean. Left: Horizontal polarization. Right: Vertical polarization.

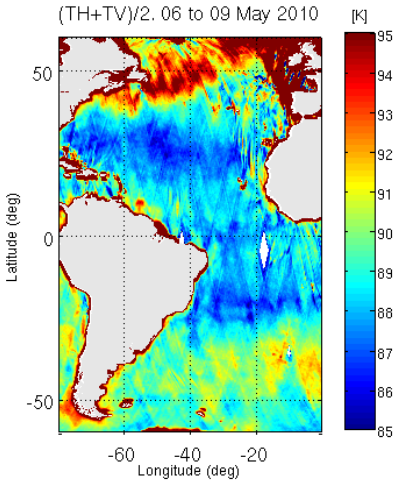

Fig. 7. Image of cumulated first Stokes parameter ($(T_H + T_V)/2$) over the Atlantic for 6th to 9th May 2010. The variation is compatible with the global maps of salinity available from NOAA climatological data.

4. CONCLUSIONS

SMOS is producing high quality brightness temperature images thanks to the accurate characterization and calibration of the instrument MIRAS, which was performed first on ground and later in flight conditions during the In-Orbit Commissioning phase. Most of the calibration parameters have very small drift with time and temperature, while the others are accurately tracked using sensitivity coefficients or specially designed internal calibration sequences. The overall time dedicated to calibration is slightly larger that 1% of the measurement time, in agreement with the mission requirements. Images of first Stokes parameter over land and ocean show geophisical features compatible with soil moisture and salinity respectively.

5. REFERENCES

[1] Hubert Barré, Berthyl Duesmann, and Yann Kerr, "SMOS. the mission and the system," *IEEE Transactions on Geoscience and Remote Sensing*, vol. 46, no. 3, pp. 587–593, March 2008.

[2] Manuel Martín-Neira and Jean Marie Goutoule, "MIRAS a two-dimensional aperture-synthesis radiometer for soil moisture and ocean salinity observations," *ESA Bulletin*, , no. 92, pp. 95–104, November 1997.

[3] Kevin McMullan, Michael Brown, Manuel Martín-Neira, W Rits, S Ekholm, J Marti, and Jerzky Lemanzyk, "SMOS: The payload," *IEEE Transactions on Geoscience and Remote Sensing*, vol. 46, no. 3, pp. 594–605, March 2008.

[4] Ignasi Corbella, Francesc Torres, Nuria Duffo, Verónica González-Gambau, Miriam Pablos, Israel Duran, and Manuel Martín-Neira, "First results on MIRAS calibration and overall SMOS performance," in *11th Specialist Meeting on Microwave Radiometry and Remote Sensing of the Environment - μRad 2010*, Washington DC, USA, 1-4 March 2010, pp. 1–4.

[5] Ignasi Corbella, Francesc Torres, Nuria Duffo, Verónica González, Adriano Camps, and Mercè Vall-llossera, "Fast processing tool for SMOS data," in *International Geoscience and Remote Sensing Symposium, IGARSS 2008*, Boston(Ma), USA, 7 - 11 July 2008, number II, pp. 1152–1155, IEEE.

[6] Ignasi Corbella, Francesc Torres, Adriano Camps, Nuria Duffo, and Mercè Vall-llossera, "Brightness temperature retrieval methods in synthetic aperture radiometers," *IEEE Transactions on Geoscience and Remote Sensing*, vol. 47, no. 1, pp. 285–294, January 2009.

[7] Adriano Camps, Mercè Vall-llossera, Ignasi Corbella, Nuria Duffo, and Francesc Torres, "Improved image reconstruction algorithms for aperture synthesis radiometers," *IEEE Transactions on Geoscience and Remote Sensing*, vol. 46, no. 1, pp. 146–158, January 2008.

[8] Manuel Martín-Neira, Martin Suess, and Juha Kainulainen, "The flat target transformation," *IEEE Transactions on Geoscience and Remote Sensing*, vol. 46, no. 3, pp. 613–620, March 2008.

[9] Michael Brown, Francesc Torres, Ignasi Corbella, and Andreas Colliander, "SMOS calibration," *IEEE Transactions on Geoscience and Remote Sensing*, vol. 46, no. 3, pp. 646–658, March 2008.

[10] Ignasi Corbella, Francesc Torres, Nuria Duffo, Manuel Martín-Neira, Verónica González-Gambau, Adriano Camps, and Mercè Vall-llossera, "On-ground characterization of the SMOS payload," *IEEE Transactions on Geoscience and Remote Sensing*, vol. 47, no. 9, pp. 3123–3133, September 2009.

[11] Ignasi Corbella, Francesc Torres, Adriano Camps, Andreas Colliander, Manuel Martín-Neira, Serni Ribó, Kimmo Rautiainen, Nuria Duffo, and Mercè Vall-llossera, "MIRAS end-to-end calibration. Application to SMOS L1 processor," *IEEE Transactions on Geoscience and Remote Sensing*, vol. 43, no. 5, pp. 1126–1134, May 2005.

[12] David M. Le Vine and Saji Abraham, "Galactic noise and passive microwave remote sensing from space at L-band," *IEEE Transactions on Geoscience and Remote Sensing*, vol. 42, no. 1, pp. 119–129, January 2004.

FIRST RESULTS ON MIRAS CALIBRATION AND OVERALL SMOS PERFORMANCE

Ignasi Corbella[(1)], Francesc Torres[(1)], Nuria Duffo[(1)], Verónica González-Gambau[(1)], Miriam Pablos[(1)], Israel Duran[(1)], Manuel Martín-Neira[(2)]

(1) Remote Sensing Laboratory, Universitat Politècnica de Catalunya (UPC).
C/ Jordi Girona 1-3. 08034 Barcelona, Spain.
(2) European Space Agency (ESA-ESTEC) Noordwijk. The Nederlands
contact e-mail: corbella@tsc.upc.edu

ABSTRACT

After the successful launching of the SMOS satellite, the first continuous streams of data are being processed and carefully analyzed in the frame of the SMOS In-Orbit Commissioning phase. Results regarding instrument calibration parameters retrieval, both internal and external, and brightness temperature imaging are presented. Images of ocean, ice and land are given as examples.

Index Terms— SMOS, interferometric synthetic aperture radiometry

1. INTRODUCTION

SMOS (acronym of Soil Moisture and Ocean Salinity) is a European Space Agency (ESA) mission designed to provide global maps of soil moisture over land and sea surface salinity over oceans [1]. It consists of a satellite in a sun-synchronous orbit at about 770 km height carrying a passive L-band sensor called MIRAS (Microwave Imaging Radiometer with Aperture Synthesis) [2]. The satellite was successfully launched the 2nd November 2009 from the Plesestz cosmodrome in northern Russia and the payload was switched on on 17th November 2009. Since then, continuous data is regularly received by the ground segment data acquisition station located in Villafranca del Castillo, near Madrid (E).

The SMOS In-Orbit Commissioning Phase (IOCP) started just after the 3-week long Switch-On and Data Acquisition Phase (SODAP), which was mainly focused at testing low level processes for data acquisition and handling. The IOCP has an overall duration of 6 months and the first half part comprises the characterization, calibration, validation and verification of the instrument [3]. The main goal is to provide a "fine tune" of MIRAS by means of: - Systematic check of all instrument modes - Retrieval of internal and external calibration parameters - Computation of temperature sensitivity coefficients - Assessment on imaging capability - Assessment on calibration rate requirement and - Instrument overall performance evaluation: Stability, Radiometric sensitivity, Radiometric accuracy and Absolute accuracy .

Most of the goals are being successfully achieved on time thanks to the combined effort of a team formed by EADS-CASA Espacio (E) as instrument manufacturer; Deimos Enginheria (P) developer of the Level 1 Prototype Processor (L1PP); the ESA Calibration Expert Center (CEC) dedicated to analyze the quality of the calibration data; and the Universitat Politecnica de Catalunya (UPC) responsible of the definition and implementation of calibration and processing algorithms. All of them are efficiently led by the ESA's principal engineer of the instrument.

The following sections provide a brief description of the activities carried out by UPC in the frame of the SMOS IOCP and shows the main results achieved, including determination of calibration parameters and their stability, as well as retrieval of brightness temperature images of ocean, ice and land. Everything has been processed using the MIRAS Testing Software, an independent software tool developed by UPC, capable of producing geolocated brightness temperature out of the raw data downloaded from the payload [4].

2. INTERNAL CALIBRATION

The procedures for MIRAS internal calibration are fully described in [5]. Essentially, calibration is carried out by injecting two-levels of correlated noise into all receivers [6] using a distributed approach to simplify the internal noise distribution network. The outcomes of the calibration procedure are three parameters: the power measurement system (PMS) gain (G_k) and offset (v_{off}) and the correlation complex gain (G_{kj}). Once these parameters are known, the calibrated visibility during scene observation is computed as

$$V_{kj} = \frac{M_{kj}\sqrt{T_{sys_k}T_{sys_j}}}{G_{kj}} \quad \text{where} \quad T_{sys_k} = \frac{v_k - v_{off_k}}{G_k} \quad (1)$$

This work was supported by the European Space Agency and EADS-CASA Space Division under ESTEC contract 17950/03/NL/FF-SMOS; and by the Spanish Ministry of Science and Technology (MCYT) under project TEC2008-06764-C02-01.

where v_k is the measured PMS voltage and M_{kj} the normalized correlation. Calibration parameters are measured at different times than when used during target observation. In order to accurately predict their values at measurement times, it is important to carefully assess their stability and temperature dependance. The following subsections show the main results obtained in specific tests carried out during the IOCP in order to measure the calibration parameters and their stability [3].

2.1. PMS gain

Figure 1 shows the relative PMS gain variation in percentage with respect to the average value. It has been computed after analyzing a total of 2499 samples measured during more than 24 hours with the instrument continuously in calibration mode. As seen, most of the receivers have PMS gain variations below 0.5% rms and all of them are well below the specified 1%. The plot at the right shows the long-term stability of the gain. It represents the difference in measured gain for 6 different calibration events separated more than one month. The result is that the PMS mean gain is stable within 1.2% peak to peak in a period of one month, and about 0.6% mean drift.

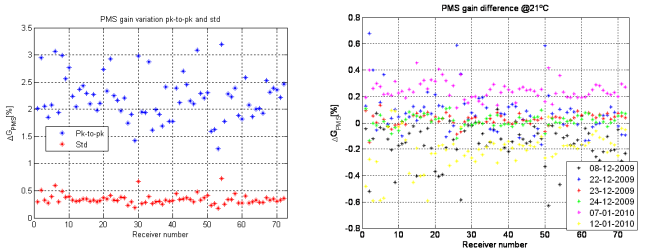

Fig. 1. Relative PMS gain variation in 24 hours continuous measurements (left) and between separated calibration events

Nevertheless, there is still a small dependance of the PMS gain with temperature. To characterize this behavior, plots of PMS voltages as a function of temperature have been produced and sensitivity coefficients computed from linear regression. An example of such plots is given in figure 2 along with a comparison between the measured gain and the one predicted from the temperature measurement. Two values of sensitivity are shown, one in blue corresponding to on ground measurement [7] and other in red obtained from flight data in the frame of the IOCP.

2.2. PMS offset

The PMS offset voltages showed unexpected jumps linked to the signal controlling the heaters in the temperature stabilization circuitry. Some receivers are more affected than others, but the effect is general. A correction has been implemented so as to estimate the offset using its mean value, the physical temperature and the heater signals. Figure 3 shows the comparison between the estimated offset and the measured one for

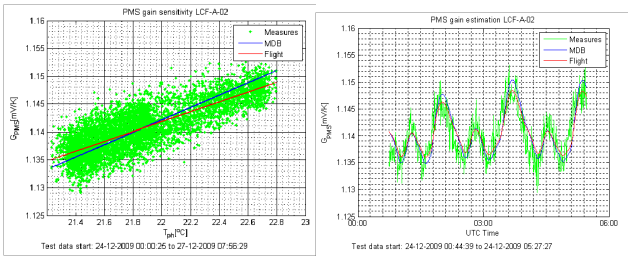

Fig. 2. PMS Gain sensitivity and estimation from physical temperature.

two particular receivers. The periodical variation corresponds to the heater signal frequency. It is apparent that the procedure devised is able to follow the actual value of the offset.

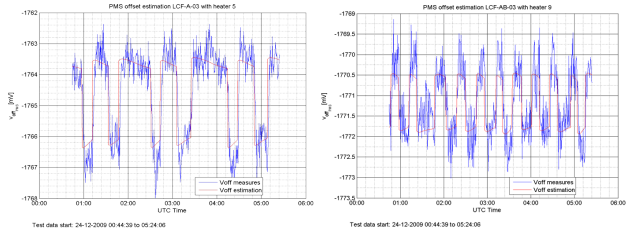

Fig. 3. PMS offset compared with its estimation using the temperature and the heater signal. Plots correspond to two sample receivers

2.3. Correlator gain

The correlator gain G_{kj} is a complex valued parameter. Its amplitude is always around unity and has small variation with time. On the other hand its phase depends on the local oscillator phases which in turn depend on the physical temperature variation with time. To account for this dependance, frequent phase calibration events are carried out interspersed with the normal measurement operation. Several strategies are being studied within the commissioning phase in order to decide the best phase calibration rate. To this end the payload has been programmed to acquire data with different LO calibration rates, ranging from 2 minutes to 14 minutes. The final value will be fixed after a complete analysis of the data acquired, bearing in mind that the final goal is to provide the maximum quality of the geophysical parameters retrievals. Figure 4 shows examples of amplitude and phase of G_{kj}. In this last case, the estimation based on a spline interpolation is also shown. As for the amplitude, in this particular case the variation is as small as 0.05% and in general most baselines present a ripple below 0.3% rms.

2.4. Internal calibration strategy

Once in a month a whole orbit is dedicated to internal calibration. Then, all measurements of PMS gain and offset as

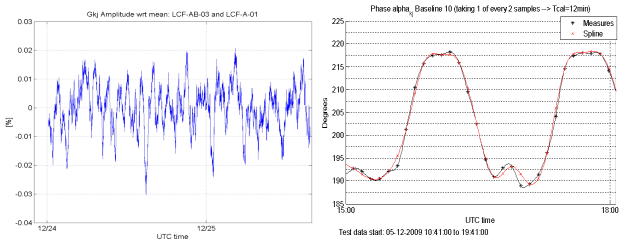

Fig. 4. Sample figures of the amplitude and phase of G_{kj} showing the phase variation due to local oscillator phase drift

well as amplitude of correlator gain are averaged and saved as reference. During science measurement operation, the PMS gain is estimated from this reference corrected using the temperature sensitivity coefficients. The offset is estimated using both the temperature sensitivity coefficient and the correction linked to the heater signal. The amplitude of the correlator gain is used just as measured and finally, the phase of this parameter is estimated by spline interpolation between interspersed measurements.

3. EXTERNAL CALIBRATION

Also once every month the platform rotates in order to point to the cold sky and acquire data for external calibration. The most important effect that must be corrected is the term of the PMS gain not included in the internal calibration procedure, namely the overall loss between the antenna plane and the switch, including the antenna ohmic efficiency. Figure 5 shows the difference in percentage between the PMS gain retrieved using internal calibration and by an independent procedure using the cold sky and the internal resistor [8]. At left, the original results are shown, which have been used to devise a procedure to correct for this inconsistency. At right the gain difference is shown after applying the correction factor. All differences remain below than ± 0.035 dB.

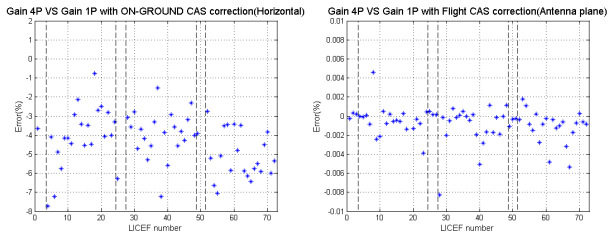

Fig. 5. Comparison between PMS gain retrieved with internal calibration and with external calibration. Left: without correction. Right: after correction

4. BRIGHTNESS TEMPERATURE IMAGES

Once the instrument is fully calibrated, the visibility is injected into the inversion algorithms in order to retrieve brightness temperature images. Examples have been produced for ocean, land and ice using the inversion approach number 3 defined in [9]. Figure 6 shows the average of horizontal and vertical brightness temperature for incidence angles below 30° for a region of the south pacific overlaying a map of salinity available from NOAA climatological data. According to the expected results the brightness temperature decreases for regions with higher salinity. At the right of the figure, the horizontal and vertical brightness temperature for the stable region of lower latitudes is shown. The consistency with the theoretical values computed using the Fresnel reflection coefficient, plot as solid lines, is remarkable, especially in vertical polarization.

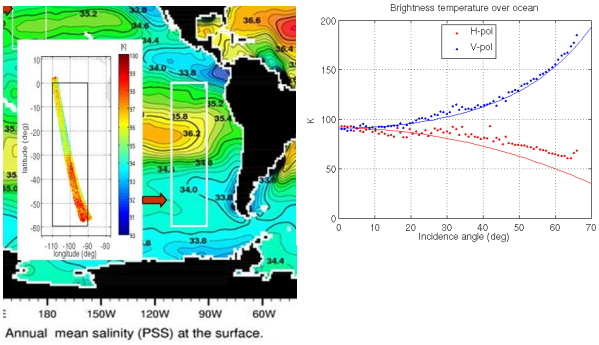

Fig. 6. Brightness temperature images over ocean. Left: map of $(T_H + T_V)/2$ for incidence angles below 30°. Right: Incidence angle dependance and comparison with Fresnel theoretical predictions

Figure 7 shows the retrieved brightness temperature over Antarctica. The figure at the left is a map of the average of horizontal and vertical brightness temperature. The small star marks the location of the Concordia Station in the Dome-C area. At right, there is a plot of the incidence angle dependence for this same area and a comparison with the data measured in the frame of the DOMEX campaign [10]. The general trend is clearly followed, but there is a small bias between both results.

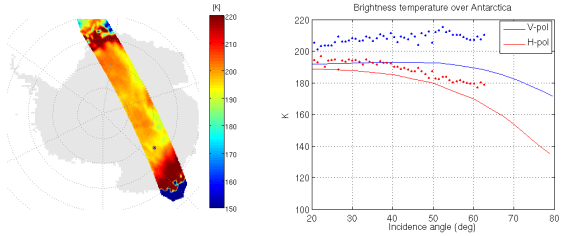

Fig. 7. Brightness temperature images over the Antarctica. Left: map of $(T_H + T_V)/2$. Right: Incidence angle dependance (dots) and comparison with experimental results of [10] (solid lines)

Finally, figure 8 shows again the average of horizontal and vertical brightness temperature for incidence angle lower than

30° in an overpass over South America. The image is superimposed to a map downloaded from Google Earth in order to show the extent of the Amazonian forest matching very well with the area of higher brightness temperature due to the shielding effect of the dense vegetation. The Amazon river itself is perfectly visualized in the image as a zone with lower brightness temperature. Other structures are seen corresponding to different terrains and humidities.

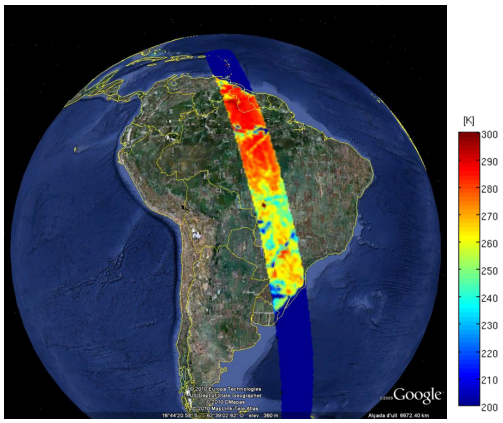

Fig. 8. Map of $(T_H + T_V)/2$ over South America and the Amazonian forest

5. CONCLUSIONS

MIRAS is already providing accurately calibrated visibility measurements as a result of using internal calibration corrected with external calibration. All parameters have been measured and found consistent with the on-ground characterization, showing high stability both in short- and long terms. Quality Brightness Temperature images are then ready to be retrieved, especially in the alias-free field of view and also in the extended part, although with some already expected degradation. Examples over sea, ice and land are given after processing data using the UPC's MIRAS testing software, an independent processing chain from raw data to geo-located brightness temperature. As a general conclusion: SMOS mission is a success and good global maps of Soil Moisture and Ocean Salinity are expected to be produced in the years to come

6. REFERENCES

[1] H. Barré, B. Duesmann, and Y. Kerr, "SMOS. the mission and the system," *IEEE Transactions on Geoscience and Remote Sensing*, vol. 46, no. 3, pp. 587–593, March 2008.

[2] K. McMullan, M. Brown, M. Martín-Neira, W. Rits, S. Ekholm, J. Marti, and J. Lemanzyk, "SMOS: The payload," *IEEE Transactions on Geoscience and Remote Sensing*, vol. 46, no. 3, pp. 594–605, March 2008.

[3] I. Corbella, F. Torres, N. Duffo, V. González-Gambau, A. Camps, and M. Vall-llossera, "On-flight characterization of the SMOS payload during the commissioning phase," in *International Geoscience and Remote Sensing Symposium, IGARSS 2009*, vol. 5. Cape Town, South Africa: IEEE, 12 - 17 July 2009, pp. V–180 – V–183.

[4] I. Corbella, F. Torres, N. Duffo, V. González, A. Camps, and M. Vall-llossera, "Fast processing tool for SMOS data," in *International Geoscience and Remote Sensing Symposium, IGARSS 2008*. Boston(Ma), USA: IEEE, 7 - 11 July 2008.

[5] M. Brown, F. Torres, I. Corbella, and A. Colliander, "SMOS calibration," *IEEE Transactions on Geoscience and Remote Sensing*, vol. 46, no. 3, pp. 646–658, March 2008.

[6] I. Corbella, F. Torres, A. Camps, A. Colliander, M. Martín-Neira, S. Ribó, K. Rautiainen, N. Duffo, and M. Vall-llossera, "MIRAS end-to-end calibration. Application to SMOS L1 processor," *IEEE Transactions on Geoscience and Remote Sensing*, vol. 43, no. 5, pp. 1126–1134, May 2005.

[7] I. Corbella, F. Torres, N. Duffo, M. Martín-Neira, V. González-Gambau, A. Camps, and M. Vall-llossera, "On-ground characterization of the SMOS payload," *IEEE Transactions on Geoscience and Remote Sensing*, vol. 47, no. 9, pp. 3123–3133, September 2009.

[8] F. Torres, V. González-Gambau, and C. González-Haro, "One-point calibration in interferometric radiometers devoted to earth observation," in *Proceedings of SPIE Europe Remote Sensing 2008*. Cardiff. Wales, United Kingdom: SPIE Europe Remote Sensing 2008. Sensors, Systems, and Next-Generation Satellites XII., 15-18 september 2008.

[9] I. Corbella, F. Torres, A. Camps, N. Duffo, and M. Vall-llossera, "Brightness temperature retrieval methods in synthetic aperture radiometers," *IEEE Transactions on Geoscience and Remote Sensing*, vol. 47, no. 1, pp. 285–294, January 2009.

[10] G. Macelloni, M. Brogioni, P. Pampaloni, A. Cagnati, and M. R. Drinkwater, "DOMEX 2004: An experimental campaign at Dome-C antarctica for the calibration of spaceborne low-frequency microwave radiometers," *IEEE Transactions on Geoscience and Remote Sensing*, vol. 44, no. 10, pp. 2642–2653, October 2006.

ONE POINT CALIBRATION IN INTERFEROMETRIC RADIOMETERS: MIRAS/SMOS PRELIMINARY RESULTS

F. Torres[(1)], I. Corbella[(1)], N. Duffo[(1)], V. González-Gambau[(1)], I. Durán[(1)], M. Pablos[(1)] and M. Martín-Neira[(2)]

[(1)]Remote Sensing Laboratory, Universitat Politècnica de Catalunya, Barcelona
SMOS Barcelona Expert Centre. e-mail: xtorres@tsc.upc.edu
[(2)]European Space Agency, European Space Research and Technology Centre, Noordwijk, Holland

ABSTRACT

After the successful launch of the SMOS satellite, on November 2009 at 02:50 CET (01:50 UT) from the Plesetsk Cosmodrome in northern Russia, a preliminary evaluation of the payload calibration strategy has been undertaken in order to assess the instrument performance and establish the operational measurement and calibration configuration. With this objective in mind, this work presents a preliminary study on the performance of the amplitude calibration strategy, a key issue in achieving a stable and accurate operation of the sensor.

Index Terms— radiometer, interferometer, aperture synthesis, amplitude calibration, error assessment.

1. INTRODUCTION

This work has been conducted in the framework of a project devoted to assess the performance of the MIRAS (Microwave Imaging Radiometer with Aperture Synthesis) instrument [1], the single payload of the ESA-SMOS mission [2]. The MIRAS consists of a Y-shape interferometric radiometer basically formed by 72 receivers called LICEF (Lightweight Cost Effective Front End) placed along the three arms. Cross-correlations of the signals collected by each receiver pairs "k,j" give the samples of the so-called visibility function, V_{kj}, which develops into a brightness temperature map by means of a Fourier synthesis technique. Amplitude calibration has a major impact in the final performance since amplitude errors in the visibility samples are directly translated into image distortion (the so-called pixel bias) through this Fourier synthesis process.

MIRAS measures normalized correlations M_{kj} by means of 1-bit digital correlators. As detailed in [3], these measurements are denormalized according to

$$V_{kj} = \frac{\sqrt{T_{sys\,Ak} T_{sys\,Aj}}}{G_{kj}} M_{kj}\,,\; T_{sys\,Ak} = \frac{v_{Ak} - v_{offk}}{G_k^A} \qquad (1)$$

A PMS (Power Measuring System) in each LICEF is used to measure the equivalent system temperature T_{sysAk} (A=V,H) at each antenna plane. The PMS gain at the antenna plane G_k^A and the offset v_{offk} are calibrated by means of the so-called *two-level four-point method* [3]. This calibration procedure makes use of two-level (HOT and WARM) noise sources (CAS=Calibration System) that injects the signals to the LICEF C port by means of the a noise distribution network. A switch placed at the LICEF front end is used to select the measurement mode.

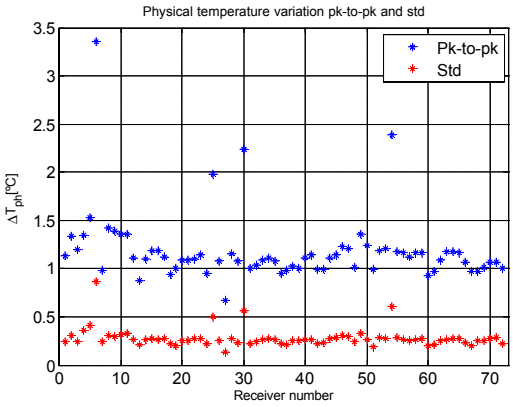

Figure 1. The physical temperature of the 72 LICEF/PMS receivers is well constrained by means of the thermal control.

2. IN-FLIGHT AMPLITUDE CALIBRATION PERFORMANCE

The orbital temperature drift of the 72 receivers is well constrained by the thermal control (fig. 1). However, this small temperature swing produces a non-negligible PMS gain drift that must be corrected for. In this sense, PMS gain in measurement mode at a physical temperature T_{phi} is estimated as

$$G_k^A(T_{ph_i}) = G_k^A(T_{ph_0})\left(1 + S_{Tph}^G\left(T_{ph_i} - T_{ph_0}\right)\right) \qquad (2)$$

PMS gain at the calibration temperature $G_k^A(T_{ph_0})$ is estimated by means of the 4P method during an orbit in calibration mode to be performed, tentatively, every month. PMS gain sensitivity to temperature drift has been measured on-ground and in-flight showing good agreement (fig. 2).

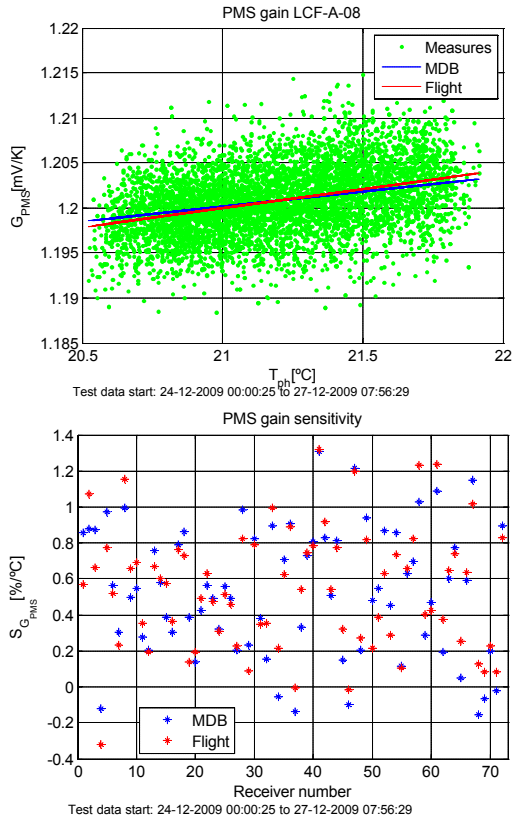

Figure 2. PMS gain sensitivity to physical temperature has been measured both on-ground and in-orbit, showing a high degree of consistency (top). The PMS gain presents low sensitivity to temperature drift (bottom).

PMS gain is foreseen to be calibrated periodically, with an estimated intercalibration period of about two weeks to be frozen by the end of the commissioning phase. Currently, more frequent calibration events during commissioning phase are showing PMS gain pk-to-pk residual drift constrained to ± 0.6 % with relation to the mean value of each PMS in an one month period, well within mission requirements (fig. 3).

3. ONE POINT CALIBRATION

The so-called "one-point calibration" [4][5] is an alternative PMS calibration method that has been developed, as a risk mitigation approach, with two objectives:

- Evaluate (and correct if required) CAS S-parameter residual errors during deep sky calibration.
- Alternative method to track PMS orbital gain drift by means of periodic U-noise injection

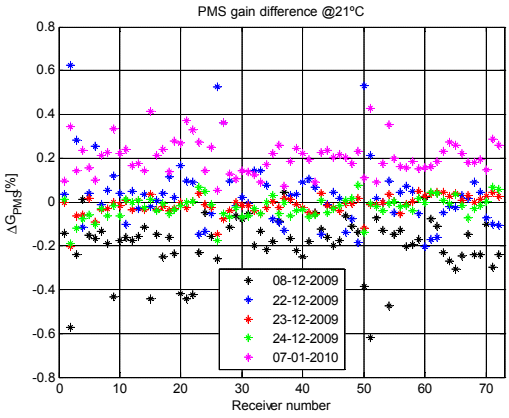

Figure 3. Mean gain drift for each of the 72 PMS gains with relation to their mean value along the one month intercalibration period. Pk-to-pk residual drift below ±0.6%, well within mission requirements.

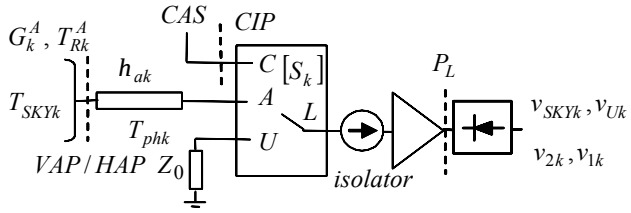

Figure 4. LICEF/PMS front-end scheme to illustrate the one-point calibration scheme.

3.1 Validation of CAS coefficients

Figure 4 gives the block diagram of the PMS front end, showing the main "1P calibration" magnitudes. During periodic (one month) deep sky views, the PMS is simultaneously calibrated by means of the internal 4P CAS system at the calibration plane CIP and by means of the external 1P calibration at the antenna plane. This last is given by

$$G_{1Pk}^A = \frac{v_{Uk} - v_{SKYk}}{T_{phk} - T_{SKYk}} \qquad (3)$$

On the other hand, when translated to the antenna plane, the internal PMS 4P gain is given by [3]:

$$G_{4Pk}^A = \frac{v_{2k} - v_{1k}}{T_{CAS\,N}^2 - T_{CAS_N}^1} \frac{\left|S_{LA_k}\right|^2}{\left|S_{LC_k}\right|^2} \frac{\left|S_{N0}\right|^2}{\left|S_{k0}\right|^2} h_{A_k} \qquad (4)$$

As these two gains are computed at the same plane and at the same temperature, they must be equal:

$$G_{1Pk}^A = G_{4Pk}^A \qquad (5)$$

In order to evaluate the error and compute a correction coefficient, the magnitudes are rearranged in the so-called C_{Nk} coefficients. One is computed from the on-ground parameters. The other uses the flight measurements and can be computed during each external calibration (deep sky views) if required:

$$C_{Nk}^{gnd} = \frac{\left|S_{LA_k}\right|^2}{\left|S_{LC_k}\right|^2} \frac{\left|S_{N0}\right|^2}{\left|S_{k0}\right|^2} h_{A_k} \qquad (6)$$

$$C_{Nk}^{A} = \frac{T_{CAS\,N}^{2} - T_{CAS_N}^{1}}{v_{2k} - v_{1k}} \frac{v_{Uk} - v_{SKYk}}{T_{Uk} - T_{SKYk}^{A}} \qquad (7)$$

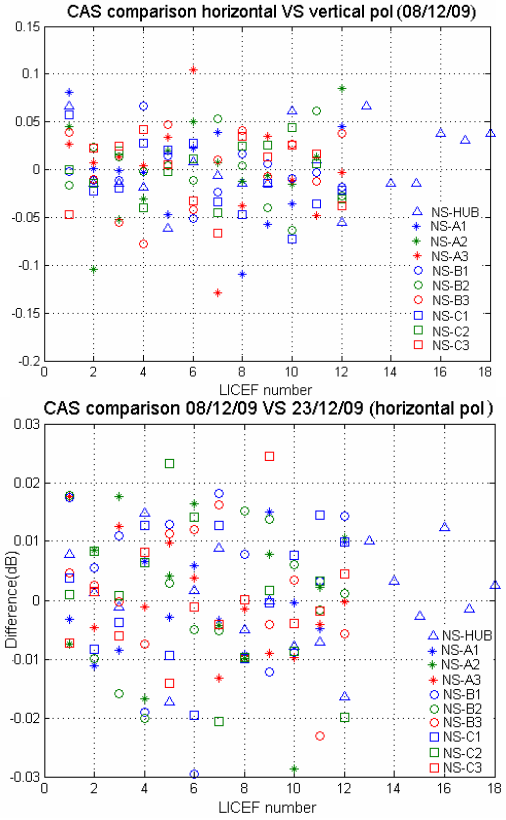

Figure 5. The CAS correction factors, measured at the antenna plane, show low dependency on polarization configuration (top) and very good one-month intercalibration stability (bottom). LICEF numbers correspond to receivers within the HUB (18) or arm segments (12).

The error in the C_{Nk} coefficients can be assigned to a CAS correction factor to force $G_{1Pk}^{A} = G_{4Pk}^{A}$. In order to check the consistency of this correction, some analysis has been undertaken. First, it has been shown that the CAS correction factor presents low dependency on the polarization configuration of the receiver (horizontal or vertical), proving that the dominant error mainly comes from the noise distribution network (fig. 5, top). In second place, the CAS correction factor shows a good repeatability between one-month external calibration events (fig. 5, bottom). After applying the external CAS correction factors the internal 4P PMS gain and the external 1P PMS gain match to 0.023 dB rms error (fig. 6).

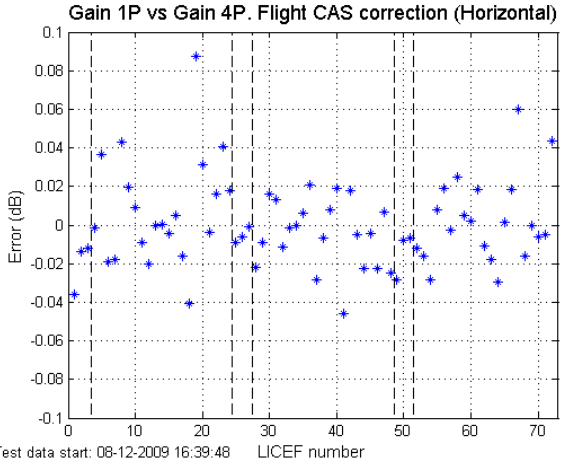

Figure 6. After CAS correction by means of external calibration PMS 1P gain and internal 4P gain match to 0.023 dB RMS

3.2 PMS gain correction by periodic U-noise injection

This method was been devised as an alternative PMS gain estimation to be used in the case that periodic inter-orbit calibration was required. On-ground tests revealed some degree of hysteresis in the behaviour of PMS gain under fast and/or large temperature swings [5]. Since receiver noise temperature showed a better behaviour, in-orbit internal calibration was foreseen by periodically switching the receiver to the internal matched load (U-noise). In this case, PMS gain at the calibration physical temperature T_{phi} is given by

$$G_k^A\left(T_{ph_i}\right) = \frac{v_{Uk} - v_{offk}}{T_{Rk}^A\left(T_{ph_i}\right) + T_{ph_i}} \qquad (8)$$

Where, receiver temperature at T_{phi} is estimated as

$$T_{Rk}^A(T_{ph_i}) = T_{Rk}^A(T_{ph_0})\left(1 + S_{Tph}^{TR}\left(T_{ph_i} - T_{ph_0}\right)\right) \qquad (9)$$

The reference receiver temperature $T_{Rk}^A(T_{ph_0})$ is estimated by means of the 4P method during external calibration (deep sky views) at physical temperature T_{ph0}. Their sensitivity to temperature (about 0.75 K/ºC) was measured during the on-ground characterization when the instrument was tested at the Large Space Simulator (LSS) in Nordwijk, Holand (ESA) [5].

Figure 7 (top), shows an example of this calibration approach applied to unit 30 (LCF-B-03), which is one of the

four outlier units presenting larger temperature swing (fig. 1). The instrument was in calibration mode during a few orbits to assess the behaviour in temperature of several calibration parameters. The black line gives PMS gain calibrations performed every 30 s. The blue line shows the estimation of PMS gain by means of (2). The reference gain has been computed as the mean value for all the orbits, whereas the orbital drift is tracked by using the temperature measurements from a thermistor placed in the front end of each unit, and the sensitivity measured in flight (fig. 2). The effect of hysteresis is clearly seen in the comparison of the two plots (black and blue lines).

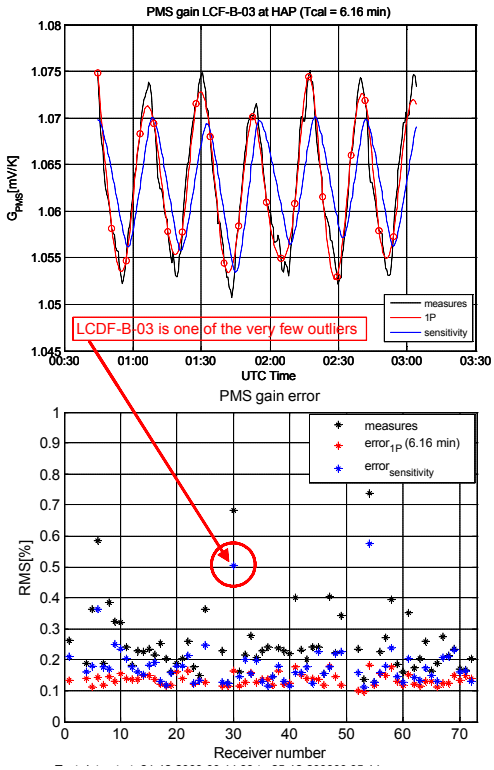

Figure 7. While PMS gain orbital drift presents a small amount of hysteresis, receiver noise temperature is well correlated to temperature drift. This allows a very good track of PMS gain by periodic (6 min) U-noise injection, aligned to the LO phase track mode (Top). However, RMS residual error well within specifications and correction by means of sensitivity has been selected to maximize observation mode (bottom).

On the other hand, the red line presents spline interpolation from 1P calibration PMS gain estimations every 6 min (red dots). In this case, since receiver temperature shows lower hysteresis [5], PMS gain can be tracked by periodic measures of the internal matched load (U-noise injection). Figure 6, bottom, shows the PMS rms gain error for the three methods analyzed from flight data during the first months of the commissioning phase:

a) PMS constant value as the mean value computed from several orbits in calibration mode (black stars). In this case, the error is caused by orbital temperature swing.
b) PMS estimation using the previous value and temperature swing compensation by means of the PMS sensitivity to temperature (blue stars).
c) PMS estimation by means of periodic (6 min) measurements of the matched load (U-noise injection).

Although method c) is the more accurate, method b) has been selected since gives an error well below the 1% PMS system gain error requirement and minimizes the loss of snap shots (maximum observation mode configuration)

4. CONCLUSIONS

In-orbit MIRAS/SMOS amplitude calibration performs well within expectations. Preliminary results during the commissioning phase show that low orbital temperature swing, very good stability and careful temperature compensations keeps PMS gain estimation well below the 1% system error requirement.

5. ACKNOWLEDGMENT

This work was supported by the European Space Agency and EADS-CASA Space Division in the frame of the SMOS project “SMOSops Receiver Technology Study” and by the Spanish Ministry of Science and Innovation and FEDER under project TEC2008-06764-C02-01.

6. REFERENCES

[1] M. Martín-Neira and J. M.Goutoule, "A two-dimensional aperture synthesis radiometer for soil moisture and ocean salinity observations ESA bulletin, no. 92 pp 95-104, November 1997.
[2] Y. Kerr, J. Font, P. Waldteufel, M. Berger. (2000). The Second of ESA's Opportunity Missions: The Soil Moisture and Ocean Salinity Mission–SMOS, ESA Earth Observation Quart. 66, 18f.
[3] I. Corbella, F. Torres, A. Camps, A. Colliander, M. Martín-Neira, S. Ribó, K. Rautiainen, N. Duffo and M. Vall-llossera. “MIRAS end-to-end calibration. Application to SMOS L1 processor.” IEEE Transactions on Geoscience and Remote Sensing. Vol. 43, May 2005, pp:1126-1134.
[4] F. Torres, I. Corbella, A. Camps, N. Duffo, M. Vall-llossera, S. Beraza, C. Gutiérrez and M. Martín-Neira. “Denormalization of visibilities for in-orbit calibration of interferometric radiometers”. IEEE Transactions on Geoscience and Remote Sensing. Vol. 44, No. 10, pp 2679- 2686. Oct. 2006.
[5] F. Torres, V. Gonzàlez-Gambau, C. Gonzàlez-Haro. “One-point calibration in interferometric radiometers devoted to Earth observation”. Proceedings SPIE Europe Remote Sensing 2008. Sensors, Systems, and Next-Generation Satellites XII. Cardiff. Wales, United Kingdom. 15-18 September 2008.

ONE POINT CALIBRATION IN INTERFEROMETRIC RADIOMETERS: MIRAS/SMOS PRELIMINARY RESULTS

F. Torres[(1)], I. Corbella[(1)], N. Duffo[(1)], V. González-Gambau[(1)], M. Pablos[(1)], I. Duran[(1)] and M. Martín-Neira[(2)]

[(1)] Remote Sensing Laboratory, Universitat Politècnica de Catalunya
SMOS Barcelona Expert Centre, Spain. xtorres@tsc.upc.edu
[(2)] European Space Agency, European Space Research and Technology Centre (ESTEC), The Netherlands

ABSTRACT

After the successful SMOS launch on November 2009 a comprehensive evaluation of the payload calibration strategy has been undertaken during a six months commissioning phase. In the frame of the activities devoted to assess the instrument performance and to establish the operational measurement and calibration configuration, this work presents a study on the performance of the so called "one-point" method, an alternative calibration scheme developed as a risk mitigation approach.

1. INTRODUCTION

This work has been conducted in the framework of a project devoted to assess the performance of the MIRAS (Microwave Imaging Radiometer with Aperture Synthesis) instrument [1], the single payload of the ESA-SMOS mission [2]. The MIRAS consists of a Y-shape interferometric radiometer basically formed by 72 receivers called LICEF (Lightweight Cost Effective Front End) placed along the three arms. Cross-correlations of the signals collected by each receiver pairs "*k,j*" give the samples of the so-called visibility function, V_{kj}, which develops into a brightness temperature map by means of a Fourier synthesis technique. Amplitude calibration has a major impact in the final instrument performance since amplitude errors in the visibility samples are directly translated into image distortion (the so-called pixel bias) through this Fourier synthesis process.

MIRAS measures normalized correlations M_{kj} by means of 1-bit/2-level digital correlators. As detailed in [3], these measurements are denormalized according to

$$V_{kj} = \frac{\sqrt{T_{sys_{Ak}} T_{sys_{Aj}}}}{G^A_{kj}} M_{kj}\,,\; T_{sys_{Ak}} = \frac{v_{Ak} - v_{offk}}{G^A_k} \quad (1)$$

A PMS (Power Measuring System) in each LICEF is used to measure the equivalent system temperature T_{sysAk} (A=V,H) at each antenna plane. The fringe-wash term G^A_{kj}, PMS gain at the antenna plane G^A_k and PMS offset v_{offk} are currently calibrated by means of the so-called *two-level four-point (4P) method* [3]. This calibration procedure makes use of the CAS (CAlibration System) based on two-level noise sources (hot and warm) that inject the signals to the LICEF calibration port C by means of a noise distribution network. A highly stable radiometer called NIR (Noise Injection Radiometer) measures the hot and warm signals at the CAS output port N, to be used as references to calibrate the PMS units. A switch placed at the LICEF front end is used to select the instrument operating configuration: measurement mode (V/H) or calibration mode (C/U).

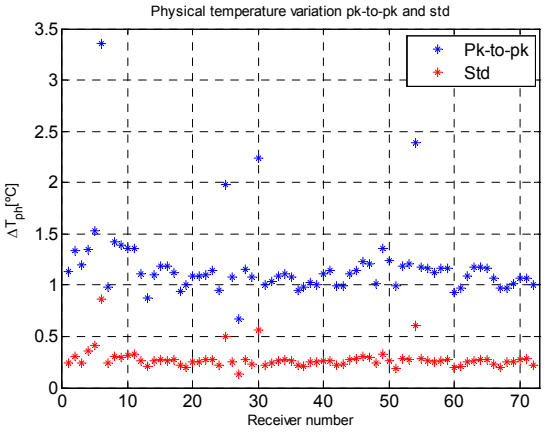

Figure 1. The physical temperature of the 72 LICEF units is well constrained by means of thermal control.

The orbital temperature drift of the 72 receivers is well constrained by the thermal control (fig. 1). However, this small temperature swing produces a non-negligible orbital PMS gain drift that must be corrected for. At each snap shot, PMS_k gain in measurement mode is estimated as

$$G^A_k(T_{phi_k}) = G^A_k(T_{ph0_k})\left(1 + S^{G_k}_{Tph}\left(T_{phi_k} - T_{ph0_k}\right)\right) \quad (2)$$

Where T_{phi_k} is the measurement physical temperature, $G^A_k(T_{ph0_k})$ is PMS gain at the calibration temperature T_{ph0_k} which is estimated by means of the *two-level four-point* method during an orbit in calibration mode to

be performed every two months. Finally, $S_{Tph}^{G_k}$ is PMS gain sensitivity to temperature drift, which has been measured both on-ground and in-flight for each LICEF, showing good agreement.

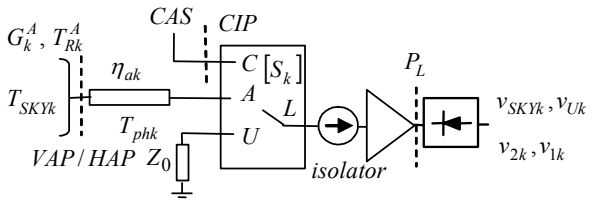

Figure 2. LICEF/PMS front-end scheme to illustrate the one-point calibration scheme.

2. ONE POINT AMPLITUDE CALIBRATION

The so-called *one-point (1P) calibration* [4][5] is an alternative PMS calibration method that has been developed, as a risk mitigation approach, with two main objectives:

- Evaluate (and correct if required) ground CAS S-parameter residual errors, during deep sky calibration.
- Alternative method to track PMS orbital gain drift by means of periodic U-noise injection

As an exploratory option, the instrument has also been tested to operate in the so-called "all-LICEF" mode. In this mode, the *one-point method* is used to estimate the antenna temperature (zero baseline visibility) as the mean value given by the 72 LICEF units.

2.1. Validation of CAS coefficients

Fig. 2 gives the block diagram of the PMS front end, showing the main 1P calibration magnitudes. During periodic (e.g. one month) deep sky views, the PMS is simultaneously calibrated by means of the internal 4P CAS system at the calibration plane CIP and by means of the external 1P calibration at the antenna planes (VAP/HAP). For a perfectly matched passive front end at a constant temperature T_{phk}, [4] shows that switching the instrument to the internal matched load (U port) is equivalent to place an absorber at the same physical temperature in front of the antenna. In this way, 1P PMS_k gain at the antenna plane is given by

$$G_{1Pk}^A = \frac{v_{Uk} - v_{SKYk}}{T_{phk} - T_{SKYk}} \qquad (3)$$

On the other hand, when translated to the antenna plane, the internal PMS 4P gain is given by [3]:

$$G_{4Pk}^A = \frac{v_{2k} - v_{1k}}{T_{CAS\,N}^2 - T_{CAS_N}^1} \frac{\left|S_{LA_k}\right|^2}{\left|S_{LC_k}\right|^2} \frac{\left|S_{N0}\right|^2}{\left|S_{k0}\right|^2} \eta_{A_k} \qquad (4)$$

Where $T_{CAS\,N}^{1,2}$, are the CAS hot and warm temperatures as measured by the reference radiometer (NIR) at CAS port N, S_{N0}, S_{k0} are the CAS s-parameters from the noise source to the reference radiometer and PMS_k calibration ports, respectively, η_{A_k} is the antenna efficiency (A=V/H) and, finally, S_{LA_k}, S_{LC_k} are the switch s-parameters. As the 1P and 4P gains are computed at the same plane and at the same temperature, an error free instrument would yield:

$$G_{1Pk}^A = G_{4Pk}^A \qquad (5)$$

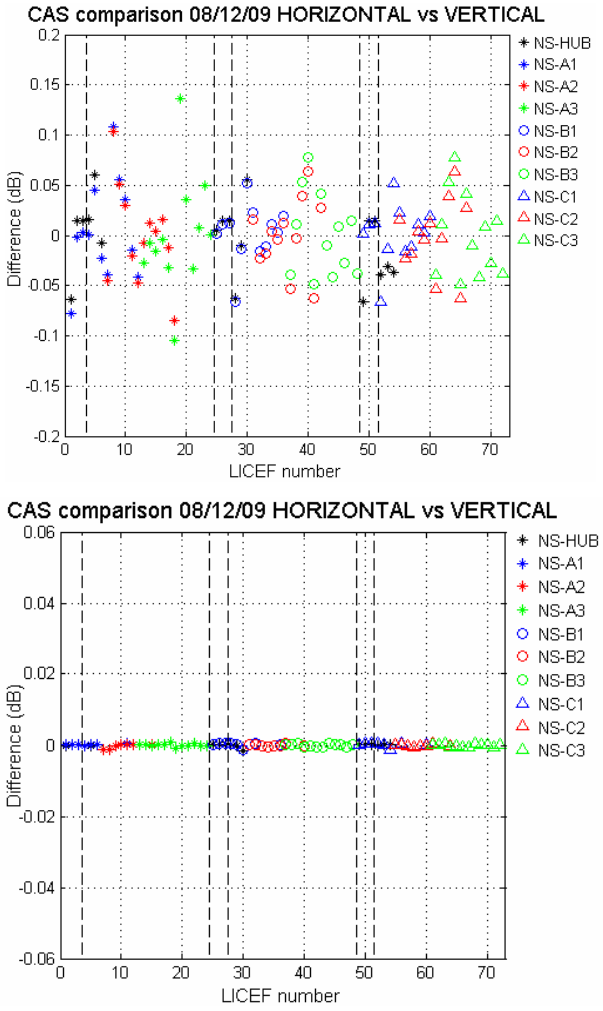

Figure 3. Comparison of CAS correction factors computed from horizontal and vertical amplitude calibrations by using ground antenna efficiencies (top) and flight antenna efficiencies (bottom).

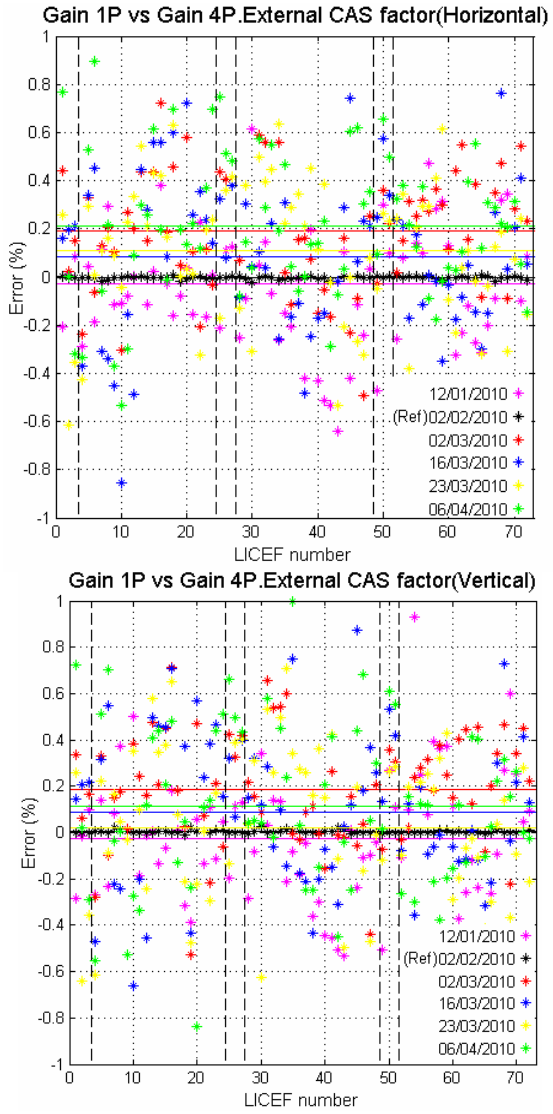

Figure 4. Matching between 1P and 4P PMS calibration after CAS and antenna efficiency correction (02/02/2010) for a number of calibration events. Matching well below the 1% RMS error requirement in a three months period.

In order to evaluate the error and compute a correction coefficient, the parameters in (5) are rearranged in the so-called C_{Nk} coefficients. One of them is computed from the on-ground parameters.

$$C_{Nk}^{gnd} = \frac{\left|S_{LA_k}\right|^2}{\left|S_{LC_k}\right|^2}\frac{\left|S_{N0}\right|^2}{\left|S_{k0}\right|^2}\eta_{A_k} \tag{6}$$

The other one uses the flight measurements and is computed during each external calibration (deep sky views):

$$C_{Nk}^{A} = \frac{T_{CAS\,N}^{2} - T_{CAS_N}^{1}}{v_{2k} - v_{1k}}\frac{v_{Uk} - v_{SKYk}}{T_{phk} - T_{SKYk}} \tag{7}$$

The error in the C_{Nk} coefficients can be assigned to a CAS correction factor to be applied to the CAS ground coefficients. In order to check the consistency of this correction, some analysis has been undertaken and presented hereafter.

The C_{Nk} coefficients can be computed from horizontal and vertical PMS gains. Both magnitudes should be equal, since each LICEF has a single CAS coefficient related to its calibration port CIP. Fig. 3 (top) shows that the ground characterization of the PMS front end is quite good since vertical and horizontal CAS coefficients match to $\pm$ 0.14 dB. However, when using antenna efficiencies computed from the external deep sky views, the match is almost perfect (fig. 3, bottom). That is, external calibration decouples the ground characterization errors in antenna efficiency (two values per PMS) from the CAS ground errors (one value per PMS). The good consistency of CAS coefficients computed from horizontal and vertical calibration reveals both the good quality of the measurements and the front-end model.

In second place, the CAS correction factors have shown very good repeatability in a three months period. In Fig. 4 the external antenna efficiency and external CAS factors have been computed from the calibration event on 02/02/2010 (reference calibration). These coefficients have then been used to calibrate the internal 4P gain in different calibration events from 12/01/2010 to 06/04/2010 to be compared with new 1P external calibrations. In this period, the match between internal and external gains remains within $\pm$ 1% pk-to-pk, well below the system requirement of 1% RMS error. There is a small 0.2% bias in the error that requires further assessment. In any case, this bias is corrected by the periodic external calibration events.

2.2. PMS gain correction by periodic U-noise injection

This method has been devised as an alternative PMS gain estimation to be used in the case that periodic inter-orbit amplitude calibration was required. On-ground tests revealed some degree of hysteresis in the behaviour of PMS gain under fast and/or large temperature swings [5]. Since receiver noise temperature showed a better behaviour, in-orbit internal calibration was foreseen by periodically switching the receiver to the internal matched load (U-noise). In this case, PMS_k gain at the calibration physical temperature T_{phi_k} is given by

$$G_k^A\left(T_{phi_k}\right) = \frac{v_{Uk} - v_{offk}}{T_{Rk}^A\left(T_{phi_k}\right) + T_{phi_k}} \tag{8}$$

Where, receiver temperature at T_{phi} is estimated as

$$T_{Rk}^{A}(T_{phi_k}) = T_{Rk}^{A}(T_{ph0_k}) + S_{Tph}^{TR}\left(T_{phi_k} - T_{ph0_k}\right) \qquad (9)$$

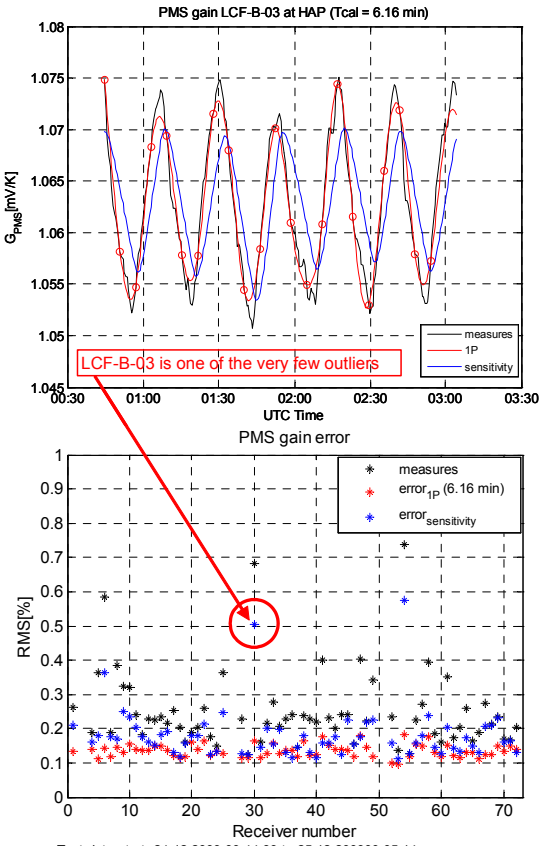

Figure 5. PMS receiver noise temperature is well correlated to temperature drift. This allows a very good track of PMS gain by periodic (6 min) U-noise injection, aligned to the LO phase track mode (Top). However, the 4P PMS gain calibration method has been selected since RMS residual error is well within the 1% rms error requirement (bottom).

The reference receiver temperature $T_{Rk}^{A}(T_{ph0_k})$ is estimated by means of the 1*P* method [5] during external calibration (deep sky views) at the calibration physical temperature T_{ph0_k}. T_{Rk}^{A} sensitivity to temperature (about 0.75 K/ºC) was measured during the on-ground characterization when the instrument was tested at the Large Space Simulator (LSS) in Nordwijk, Holland (ESA) [5].

Figure 5 (top), shows an example of the 1P calibration approach applied to unit 30 (LCF-B-03), which is one of the four outlier units presenting the largest temperature swing (fig. 1). The instrument was in calibration mode during a few orbits to assess the behaviour in temperature of several calibration parameters. The black line gives PMS gain calibrations performed every 30 s. The blue line shows the estimation of PMS gain by means of (2). The reference gain has been computed as the mean value for all the orbits, whereas the orbital drift is tracked by using the temperature measurements from a thermistor placed at the front end in each unit. The effect of a certain amount of hysteresis is clearly seen in the comparison of the two plots (black and blue lines), yielding a moderate rms error (red circle in fig. 5, bottom).

On the other hand, the red line presents spline interpolation from 1P calibration PMS gain estimations every 6 min (red dots). In this case, since receiver temperature shows lower hysteresis [5], PMS gain can be tracked by periodic measures of the internal matched load (U-noise injection). Figure 5, bottom, shows the PMS rms gain error for the three methods analyzed from flight data during the first months of the commissioning phase:

a) PMS gain constant as the mean value computed from several orbits in calibration mode (black stars). In this case, the error is caused by orbital temperature swing.
b) PMS gain estimation using the last calibration (more than one orbit apart) and temperature swing compensation by means of the PMS sensitivity to temperature (blue stars).
c) Inter-orbit PMS estimation by means of periodic (E.g. 6 min) measurements of the matched load (U-noise injection).

Although method c) is the most accurate, method b) has been selected since gives an error well below the 1% RMS system gain error requirement and minimizes the loss of snap shots (maximum observation mode configuration).

2.3. All-LICEF antenna temperature

Fig. 6 shows SMOS antenna temperature -V(0,0)- computed as the mean antenna temperature estimated by the 66 LICEF units. For each LICEF, antenna temperature at the antenna plane is computed as

$$\hat{T}_{Ak} = \frac{v_{Ak} - v_{offk}}{\hat{G}_k^A} - \hat{T}_{Rk}^A \qquad (10)$$

Where PMS gain $\hat{G}_k^A$, offset v_{offk} and receiver temperature $\hat{T}_{Rk}^A$ are computed by means of the external PMS cold sky calibration directly at VAP/HAP, and corrected in physical temperature T_{phk} for each snap shot, as given in (9).

All-LICEF antenna temperature is compared in H/V to the mean antenna temperature measured by the three NIR units. The plots show antenna temperature evolution (horizontal and vertical polarizations) within

an orbit on 02/02/2010. As shown in fig. 6, the coarse behaviour given by the NIR units and the All-LICEF mode is very similar. Some additional analysis reveals that the performance of each single LICEF unit yields a moderate error in the estimation of antenna temperature, however, the average of the 66 LICEF estimations gives a performance similar to the NIR units. Fig. 6 shows the capability of both, the NIR and the all-LICEF mode to track antenna temperature orbital evolution. However, further analysis is still required to fully assess the absolute accuracy of the measurements.

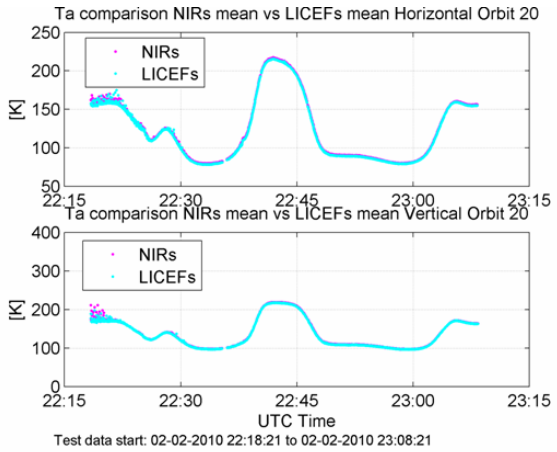

Figure 6. Comparison of antenna temperature (horizontal and vertical polarizations) measured by the all-LICEF mode and by the NIR units on 02/02/2010, showing similar performance.

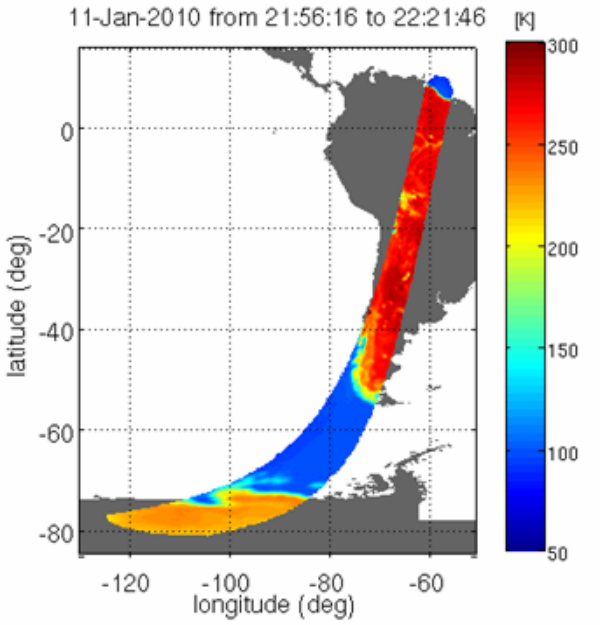

Figure 7. Brightness temperature map retrieved from one orbit in all-LICEF configuration (11-01/2010 all-LICEF test).

In order to illustrate the capability of the one-point calibration method in retrieving V(0,0), fig. 7 presents the brightness temperature retrieval from data collected on January 2010 within the "all-LICEF" test.

3. CONCLUSIONS

In-orbit MIRAS/SMOS amplitude calibration performs well within expectations. First analysis performed during the commissioning phase show that low orbital temperature swing, very good stability and careful temperature compensations keep PMS gain estimation well below the 1% rms system error requirement.

The one point method has proved to work properly both to check (and fine tune) the performance of the current *four point two level* amplitude calibration method and as a risk mitigation alternative to be used, if required, to retrieve the antenna temperature (all-LICEF mode) or to track orbital PMS gain drift.

4. ACKNOWLEDGMENT

Work supported by the European Space Agency and EADS-CASA Space Division in the frame of the SMOS project and by the Spanish Ministry of Science and Innovation and FEDER under projects TEC2008-06764-C02-01 and MIDAS-5 ESP2007-65667-C04-0

6. REFERENCES

1. Martín-Neira, M. and Goutoule, J. M. "A two-dimensional aperture synthesis radiometer for soil moisture and ocean salinity observations *ESA bulletin*, no. 92 pp 95-104, November 1997.
2. Kerr, Y.; Font, J.; Waldteufel, P. & Berger, M. (2000). The Second of ESA's Opportunity Missions: The Soil Moisture and Ocean Salinity Mission–*SMOS, ESA Earth Observation Quart.* 66, 18f.
3. Corbella, I.; Torres, F.; Camps, A.; Colliander, A.; Martín-Neira, M.; Ribó, S.; Rautiainen, K.; Duffo, N & Vall-llossera, M. "MIRAS end-to-end calibration. Application to SMOS L1 processor." *IEEE Transactions on Geoscience and Remote Sensing*. Vol. 43, May 2005, pp:1126-1134.
4. Torres, F.; Corbella, I.; Camps, A.; Duffo, N. Vall-llossera, M.; Beraza, S.; Gutiérrez, C. & Martín-Neira, M. "Denormalization of visibilities for in-orbit calibration of interferometric radiometers". *IEEE Transactions on Geoscience and Remote Sensing*. Vol. 44, No. 10, pp 2679- 2686. Oct. 2006.
5. Torres, F.; Gonzàlez-Gambau, V. & Gonzàlez-Haro, C. "One-point calibration in interferometric radiometers devoted to Earth observation". *Proceedings SPIE Europe Remote Sensing 2008. Sensors, Systems, and Next-Generation Satellites XII. Cardiff*. Wales, United Kingdom. 15-18 September 2008.

One point calibration in interferometric radiometers: MIRAS/SMOS preliminary results

F. Torres[1], I. Corbella[1], N. Duffo[1], V. González-Gambau[1], I. Durán[1], M. Pablos[1] and M. Martín-Neira[2]
[1]Remote Sensing Laboratory, Universitat Politècnica de Catalunya, SMOS Barcelona Expert Centre. xtorres@tsc.upc.edu
[2]European Space Agency, European Space Research and Technology Centre (ESTEC), Noordwijk, Holland

INTRODUCTION. After the successful launch of the SMOS satellite, on November 2009 at 02:50 CET (01:50 UT) from the Plesetsk Cosmodrome in northern Russia, a preliminary evaluation of the payload calibration strategy has been undertaken in order to assess the instrument performance and fix the operational measurement and calibration configuration. This work presents the performance of the amplitude calibration strategy, a key issue in achieving a stable and accurate operation of the sensor.

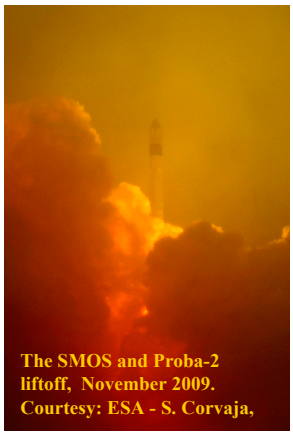

Calibrated visibility at the antenna plane

$$V_{kj}^{A} = \frac{\sqrt{T_{sys_{Ak}} T_{sys_{Aj}}}}{G_{kj}^{A}} M_{kj}$$

FWF at t =0 — Normalized correlation

System temperature at the antenna plane is measured by means of the Power Measurement System (PMS):

$$T_{sys_{Ak}} = \frac{v_{Ak} - v_{offk}}{G_k^A}$$

PMS gain orbital drift correction

$$G_k^A(T_{ph_i}) = G_k^A(T_{ph_0})\left(1 + S_{Tph}^G\left(T_{ph_i} - T_{ph_0}\right)\right)$$

Meas T_{ph} — Cal T_{ph} — Gain sensitivity

SMOS baseline amplitude calibration approach by internal noise injection

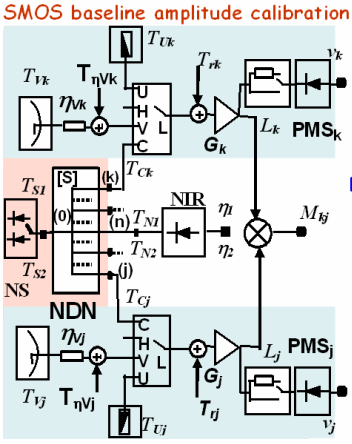

PMS calibration: 2-level 4-point method

$$v_{1k} = v_{offk} + G_k^C T_{sysC_k}^{WARM} \qquad v_{2k} = v_{offk} + G_k^C T_{sysC_k}^{HOT}$$

$$v_{3k} = v_{offk} + \frac{G_k^C}{L_k} T_{sysC_k}^{WARM} \qquad v_{4k} = v_{offk} + \frac{G_k^C}{L_k} T_{sysC_k}^{HOT}$$

PMS offset from the 4 point PMS voltages

$$v_{offk} = \frac{v_{2k}v_{3k} - v_{1k}v_{4k}}{(v_{2k} - v_{4k}) - (v_{1k} - v_{3k})}$$

PMS gain calibrated at plane C relative to the NIR reference radiometer

$$G_k^C = \frac{v_{2k} - v_{1k}}{T_{N2} - T_{N1}} \frac{|S_{n0}|^2}{|S_{k0}|^2}$$

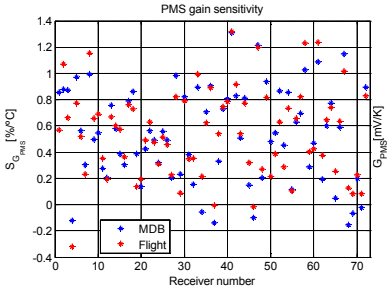

The 72 PMS gains show low sensitivity to temperature drift: a mean value of 0.6 %/ºC.

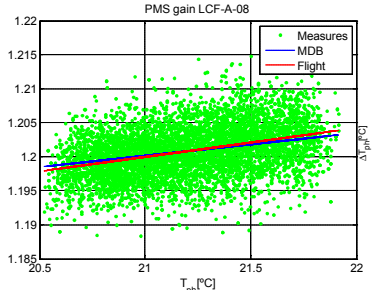

The 72 PMS gain sensitivities to temperature drift measured in-flight along several orbits in calibration mode show good agreement with the on-ground values

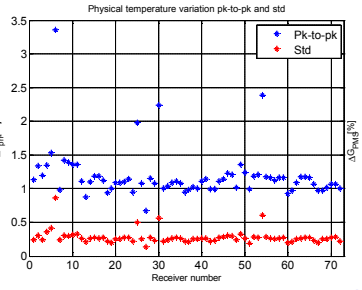

The orbital temperature swing of the 72 receivers is well constrained by the thermal control.

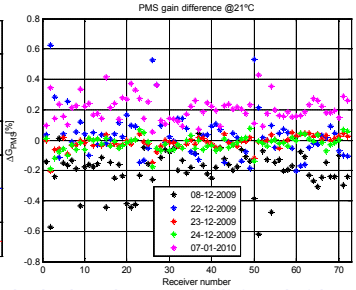

The plot shows the mean gain drift for each of the 72 PMS gains wrt to their mean value along the one month intercalibration period. Pk-to-pk residual drift below ±0.6%, well within mission requirements

ONE POINT CALIBRATION: 1) Used to correct CAS S-parameter residual errors during deep sky calibration.
2) Alternative method to correct PMS orbital drift by means of U-noise injection: Risk mitigation approach.

1) CAS 4P and external 1P PMS gains must be equal during deep sky calibration

$$G_{1Pk}^A = G_{4Pk}^A \qquad C_{Nk}^{gnd} = C_{Nk}^A$$

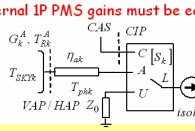

CAS 4P PMS gain at HAP/VAP — Ground C_{blk} Coefficient

$$G_{4Pk}^A = \frac{v_{2k} - v_{1k}}{T_{CAS\,N}^2 - T_{CAS\,N}^1} \frac{|S_{LA_k}|^2}{|S_{LC_k}|^2} \frac{|S_{N0}|^2}{|S_{k0}|^2} \eta_{A_k} \qquad C_{Nk}^{gnd} = \frac{|S_{LA_k}|^2}{|S_{LC_k}|^2} \frac{|S_{N0}|^2}{|S_{k0}|^2} \eta_{A_k}$$

External 1P PMS gain at HAP/VAP — Deep sky C_{blk} Coefficient

$$G_{1Pk}^A = \frac{v_{Uk} - v_{SKYk}}{T_{phk} - T_{SKYk}} \qquad C_{Nk}^A = \frac{T_{CAS\,N}^2 - T_{CAS\,N}^1}{v_{2k} - v_{1k}} \frac{v_{Uk} - v_{SKYk}}{T_{Uk} - T_{SKYk}^A}$$

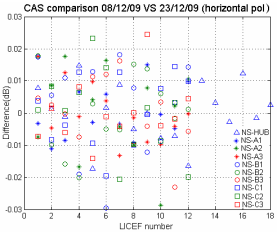

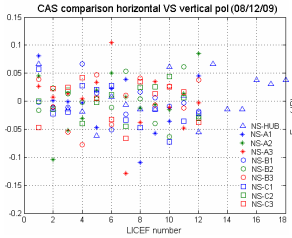

The CAS correction factors, measured at VAP/HAP, show very good one-month intercalibration stability (left) and low dependency on polarization configuration. LICEF numbers correspond to receivers within the HUB (18) or arm segments (12)

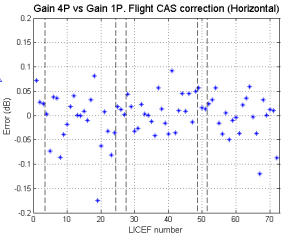

After CAS correction by means of external calibration PMS 1P gain and internal 4P gain match to 0.046 dB RMS

2) PMS 1P gain orbital drift correction by periodic U-noise injection (backup method)

$$G_k^A(T_{ph_i}) = \frac{v_{Uk} - v_{offk}}{T_{Rk}^A(T_{ph_i}) + T_{ph_i}} \qquad T_{Rk}^A(T_{ph_i}) = T_{Rk}^A(T_{ph_0})\left(1 + S_{Tph}^{TR}\left(T_{ph_i} - T_{ph_0}\right)\right)$$

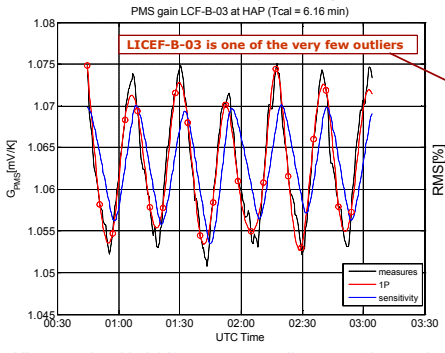

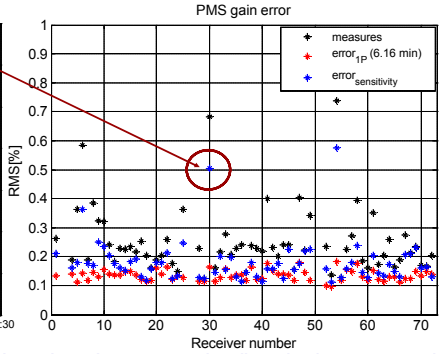

While PMS gain orbital drift presents a small amount of hysteresis, receiver noise temperature is well correlated to temperature drift. This allows a very good track of PMS gain by periodic (6 min) U-noise injection, aligned to the LO phase track mode. However, RMS residual error well within specifications and correction by means of sensitivity has been selected to maximize observation mode.

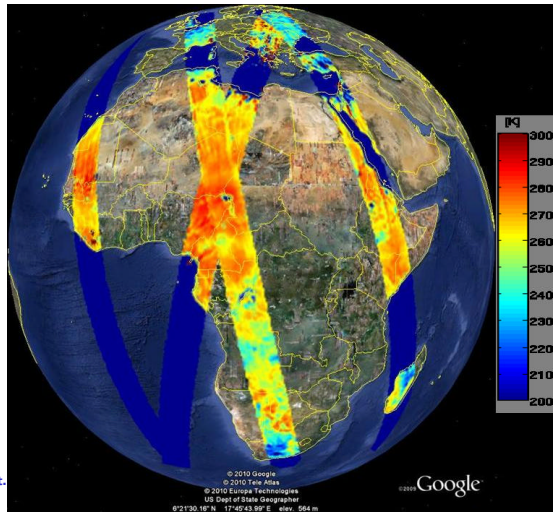

CONCLUSIONS

- **In-orbit MIRAS/SMOS amplitude calibration performs well within expectations. Low temperature swing, very good stability and careful temperature compensation keeps PMS gain estimation well below the 1% RMS system error requirement.**

Acknowledgments: This work was supported by the European Space Agency and EADS-CASA Space Division in the frame of the SMOS project. This work has been partially funded by the Spanish Ministry of Science and Innovation and FEDER under project TEC2008-06764-C02-01.